University of Southampton

Faculty of Engineering and Physical Sciences

School of Engineering

Numerical modelling and development of design rules for novel demountable steel-concrete composite bridges

by

Eirini Tzouka

ORCID ID: 0000-0003-4624-7837

Thesis for the degree of Doctor of Philosophy in Engineering and the Environment

November 2020

University of Southampton

Abstract

Faculty of Engineering and Physical Sciences

School of Engineering

Thesis for the degree of Doctor of Philosophy in Engineering and the Environment

Numerical modelling and development of design rules for novel demountable steel-concrete composite bridges

by

Eirini Tzouka

This research project aims to study the structural behaviour of novel demountable shear connectors for steel-concrete composite bridges. Two shear connectors are investigated, namely locking-nut shear connector (LNSC) and friction-based shear connector (FBSC). The investigated shear connectors promote precast construction, and therefore significantly reduce the construction costs. In addition, they allow full disassembly of bridges and as a result, deteriorating bridge components can be easily replaced. In this way, the bridge design life is extended, and the deteriorating components can be recycled or reused. Both connectors use high-strength bolts instead of conventional headed studs to achieve composite action. The bolts are fastened to the top flange of the steel beam using either a locking-nut (LNSC) or grouted countersunk hole configurations (FBSC) that prevent the bolts to slip within their holes. The connectors also use precast concrete to speed up the construction process.

In this research thesis, three-dimensional (3D) finite element (FE) models are developed in ABAQUS software to study the structural behaviour of LNSCs and FBSCs in steel-concrete composite bridges. Firstly, steel-concrete push-out FE models are built and tested in order to evaluate the shear capacity of the connectors. Subsequently, full-scale steel-concrete composite beams equipped with FBSCs are numerically tested using a four bending configuration to assess their flexural behaviour. The accuracy of the FE models is verified by comparing the FE results with experimental results available in the literature. Extensive parametric studies are also carried out, using the FE models, to expand the experimental data bank. The effect of significant parameters on the structural behaviour and the capacity of the connectors is evaluated. Based on the parametric results, simple design rules are proposed to calculate the shear resistance of both connectors.

Table of Contents

Table of Tables

Table of Figures

Symbols

Latin upper-case letters

A_f	Area at fracture
A_s	Tensile stress area of the bolt
C	Neutral axis of composite section
C_c	Neutral axis of concrete slab
C_s	Neutral axis of steel beam
D	Damage variable
D_c	Compressive damage variable
D_t	Tensile damage variable
E	Modulus of elasticity
E_{cm}	Secant modulus of elasticity of concrete
F_c	Compressive force
F_t	Tensile force
G_f	Energy required to open a unit area of crack
K_c	Ratio of the second stress invariant on the tensile meridian to that on the compressive meridian
L_{ch}	Characteristic length of an element
$M_{pl,Rd,f}$	Design value of the plastic resistance moment of the composite section with full shear resistance
$M_{pl,Rd,p}$	Design value of the plastic resistance moment of the composite section with partial shear resistance
N_c	Axial force of concrete
N_{FBSC}	Axial force of friction-based shear connectors
N_S	Axial force of steel beam
P	Instantaneous load
P_f	Load at fracture
P_{Rd}	Design value of the shear resistance of a single connector
P_{Rk}	Characteristic value of the shear resistance of a single connector
S_{ult}	Slip at fracture
T	Pretension force

Latin lower-case letters

b_{eff}	Total effective width
b_f	Width of the flange of a steel section
d	Diameter

d_{max}	Maximum aggregate size
d_{sh}	Shank diameter of the stud
e	Eccentricity
f_{b0}/f_c'	Ratio of the compressive strength under biaxial loading to uniaxial compressive strength
f_c	Compressive strength of concrete
f_{ck}	Characteristic compressive cylinder strength of concrete at 28 days
f_{cm}	Mean value of concrete cylinder compressive strength
f_{ctm}	Mean value of axial tensile strength of concrete
f_t	Tensile strength of concrete
f_y	Yield strength of steel
f_u	Ultimate strength of steel
h_c	Thickness of the concrete slab
h_s	Total height of the steel beam
h_{sc}	Overall height of a stud connector
k_{sc}	Stiffness of a shear connection
l	Instantaneous gauge length
l_0	Initial gauge length
n	Material parameter for concrete
s	Engineering area
t_f	Thickness of a flange of the structural steel section
t_w	Thickness of the web of the structural steel section
u^{pl}	Equivalent plastic displacement
u_f^{pl}	Equivalent plastic displacement at fracture

Greek lower-case letters

α	Factor; parameter
α_v	Factor; parameter
β	Factor; parameter
γ_{M0}	Partial factor for structural steel applied to resistance of cross-sections
γ_V	Partial factor for design shear resistance of a headed stud
δ_u	Maximum slip measured in a test at the characteristic load level
ε_{cu1}	Compressive strain in the concrete at the peak stress f_c
ε_D^{pl}	Equivalent plastic strain at the onset of damage
ε_f	Strain at fracture
ε_n^{pl}	Uniaxial true plastic strain at the onset of necking
ε_y	Yield strain

ε_u	Ultimate strain
η	Stress triaxiality factor
μ	Friction coefficient
σ	True stress
σ_c	Compressive stress
σ_f	True stress at fracture
σ_t	Tensile stress
ψ	Dilation angle

Research Thesis: Declaration of Authorship

Print name: Eirini Tzouka

Title of thesis: Numerical modelling and development of design rules for novel demountable steel-concrete composite bridges

I declare that this thesis and the work presented in it are my own and has been generated by me as the result of my own original research.

I confirm that:

1. This work was done wholly or mainly while in candidature for a research degree at this University;
2. Where any part of this thesis has previously been submitted for a degree or any other qualification at this University or any other institution, this has been clearly stated;
3. Where I have consulted the published work of others, this is always clearly attributed;
4. Where I have quoted from the work of others, the source is always given. With the exception of such quotations, this thesis is entirely my own work;
5. I have acknowledged all main sources of help;
6. Where the thesis is based on work done by myself jointly with others, I have made clear exactly what was done by others and what I have contributed myself;
7. Part of this work has been published as:
   Tzouka, E., Karavasilis, L.T., Kashani, M.M., Sheida, A., (2019), Finite element model for a novel demountable shear connector for steel-concrete composite bridges, presented at International Accelerated Bridge Construction Conference, including Automation, Service Life and Ultra-High Performance Concrete, Miami, 12-13 December 2019.

Signature: E.Tzouka Date:14/11/2020

Acknowledgements

I would like to express my sincere gratitude to my supervisors, Dr Theodore L. Karavasilis, Dr Mohammad M. Kashani and Dr Sheida Afshan for their guidance, generous help, continuous encouragement and support throughout the whole period of this research. Their immense knowledge and plentiful experience have encouraged me in all the time of my academic research and daily life.

Besides my supervisors, I would like to thank Prof Richard Jat Yuen Liew for his interesting ideas, suggestions and corrections during my short-term visit at National University of Singapore. I cannot express how grateful I am for having the opportunity to work with and learn from him.

Getting through my dissertation required more than academic support, and I have many people to thank for making this experience much easier and enjoyable. First and foremost, I would like to thank my partner, Vasileios Pantazopoulos, for providing me with unfailing support and continuous encouragement throughout my years of study and through the process of researching and writing my thesis. It would have been impossible for me to complete this thesis without his support. I would also like to thank my friends, Angelis Karlos, Athanasios Papaioannou, Audrey Hu, Despoina Manouseli, Elena Perdomo, Felipe Vasquez Stuardo, Giannis Katsivalis, Orestis Vryonis and Tatiana Alvares Sanches for always being available and listening to my thoughts and problems.

Finally, I must also express my very profound gratitude to my parents Georgios and Zoi and my sister Paraskevi for providing me with support and encouragement, not only during my thesis but during my entire life. This accomplishment would not have been possible without you!

Chapter 1 Introduction

1.1 Introduction – Research gap

During the last two decades, rapid deterioration of bridges has become a major issue that causes severe economic and socio-economic losses to the states. The failure of the bridge components is mainly attributed to the poor construction and the limited maintenance of the bridge. Furthermore, the rampant increase in the population of the planet and the urbanization has led to a change in bridge design regulations. Therefore, many of the existing bridges no longer fulfil the current functional requirements and safety standards. On the top of that, unforeseen natural phenomena such as floods and strong winds, usually attributed to the climate change, contribute to the faster deterioration of the infrastructure.

Rehabilitation projects involve inspection, repair and strengthening of the bridge. In some cases, where the bridge components present serious damaged, their replacement is even necessary. These operations usually lead to huge economic losses as well as socio-economic loses caused by the disruption in transport networks. Consequently, the EU must invest in rehabilitation projects to ensure the serviceability and the safety of their bridges. According to EU funded BRIME project in 2001, 37% of the bridges in the UK present deficiencies, with the main cause being the corrosion of the reinforcement [1]. In the USA, 39% of the nation's bridges are 50 years or older, meaning that they are approaching the end of their design life and 9.1% of them were characterised as structurally deficient [2].

One of the most serious problems in maintaining and rehabilitating bridges is the deterioration of bridge decks. In the case of steel-concrete composite bridges, removing and replacing the deteriorating deck is a challenging process due to the connection between the deck and the steel beam. The connection is usually achieved through conventional headed studs, which are welded on the top flange of the steel beam and are fully embedded within the concrete deck. Therefore, removing the deck involves drilling and crushing the concrete around the shear connectors and then breaking the deck into manageable sections [3]. As an alternative to the conventional headed studs, bolted shear connectors that allow rapid bridge disassembly and allow the easy replacement of the deteriorating bridge components have been investigated over the last decades. Bolted shear connectors facilitate installing and dismantling of steel-concrete composite structures without reducing their structural integrity and efficiency and therefore extend the bridge design life.

The use of bolted shear connectors in steel-concrete composite beams is also considered a sustainable design method that may contribute to the reduction of the greenhouse gas (GHG) emissions from the construction industry. In 2014, about a fifth of the EU's total greenhouse gas (GHG) emissions came from manufacturing industries and construction [4]. In its White Paper published in 2011, the European Commission set a target of 60% reduction of GHG emissions from 1990 levels by 2050 [5]. To achieve GHG emissions reductions in the construction industry, structures may be designed using sustainable methods that minimize the consumption of non-renewable resources and promote the reuse of the construction materials. Among other materials, structural steel can be reused many times without compromising its material properties. Therefore, the use of bolted shear connectors in steel-concrete composite beams will allow the easy dismantling of the steel beams and their subsequent recycling.

Bolted shear connectors also promote the prefabrication of the various structural components of bridges. Steel-concrete composite beams using prefabricated members require significantly less time to build than on-site construction. This is due to better upfront planning; elimination of on-site weather factors and quicker fabrication as multiple pieces can be constructed simultaneously. The reduction in construction time can significantly save on construction financing costs that allows construction companies to grow. In addition, since sub-assemblies are created in a factory-controlled environment, the risk of problems associated with moisture, environmental hazards and dirt are minimized.

Their structural behaviour of shear connectors for steel-concrete composite beams is usually investigated by conducting push-out tests in accordance with Eurocode 4 [6], [7]. Although push-out tests are considered a straightforward method to determine the capacity of the shear connector and provide a clear insight to their behaviour, they are costly and time consuming. As an alternative, finite element (FE) modelling has gained increasing awareness and became well accepted in the research community as an effective method to study the behaviour of shear connections. Apart from the cost-effectiveness of the method, finite element (FE) modelling of shear connections is an effective tool to investigate in detail the behaviour of the connections and evaluate the effect of significant parameters on their capacity.

Although bolted shear connectors present several advantages discussed in the paragraphs above, there is limited research on their behaviour. In addition, the current design codes (Eurocode [6],[7]) do not provide design rules and recommendations for bolted shear connectors in steel-concrete composite beams. Therefore, the aim of this research is to produce effective design equations that estimate the shear capacity of bolted shear connectors in steel-concrete composite bridges. The project investigates the behaviour of bolted shear connectors by developing accurate FE models and by conducting extensive parametric studies that evaluate the parameters that affect the capacity of the connectors.

1.2 Aims and objectives

The aim of the project is to investigate the behaviour of bolted shear connectors in steel-concrete composite bridges and produce effective design rules.

The objectives of the project are:

1. Investigate the shear behaviour of a novel demountable locking-nut shear connectors (LNSC) in steel-concrete composite bridges by developing an accurate three-dimensional (3D) FE model. Steel-concrete composite specimens in a push-out configuration will be tested using ABAQUS software to assess their shear capacity and stiffness.
2. The effect of various parameters on the shear resistance, slip capacity and stiffness of LNSCs will be evaluated by conducting an extensive parametric study. The parameters include the bolt diameter, the bolt pretension force, the bolt tensile strength, the plugs compressive strength and the height to diameter ratio of the bolt connectors.
3. Explore the behaviour of friction-based shear connectors (FBSCs) in steel-concrete composite structures that allow full disassembly by building and testing, in a push-out testing arrangement, detailed 3D FE models.
4. Conduct a parametric study using the developed 3D FE models to evaluate the various parameters that affect the shear behaviour of FBSCs and therefore, expand the experimental databank existed in the literature.
5. Numerically test a full-scale steel-concrete composite beam equipped with FBSCs using a four-point bending configuration to define its flexural behaviour. The ability of FBSCs to achieve composite action will be studied as well as the influence of several parameters on its structural behaviour, including the concrete strength of the concrete slab, the yield strength of the steel beam and the tensile strength of the bolt connectors.
6. Produce design rules to predict the shear resistance of LNSCs and FBSCs in steel-concrete composite beams in the framework of Eurocode 4 [6, 7].

1.3 Thesis outline

The section provides an overview of the structure of the thesis.

Chapter 1 serves as an introduction to the topic, presenting the research question along with the aims and objectives of this research project. A brief outline of the thesis is also presented in this chapter.

Chapter 2 provides an extended review of the literature of the topic. The review is focused on previous researches conducted on bolted shear connectors for steel-concrete composite bridges, highlighting the relevant experimental and numerical work that has been published over the past 40 years. The chapter also includes a short overview of conventional welded headed studs.

Chapter 3 studies the shear behaviour of LNSCs in steel-concrete composite structures, by testing steel-concrete specimens in a push-out test configuration. Special attention is given to the material modelling of the various components of the shear connector to accurately predict its failure modes. Results of the FE analyses are validated against experimental results available in the literature. A parametric study is also conducted to evaluate the effect of significant parameters on the shear behaviour of LNSCs. Their effect on the shear resistance, the slip capacity and the stiffness of LNSCs is closely investigated. Parameters considered in the analysis are the bolt pretension force, the concrete compressive strength, the tensile strength, the diameter and the height to diameter ratio of bolt connectors. Using the results obtained from the parametric analysis, design recommendations are proposed at the end of this chapter to calculate the shear resistance of LNSC in steel-concrete composite beams.

The shear behaviour of FBSCs in steel-concrete composite bridges is assessed in Chapter 4. FBSCs are numerically tested using a push-out configuration to determine their shear resistance. The failure modes of the connectors are also discussed. The results are verified against experimental data in the literature. The results of an extensive parametric study that was conducted in order to assess the various parameters that affect the shear behaviour of FBSCs in steel-concrete composite structures is also presented in this chapter. Their effect on the shear resistance, the slip capacity and the stiffness of the connectors are discussed.

A full-scale steel-concrete composite beam equipped with FBSCs is numerically tested on Chapter 5. The flexural behaviour of the beam is investigated by testing it using a four-point bending configuration. The effect of the shear connection ratio, the slab compressive strength, the tensile strength of the bolt connectors and the yield strength of the steel beam on the structural behaviour of steel-concrete composite beams with demountable FBSCs is also addressed in this chapter.

In Chapter 6, the conclusions that were drawn from this research thesis are summarised and presented. In addition, the limitations of the current study are reported, and future work is suggested.

Chapter 2 Literature Review

2.1 Introduction

This chapter presents an overview of previous research conducted on welded headed studs and bolted shear connectors for steel-concrete composite bridges. The chapter enables the reader to understand and fully appreciate the urgent need to develop design rules for novel demountable shear connectors that enable full bridge disassembly and allow the rapid replacement of their deteriorating structural components. Firstly, a brief introduction of the conventional headed studs is presented. Their advantages and disadvantages are discussed, and the current European design recommendations [6] are presented. Subsequently, a summary of the previous experimental researches on bolted shear connectors for steel-concrete composite bridges is presented. An extensive review of previous numerical researches on bolted shear connectors for steel-concrete composite structures is also included this chapter.

2.2 Welded headed studs

Headed stud connectors that are welded to the top flange of the steel beam and they are fully embedded in the concrete slab are the most common way to achieve composite action in steel-concrete composite beams. This type of shear connection present significant advantages, such as rapid installation and little obstruction to reinforcement of the concrete slab. However, the main reason why welded headed studs are more commonly used than bolted connectors in construction industry is the availability of standards and design recommendations.

Research on headed studs in steel-concrete composite structures extends back to the 1950's when Viest [8] performed the first push-out tests to study their behavior and load carrying capacity. Ever since, welded headed studs became very popular; their behavior was studied by many researchers and it is well documented. Significant research has been conducted by Oehlers and Bradford [9], Ollgaard et al. [10], Oehlers and Coughlan [11] and Johnson [12].

The shear behavior of headed studs is determined by push-out tests performed according to Annex B of BS EN 1994-1-1 [6], which provide instructions for the test set up, the casting, the reinforcement layout and the characteristic strength derivation. EC4 also provides detailed design rules for welded headed studs. Although different heights can be used for welded studs, their height to diameter ratio should be higher than 4 according to EC4. Oehlers and Bradford [9] explained this as a measure to avoid a concrete pull-out failure. The diameter of the welded studs is limited to a range of 16 mm to 25 mm. The former limit of 16 mm is in accordance to the 6 mm slip capacity required for ductile shear connectors. According to EC4, studs having slip capacity equal or higher than 6 mm allow the

composite beam to achieve inelastic redistribution of the shear forces. Oehlers and Bradford proposed Eq. (2.1) to calculate the slip capacity of welded studs at fracture.

$$S_{ult} = (0.48 - 0.0042f_c)d_{sh} \quad (2.1)$$

Where S_{ult} is the slip at fracture (mm), f_c is the compressive cylinder strength of concrete (N/mm^2) and d_{sh} is the shank diameter of the stud (mm).

For a stud with 16 mm diameter and compressive strength equal to f_c = 25 N/mm^2, the slip at fracture equals to 6 mm. Therefore, studs with diameter less than 16 mm are not able to provide the minimum required slip capacity. According to Johnson [12], the upper limit of 25 mm was established because of the difficulties that may occur in the welding process.

The design shear resistance of a headed stud in accordance with EN 14555 [13] should be determined from Eq. (2.2) and Eq. (2.3).

$$P_{Rd} = \frac{0.8f_u\pi d^2/4}{\gamma_V} \quad (2.2)$$

Or:

$$P_{Rd} = \frac{0.29\alpha d^2\sqrt{f_{ck}E_{cm}}}{\gamma_V} \quad (2.3)$$

Whichever is smaller, with:

$$\alpha = 0.2(h_{sc}/d + 1) \quad \text{for } 3 \le h_{sc}/d \le 4 \quad (2.4)$$

$$\alpha = 1 \quad \text{for } h_{sc}/d > 4 \quad (2.5)$$

where γ_V is a partial factor for shear resistance (=1.25), d is the diameter of the shank of the stud in mm, f_u is the specified ultimate tensile strength of the material of the stud, but not greater than 500 N/mm^2.

The main problems related to welded headed studs are listed as follows:

First, for the installation of headed studs, specific welding devices and/or high-power generator are needed on site, which is difficult and/or expensive to have in remote locations. The welding procedure is also severely affected by the weather conditions. Therefore, the installation of welded headed studs in countries with high annual precipitation is quite challenging.

Headed studs impose very high concentrations of load onto the concrete slab. The load is transferred from the steel stud to the concrete slab through the dowel action of the connectors. As shown in Figure 2.1, the headed studs are simply steel dowels embedded in the concrete slab. The concentrated load is dispersed into the concrete slab and as a result it may induce tensile cracking. The tensile cracks are induced by ripping, shear and splitting actions. Oehlers and Bradford [9] reported that splitting can reduce the resistance of the shear connectors to less than 20%. To alleviate the problem, transverse reinforcement may be placed in the concrete slab as recommended by Clause (6.6.5.3.2.)

of BS EN 1994-1-1 [6]. However, according to Oehlers and Bradford, the splitting of the slab cannot be avoided by placing transverse reinforcement to the concrete slab, but the failure mode of the slab may change from brittle failure to a more ductile one.

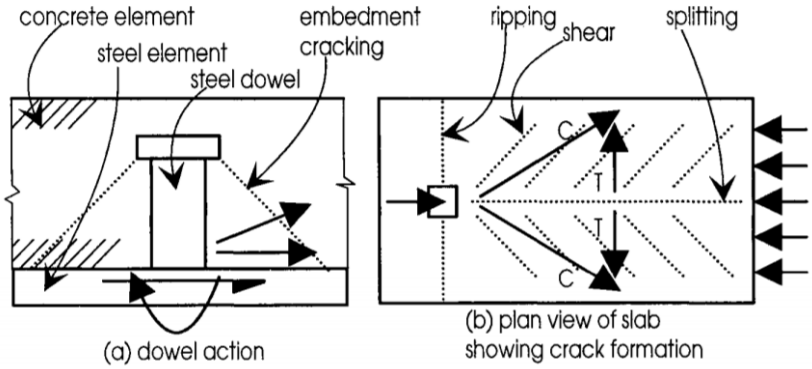

Figure 2.1: Transfer of connector force [9].

Finally, one of the most significant problems related with the welded studs in composite construction is that they don't allow the disassembly of the structure because of the monolithic nature of the connection. Any potential effort to remove the concrete deck involves drilling and crushing the concrete around the shear connectors and then breaking the deck into manageable sections. These operations may cause unrecoverable damages to the structural components and therefore they may not be able to reuse/recycle them.

2.3 Bolted shear connectors

The research on bolted shear connectors for steel-concrete composite structures is limited compared to the most commonly used welded headed studs. Various types of bolted shear connectors are presented in this paragraph. The paragraph presents both experimental and numerical studies available in the literature review.

2.3.1 Experimental research

Dallam et al. [14] investigated high-strength friction grip bolts in push-out tests as shown in Figure 2.2 (a). ASTM 325 bolts with ½ in. diameter and ASTM A449 bolts with 5/8 and 3/4 in. were used. The bolts were attached to the steel beam section in predrilled holes and held in place during the casting of the slabs with the aid of a wire spring chair as shown in Figure 2.2 (b). The slabs were cast on edge and was cured for 28 days. At the end of the 28 days, the bolts were tightened by the "turn-of-nut" method.

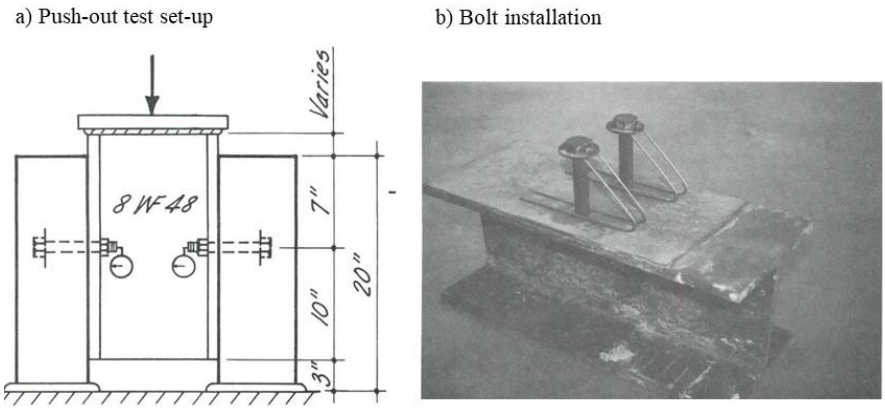

Figure 2.2: Push-out tests set up – Dallam et al. [14].

The load-slip behaviour of the push-out test specimens with high-strength friction grip bolts (N5S4TB1 specimen) is compared with push-out test specimens with welded headed studs (N5B4a specimen) in Figure 2.3. The high-strength bolts offered zero slip in the working range of the load and higher ultimate shear resistance compared to welded studs with same dimensions.

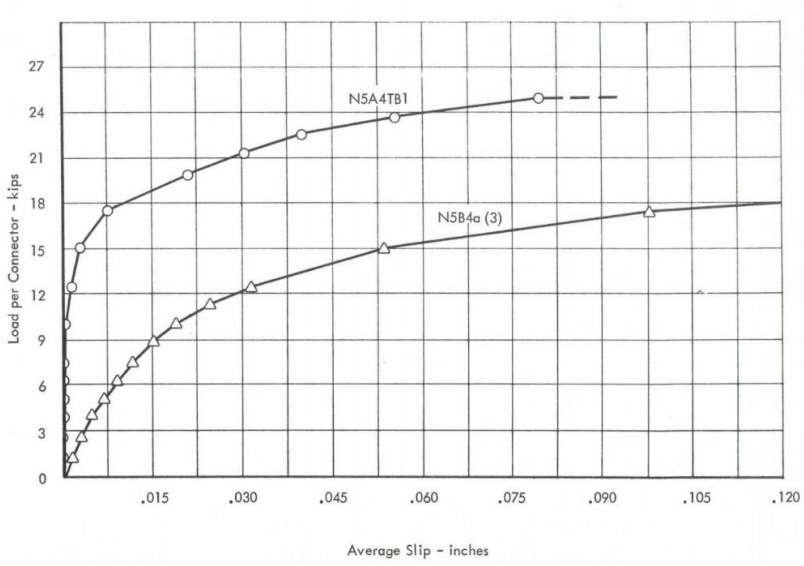

Figure 2.3: Force-slip curves for 15.9mm bolts – Dallam et al. [14].

The high-strength friction grip bolts and welded headed studs examined by Dallam et al. [14] had the same dimensions, but different material properties; the tensile strength of the studs was 493 MPa, while the tensile strength of the bolt connectors was 969 MPa. This explains why the push-out test specimens with high-strength friction grip bolts showed much higher shear resistance than the push-out test specimen with welded studs.

These connectors are also limited to in-situ construction. Precast construction is not possible, since very high tolerances would need to be overcome to coincide the pre-embedded bolts in the slab with their corresponding holes on the steel beam. In addition, replaceability is only possible if the whole

slab, including the bolts, is lifted up and replaced. Therefore, in case that only the shear connectors need to be replaced (e.g. due to corrosion), the whole slab has to be replaced.

Another drawback in Dallam's work is that the bolts were tightened with the "turn-of-nut" method to bring the bolts to a "snug tight" condition which was accomplished by "the full effort of a man using an ordinary spud wrench". Therefore, the magnitude of the pretension may vary between the bolts, causing different frictional forces at each bolt and consequently, it will affect the vertical alignment of the push-out specimens and the eccentricity of the point load. Possibly this is the reason why Dallam reported poor alignment in one of the push-out tests tested that enforced him to exclude its results from his research report. As a result, the shear capacity of the push-out tests may not correspond to the mean value of the four bolts, but to the capacity of the one with the lowest pretension force, which is always less than the expected average value that can be achieved when all the bolts fail simultaneously.

The bolts were tightened when the concrete was hardened, and therefore the tensile forces developed in the bolt connectors were transferred into the slab. In that case, if there was a gap between the concrete slab and the steel beam, flexural tensile stresses would be developed at the bottom face of the concrete slab, which increases the possibility of crack initiation around the bolts. Dallam reported that a total of six specimens failed due to split cracking during the tensioning of the bolts before the required nut rotation was reached.

Dallam and Harpster [15] tested six full-scale composite beams using high-strength bolts as shear connectors. The tests were conducted in two series having different a) size steel beam, b) geometry of loading, c) size, number and spacing of shear connectors and d) strength and type of concrete and the details of the specimens are shown in Figure 2.4. The high-strength bolts provided a very rigid connection between the steel beam and the concrete slab in the serviceability level and a reserve capacity sufficient to develop the ultimate moment capacity of the fully composite section.

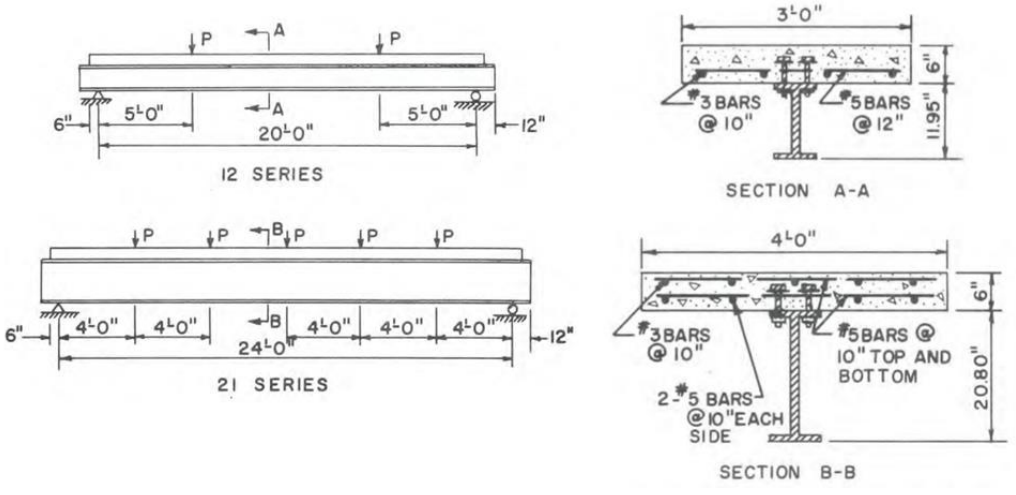

Figure 2.4: Details of the steel-concrete composite beams tested by Dallam and Harpster [15].

Marshall et al. [16] conducted static push-out tests with friction-grip bolts as shown in Figure 2.5 (a). Hardened washers and nuts were attached to the specimens from both sides. Helical reinforcement was used to reinforce the concrete around the bolt holes. As shown in Figure 2.5 (b), the principle variables investigated were the level of pretension force applied to the bolts, the concrete strength and the condition of casting (either precast or in-situ). In total eleven push-out tests were examined, and all failed by shearing of the bolts, except from one specimen that failed by crushing the concrete. The crushed slab had a cube strength of 36 MPa, while the strength of the other specimens was 40-50 MPa. Thus, concrete strength controlled the mode of failure. The load-slip response of one of the push-out specimens examined by Marshall is shown in Figure 2.5 (c). It was concluded that the first slip occurred after the friction force was overcome, while the ultimate shear resistance was up to two times higher (Figure 2.5 (d)).

a) Push-out specimens

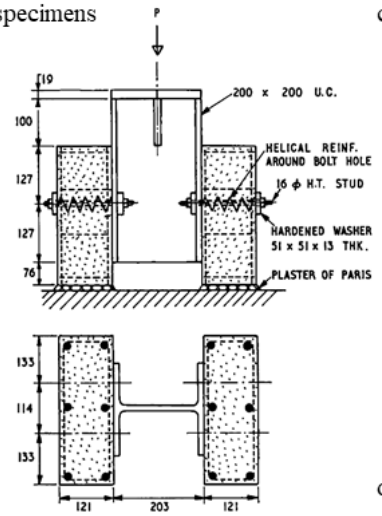

c) Load slip curve for push-out specimen 3/1

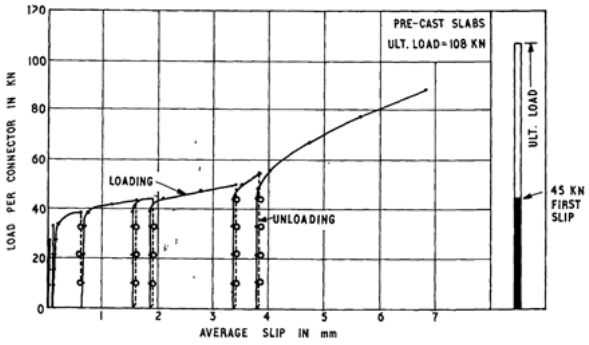

b) Details of the push-out specimens

Series	No. of speci-mens	Method of casting	Principal variable investigated	Cube strength of concrete
1	3	All cast *in situ*	Bolt pre-load	40·35
2	2	All cast *in situ*	Bolt pre-load	49·80
3	3	One pre-cast (3·1) Two *in situ* (3·2 and 3·3)	Concrete strength and casting method	48·4
4	3	All pre-cast	Concrete strength	1 – 36·2 2 – 48·3 3 – 44·8

d) Summary of the push-out tests results

Speci-men No.	Load per connector kN: First major slip	Load per connector kN: Ultimate	Type of failure	Average bolt preload kN	μ
1/1	41·1	100·0	Bolt-shear	81·4	0·504
1/2	47·8	114·0	Bolt-shear	84·5	0·565
1/3	52·8	111·7	Bolt-shear	92·5	0·571
2/1	54·4	112·1	Bolt-shear	95·5	0·570
2/2	53·4	111·0	Bolt-shear	92·6	0·576
3/1	44·5	107·7	Bolt-shear	94·5	0·470
3/2	61·0	Not completed		105·0	0·583
3/3	63·2	122·0	Bolt-shear	104·5	0·613
4/1	44·5	120·0	Slab cracked	94·5	0·470
4/2	45·3	122·0	Bolt-shear	94·5	0·479
4/3	48·9	121·0	Bolt-shear	94·5	0·475

Figure 2.5: Push-out tests specifications and results - Marshall et al. [16].

Dedic and Klaiber [17] examined the use of high-strength bolts as shear connectors in rehabilitation of bridges and other structures. Two types of shear connectors were examined as shown in Figure 2.6 (a) and (b); double-nutted high strength bolt shear connectors and epoxied high-strength bolt connectors. The load-slip behaviour of the new bolted shear connectors is compared with welded studs in Figure 2.6 (c). It was concluded that the bolted connectors could offer higher shear resistance and ship capacity compared to the welded studs that exhibited reduced ductility below 4 mm. The bolted connectors provided slightly higher stiffness against slip than welded studs for loads up to 89

kN. After this point, and up to approximately 200 kN, the slip resistance of the bolted connectors was lower, due to the deformations of the bolts inside the drilled holes of the upper flange of the steel beam until complete bearing could be achieved. In terms of failure modes, shear failure of the bolts was observed above the upper flange of the steel beam, along with tensile cracking in the concrete slab.

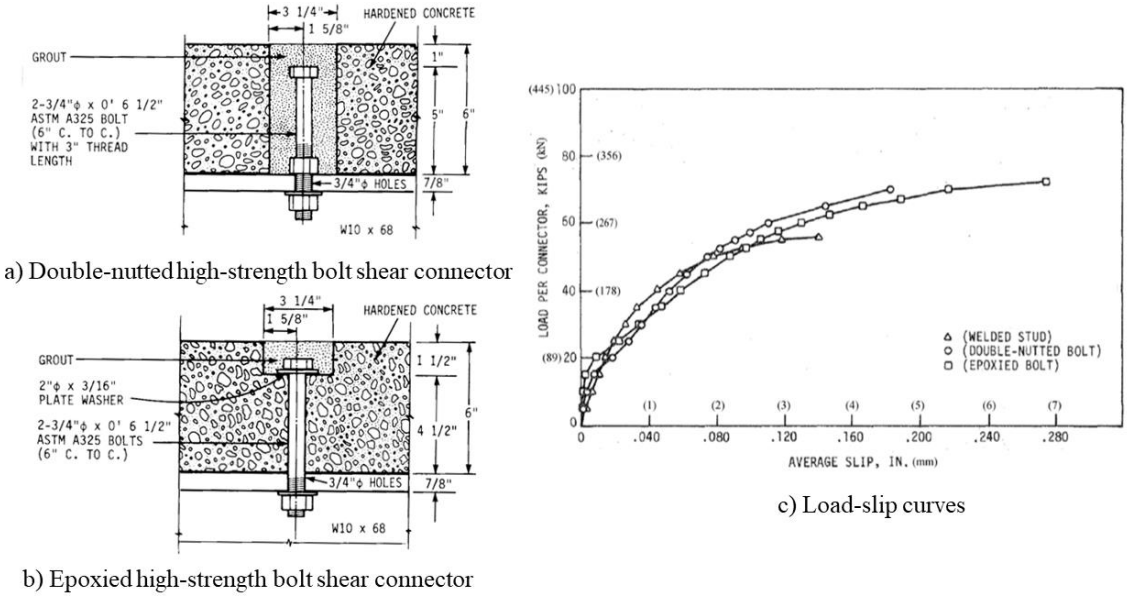

Figure 2.6: Bolted shear connectors proposed by Dedic and Klaiber [17].

Kwon et al. [18] investigated the behaviour of high-strength bolts as post-installed shear connectors for use in strengthening existing non-composite beams that do not satisfy current load requirements. Three-types of post-installed shear connectors with 22mm diameter were proposed: a) the double-nut bolt (DBLNB) b) the high-tension friction grip bolt (HTFGB), and c) the adhesive anchor connector (HASAA). The shear connectors are illustrated in Figure 2.7.

An ASTM A193 B7 threaded rod, with 860 MPa minimum specified tensile strength, similar to an ASTM A325 high-strength bolt, was used for the DBLNB connector. For the installation of the shear connector, a 57mm diameter hole was drilled through the concrete slab and a 24mm diameter hole was drilled through the steel flange. The connector was installed with two nuts above the steel plate and a single nut on the bottom side of the plate. The nut beneath the steel plate was tightened to induce a pretension of 175kN, which corresponds to the specified pretension force for a 22mm diameter A325 bolt. Finally, the concrete slab was placed on the top of the steel plate and the hole was filled with high-strength grout.

ASTM A325 high-strength bolts with specified tensile strength equal to 825 MPa were used for the HTFGB connector. Two holes were drilled in the concrete slab; a 25mm diameter hole with 125mm depth was drilled from the one side of the concrete slab and a 51mm diameter hole with a depth of

approximately 75mm was drilled from the other side. A 24mm diameter hole was drilled through the flange of the steel beam. The high-strength bolt was inserted from the top and tightened to a 175kN pretension force underneath the slab using an impact wrench. Finally, the hole on the surface of the concrete block was filled with high-strength grout.

An ASTM A193 B7 threaded rod was also required for the HASAA connector, along with a two-component structural adhesive with 69.2 MPa minimum specified compressive strength. A 24mm diameter hole was drilled through the steel beam and the concrete slab. The threaded rod was inserted after the adhesive was injected in the hole. After the specified cure time had passed, a nut was installed and tightened.

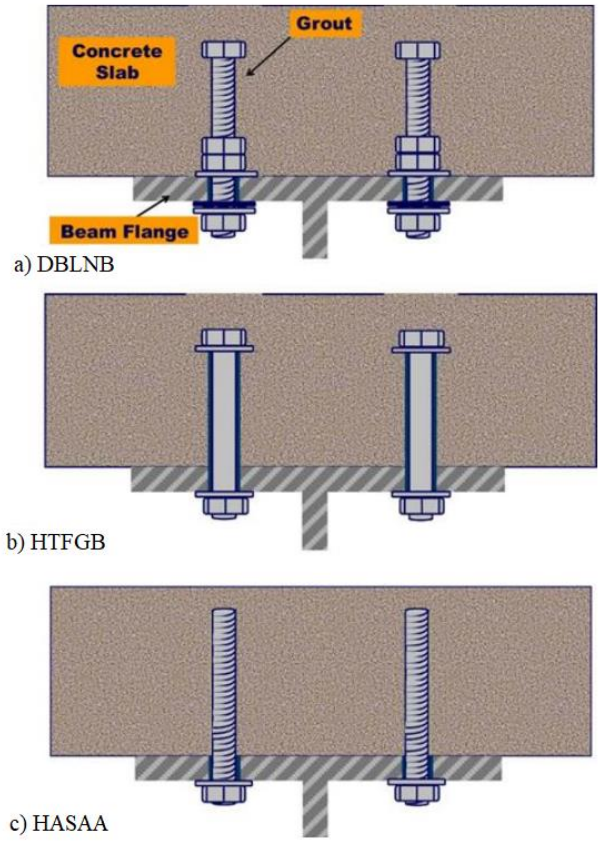

Figure 2.7: Shear connectors proposed by Kwon et al. [18].

The shear connectors were tested under static loading in order to evaluate their initial stiffness, shear resistance and slip capacity. All post-installed shear connectors showed more than 6mm slip capacity, which is considered to be adequete according to BS EN 1994-1-2 [7] to clasify them as ductile shear connectors. Therefore, it was assumed that they can provide enough slip capacity to redistribute shear force to adjacent shear connectors after yielding. The HTFGB connector showed the highest initial stiffness since the shear at steel-concrete interface was transferred by friction and therefore a full composite action without slip at the steel-concrete interface could be achieved before the friction force was overcome. Similarly, the DBLNB connectors showed high initial stiffness due to the large bearing area of the embedded nuts that minimizes the crushing of the concrete in front of the shear

connector. On the other hand, the HASSA connector showed low initial stiffness, which according to the author it is attributed to the fact that the applied torque to the connector was not sufficient to create the necessary friction at steel-concrete interface.

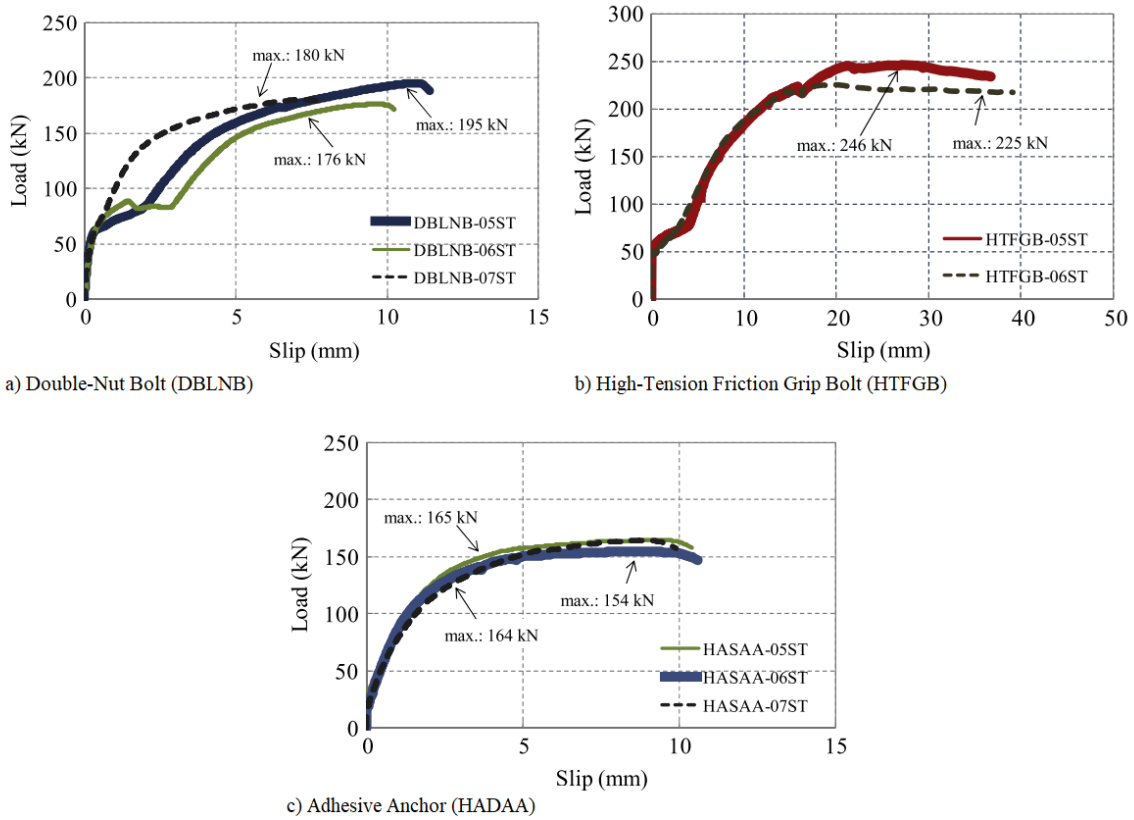

Figure 2.8: Push-out test results - Kwon et al. [18].

Kwon et al. [19] conducted large-scale tests on girders strengthened with post-installed shear connectors. Five non-composite beams were constructed: one beam was tested as a reference specimen and four beams were retrofitted with post-installed shear connectors with 30% shear connection ratio. The load-deflection response at midspan of the specimens is illustrated in Figure 2.9. The specimens with post-installed shear connectors showed 40-50% higher stiffness and strength compared to the baseline non-composite specimen, even with a small number of shear connectors. A sudden strength drop was observed in specimens with the DBLNB and HASAA shear connectors due to the failure of multiple shear connectors. After the failure of the connectors, the composite beams showed a similar behaviour with the non-composite beams.

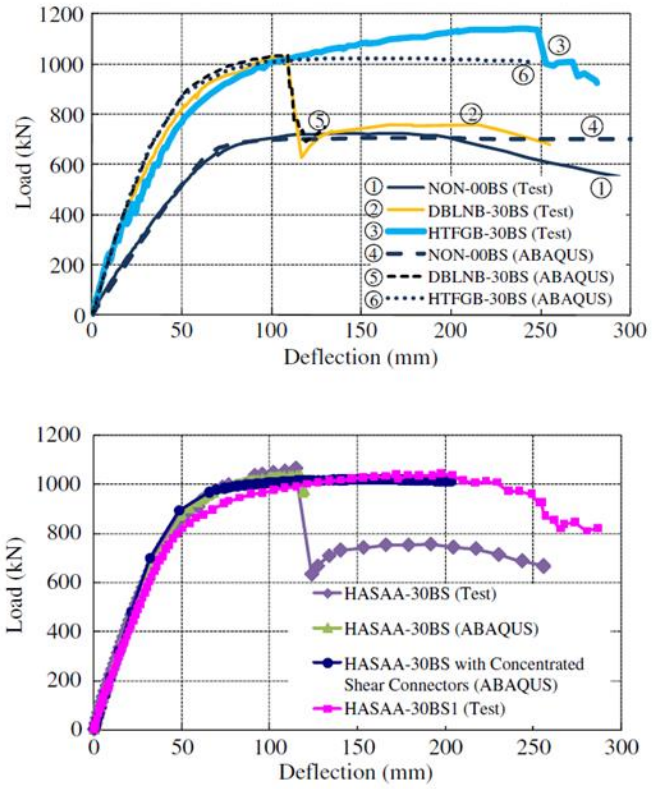

Figure 2.9: Load versus mid-span deflection curves – Kwon et al. [19].

A new demountable shear connector manufactured from standard headed studs was proposed by Lam and Saveri [20, 21] and it is shown in Figure 2.10. The only difference between the proposed demountable shear connector and welded studs is that the studs have a welded collar (increase in diameter), while the new type has a collar shaft (decrease in diameter) and a nut. Eight-push out tests were conducted, where two failure mechanisms were observed: fracture of shear connectors near the threaded end and concrete crushing. It was pointed out that for the specimens that failed by concrete crushing, the slabs were easily detached from the steel beams. However, the proposed connector does not provide full disassembly of the composite beams, i.e. replacement of the shear connectors in case of damage due to corrosion, since the connectors are fully embedded within the concrete slab.

Figure 2.10: Demountable shear connector manufactured from standard headed studs – Lam and Saveri [20].

The load-slip response of the push-out tests with demountable shear connectors is shown in Figure 2.11. The results showed that the specimens with demountable shear connectors (PT5) had similar resistance as the specimens with welded headed studs (PT8). They also had better performance in terms of ductility, but lower initial stiffness. It should be mentioned that the slip capacity of the specimens exceeded the 6mm limit specified by BS EN 1994-1-1 [6] and therefore the demountable shear connectors manufactured from standard headed studs are suitable for partial shear connection design of steel-concrete composite beams.

Ref.	Concrete Cube Strength, f_{cu} (MPa)	Stud Type	Max. Load per stud (kN)	Slip at Max. Load (mm)	Mode of Failure
PT 1	19.85	16mm	75.0	8.75	Stud fracture
PT 2	21.45	17mm collar	93.5	7.94	Stud fracture
PT 3	20.10	18mm collar	71.9	22.03	Concrete crushing
PT 4	25.20	18mm collar	81.5	18.22	Concrete crushing
PT 5	29.90	18mm collar	90.0	21.25	Concrete crushing
PT 6	61.38	18mm collar	107.5	22.03	Stud fracture
PT 7	20.10	19mm welded	71.6	5.20	Concrete crushing
PT 8	29.90	19mm welded	92.7	9.00	Concrete crushing

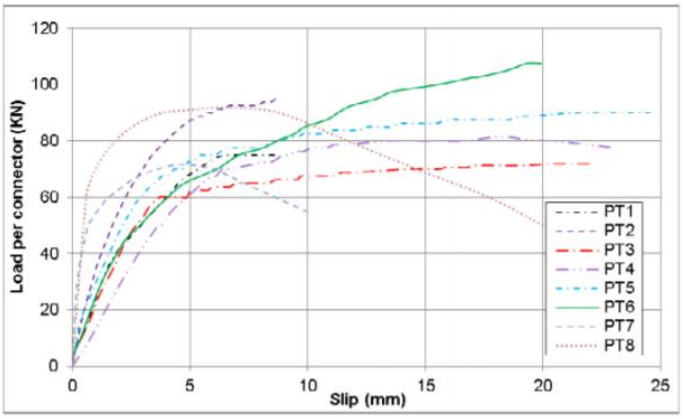

Figure 2.11: Load-slip behaviour of demountable shear connector manufactured from standard headed studs – Lam and Saveri [20].

Lee and Bradford [22] proposed a bolted shear connector that uses precast geopolymer concrete slabs to minimize the use of ordinary Portland cement concrete in construction. Geopolymer concrete is consider a sustainable solution against the use of ordinary Portland cement concrete that releases huge amounts of greenhouse gases into the atmosphere for its production. Five push-out tests were conducted to study the behaviour of the aforementioned bolted shear connectors and the results are shown in Figure 2.12. Three distinctive regions were identified in the load-slip behaviour of the shear connectors: a region of “full interaction”, a region of “zero interaction” and a region of “partial interaction”. The researchers also studied the deconstructability of the shear connectors under service loads by unloading the bolts and then pre-tensioned again and reloading to failure.

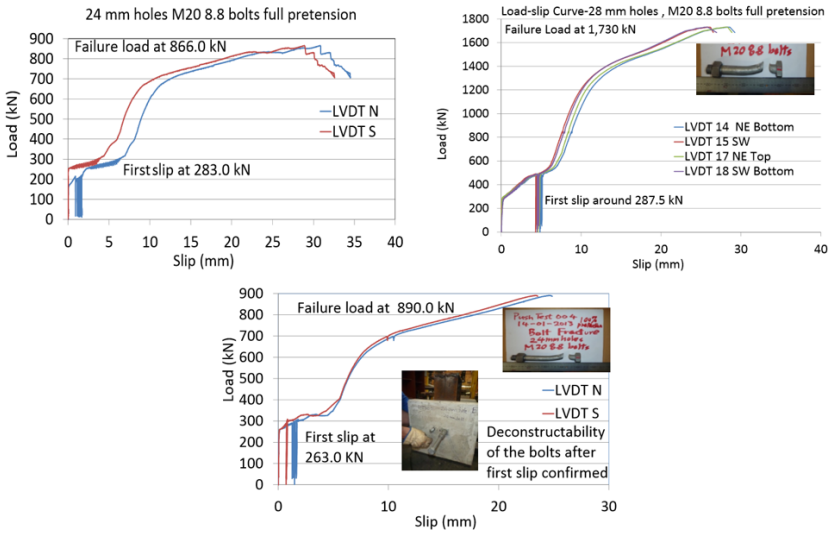

Figure 2.12: Load - slip curves of push-out tests using bolted shear connectors and geopolymer concrete slabs – Lee and Bradford [22].

Moynihan and Allwood [23] tested three composite beam specimens, of lengths 2m, 10m and 5m, using M20 bolts to investigate their behaviour as demountable composite connectors. The beams were tested in three-, four- and six-point bending, respectively. All specimens were initially loaded to service loads. They were then unloaded and successfully demounted – the bottom nuts released, and the beams lowered clear of the slabs – reassembled and reloaded in cycles to increasingly higher loads until failure occurred. The results showed that the specimens were able to achieve higher moment resistance than the values predicted by BS EN 1994-1-1. The behaviour of the 10 m and 5 m specimens were compared against the results of previously published comparable welded-connector composite beam. The moment capacities of the 10m and 5 m specimens were found to be 2% and 12% lower than the corresponding welded-connector composite beams, which according to the author was mainly attributed to the lower concrete strength used for the construction of the specimens, and to the holes drilled in the top flange of the beam. This suggests that the demountable connector proposed by Moynihan and Allwood could potentially be safely used and reused, thus reducing carbon emissions.

Pavlović et al. [24] proposed the use of bolted shear connectors in prefabricated concrete slabs in order to achieve higher level of prefabrication in steel-concrete composite structures. Standard push-out tests using M16 shear connectors with single embedded nut in the concrete slab were performed and the results were compared to experimental results conducted by Spremic et al. [25] for headed studs. The results showed that bolted shear connectors achieved comparable shear resistance, but less slip capacity as compared to welded studs; below the 6mm limit of BS EN 1994-1-1 [7]. Bolt shear connectors with single embedded nuts also showed earlier onset of nonlinearity, as shown in Figure 2.13 (a), due to the reduced bearing capacity of the concrete in front of the embedded nuts. The proposed connectors also showed less stiffness at serviceability loads as shown in Figure 2.13 (b),

which according to the author is mainly attributed to the random distribution of bolt-to-hole clearances within 8 bolts in one push-out test specimen.

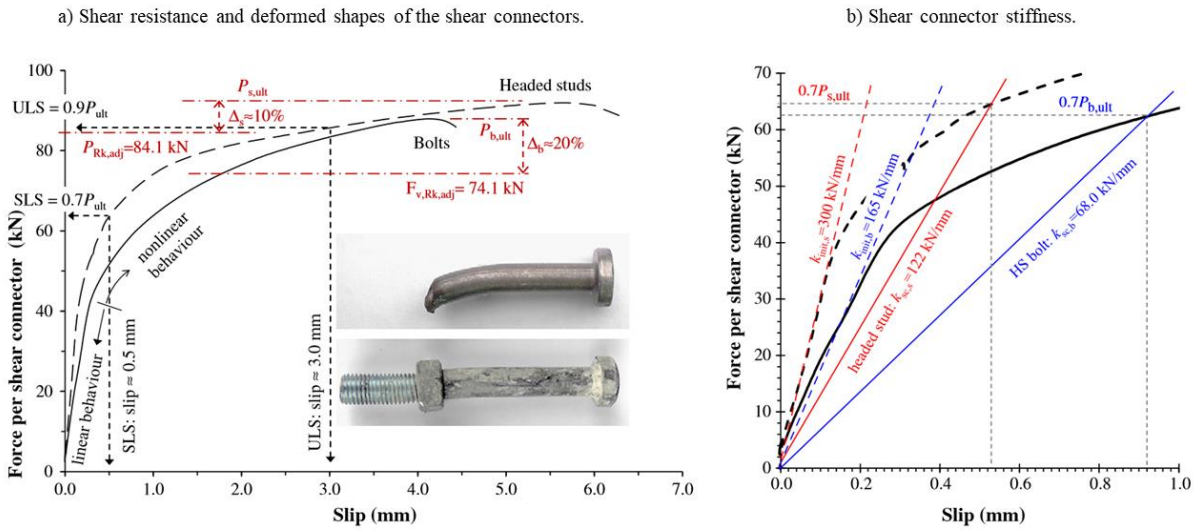

Figure 2.13: Force-slip behaviour of bolted shear connectors with single embedded nut and headed studs - Pavlovic et al. [24].

Chen et al. [26] proposed an alternative connection system that do not rely on grouting for composite action. The connection system is shown in Figure 2.14 and consists of high-strength bolts which are not embedded in the concrete slab, but located in empty through-holes, that are intended not to be grouted to allow future demountability. Ten push-out tests were conducted to evaluate the different parameters that affect the behaviour of the proposed connectors. Various bolt sizes, bolt pretension forces and steel-concrete interfaces were considered in the experimental analysis as shown in Figure 2.15. The specimens exhibited low initial slip load, but ductility and peak load comparable to that of a conventional shear stud. In addition, the parametric analysis showed that the initial slip and the shear resistance were increased as the bolt pretension force and/or diameter increased. However, the shear load capacity of the specimens was not altered by modifying the contact surface between the steel beam and concrete slab, due to the presence of larger aggregate particles in the concrete sand.

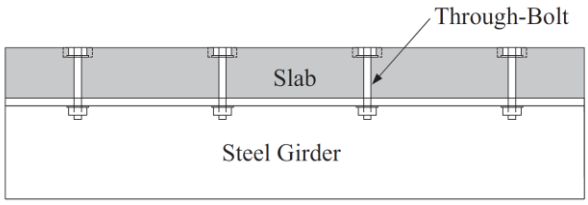

Figure 2.14: Demountable through-bolt shear connectors proposed by Chen et al. [26].

Table 1
Push test matrix.

		Studs	ASTM A325 bolts				
Stud/bolt diameter (mm)		19.05	12.70	15.88	19.05	15.88	19.05
Bolt tension (kN)		–	53	85	125	53	53
Nelson stud specimen		NS-0	–	–	–	–	–
Through-bolt specimens	Contact surface 1	–	–	CS1-M-85	–	–	–
	Contact surface 2	–	CS2-S-53	CS2-M-85	CS2-L-125	CS2-M-53	CS2-L-53
	Contact surface 3	–	CS3-S-53	CS3-M-85	CS3-L-125	–	–

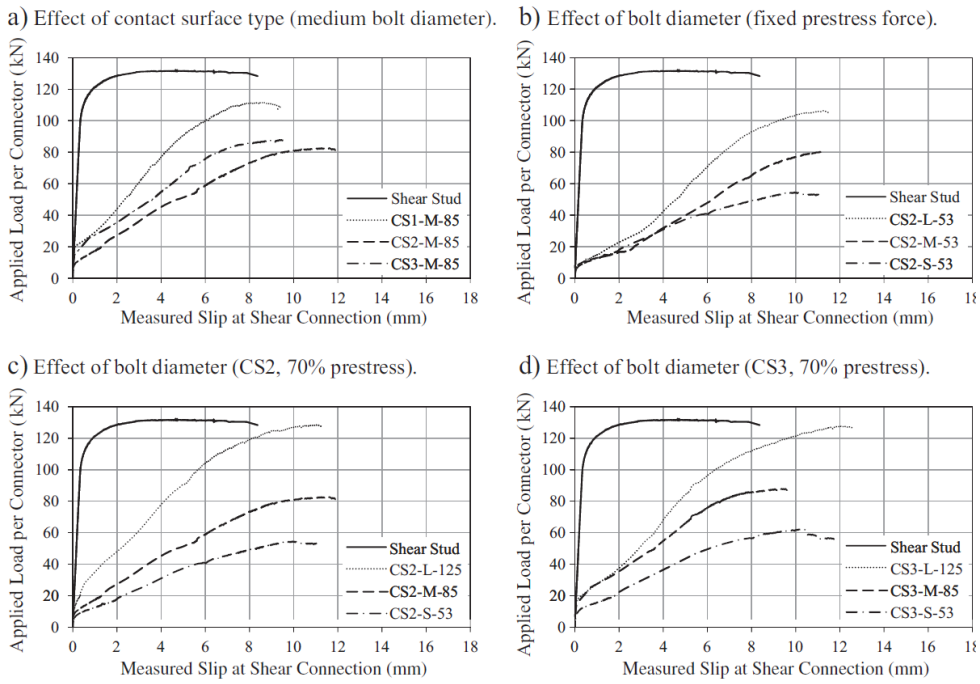

Figure 2.15: Load - slip curves behaviour of demountable through-bolt shear connectors proposed by Chen et al. [26].

Ataei et al. [27] investigated the structural performance of high-strength friction grip bolts in geopolymer precast slab units in three full-scale composite beam tests subjected to monotonic loading. One additional beam test was designed and constructed with single embedded bolted shear connectors in in-situ geopolymer slabs to act as a reference beam. As shown in Figure 2.16, the composite beams with single embedded bolted shear connectors with a monolithic slab have a higher ultimate load capacity than counterpart beams with precast concrete panels and post-tensioned friction grip bolted shear connectors. However, precast concrete beams proved to be far more ductile than the in-situ beams.

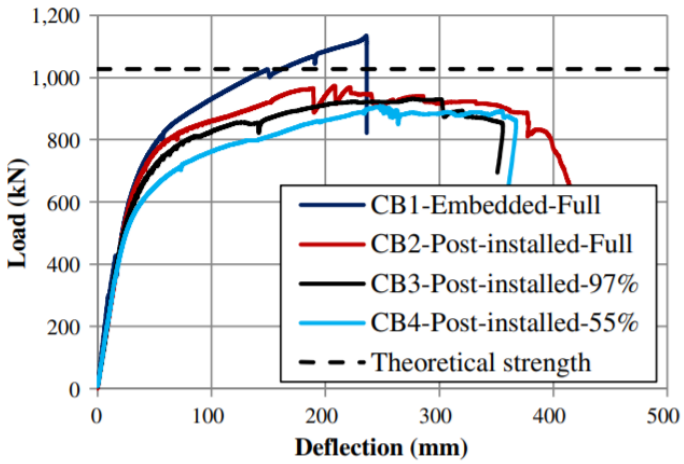

Figure 2.16: Load - Deflection curves of the beam tests conducted by Ataei et al. [27].

Pathirana et al. [28] investigated the behaviour of blind bolts in push-out tests. Two types of push-out test specimens, normal specimens and retrofitted specimens were tested using proposed blind bold connectors, named BB1 and BB2 shown in Figure 2.17. Push-out tests with welded headed studs as shear connectors were included in the analysis for comparison purposes.

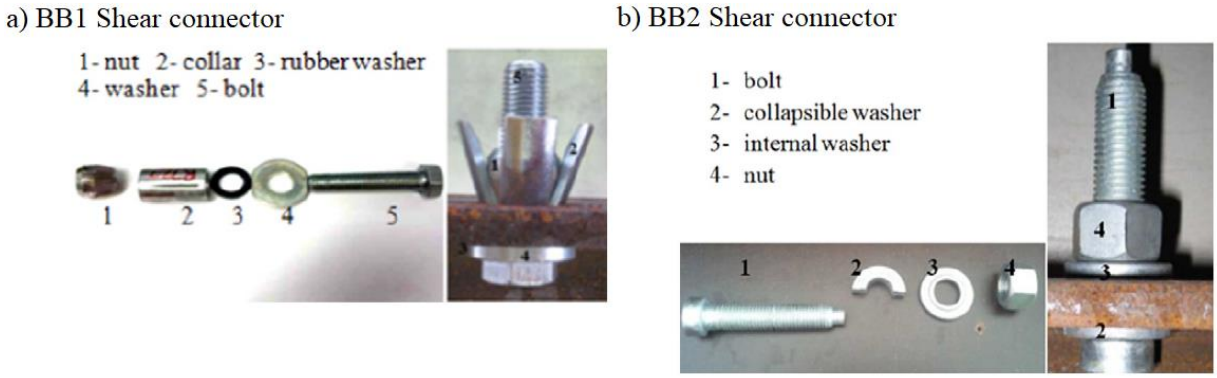

Figure 2.17: Blind bolts used as shear connectors – Pathirana et al. [28].

The load-slip behaviour of the three connector types in the normal and retrofitted specimens is illustrated in Figure 2.18. The WS and BB1 connectors demonstrated much higher stiffness than the BB2 connectors, both in normal and in the retrofitted test specimens. BB1 and BB2 connectors exhibited much higher ultimate shear resistance than WS connectors, particularly in the retrofitted specimens. However, BB2 connectors showed very low initial shear load capacity and stiffness.

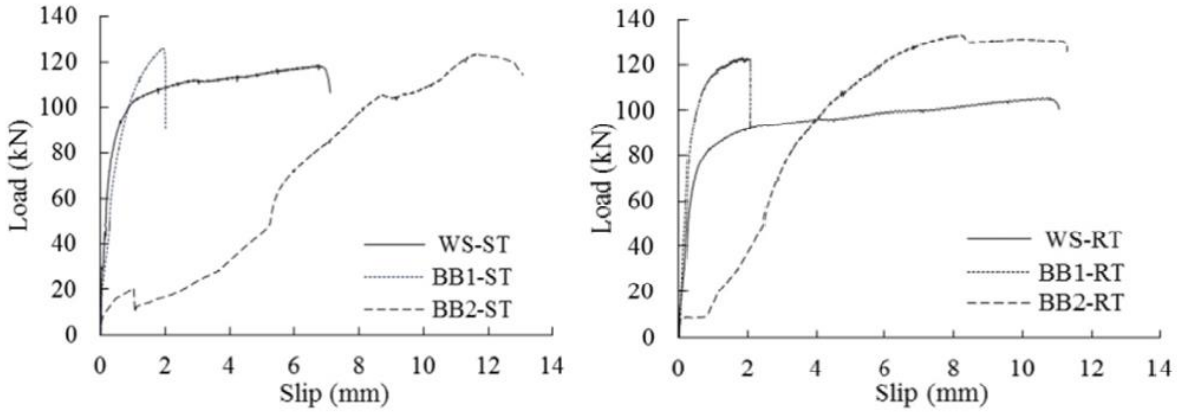

Figure 2.18: Load-slip behaviour of blind bolts in push-out tests – Pathirana [28].

The behaviour of blind bolts in retrofitting existing composite steel-concrete composite beams was also assessed by Pathirana et al. [29]. Seven full-scale beam specimens were constructed and subjected to flexural loading by using a four-point loading setup. The vertical deflections of the specimens were measured throughout the test at mid-span. The load-slip behaviour of the specimens is shown in Figure 2.19. All three normal beam specimens demonstrated comparable initial stiffness up to a load of about 150kN. The CBB2-ST specimen recorded the highest ultimate load and the highest ductility among the test specimens, while the CBB1-ST exhibit the lowest. For the retrofitted specimens, the stiffness of the CBB2-RT specimen was much lower compared with that of the other

two specimens which demonstrated comparable stiffness. However, CBB2-RT exhibited the highest strength among the retrofitted beams.

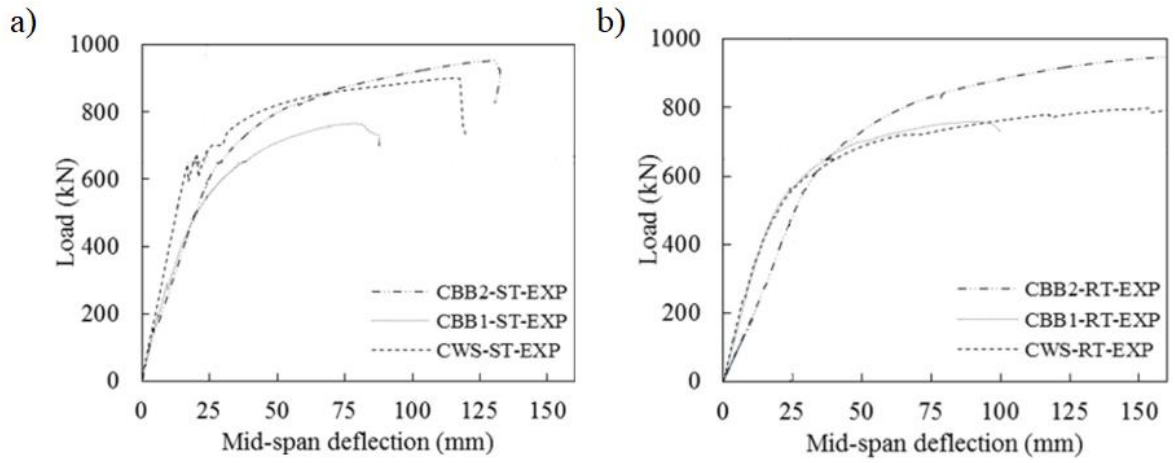

Figure 2.19: Load-slip behaviour of blind bolts in full scale a) normal and b) retrofitted beam specimens – Pathirana [29].

Rehman et al. [30] conducted twelve push-out tests with different reinforcement cages as shown in Figure, to study the behaviour of demountable shear connectors in metal decking composite slabs. The author stated that the specimens with single layer of steel reinforcement (Figure 2.20 (a)) showed a premature failure due to buckling of the slabs. To overcome this premature failure, double layer of reinforcement was used (Figure 2.20 (b)). However, these specimens developed a local premature failure at the toes of the specimens, yet again preventing the shear connector capacity to be obtained. To prevent local premature failure due to buckling of the slab or failure to the toe, the reinforcement cage was modified with toe reinforcement as shown in (Figure 2.20 (c)). The results showed that the use of the modified reinforcement has improved the splitting resistance of the concrete slab and overcomes the possibility of premature failure of the concrete slabs. Therefore, the author recommended its use for all push-out tests.

The experimental results showed that the demountable shear connectors in metal decking composite slabs have high ductility and similar shear capacity and behaviour as welded shear studs and fulfilled the 6 mm required by BS EN 1994-1-1. Similar to welded shear connectors, demountable shear connectors had two failure modes: connector failure and concrete crushing. The shear capacity of the specimens was compared against the prediction methods used for welded shear connections given in Eurocode 4, AISC 360-10, ACI 318-08 and method used for bolted connection in Eurocode 3, since there is no specific assessment method available for demountable shear connectors. It was concluded that Eurocodes slightly underestimated the shear resistance of demountable shear connectors, while the AISC code overestimated the shear resistance of the specimens in both concrete and connector shear failure. The ACI 318-08 method was found to be conservative for high strength concrete and slightly overestimated the capacity for lower concrete strength specimens.

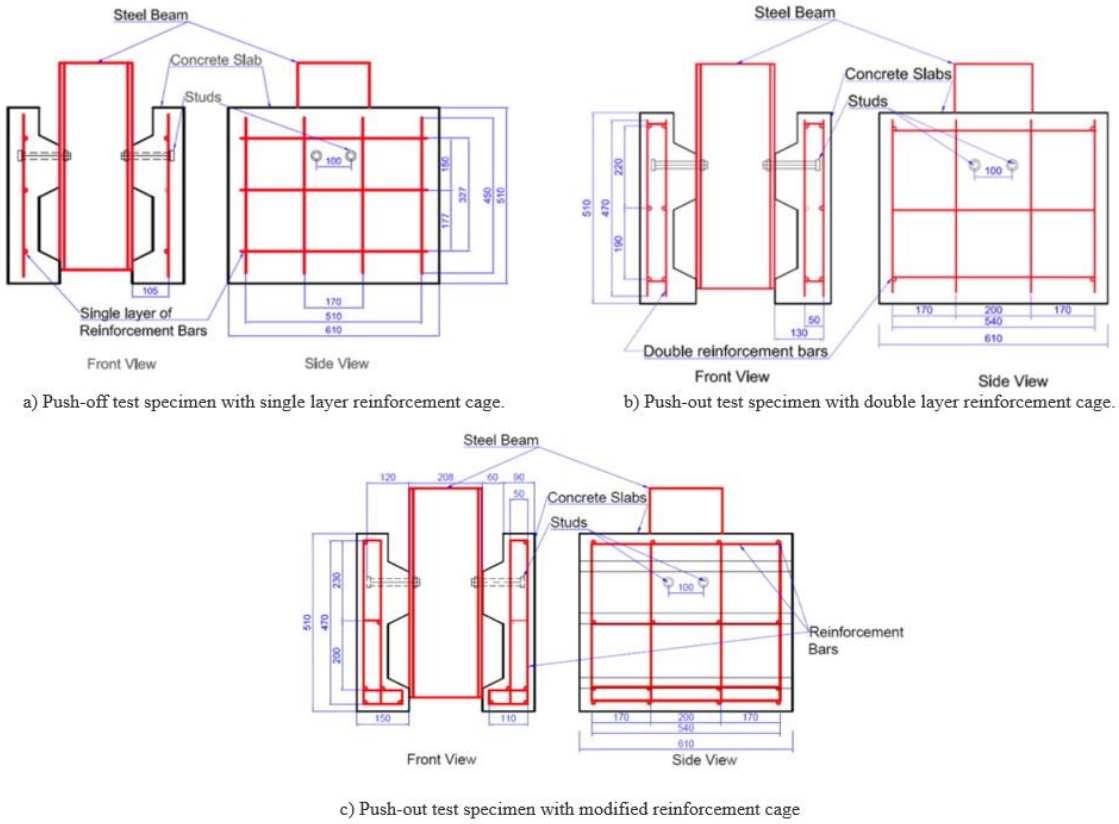

Figure 2.20: Push-out test specimens tested by Rehman et al. [30].

Suwaed and Karavasilis [31] presented a novel demountable shear connector for precast steel-concrete composite bridges that allows full bridge disassembly. The shear connector uses high-strength bolts which are fastened to the steel beam with the aid of a special locking nut configuration, which consists of a lower hexagonal nut (Nut 1) and an upper conical nut (Nut 2), that prevents bolts slipping within their holes. The details of the connector are shown in Figure 2.21.

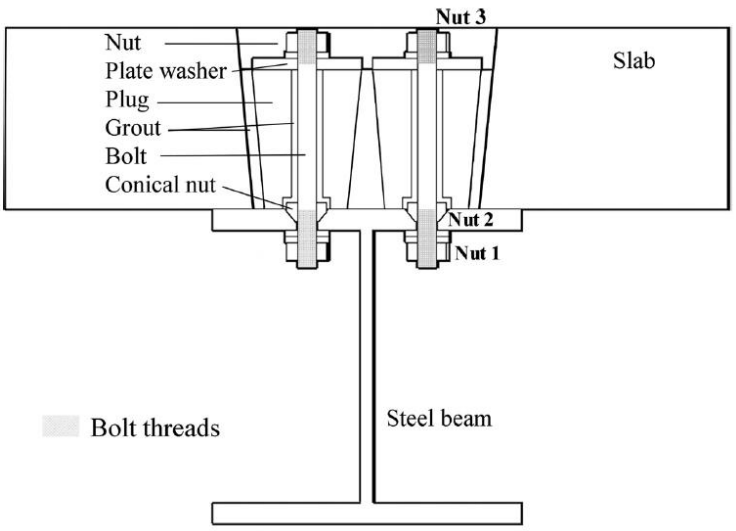

Figure 2.21: Cross-section of the LNSC – Suwaed and Karavasilis [31].

The upper part of the bolt hole in the steel beam is a countersunk seat with chamfered sides following an angle of 60°. The upper conical nut has a geometry that follows the same angle so it can perfectly fit in the countersunk seat. In this way, the nut provided a mechanical stop within the countersunk area and prevents the slip of the bolt within the bolt hole. To delay the concrete crushing, the conical nut was designed to protrude from the steel beam flange to increase the contact area between the concrete and the bolt. The concrete slabs have several holes (pockets) with an inclination of 5° to accommodate the shear connectors. Inside each slab pocket, there were two inverted conical precast concrete plugs with geometry that follows the inclination angle of the slab pocket. Each plug has a central circular hole that accommodates the high-strength bolt. Rapid hardening grout is used to fill the gaps between the bolt and the hole of the plug as well as the gaps between the plugs and the slab pocket. A hardened plate washer was used to ensure the uniform distribution of the bolt thrust on the upper face of the concrete plug without inducing cracks. Finally, the tightening of Nut 3 is performed before the hardening of the grout to avoid developing of internal stresses in the concrete slab. With this approach, the bolt tightening does not result in cracking of the slab due to imperfections in the steel-concrete interface.

The experimental results showed that the LNSC has very high shear resistance (170kN for an M16 bolt) and stiffness (100kN/mm for an M16 bolt). The proposed shear connector also provides a very large capacity up to 14mm for an M16 bolt.

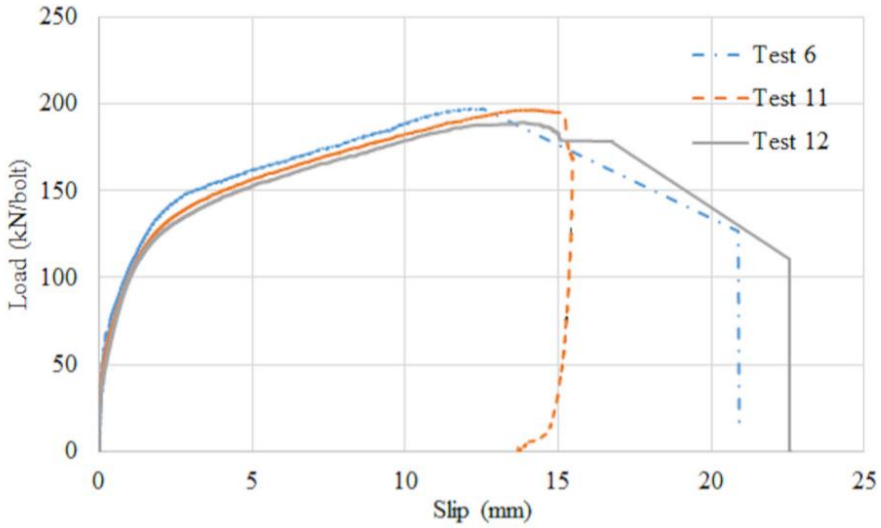

Figure 2.22: Load-slip behaviour of the LNSC from three identical push-out tests [31].

A friction-based shear connectors (FBSC) was proposed by Suwaed and Karavasilis [32]. The FBSC consists of several components, which are shown in Figure 2.23. The FBSC allows bridge disassembly and therefore the deteriorating structural components such as the precast deck panels, the shear connectors and the steel beams can be easily replaced. The FBSC also promoted accelerated bridge construction by taking full advantage of pre-fabrication. More specifically, all its structural components are fabricated in the shop and the bridge assembly is carried out on site. The connector

has a similar geometry with the LNSC except that in this case the geometry does not include a conical nut and the shear resistance of the connector is developed through friction at the concrete plug – steel beam interface. The connector uses high-strength bolts that pass through chamfered countersunk seat holes drilled on the top flange of the beam and placed in their final position with the aid of retaining washers.

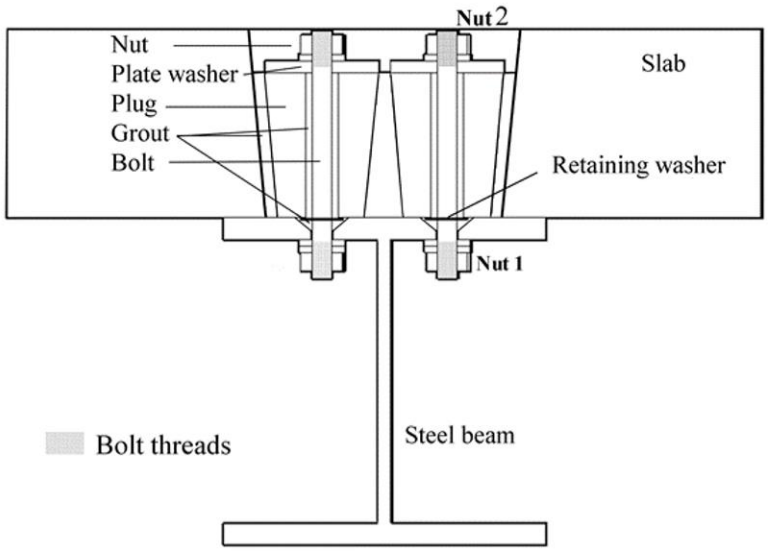

Figure 2.23: Cross-section of the FBSC – Suwaed and Karavasilis [32].

The load-slip behaviour of the FBSC is shown in Figure 2.24. The connector offers high shear resistance and stiffness in comparison with welded studs. The characteristic shear resistance and stiffness of the FBSC for an M16 bolt were found equal to 161 KN and 104 KN/mm, respectively. The FBSC has also large slip capacity, i.e. about 16mm and therefore allows partial shear design of steel-concrete composite bridges with large spans.

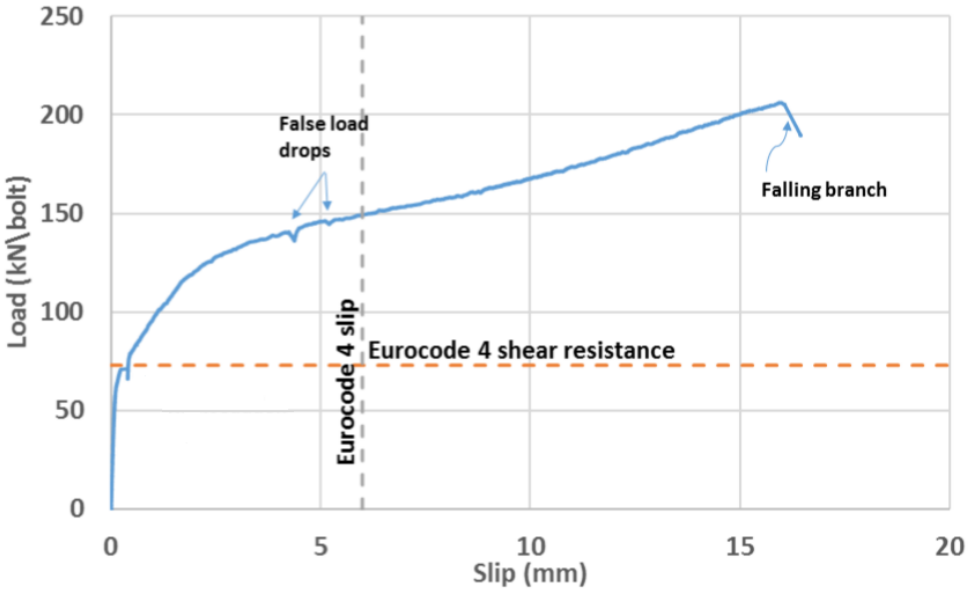

Figure 2.24: Load-slip behaviour of FBSC – Suwaed and Karavasilis [32].

Feidaki et al. [33] proposed a demountable steel-yielding shear connector shown in for use in composite floors with precast hollow-core slab units (HCUs). The proposed shear connector consists of a steel square hollow tube welded on a steel plate that is bolted on the steel section's top flange using four high-strength bolts. Concrete is cast only around the connector, and therefore it allows the easy separation of the precast slab units from the steel sections during the deconstruction phase. The proposed composite floor system uses precast concrete slab units and therefore offer several advantages such as off-site quality-controlled fabrication and fewer operations on site. The use of precast HCUs offers the additional advantage of large spans without the need for secondary beams, enabling even greater economy in steel and fewer operations on site.

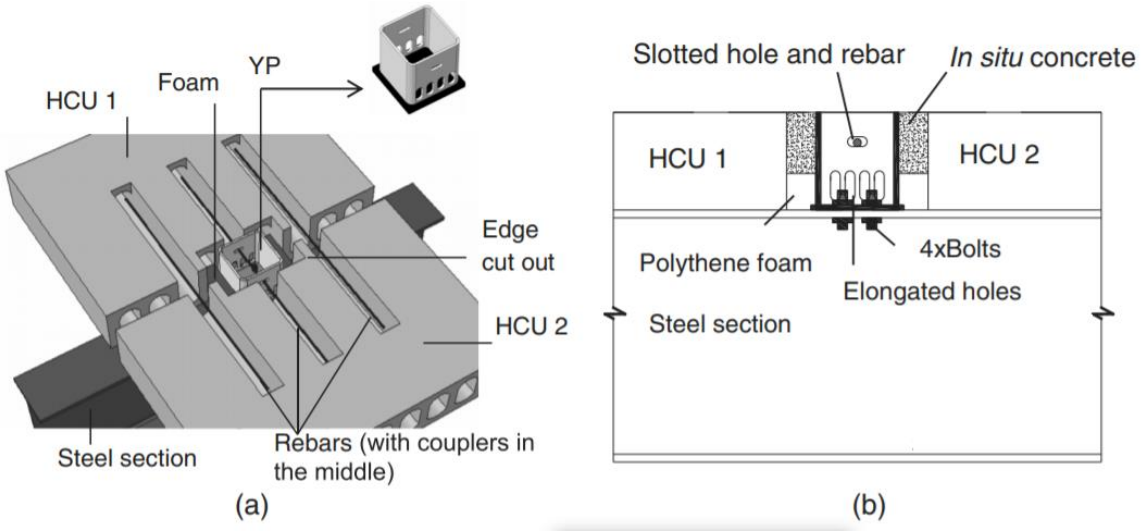

Figure 2.25: (a) Three-dimensional view and and (b) longitudinal view of the demountable shear connector proposed by Feidaki et al. [33].

The structural behaviour of the connector was evaluated through 10 push-out tests using a horizontal testing arrangement instead of the standard vertical setup prescribed in Eurocode 4 due to the size of the HCUs. The results showed that the shear connector had similar stiffness to that of a welded shear stud and provided very high longitudinal shear resistance in the range of 170-320 kN. The slip capacity of the specimens was also high; the specimens designed to fail in a ductile mode had at least a 30 mm slip capacity, while the specimens that failed due to concrete shear cracking still achieved a slip capacity much higher than that required by Eurocode 4 [6], i.e. higher than 6 mm, for ductile connectors.

A novel steel-concrete bolted shear connector was proposed by Yang et al. [34]. The connectors were fully embedded in in-situ concrete and consisted of a short bolt, firstly installed during construction, a long bolt and a coupler between them as shown in Fig. The aim of the project was to simplify the deconstruction procedure by unscrewing the bolts only from the bottom side of the beam (working only from the one side). The connectors exhibited inadequate ductility below 6mm and similar shear bearing capacity as the conventional welded studs.

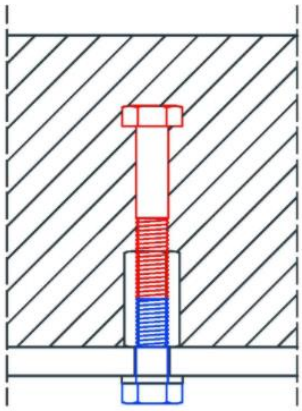

Figure 2.26: Bolted shear connector proposed by Yang et al. [34].

Two types of demountable shear connectors have been developed and tested by Kozma et al. [35]. The connectors use prefabricated composite slabs and high strength bolts. L-shaped steel profiles were cast into the concrete to provide edge protection during the repeated use of the elements and increase the friction resistance between the slab and the beam. The layout of the proposed connectors is shown in Figure 2.27. Shear connector type P3 used a cast-in steel cylinder welded to the L-profile, a top plate welded to the cylinder and a pre-tensioned M20 bolts with a grade of 8.8.The steel cylinder is used to eliminate the effects of creep and shrinkage that can cause loss of prestress in through bolts but also to protect the concrete from any damage that might occur due to bearing. Shear connector type P15 uses an embedded mechanical coupler, an embedded bolt and a removable bolt placed from below. Two variants of this connection type were developed, that were mostly identical, but P15.1 uses pre-tensioned bolts and P15.2 uses epoxy resin injected bolts, which allow larger hole clearance in the steel beam as the resin prevents the slippage of the bolt.

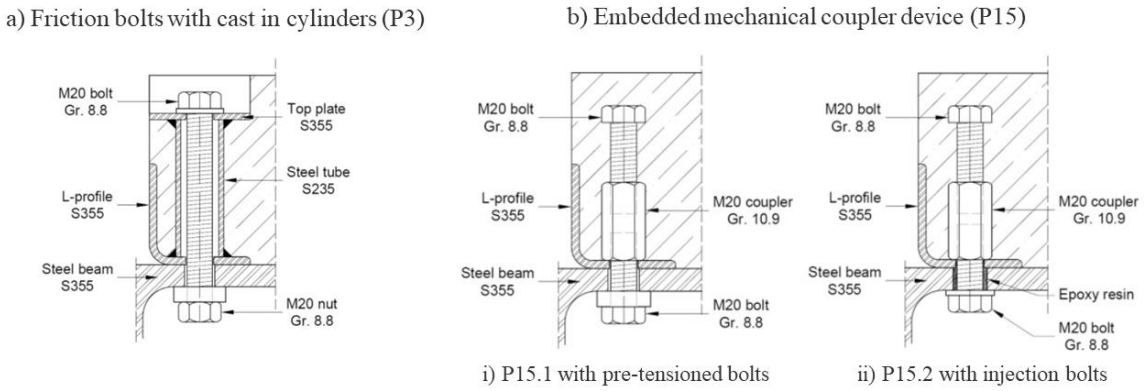

Figure 2.27: Bolted connectors proposed by Kozma et al. [35].

The load-slip curves of the new connectors are presented in Figure 2.27. It was concluded that the cylinder system (P3) was able to offer higher resistances and slip capacity than the coupler system (P15). The fabrication and installation process of the proposed connectors requires special care for

tolerances: if the tolerances are too small, the construction process can become difficult or even impossible, if the tolerances are too large, they may lead to an increase in slip and a reduction in stiffness. Furthermore, the tested shear connections shown lower stiffness than standard welded studs, which can lead to increased deflections when applied in a beam. Finally, the observed load-slip behaviour is different from the ideally plastic curve that can represent the traditional shear studs, which may affect the design of the composite beams or the definition of the ultimate load-bearing capacity of the shear connection. As a result, the design and the application of the proposed connectors is considered a challenging process.

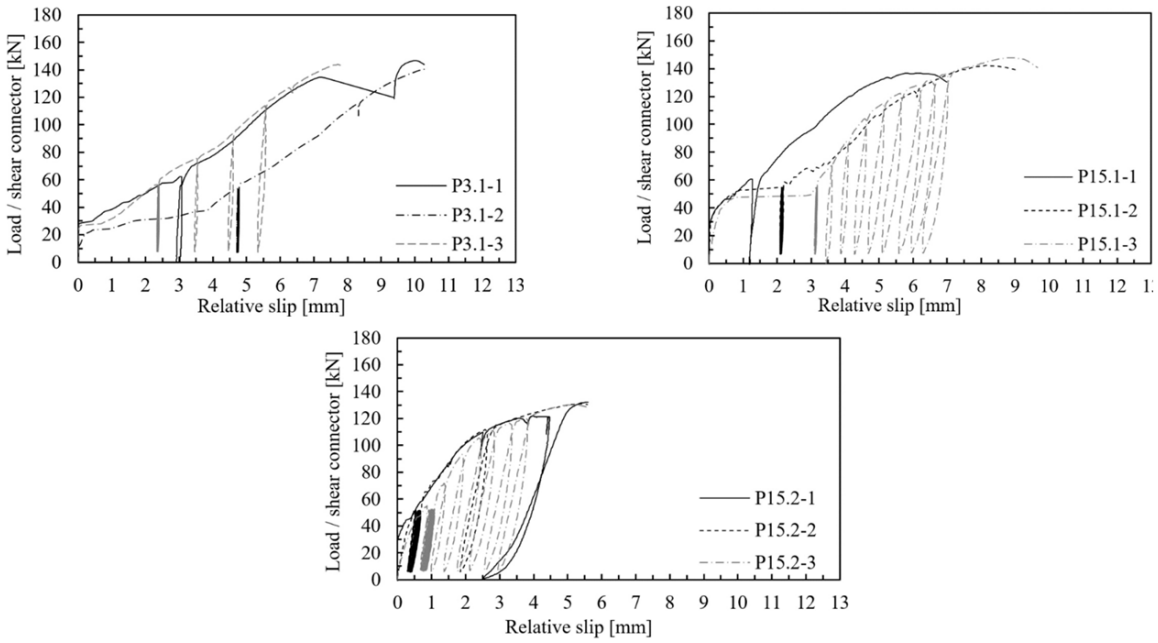

Figure 2.28: Load-slip curves for P3 and P15 connectors proposed by Kozma et al. [35].

Suwaed and Karavasilis [36] tested a full-scale precast steel-concrete composite beam of a 9m length equipped with FBSCs. The connectors were distributed along the length of the beam in pairs at 0.6m spacing. The test was conducting in a four-point bending set up. The composite beam was designed with only 32% degree of shear connection, which is considerably less than the minimum degree recommended by BS EN 1994-1-1 [6], to examine the performance of the FBSC. The load-deflection curve of the beam is shown in Fig. The author reported that the limited stroke of the jack had caused the test procedure to use several cycles of load. The experimental results showed that the moment capacity of the beam exceeded the design strength safely, since the maximum moment was higher than the partial plastic strength. The high moment capacity of the beam was attributed to the fact that FBSCs can offer high strength and ductility to the connection compare to the conventional headed studs, even if the beam was designed with only 32% shear connection.

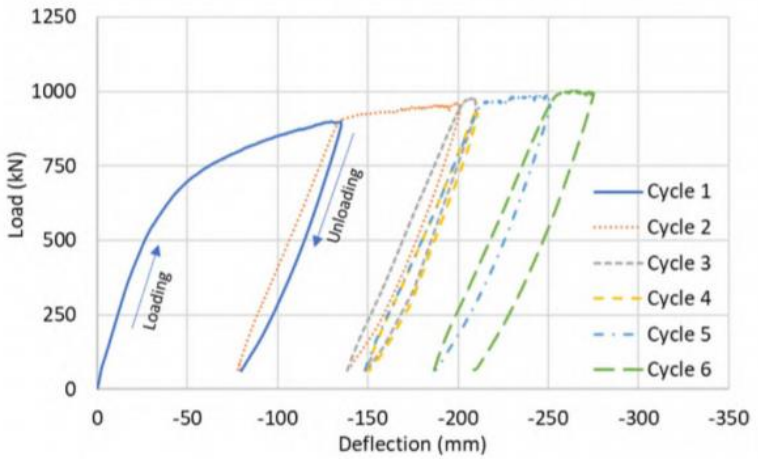

Figure 2.29: Load-deflection curve for steel-concrete composite bridges equipped with FBSCs - Suwaed and Karavasilis [36].

2.3.2 Numerical research

Kwon et al. [19] numerical tested four large-scale beam specimens retrofitted with post-installed shear connectors in ABAQUS software using FE modelling. The FE results were verified against experimental results presented in the same research project. An elastic-perfectly plastic model was used to define the material behaviour of both steel beams and steel reinforcement. For the post-installed shear connectors, the load-slip behaviour proposed by Ollgaard et al. [10] was adopted. The Riks method used for the analysis, which is generally used to predict the nonlinear collapse of structures. Steel beam and concrete slab were modelled using four-node shell elements, while cartesian connector elements were used to model the shear connectors. Bond and friction were not considered in the FE model. As shown in Figure 2.30, the FE model was able to predict the load-slip behaviour of the retrofitted beams up to the shear failure of the connectors. After this point, the FE model was unable to simulate the behaviour of the beams due to convergence issues.

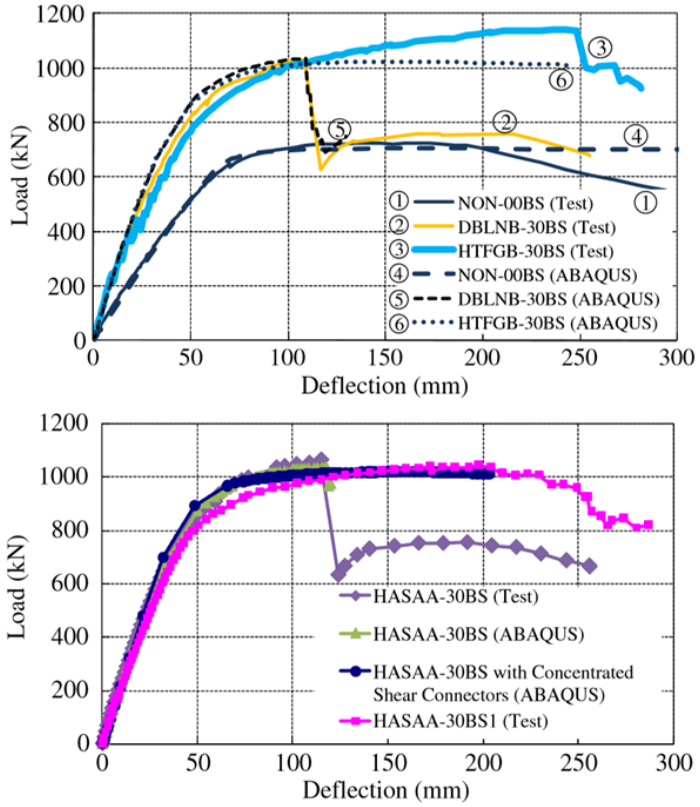

Figure 2.30: Experimental and FEA load-deflection curves for post-installed shear connectors [19].

Pavlovic et al. [24] performed advanced three-dimensional FE analysis using ABAQUS/Explicit to study the failure modes of bolted shear connectors with single embedded nut in the concrete slab. Damage initiation criterions and damage evolution laws were included in the definition of the material properties of high-strength bolts to accurately predict their failure modes, while concrete damage plasticity was used to capture the concrete degradation. The exact geometry of the heads and the threads of the bolts was used, while the bolt pretension was modelled by applying intermediate 'wrenching' boundary conditions on nuts in their local cylindrical coordinate system. The model was capable to accurately predict the load-slip behaviour of the specimens and therefore, it was used to conduct a parametric study on the shear connector height. It was concluded that the height of the shear connectors affected both the shear resistance and the slip capacity of the specimens. More specifically, as the height-to-diameter ratio increased, the shear resistance increased as well, while the slip capacity considerably decreased. Most of the specimens failed due to shear failure of the bolts. However, for shear connectors with height-to-diameter ratio less than 2.5, the dominant failure mode was the concrete crushing in front of the shear connector.

Lam and Saveri [20] developed three-dimensional FE models to investigate the behaviour of demountable shear connectors manufactured from standard headed studs. Due to the symmetry of the specimens, only half of the push-out test arrangement was modelled. Concrete damage plasticity was used to define the material properties of concrete slab. Steel beam, shear connectors and steel reinforcement were assumed to be elastic perfectly plastic materials. Surface-to-surface contact

interaction was used to properly model the interactions between all contact surfaces of the model, except from the interaction between the studs with their nuts, where a tightening interface was used. As shown in Figure 2.31, the FE model was capable to predict the ultimate shear resistance of the connection. However, there is a big difference between the experimental and FE results is in terms of the initial stiffness. According to the author, the low stiffness observed in the experimental results is attributed to the fact that the demountable connectors were tightened manually, resulting in some initial bolt slip. This phenomenon was not reproduced in the FE analysis.

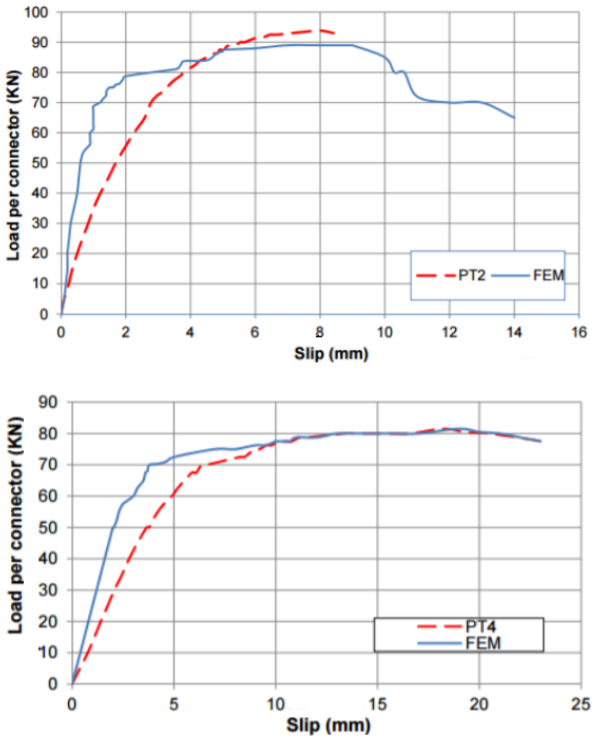

Figure 2.31: Experimental and FEA load-slip curves for demountable shear connector manufactured from standard headed studs – Lam and Saveri.[20].

Liu et al. [37] developed a FE model to investigate the behaviour of high strength friction grip bolts (HSFGB) as shear connectors in composite beams with precast geo-polymer concrete (GPC) slabs. Only one quarter of the push-out test arrangement was modelled due to the symmetry of the specimens. The nonlinear behaviour of the GPC material in the push-out tests was represented by using the PLASTIC model available in ABAQUS that uses the von-Mises yield criterion. However, this option is not able to represent accurately the complex behaviour of the concrete, especially in the part in front of the shear connectors, where the concrete is subjected to triaxial stresses. In addition, this simplified assumption precludes the consideration of tensile stresses in the concrete greater than its tensile strength.

The analysis consisted of several steps. In the first step, the contact interactions were established to ensure that numerical problems resulting from the contact formulation will not be encountered at following steps. The pretension of the bolts was simulated in the second step of the analysis by using

the BOLT LOAD function available in ABAQUS. In the last step, a displacement-controlled nonlinear analysis was performed by using the RIKS method which is generally used to predict the unstable and nonlinear collapse of a structure. However, using the implicit solver with complex geometries and interactions is generally an unfavourable practice, since it creates convergence issues and it needs more computational effort.

The accuracy of the FE model was verified against experimental results of push-out tests conducted as part of the same research program. As shown in Figure 2.32, the FE model was able to accurately predict the load-slip behaviour of the specimens. The connectors offered high shear resistance and slip capacity. However, a significant drawback was observed. The bolts had initial pretension which created friction resistance at steel-concrete interface. When the shear force overcome the frictional resistance there was no additional shear resistance. Therefore, a sudden slip occurred until the bearing resistance was achieved, meaning that the slab was continuing to slip until the gap clearance was closed. During this slip, the connection did not have resistance. The phenomenon can be observed in push-out test results in **Figure 2.32**.

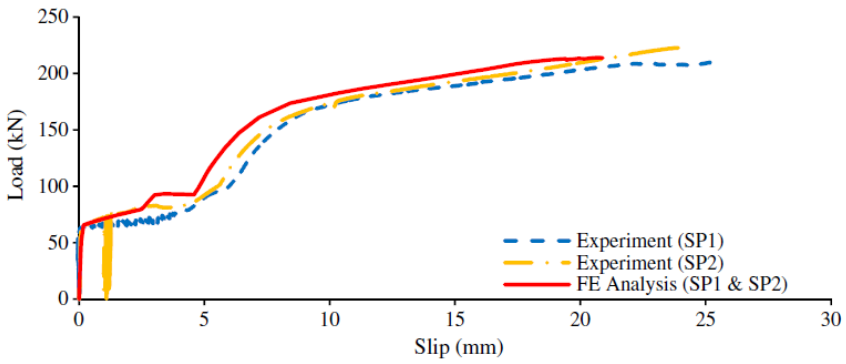

Figure 2.32: Load-slip behaviour of HSFGP shear connectors in push-out tests with precast Geo-Polymer Concrete (GPC) slabs – Liu et al. [37].

A parametric study was also conducted that showed that the ultimate shear resistance of the specimens was considerably affected by changing the diameter and/or the tensile strength of the bolts. On the contrary, it was observed that the bolt pretension force had no significant effect on the shear resistance of the connector. Finally, it was concluded that the clearance between the bolts and their holes affected the value of the first critical slip. More specifically, the specimens with a significantly large clearance hole (8mm) required a smaller force to cause the first slip compared to the other specimens with smaller clearance holes (2 and 4mm).

Liu et al. [38] developed a FE model to investigate the behaviour of simply supported steel-concrete composite beams with HSFGB shear connectors. Concrete damage plasticity was used to simulate the complex behaviour of concrete, while simpler tri-linear models were used for steel beam and steel bolt connectors. A dynamic explicit analysis was performed using ABAQUS software

consisting of two steps. For the first step, the post-tensioning forces were applied to the bolts using the orthotropic EXPANSION option, while the loads were imposed on the beam during the second step of the analysis. The results obtained from the FE analysis were verified against available test results presented by Kwon et al. [19] and Marshall et al. [16]. As shown in Figure 2.33, the FE model could capture the fundamental behaviour of composite beams accurately. A parametric study was also included in the analysis that showed that a composite beam with low degree of shear connection was still able to achieve a much higher ultimate strength than its non-composite counterpart.

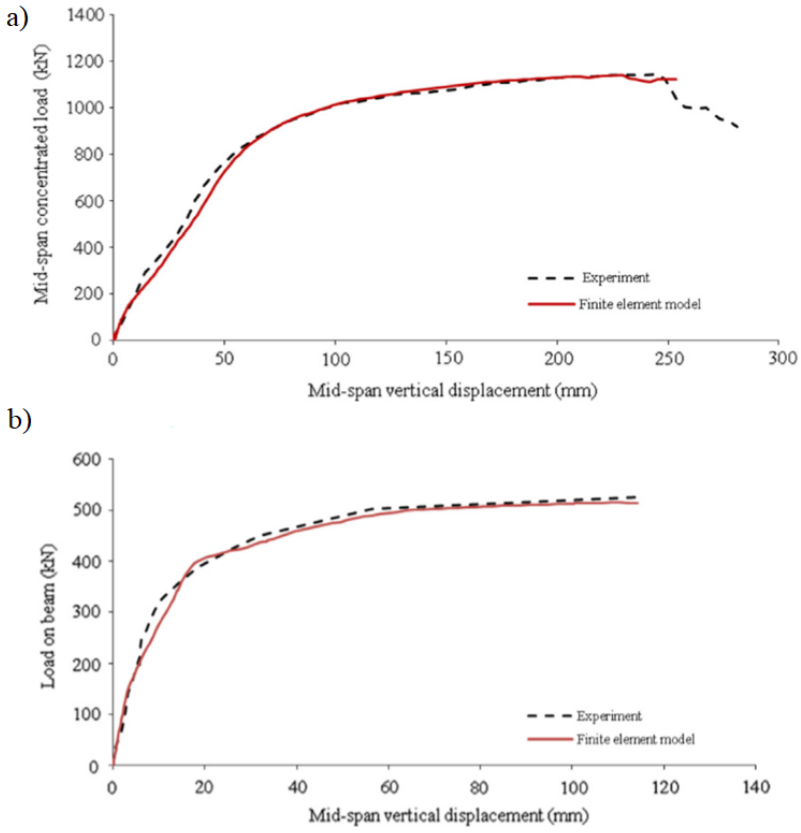

Figure 2.33: Validation of the FE model proposed by Liu et al. [38] using experimental results of a) Kwon et al. [19] and b) Marshall et al. [16].

Pathirana et al. [28] developed a FE model to investigate the behaviour of blind bolts in push-out tests. Two push-out test specimens were built in ABAQUS software, one using welded headed studs and one using the BB2 shear connectors shown in Figure 2.17. The behaviour of concrete and grout materials was modelled using concrete damage plasticity. The interactions between the different parts of the push-out specimens were modelled using the surface-to-surface contact interaction. However, tie constraint option was used to model the interaction between the steel beam and the shear connectors as well as between the concrete slab and grout. The load-slip behaviour of the retrofitted push-out tests on the welded stud shear connectors and BB2 bolt connectors is compared in Figure 2.34 with the corresponding FE simulated load-slip curves, where a relatively good agreement between experimental and numerical results is observed. A parametric study was also included in the

analysis where the effect of compressive strength of grout and the height of the connectors on the structural behaviour of the connectors was evaluated.

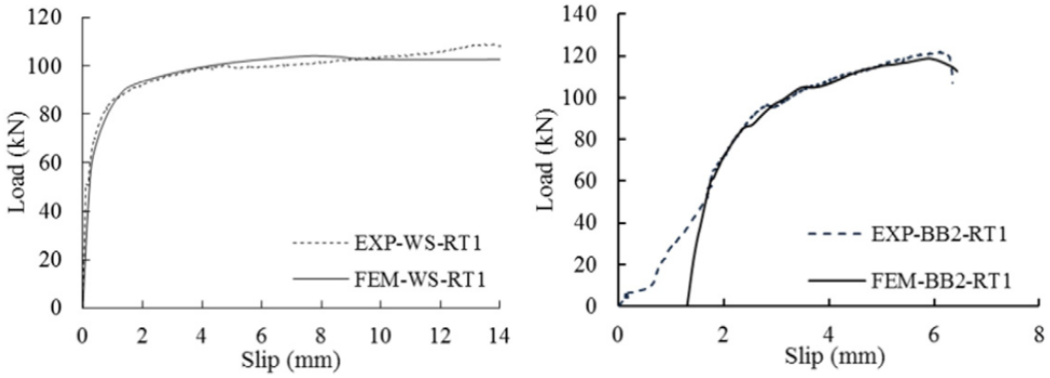

Figure 2.34: Experimental and FEA load-slip curves for blind bolts used as shear connectors in push-out tests – Pathirana [28].

Using the same approach, Pathirana et al. [29] studied the behaviour of blind bolts in full-scale beams using FE modelling. The FE models were validated using experimental results of beam specimens retrofitted with WS, BB1 and BB2 shear connectors, accordingly, as shown in Figure 2.35. It was concluded that the FE models were able to predict the load-deflection behaviour of the retrofitted beams with reasonable accuracy. The effects of the concrete compressive strength, the grout compressive strength, the grout hole size and the shear connection ratio on the flexural behaviour of the retrofitted composite beams were also assessed by carrying out parametric studies.

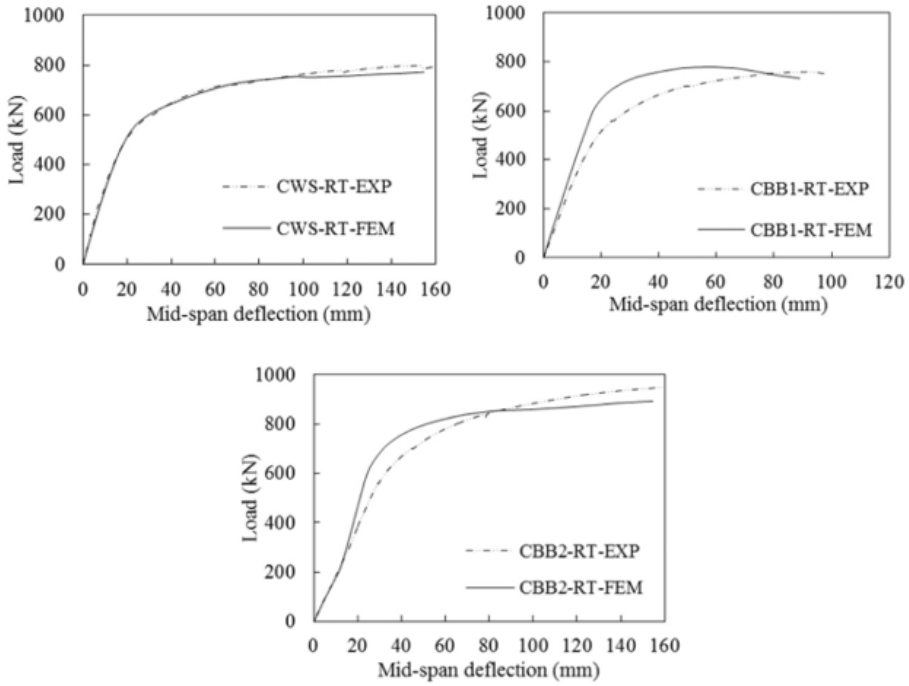

Figure 2.35: Experimental and FEA load-slip curves for blind bolts used as shear connectors in full-scale beams – Pathirana et al. [29].

Dai et al. [39] conducted a parametric study using FE method to evaluate the effect of significant parameters on the behaviour of demountable shear connectors manufactured from standard headed studs previously proposed by Lam and Saveri [20, 21]. Considering the symmetrical arrangement of the specimens, only half of the push-out testing specimen was simulated. The steel beam and the shear connectors were assumed to be elastic, with Young's modulus equal to 210 GPa and Poisson's ratio 0.3. The concrete damage plasticity was used for slabs to capture the complex brittle behaviour of the concrete. The accuracy of the FE model was verified by comparing the load-slip curves and the failure modes of the specimens against experimental results. The model was capable to predict the typical failure modes observed during the experimental tests; fracture of the shear connectors at the stud collar or concrete crushing following by splitting of the concrete slab.

The FE model was also used to assess the effect of the shear stud collar size and the compressive strength of the slabs to the shear behaviour of the connectors. It was found that the shear resistance of the specimens was slightly increased when the slab concrete strength increased from C20 to C60. Similarly, the shear resistance of the connection was considerably increased when studs with large collar diameter were used. For shear connectors with large collar diameter, the slab concrete grade also affected the failure mode of the connection. More specifically, the shear resistance of the specimens was dominated by the concrete strength in specimens with low concrete strength and shear stud strength in specimens with high concrete strength. On the contrary, for shear connectors with small collar diameter, the slab concrete grade does not alter the failure mode of the specimens, since all specimens failed by stud fracture.

2.4 Conclusions

The literature review presented in this chapter highlight the urgent need to develop innovative solutions to design sustainable bridges. Material production and associated carbon emissions could be reduced by reusing product instead of landfilling or recycling them. Steel beams are suited to reuse but are difficult to reuse when connected compositely to concrete slabs using welded studs. Demountable shear connectors that allow composite performance but also permit reuse of both components at the end of life were proposed by many researchers as an alternative to conventional headed studs and their findings were summarized in this chapter.

Even though demountable shear connectors offer many advantages according to the literature review, such as high strength, demountability to steel-concrete composite beams, and promote precast construction, there are no specific design guidelines in Eurocode 4 (reference). Therefore, the aim of this project is to study in detail their behaviour by using numerical methods and propose simple design rules to predict their capacity. In the following chapters, the behaviour of LNSC and FBSC proposed by Suwaed et al. [31, 32] are investigated. The experimental results presented by Suwaed et al. showed that the connectors offer high strength and ductility and they both allow rapid

disassembly and replacement of any deteriorating structural component of precast steel-concrete composite beams. As part of this research program, FE models using ABAQUS software will be built to simulate the behaviour of the connectors in push-out tests. The FE analysis method was preferred against experimental investigated due to its cost and time effectiveness. The FE models will be then used to conduct extensive parametric analyses to evaluate the effect of significant parameters on the structural behaviour of the connectors in steel-concrete composite bridges. The results of the parametric study will then be used to produce simple design rules in the framework of Eurocode 4.

Chapter 3 Finite modelling of Locking nut shear connectors in push-out tests and parametric study

3.1 Introduction

Three-dimensional (3D) finite element (FE) models were developed using the commercial software ABAQUS to analyse the behaviour of locking-nut shear connectors (LNSCs) in push-out tests. The FE models were validated using experimental results available in the literature [31]. The load-slip behaviour and the failure modes of the specimens are discussed.

The geometry of the FE models, the boundary conditions used, the application of loads, the analysis methods and mesh techniques used in the FE models are presented in this chapter. The explicit solver was used for the analysis, which is suitable for models with complex interactions and geometries. Damage models were included in the definition of the material properties of the various components of the connectors to capture the actual failure modes of the specimens. To calibrate the material properties of the LNSC components, additional FE models were developed corresponding to experimental material tests.

An extensive parametric study is also presented in this chapter that investigates the effect of various parameters on the shear behaviour of the LNSC. The effects of variations in the compressive strength of precast concrete plugs, the diameter, the pretension force and tensile strength of bolt connectors, and finally the bolt height to diameter ratio on the shear resistance, stiffness and the slip capacity of the connection are evaluated.

Finally, the shear resistance of the LNSCs is compared with the shear capacity the conventional welded headed studs can offer and an equation is proposed to calculate the shear resistance of the LNSCs. The accuracy of the proposed equation to predict the shear resistance of the LNSCs in steel-concrete composite structures is verified by using the results from the parametric study.

3.2 Summary of literature push-out tests

The specifications of the push-out test specimens are given in Table 3.1. LNSC_Test 1 corresponds to Test 7 conducted by Suwaed and Karavasilis [31]. Similarly, LNSC_Test_2, LNSC_Test_3 and LNSC_Test_4 correspond to Test 8, Test 10 and Test 12 presented by Suwaed and Karavasilis [31]. Details of the geometry of the push out specimens are shown in Figure 3.1 and Figure 3.2. The LNSC connector consists of a pair of high-strength steel bolts, which are fastened to the top flange of the beam using a double nut configuration, which consists of a standard lower hexagonal nut and an

upper conical nut. The steel beam has a 254×254×89 UC section with a length equal to 700mm. Four holes were drilled on the beam flanges in order to accommodate the high strength bolts along with their conical nuts. The upper part of the bolt holes is a countersunk seat with chamfered sides following an angle of 60°. The geometry of the conical nut follows the same angle so that it can perfectly fit within the countersunk seat. In this way, the conical nut prevents the slip of the bolts within their holes by providing a mechanical stop within the countersunk seat. An upper hexagonal nut is also provided to securely lock the bolts within their holes.

The geometry of the slabs is 650×600×150mm and there is a central countersunk conical pocket with the exact dimensions shown in Figure 3.2. Rapid hardening grout was poured into the slab pockets and then a precast plug (exact dimensions shown in Figure 3.2) was placed around each bolt and gradually inserted into the slab pocket. A hardened plate washer was used to uniformly distribute the bolt thrust on the upper face of the concrete plug without inducing cracks. Finally, the tightening of Nut 3 was performed before the hardening of the grout to avoid developing internal stresses in the slab.

Table 3.1. Specifications of the push-out tests.

Test Number	Bolt Diameter (mm)	Slab		Plugs		Grout
		Compressive Strength (MPa)	Tensile Strength (MPa)	Compressive Strength (MPa)	Tensile Strength (MPa)	Compressive Strength (MPa)
LNSC-Test_1	12	50	4	91	4.8	28
LNSC-Test_2	14	50	4	95	4.6	32
LNSC-Test_3	16	43	3.1	50	3.7	27
LNSC-Test_4	16	42	3.5	91	4.9	28

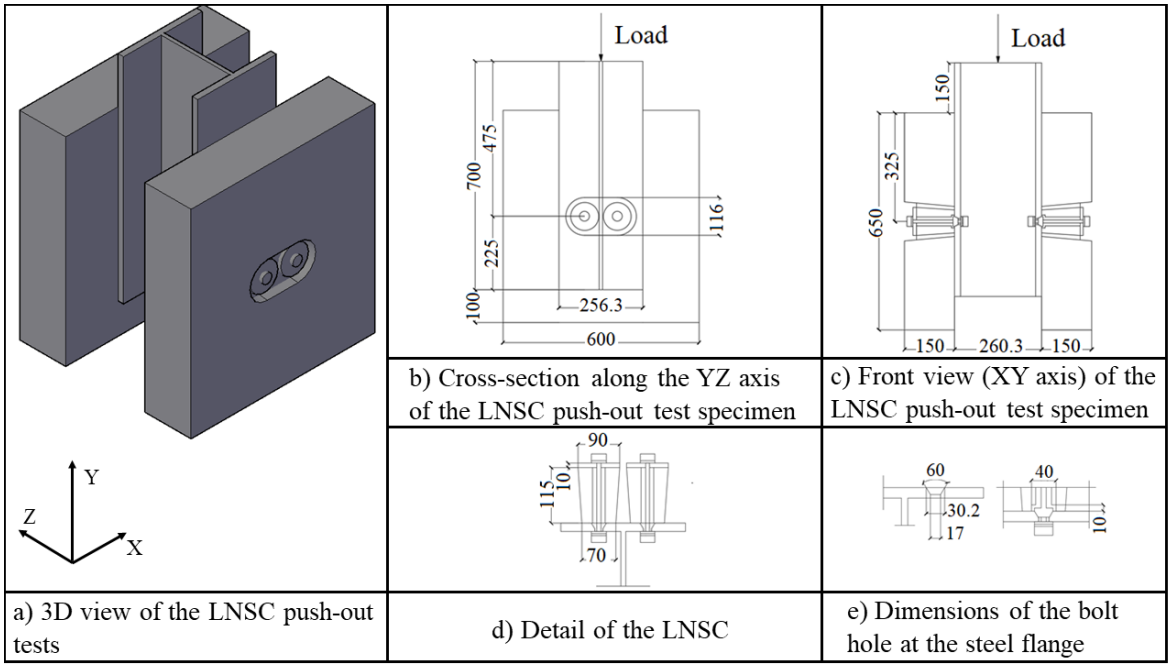

a) 3D view of the LNSC push-out tests

b) Cross-section along the YZ axis of the LNSC push-out test specimen

c) Front view (XY axis) of the LNSC push-out test specimen

d) Detail of the LNSC

e) Dimensions of the bolt hole at the steel flange

Figure 3.1: Geometry of the push-out specimens with LNSC connectors.

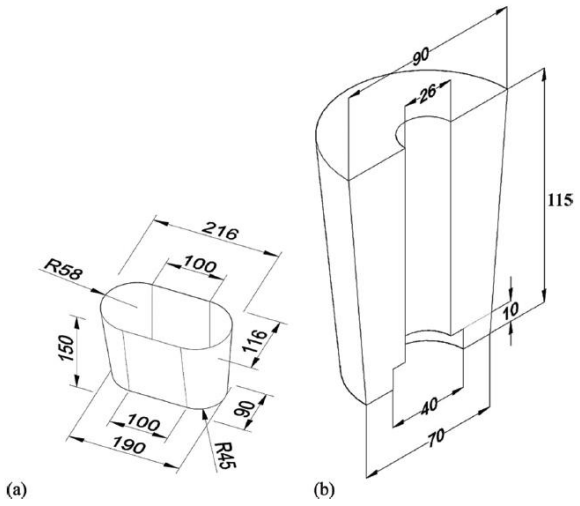

Figure 3.2: Dimensions of (a) slab pocket and (b) half plug [31].

3.3 Geometry and mesh

An overview of the FE model developed in this study is provided in Figure 3.3, together with the relevant coordinate system in which Y represents the longitudinal direction and Z represents the transverse direction of the specimen. Because of the symmetry of the specimens and the loading conditions, only one quarter of the push-out test arrangement was modelled, using double vertical symmetry condition. All the components of the push-out test specimens were included in the FE model to achieve high accuracy of the results: precast concrete plugs and slabs, high-strength bolts, plate washers, grout, steel beam and steel reinforcement bars. High-strength bolts, hexagonal nuts, washers and conical nut were modelled as one part as shown in Figure 3.4 to avoid convergence difficulties due to complicated contact interactions. The steel reinforcement of the precast concrete slab was designed according to Annex B of BS EN 1994-1-1 [6] and it is shown in Figure 3.5.

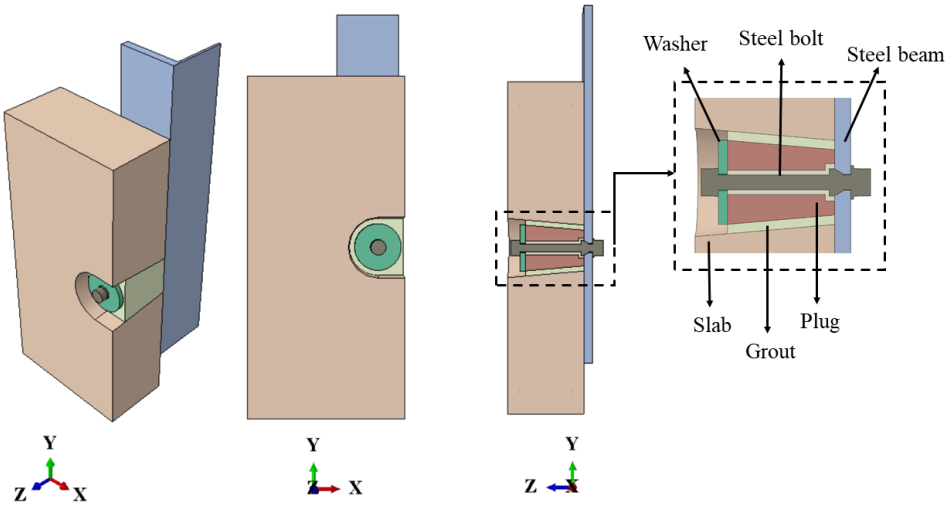

Figure 3.3: Overview of the LNSC FE model.

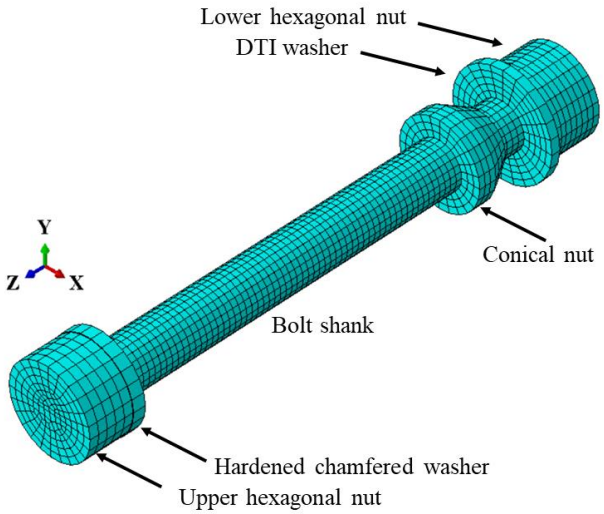

Figure 3.4: High strength bolt connector along its nuts and washers modelled as one part.

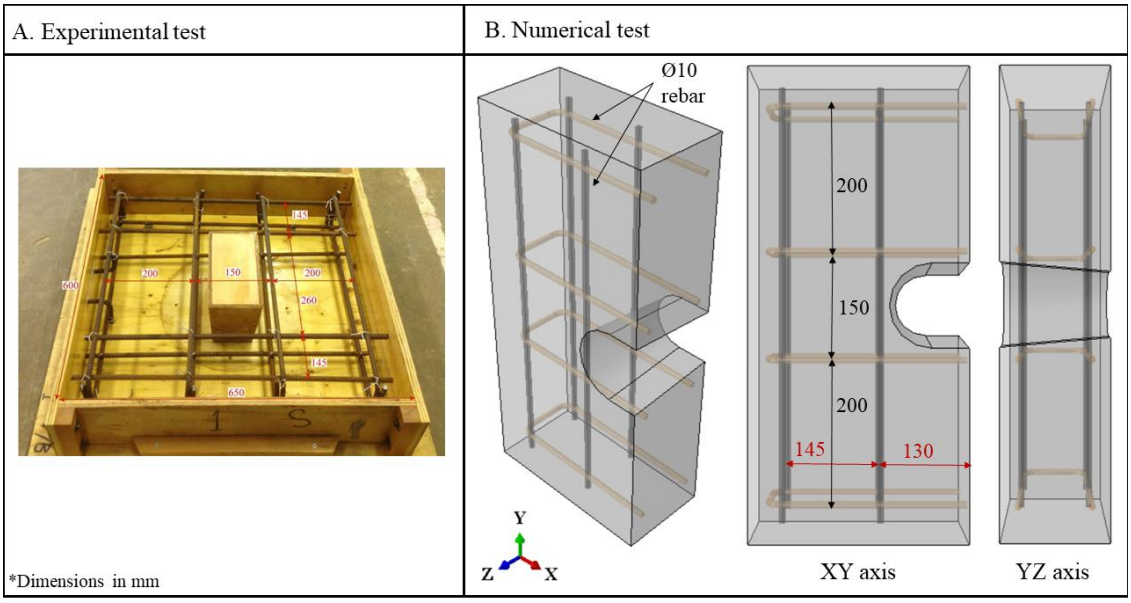

Figure 3.5: Reinforcement details of the LNSC push-out tests.

Three-dimensional eight-node linear hexahedral solid elements with reduced integration and hourglass control (C3D8R) were used to model the precast concrete slabs and plugs, the grout, the steel beam and the bolt connectors. In general, linear elements were adopted in the analysis of bolted shear connectors because quadratic elements are computationally expensive. Reduced integration elements use one fewer integration point in each direction than the fully integrated elements. More specifically, reduced integration linear elements have just a single integration point located at the element's centroid. Therefore, reduced integration elements were adopted in the FE analysis to reduce the computational time and improve the convergence rate of the model. The reinforcing bars were modelled with two node linear three-dimensional truss elements (T3D2).

To reduce the computational time, a coarse mesh was adopted for the overall push-out specimen, with a fine mesh being used for the region around the shear connector, which is the critical area, to improve the accuracy of the model. The mesh size ranges from 2mm for high-strength bolts to 8mm for precast concrete slabs. Following a mesh sensitivity analysis, the adopted mesh sizes were found to give optimum accuracy and computational efficiency. The mesh of the different components of the LNSC are shown in

Figure **3.6**.

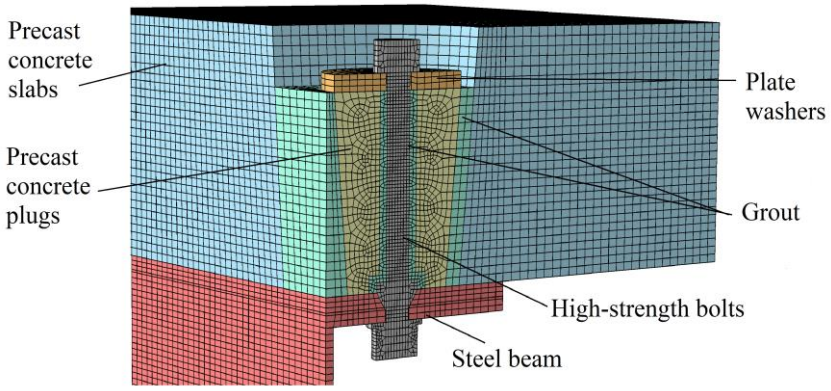

Figure 3.6: Mesh of the LNSC push-out models.

A mesh sensitivity analysis was conducted to determine the minimum element size in the critical areas of the models. For bolted connections, the critical locations are around the bolt holes and they are indicated in Figure 3.7. The mesh sensitivity of the model was minimized by evaluating the effect of mesh refinement around the bolt holes on the ultimate shear resistance prediction of the LNSC. 20 elements were used to model the area around the bolt hole, 6 elements were used through the thickness of the bolt hole and 6 in the surrounding area. As shown in Figure 3.7, the number of the elements in the critical areas were chosen in way to prevent the mesh sensitivity of the results and at the same time to require the minimum computational effort. The adopted mesh sizes for the various components of the LNSC are summarized in Table 3.2. The mesh size of each part is not uniform to allow the smooth load transfer at contact surfaces. Therefore, the mesh size of each part is given in terms of minimum and maximum element size.

Table 3.2: Mesh sizes of the different components of the FBSC.

FBSC components	Minimum element size (mm)	Maximum element size (mm)
Steel beam	5.15	7
Steel bolt	2.5	4.6
Grout	2.5	4.1
Precast concrete	2.5	14.1
Precast concrete	6	8.8
Washers	2.8	14.1

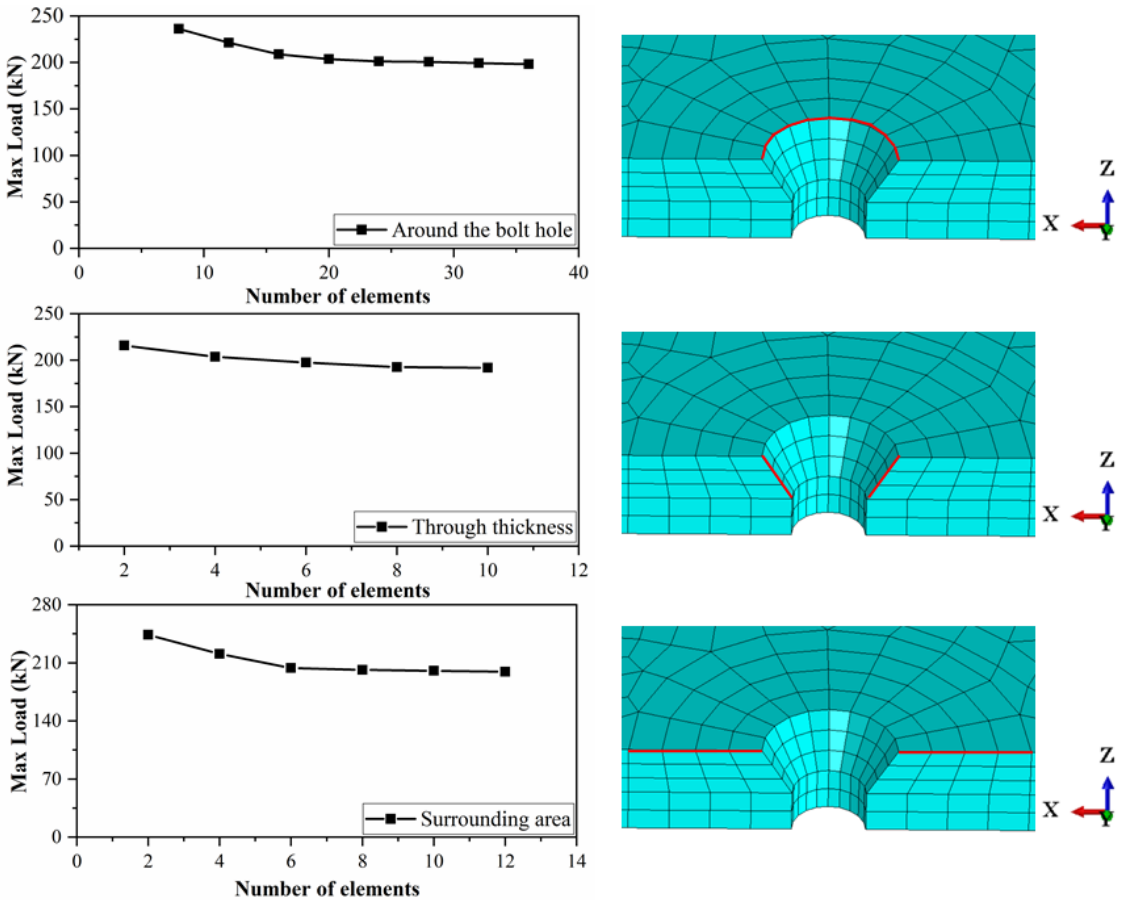

Figure 3.7: Mesh sensitivity analysis.

3.4 Interactions and boundary conditions

The contact pair algorithm was used to define the interactions between the various components of the LNSC. For the contact pair algorithm, ABAQUS/Explicit uses a kinematic contact formulation by default that achieves precise compliance with the contact conditions using a predictor/corrector method. The increment at first proceeds under the assumption that contact does not occur. If at the end of the increment there is an overclosure, the acceleration is modified to obtain a corrected configuration in which the contact constraints are enforced.

For the contact pair algorithm, ABAQUS/Explicit decides which type of weighting to use, pure or balanced master-slave contact, for a given contact pair based on the nature of the two surfaces involved and the constraint enforcement method used. The weight parameter can be specified by the user for the balanced master-slave contact. A pure master-slave relationship is defined when the weight parameter is set to 1.0, with the first surface to act as the master surface and the second as the slave surface. On the contrary, a weight parameter of zero means that the second surface is the master surface and the first one is the slave surface. In the FE model developed, the default weight value 0.5 was used.

The normal and tangential behaviour of the contact surfaces was described using the “hard” and “penalty” formulation respectively. The following friction coefficients were used for the contact interaction between the various components of the connector: 0.45 for steel-concrete interfaces, 0.4 for concrete-concrete interfaces and 0.25 for steel beam – steel bolts interfaces [38]. Finally, the embedded constraint option was applied to the reinforcement bars and concrete slab, in order to constrain the translational DOF of the nodes on the rebar elements to the interpolated values of the corresponding DOF of the concrete elements.

One quarter of the push-out test arrangement was modelled using double vertical symmetry. The two planes of symmetry are shown in Figure 3.8. “Surface 1” was restrained from translating in the Z direction and rotating in the X and Y directions, while “Surface 2” was restrained from translating in the X direction and rotating in the Y and Z directions. All nodes at the bottom end of the concrete slab (“Surface 3”) were restrained against all translational and rotational degrees of freedom.

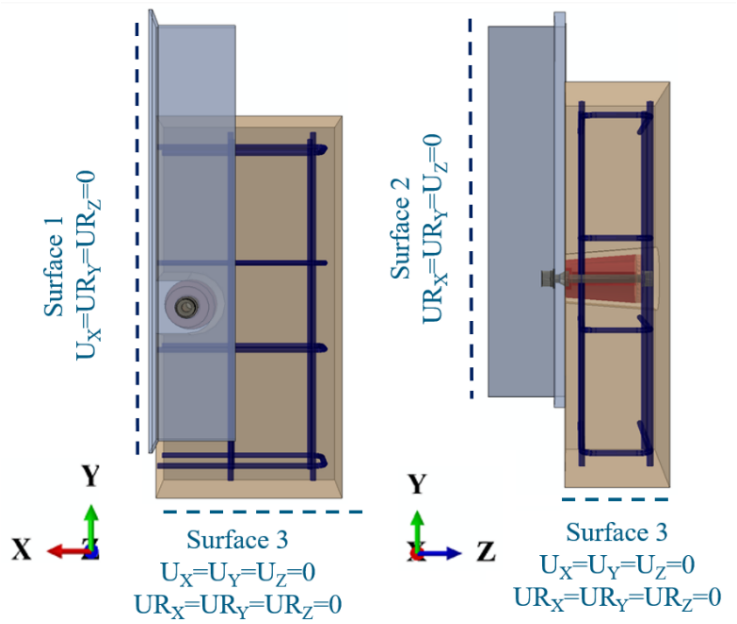

Figure 3.8: Boundary conditions of the LNSC FE models.

3.5 Loading steps

Loading was defined in two subsequent steps, corresponding to the experimental testing. In the first step, the pre-tensioning of the bolts was simulated, while in the second step, the uniformly distributed test load was applied as an imposed downward displacement at the top (cross-sectional surface) of the steel beam.

In ABAQUS/Explicit, bolt load is not available. Therefore, the pre-tensioning of the bolt was achieved in the implicit solver using an in-built ABAQUS function at the first step of the analysis. Subsequently, a predefined temperature field was calibrated and was used in the explicit solver to create the same effect by thermal contraction of the bolt. Figure 3.9 shows the distribution of axial

stresses through the thickness of the bolt using the in-build ABAQUS function and predefined temperature field. The two methods have a relatively good agreement.

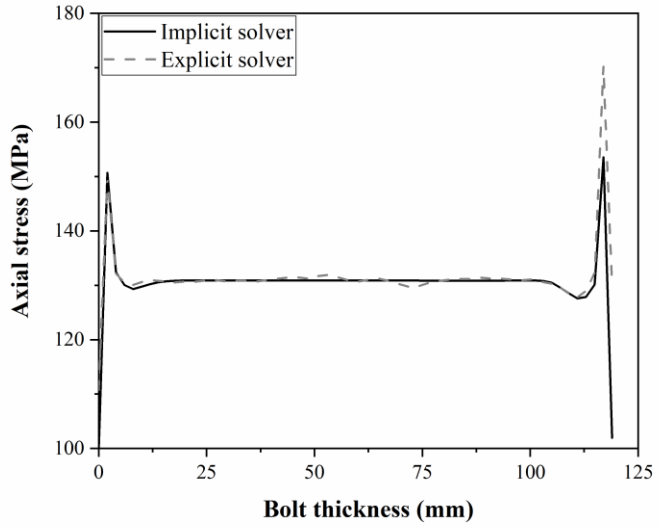

Figure 3.9: Distribution of axial stresses through the bolt length.

Appropriate smoothing was adopted for time dependent amplitude functions in all loading steps to avoid large inertia forces in the quasi-static analysis. An example is shown in Figure 3.10, where the vertical displacement imposed at the top of the steel beam in Test 12 is illustrated as a function of step time.

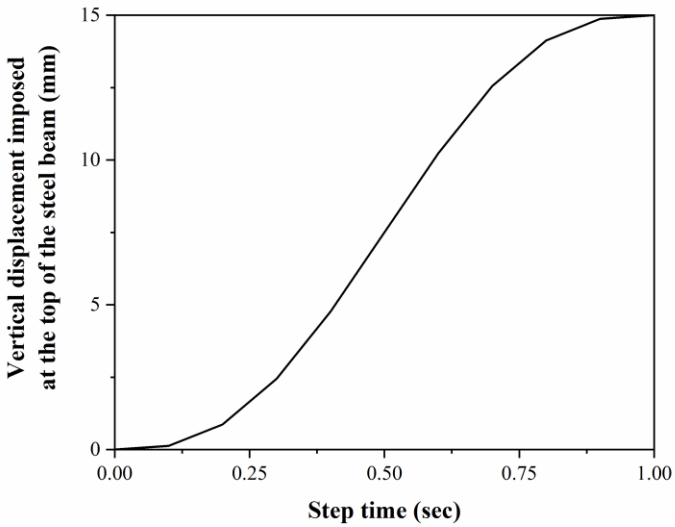

Figure 3.10: Smooth loading amplitude function.

3.6 Analysis method

A quasi-static analysis was performed using the explicit dynamic solver that has the ability to handle severely nonlinear behaviour without having the usual convergence issues that implicit static solver does. The explicit dynamic analysis method uses direct integration by using many small increments to integrate the global equation of motion through time. More specifically, the explicit dynamic analysis method is based on the central difference method combined with the use of diagonal element mass matrix to calculate the state of the next increment. The dynamic equilibrium equations are satisfied at the beginning of each increment and the use of the lumped mass matrix, allows the calculation of the nodal accelerations at any given time, t, using the following expressions:

Dynamic equilibrium:

$$M\ddot{u} = P - I \tag{3.1}$$

Calculation of nodal accelerations at any given time:

$$\ddot{u}_i = [M^{-1}(P - I)]_i \tag{3.2}$$

Then the nodal accelerations are used to define the velocity solution at time i+1:

$$\dot{u}_{\left(i+\frac{1}{2}\right)} = \dot{u}_{\left(i-\frac{1}{2}\right)} + \frac{\Delta t_{(i+1)} - \Delta t_{(i)}}{2} \times \ddot{u}_i \tag{3.3}$$

$$u_{(i+1)} = u_i + \Delta t_{(i+1)} \times \dot{u}_{\left(i+\frac{1}{2}\right)} \tag{3.4}$$

The explicit dynamic analysis method is conditionally stable, which means that the size of the time increments has to be small enough to preserve the stability of the result. Relatively small increment steps ensure that the increment result rarely deviates from the exact solution.

Mass scaling option offered by ABAQUS/Explicit was used for computational efficiency. Mass scaling is an automated procedure whereby the code increases the time step by scaling up the density in specific elements on the model which are controlling the time step. ABAQUS requires from the user to specify a minimum time step size. Therefore, the density in those elements that have time steps smaller the value specified, are increased to the point where the time step is equal to this value. Mass scaling with desired time increment of 1e-07 sec was used in the analysis. Both kinetic and internal energy were monitored throughout the analysis, to ensure that the quasi-static conditions are maintained; the kinetic energy was less than 5% of the internal energy. An example is shown in Figure 3.11, where the kinetic over internal energy over step time of the analysis for LNSC Test 12 are presented.

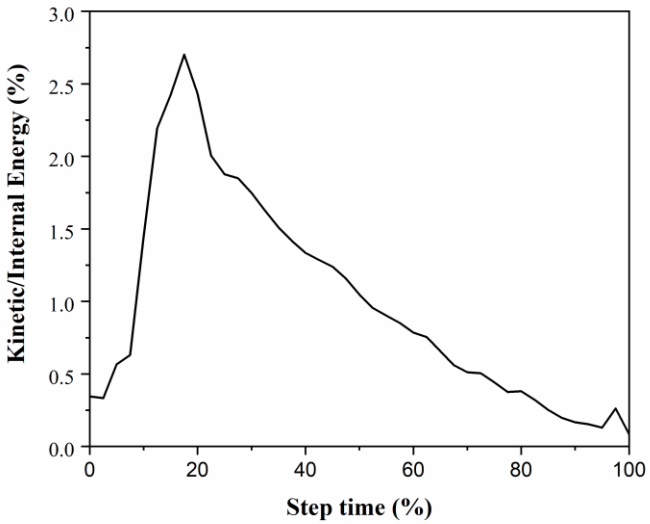

Figure 3.11: Energy monitoring for quasi-static analysis.

3.7 Material Models

3.7.1 Steel material properties

A plastic model with von Mises yield function, associated plastic flow and isotropic hardening was used to model the steel beam. The modulus of elasticity and Poisson's ratio of the steel beam were taken as 210 GPa and 0.3 respectively. The material behaviour was represented by the bilinear plus nonlinear hardening model proposed by Yun [40] as shown in Figure 3.12. The stress-strain behaviour can be determined from Eq. (3.5 – 3.9).

$$f(x) = \begin{cases} \varepsilon E, & \varepsilon \leq \varepsilon_y \\ f_y, & \varepsilon_y < \varepsilon \leq \varepsilon_{sh} \\ f_y + (f_u - f_y)\left\{0.4C_1 + \dfrac{2C_1}{[1 + 400C^5]^{1/5}}\right\}, & \varepsilon_{sh} < \varepsilon \leq \varepsilon_u \end{cases} \tag{3.5}$$

Where:

$$C_1 = \frac{\varepsilon - \varepsilon_{sh}}{\varepsilon_u - \varepsilon_{sh}} \tag{3.6}$$

$$\varepsilon_{sh} = 0.1\frac{f_y}{f_u} - 0.055 \tag{3.7}$$

$$E_{sh} = \frac{f_u - f_y}{0.4(\varepsilon_u - \varepsilon_{sh})} \tag{3.8}$$

$$\varepsilon_u = 0.6\left(1 - \frac{f_y}{f_u}\right) \tag{3.9}$$

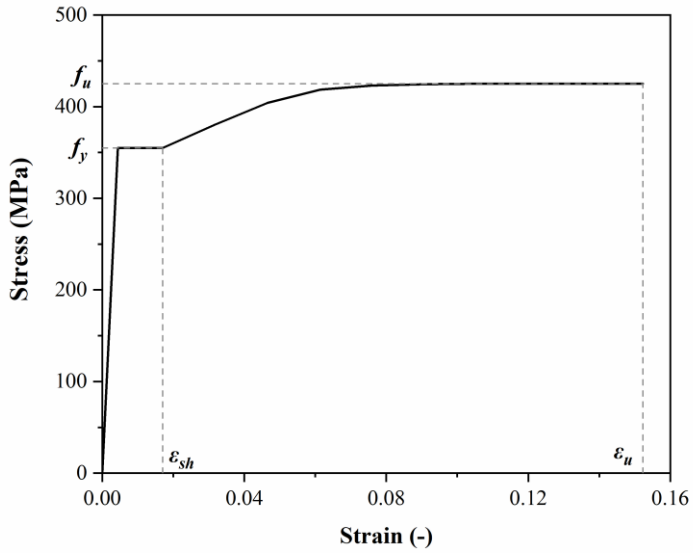

Figure 3.12: Engineering stress-strain curve for steel beams.

For the steel reinforcement, a simpler elastic-perfectly plastic model, without strain hardening, and yield strength equal to 500MPa was employed [41].

To define the material properties of high-strength bolts, the engineering stress-strain curves extracted from the experimental results conducted by Suwaed et al. [42] were used. The engineering stress-strain curves were constructed by assuming that both length and diameter of the coupon specimens remain constant throughout the experimental procedure. The engineering stress-strain curve for high-strength steel bolts is shown in Figure 3.13.

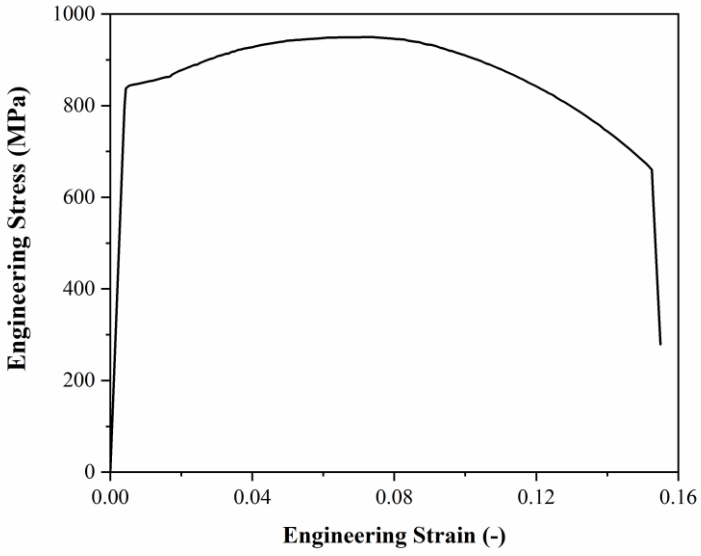

Figure 3.13: Engineering stress-strain curve for high-strength steel bolts.

The proof stress was determined by drawing a parallel to elastic part of the engineering stress-strain curve at 0.2% strain as shown in Figure 3.14.

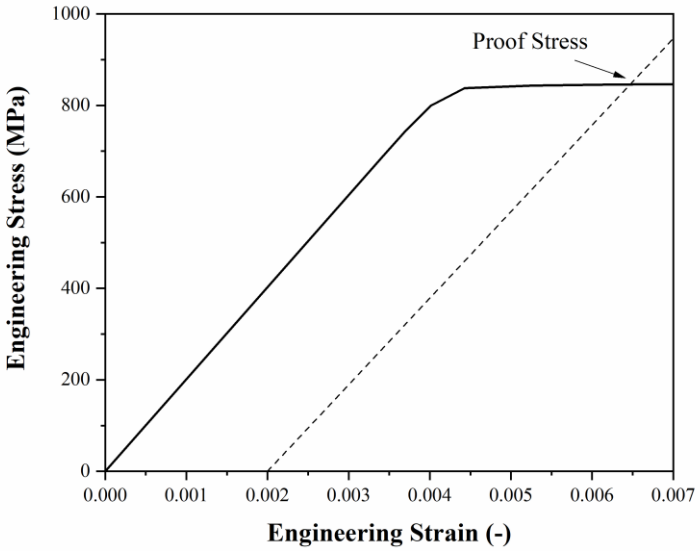

Figure 3.14: Proof stress of high-strength bolts.

A plastic model was defined using the true stress-strain curve for high-strength bolts. For the determination of the true stress-strain curve, the material volume is assumed to remain constant during loading:

$$A \times l = A_0 \times l_0 \tag{3.10}$$

Where A is the instantaneous cross-sectional area of the tensile specimen, l is the instantaneous gauge length, A_0 is the initial cross-sectional area of the tensile specimen and l_0 is the initial gauge length.

The true strain is related to the engineering strain with the following equation:

$$\varepsilon = \int \frac{dl}{l} = ln\left(\frac{l}{l_0}\right) = \ln(1 + e) \tag{3.11}$$

The true stress is defined as the instantaneous load, P, acting on the instantaneous cross-sectional area, A:

$$\sigma = \frac{P}{A} \tag{3.12}$$

The true stress is related to the engineering stress with the above formula:

$$\sigma = s \times (1 + \varepsilon) \tag{3.13}$$

When the ultimate strength of the material is reached, the strains start to localize in a weak zone of the specimen, which is not able to carry the applied load. Due to strain localization, the cross-sectional area in this zone is reduced dramatically until fracture. Beyond the onset of necking, the strain field becomes inhomogeneous and the stress state triaxial. Therefore, the true stress-strain

curve cannot be obtained using Eq. (3.11) and Eq. (3.13). A complete true stress-strain curve can be drawn if the necking area is monitored throughout the tensile test, using Eq. (3.14).

$$\frac{l}{l_0} = \frac{A}{A_0} \rightarrow \varepsilon = ln\left(\frac{l}{l_0}\right) = ln\left(\frac{A}{A_0}\right) \tag{3.14}$$

Since the necking area was not monitored throughout the tensile test, a linear relationship between true stress and true strain was used to describe the material behaviour up to the fracture point. The fracture point was defined using Eq. (3.15) and Eq. (3.16).

$$\sigma_f = \frac{P_f}{A_f} \tag{3.15}$$

$$\varepsilon = ln\left(\frac{A_f}{A_0}\right) \tag{3.16}$$

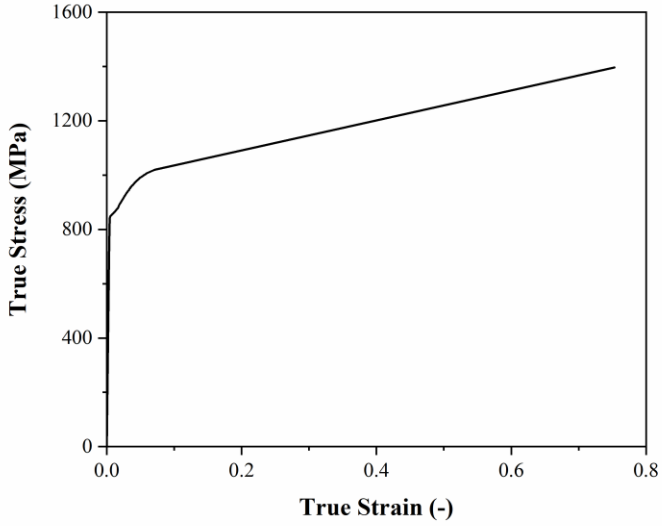

Figure 3.15: True stress-strain curve for high-strength bolts.

To evaluate the material model, standard tensile test specimens (coupons) were built in ABAQUS software to simulate the tensile tests conducted by Suwaed et al. [42]. Subsequently these material models were used in the FE models of the push-out tests.

For the accurate prediction of the force-displacement response of the specimen, only the gauge length of the coupon specimen was simulated in the analysis. Two reference points were used for the application of the boundary conditions. In reference point 1 (RF-1), a displacement load was applied, while in reference point 2 (RF-2), all translational degrees of freedom were restrained. The reference points were attached in the model using the coupling constrain option to constrain the motion of the surfaces to the motion of the reference points. The model was meshed by using C3D8R elements, and the mesh size is shown in Figure 3.16.

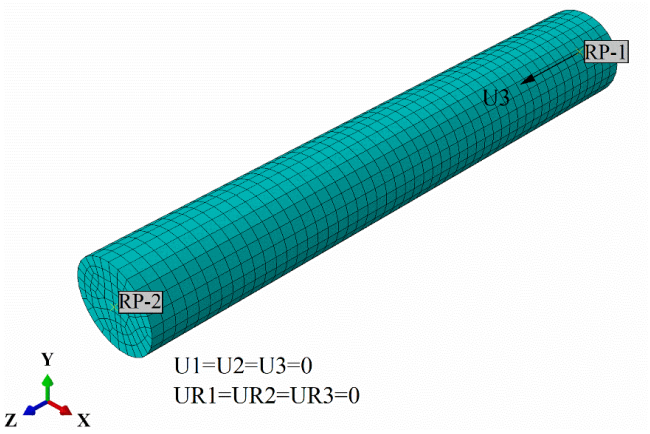

Figure 3.16: Mesh and boundary conditions of tensile test specimens.

The results obtained from the FE analysis are compared against the experimental data [42] in Figure 3.17. The FE model predicted with great accuracy the force-displacement response of the tensile specimens until the material's ultimate strength. However, the FE model was unable to predict the stiffness degradation of the material.

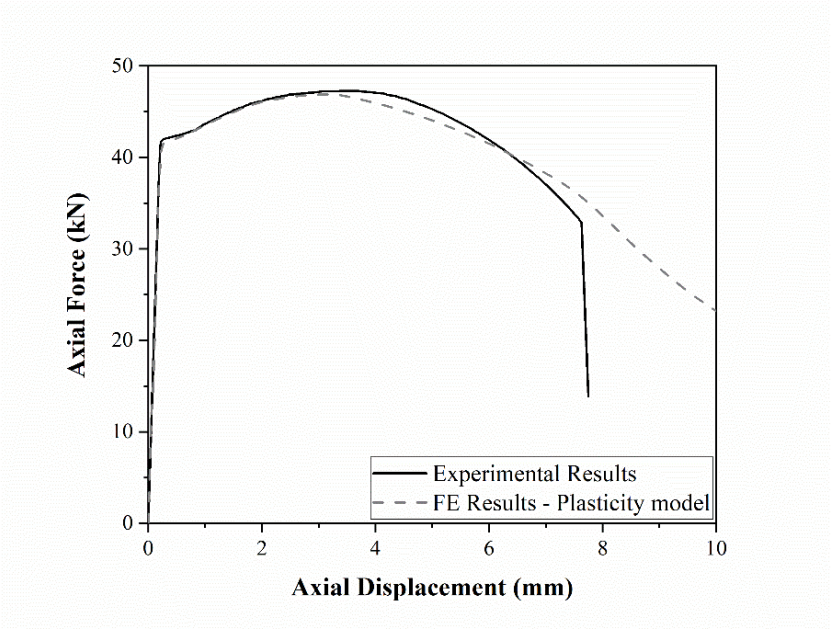

Figure 3.17: Experimental and numerical (plasticity model) force - displacement response of tensile test specimens.

A damage evolution model, which employs both plasticity and damage models, was developed, since the plasticity model was unable to predict the material degradation after the ultimate strength of high-strength bolts. The damage model requires the specification of the following:

- the undamaged response of the material
- a damage initiation criterion
- a damage evolution response

The undamaged response of the material was used as an input in the plasticity tab of Concrete Damage Plasticity model in Abaqus. The true stress-strain until the ultimate strength of the material was used to define the undamaged response of the material. After the ultimate strength, the material behaviour was assumed to be linear with tangent modulus being defined using the data point right before the ultimate strength point. The undamaged response for high-strength bolts is shown in Figure 3.18.

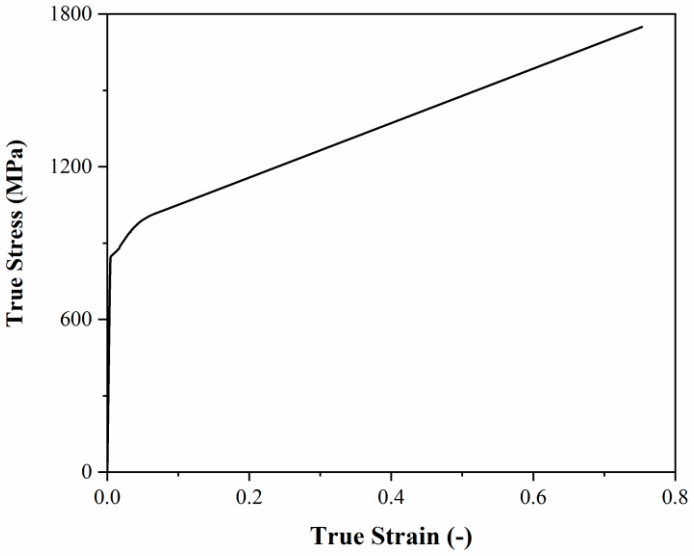

Figure 3.18: Undamaged response of high-strength bolts.

Due to absence of experimental data, recommendations proposed by Pavlovic et al. [24] were used to define the damage initiation criterion for high-strength bolts. The strain rate was not considered in the analysis, since the load application is relatively low in a quasi-static analysis. For uniaxial tension, stress triaxiality factor equals to $\eta = {}^{1}/_{3}$ and the equivalent plastic strain at the onset of damage, $\bar{\varepsilon}_D^{pl}$ equals to uniaxial true plastic strain at the onset of necking obtained from experimental results of standard tensile tests, ε_n^{pl}. Therefore, the Stress Modified Critical Strain Model for uniaxial tension is defined using Eq. (3.17).

$$\bar{\varepsilon}_D^{pl} = \alpha \times \exp\left(-1.5 \times {}^{1}/_{3}\right) \tag{3.17}$$

By forming the ratio of the equivalent plastic strain at the onset of damage to uniaxial true plastic strain at the onset of necking, the equivalent plastic strain at the onset of damage can be expressed as a function of triaxiality:

$$\bar{\varepsilon}_D^{pl}(k) = \varepsilon_n^{pl} \times \exp\left(-1.5 \times {}^{1}/_{3}\right) \tag{3.18}$$

The value of ε_n^{pl} for high-strength bolts was defined using the experimental data of tensile tests conducted by Suwaed et al. [42]. The damage initiation criterion for high-strength bolts defined by Eq. (3.18). is shown in Figure 3.19.

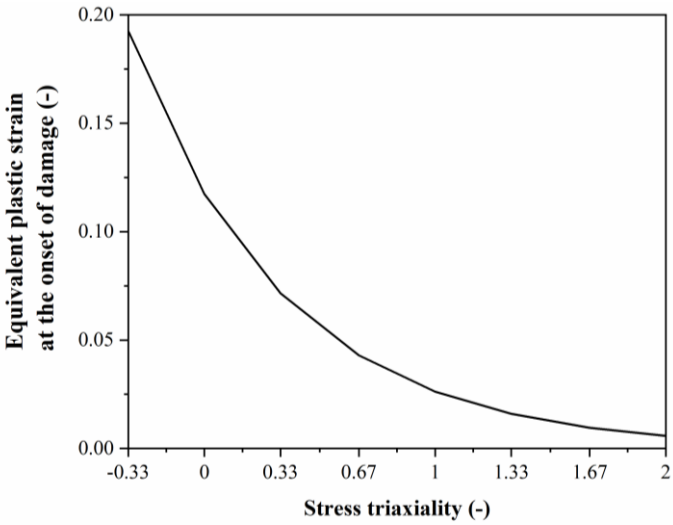

Figure 3.19: Damage initiation criterion for high-strength bolts.

The damage evolution was defined as tabular relationship between the scalar damage variable, D and the equivalent plastic displacement, u^{pl}. The equivalent plastic displacement at fracture, u_f^{pl} was defined by running the model without the damage initiation criterion. The average value of the equivalent plastic strain in the elements that are expected to fail was measured at the time increment when the final fracture was expected to happen. The value was then used to calculate the equivalent plastic displacement at failure using Eq. (3.19).

$$\dot{u}_f^{pl} = L\varepsilon_f^{pl} \tag{3.19}$$

Where L accounts for the characteristic length, which depends on the element geometry and formulation. Subsequently, the input data for damage evolution law were calibrated using an iterative procedure until the force-displacement curve matched the experimental results. Damage evolution for high-strength bolts is shown in Figure 3.20.

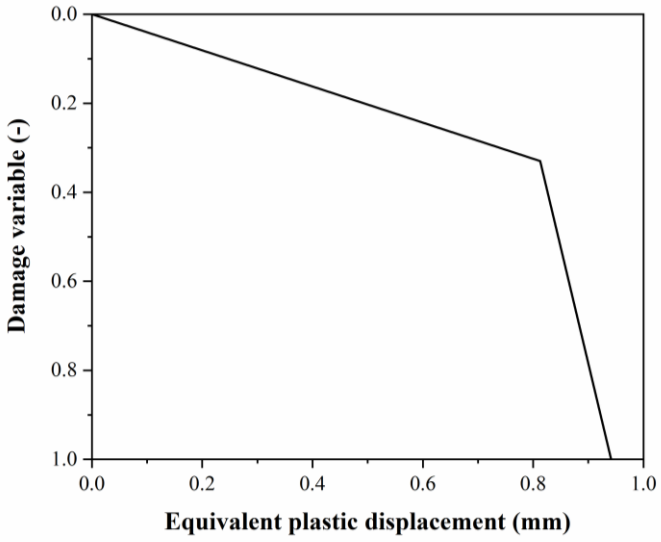

Figure 3.20: Damage evolution for high-strength bolts.

The results obtained from the FE analysis are compared against the experimental data [42] in Figure 3.21. The FE model predicted with great accuracy the force-displacement response of the tensile specimens as well as the stiffness degradation of the material. The stiffness degradation of the specimens is shown in Figure 3.22. The elements that had reached the maximum degradation (D_{max}) were removed from the mesh using the element deletion option.

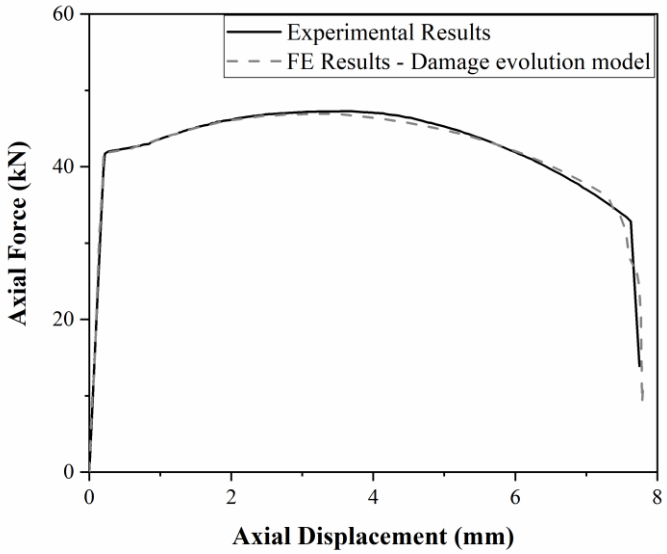

Figure 3.21: Experimental and numerical (damage evolution model) force - displacement response of tensile test specimens.

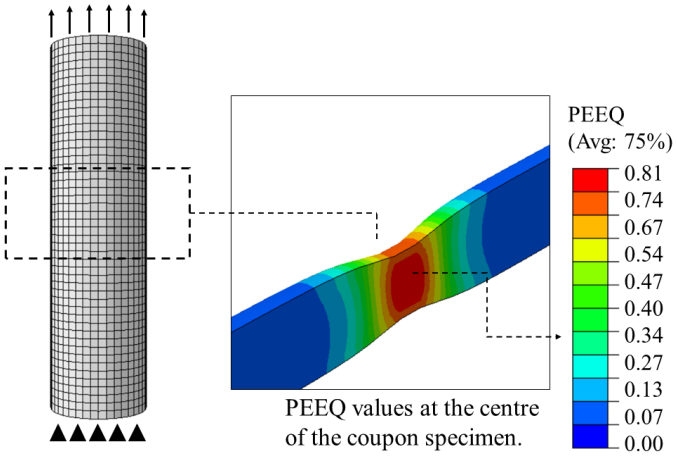

Figure 3.22: Localized strains and formation of a "necking" region at the centre of the coupon specimens.

According to the FE results, the fracture due to growth and coalescence of voids initiated at the centre of the cross-section of the specimens. After damage initiation, the elements inside the necking zone are strained in tension in the direction of loading and compressed in the two transverse directions since both thickness and width of the specimen are reduced by necking phenomenon. This results to a state of high hydrostatic stress and therefore to a higher state of triaxial stress in the element.

The hydrostatic stress in the elements located at the centre of the cross section showed higher hydrostatic stress compared to the elements located nearer the edge of the specimen. This is attributed to the fact that the straining of these elements are more of a shape altering strain than a volume changing one. The influence of the stress triaxiality on the behaviour of the material after the initiation of damage is shown in Figure 3.23 and Figure 3.24. Up to the necking point, the hydrostatic state of the two elements is relatively the same. After damage initiation, the hydrostatic stress of the element located at the centre of the cross-section is considerably higher that the hydrostatic stress of the element located at the edge of the cross-section. On the other hand, von Mises stress in both elements is approximately the same. As a result, the element located at the centre of the cross-section fail before the element located on the edge of the cross-section, because of the increasing value of the stress-triaxiality.

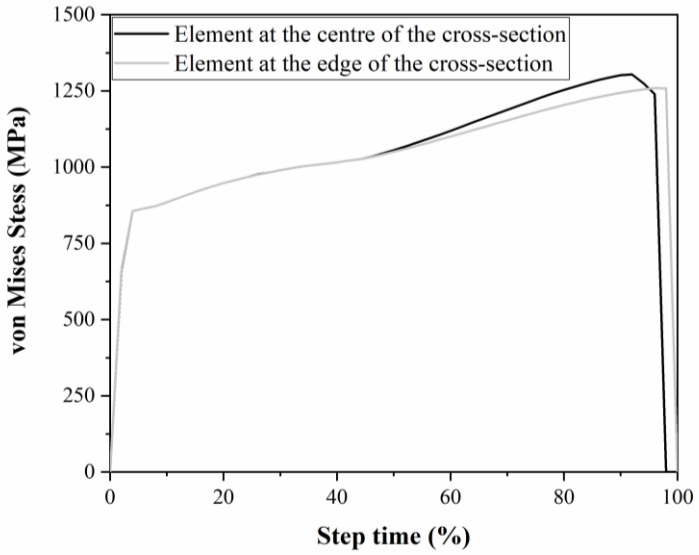

Figure 3.23: Von Mises stress at the central cross-section of the tensile test specimens.

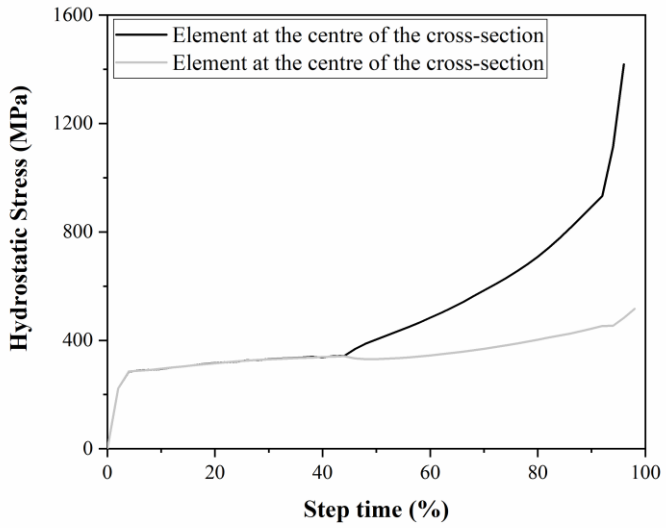

Figure 3.24: Hydrostatic stress at the central cross-section of the tensile test specimens.

The shear damage initiation criterion for predicting the onset of damage due to shear band localization was also used in the material definition of the bolts. The model assumes that the equivalent plastic strain at the onset of damage, $\bar{\varepsilon}_S^{pl}$, is a function of the shear stress ratio, θ_S and the strain rate $\dot{\bar{\varepsilon}}_S^{pl}$. The shear stress ratio is defined as a function of the equivalent stress q, the hydrostatic stress, p and the maximum tangential stress τ_{max}. A material parameter $k_s$is also introduced in the equation.

$$\theta_S = (q + k_s p)/\tau_{max} \tag{3.20}$$

As with the ductile criterion, a state variable that increases monotonically with plastic deformation proportional to the incremental change in equivalent plastic strain ws is defined. The shear damage initiation criterion is met when the following condition is satisfied:

$$\omega_S = \int \frac{d\bar{\varepsilon}^{pl}}{\bar{\varepsilon}_S^{pl}(\theta_S, \dot{\bar{\varepsilon}}_S^{pl})} \tag{3.21}$$

At each increment, the incremental increase in ws is computed by using the following equation.

$$\Delta\omega_S = \frac{\Delta\bar{\varepsilon}^{pl}}{\bar{\varepsilon}_S^{pl}(\theta_S, \dot{\bar{\varepsilon}}_S^{pl})} \geq 0 \tag{3.22}$$

Suwaed et al. [31, 32] didn't perform shear tests on the bolts used in LNSC and FBSC specimens. Therefore, the results of the shear tests conducted by Fisher et al. [43] were used to calibrate the shear damage parameters of the bolts. Fisher et al. conducted an experimental analysis to study the shear behaviour of A325 and A490 bolts with various diameters using the compression jig shown in Figure 3.25. The jig consisted on two 1 in. (25.4 mm) lap plates connected to 1 in. main plated by a single test bolt. The material properties of the bolts and the steel plated were determined from tensile tests.

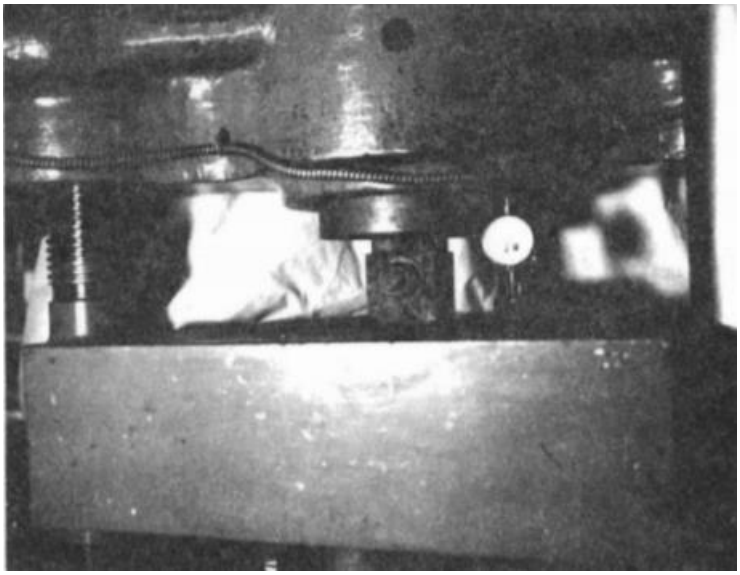

Figure 3.25: Shear test set up - Fisher et al. [43].

Finite element models were built to simulate the compressive joints. The geometry of the model precisely followed the geometry of the experimental test. A three-dimensional continuum (solid) 8-node linear brick element with reduced integration was used to mesh the components of the compression jig, which is shown in Figure 3.26.

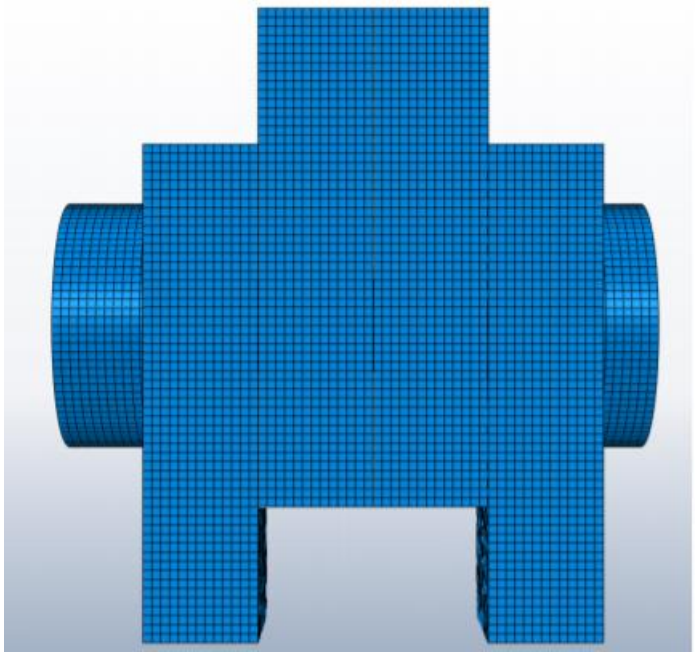

Figure 3.26: FE model of the bolts' shear test.

The interaction between the four plated, as well as between the bolt shank and the plates was defined by using a surface-to-surface formulation. The normal behaviour of the contact surfaces was described using the “hard” formulation to prevent penetration of the slave nodes into the master surfaces. The tangential behaviour was described by assuming no friction between the surfaces. Finally, the bolt head and the nut were “tied” to the plates to avoid relative motion between them.

Loading was defined in two subsequent steps, corresponding to the experimental procedure: bolt pretension performed on the first step, while on the second step a vertical displacement load was applied in the middle plated up to failure of the specimens. In terms of boundary conditions, the bottom end of the right and left plated was restrained in all degrees of freedom.

To obtain accurate results, ductile damage model was also included in the analysis. To calibrate the ductile damage parameters, two additional FE models were built. The engineering and true stress-strain relationships of bolts and plate materials were defined following the procedure used for the LNSC bolts. The ductile damage initiation criterion for bolts and plates was established using the experimental results presented by Fisher et al. [43], where the uniaxial true plastic strain at the onset of necking can be defined as 0.05225 for the bolts and 0.1533 for the plates. The damage evolution laws were defined by following an iterative process. As shown in Figure 3.27 and Figure 3.28, the

two additional FE models built to calibrate the ductile damage parameters were able to accurately predict the tensile behaviour of the bolts and plates.

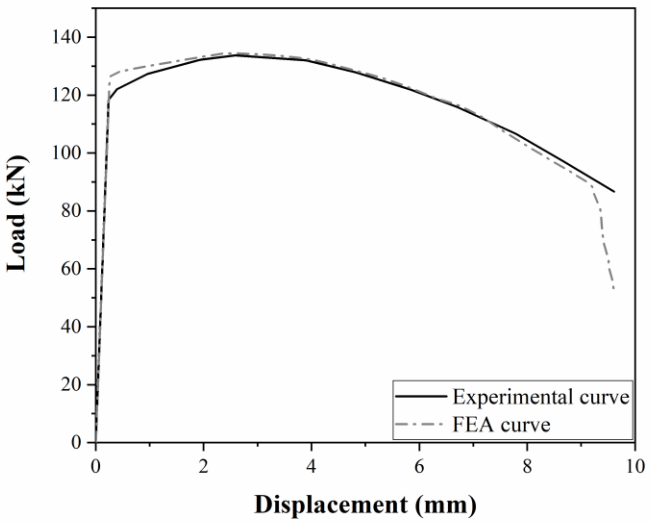

Figure 3.27: Experimental and FEA load-displacement curves for bolts - Fisher et al. [43].

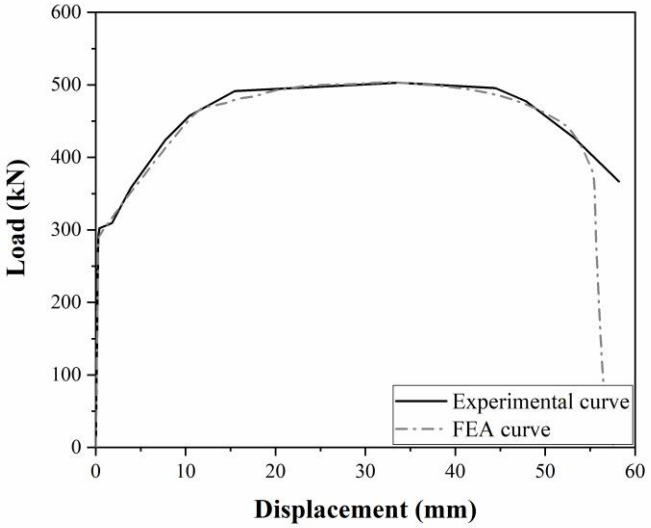

Figure 3.28: Experimental and FEA load-displacement curves for plates - Fisher et al. [43].

Once the ductile damage parameters were obtained, the compression jip was built. The shear damage parameters were calibrated by comparing the FE results with experimental results presented by Fisher et al. Since shear was the predominant failure mode of the bolts, the shear stress ratio was set equal to $\theta_S = \sqrt{3}$ =1.732 (pure shear condition). Therefore, shear damage initiation criterion was calibrated to constant value of equivalent plastic strain at the onset of damage. The value of the equivalent plastic strain at the onset of damage was obtained by running the model using ductile damage only. Displacement control damage evolution law was used to rule out the mesh dependency of the results.

Multiplicative degradation was assumed in the analysis to allow interaction between the shear and ductile damage models. The equivalent plastic displacement, $\dot{\tilde{u}}_f^{pl}$ was calculated using equation 3.19. Then, the damage evolution law was established by iteratively running the model. The results obtained from the FE analysis are compared with the experimental data presented by Fisher et al. [43] in Figure 3.29.

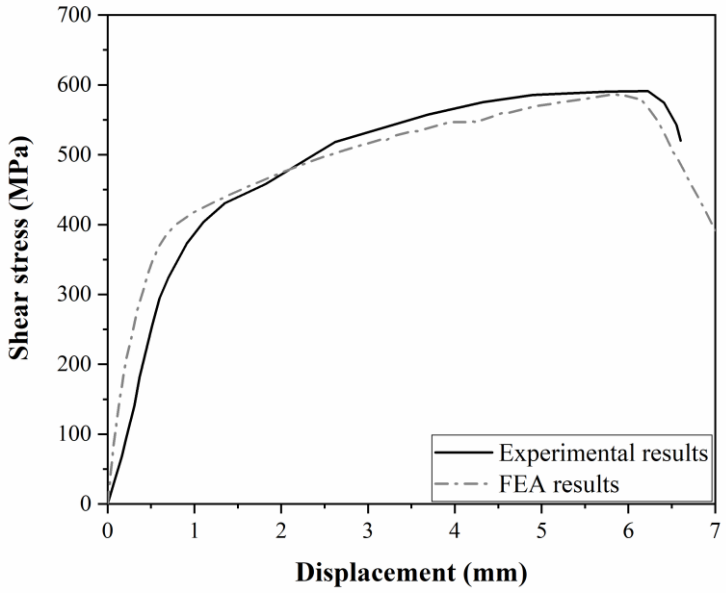

Figure 3.29: Experimental and numerical results - shear test of the bolts - Fisher et al. [43].

3.7.2 Concrete material properties

Concrete Damage Plasticity (CDP) model was employed to simulate the behaviour of concrete materials; plugs, slabs and grout. Concrete Damage Plasticity uses concepts of isotropic damaged elasticity in combination with isotropic tensile and compressive plasticity to represent the inelastic behaviour of concrete. The mechanical properties of plugs, slabs and grout are presented in Table 3.1. The compressive strength of the slabs and the plugs were evaluated using standard cubes with 100mm length, while the compressive strength of grout by using cubes with 75mm length. The tensile strength of slabs and plugs were obtained by using standard cylinders of 100mm diameter and 200mm length [42].

The uniaxial stress-strain relationship as given by Eq. (3.20), proposed by Carreira & Chu [44], was used for concrete slabs and grout in compression.

$$\frac{f_c}{f_c'} = \frac{\beta(\varepsilon - \varepsilon_c')}{\beta - 1 + (\varepsilon - \varepsilon_c')^{\beta}} \tag{3.23}$$

Where β is a material parameter that depended on the shape of the stress-strain diagram, f_c' is the strength of concrete and ε_c' is the strain corresponding to f_c'. Parameter β can estimated using Eq. (3.21).

$$\beta = \left[\frac{f_c'}{32.4}\right]^3 + 1.55 \tag{3.24}$$

While the strain corresponding to concrete strength is given by Eq. (3.22):

$$\varepsilon_c' = (0.71 f_c' + 168) \times 10^{-5} \tag{3.25}$$

Plug's material properties were defined by using the modified uniaxial stress-strain relationship for high strength concrete proposed by Hsu & Hsu [45]. The complete stress-strain relationship under uniaxial compression testing can be represented by Eq. (3.23).

$$\frac{f_c}{f_c'} = \frac{n\beta(\varepsilon - \varepsilon_c')}{n\beta - 1 + (\varepsilon - \varepsilon_c')^{n\beta}} \tag{3.26}$$

Where n is a material parameter that depends on the strength of the material. The values of n are obtained by the following conditions:

For $0 \leq x \leq 1$:

$$n = 1 \tag{3.27}$$

For $1 \leq x \leq x_d$, $n = 1$, if:

$$0 < f_c' < 62MPa \tag{3.28}$$

$n = 2$ if

$$62MPa \leq f_c' < 76MPa \tag{3.29}$$

$n = 3$ if

$$76MPa \leq f_c' < 90MPa \tag{3.30}$$

$n = 5$ if

$$90MPa \leq f_c' \tag{3.31}$$

The stress-strain curve used in the FE model for concrete materials in Test 12 are shown in Figure 3.30.

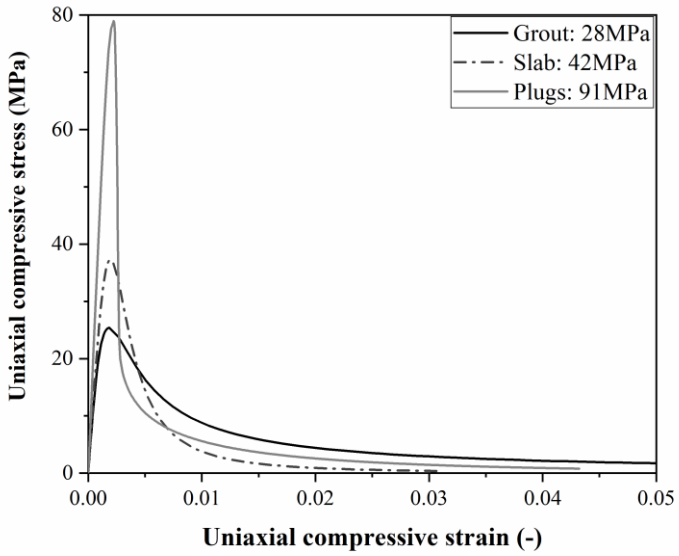

Figure 3.30: Concrete compression stress-strain behaviour.

The part of the concrete plug in front of the conical nut is under nearly triaxial stress confinement conditions due to the pre-tensioning of Nut 3. Therefore, stresses higher that its 80-100MPa design strength were developed. In addition, the existence of ordinary strength grout enables the bolts to deflect by crushing the grout in the plug-bolt interface, which enables the LNSC to develop its large slip capacity. To take into account the complex nature of passively confined concrete, key material parameters need to be determined; the ratio of the second stress invariant on the tensile meridian to that on the compressive meridian (K_c), dilation angle (ψ), flow potential eccentricity (e), and the ratio of the compressive strength under biaxial loading to uniaxial compressive strength (f_{b0}/f_c'). Papanikolaou and Kappos [46], proposed Eq. (3.29) to determine the ratio of f_{b0}/f_c'.

$$\frac{f_{b0}}{f_c'} = 1.5\ (f_c')^{-0.075} \tag{3.32}$$

Yu et al. [47] proposed Eq. (3.30) to express K_c as a function of the compressive strength of the concrete.

$$K_c = \frac{5.5}{5 + 2(f_c')^{0.075}} \tag{3.33}$$

A value of e =0.1 was adopted for the flow potential eccentricity, according to Abaqus user manual recommendations [48]. Dilation angle values for grout, slab and plugs respectively, were iteratively calibrated to match push-out tests results.

The tensile behaviour of concrete was assumed linear until the tensile strength of concrete was reached. Beyond the failure stress, Hillerborg's [49] fracture energy approach was adopted in order to minimize the mesh sensitivity of the results. Hillerborg used Eq. (3.31) to define the energy required to open a unit area of crack as a material parameter, using brittle fracture concepts. Therefore, the tensile softening response is characterized by means of fracture energy [50],[51]:

$$G_f = (0.0468{d_{max}}^2 - 0.5d_{max} + 26){f_t}^{0.7} \quad (3.34)$$

Where f_t is in MPa and d_{max} is the maximum coarse aggregate size (in mm).

A linear loss of strength was assumed in this model (Figure 3.31) [48].

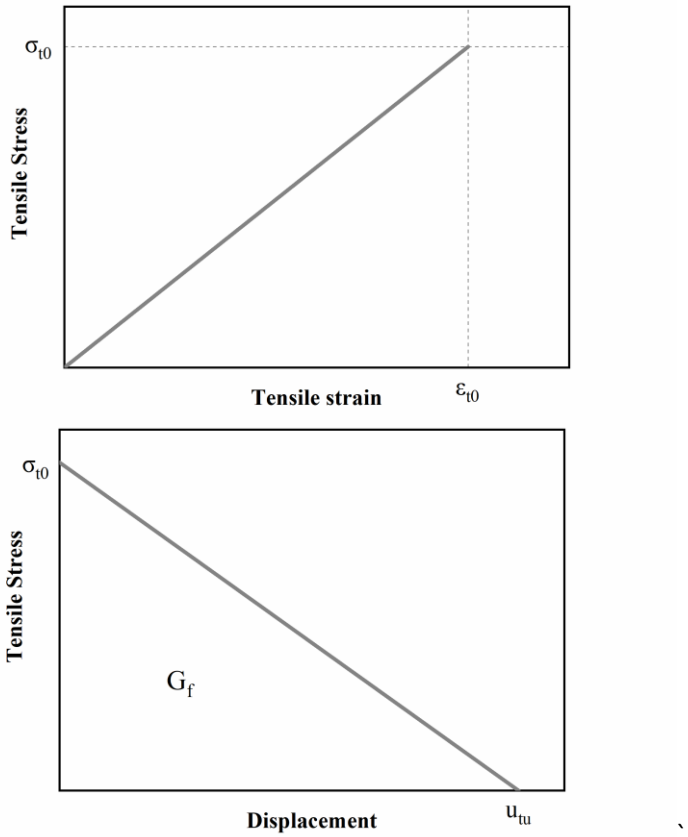

Figure 3.31: Concrete behaviour in tension.

Scalar damage variables, defined as $D_c = 1 - \sigma_c/f_c$ and $D_t = 1 - \sigma_t/f_t$ were included in the material models to account for compression and tension damage for the different concrete parts.

3.8 Validation of numerical results

Load-slip response, deformation/damage patterns and failure modes of the specimens were predicted and verified against the experimental results [31]. Four specimens were used for the validations and their specifications are presented in Table 1. The experimental load-slip response of the LNSC push-out specimens are compared with the FE predictions in Figure 3.32 to Figure 3.35 and a relatively good agreement between the predicted and the experimental curves is observed.

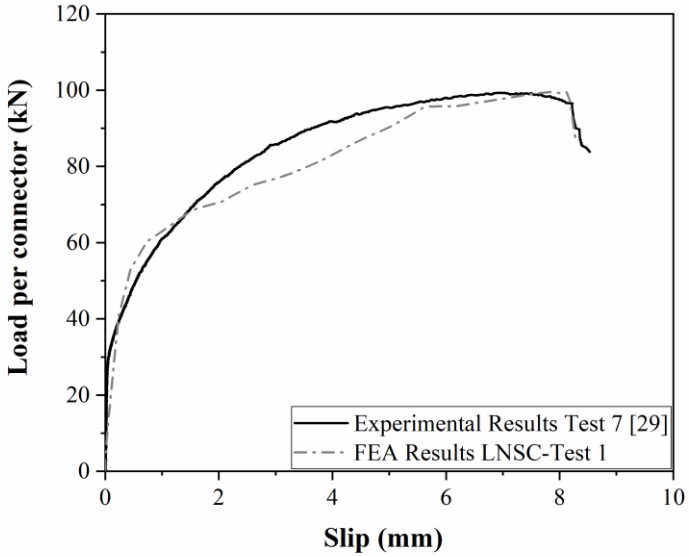

Figure 3.32: Experimental and numerical force-slip curves for LNSC-Test 1.

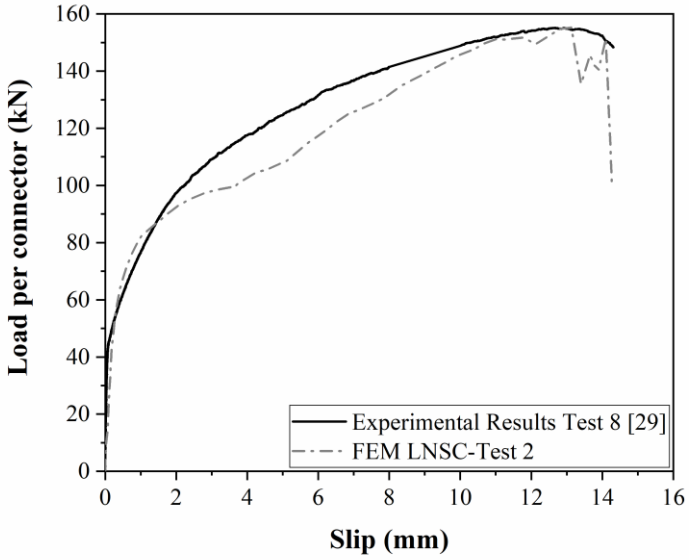

Figure 3.33: Experimental and numerical force-slip curves for LNSC-Test 2.

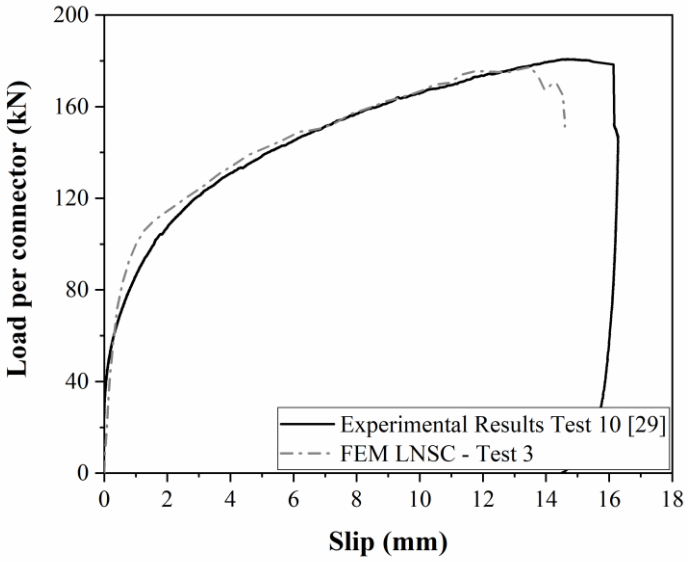

Figure 3.34: Experimental and numerical force-slip curves for LNSC-Test 3.

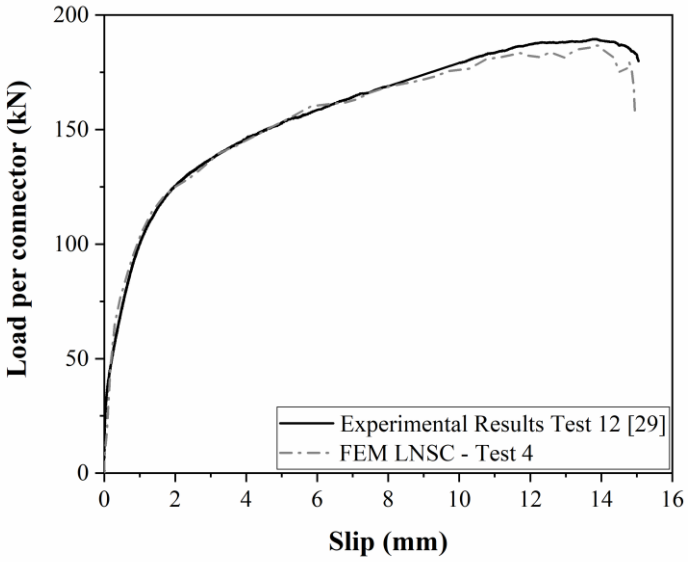

Figure 3.35: Experimental and numerical force-slip curves for LNSC-Test 4.

The FE model could predict the load-slip response characteristics exhibited by the LNSC. Initially, the shear-load slip response is linear up to about 20% of the ultimate shear resistance of the LNSC. The applied forces are transmitted smoothly from steel beam to the concrete slabs through friction resistance at the interface. As the applied force increases, the friction resistance of LNSC is overcome and the bolted connection starts resisting shear force through bearing. The response of the shear connectors becomes nonlinear with the gradual yielding of the bolts and crushing of the grout in front of the conical nut and the bolt shank. As the shear load reaches its maximum values, the conical nut and the bolt shank start to bear against the precast concrete plug. As a result, the concrete shear strains

in the part of the plug that is in front of the conical nut increase and a concrete shear failure plane forms which passes through the grout-plug-slab interface.

The FE model was also validated against the experimental results in terms of characteristic resistance, slip capacity and stiffness of the connection and the results are summarized in Table 3.3. According to Eurocode 4 [6], the characteristic resistance P_{Rk} of the specimens was measured as the minimum failure load (divided by the number of the connectors) reduced by 10%. It was concluded that the FE model was able to predict the characteristic shear resistance of the LNSC specimens with great accuracy; less than 3% difference between numerical and experimental results. The stiffness of the LNSC was defined following the recommendations of Annex A of Eurocode 4 [6] as $0.7P_{Rk}/s$, where s is the slip at a load of $0.7P_{Rk}$. The characteristic slip capacity of the specimens was defined as the slip measured at the characteristic load level reduced by 10% [6].

Table 3.3: Comparison of the shear resistance, stiffness and slip capacity captured by the FE models with tests data.

Test Number	Characteristic resistance (kN)			Shear connection stiffness (kN/mm)			Characteristic slip capacity (mm)		
	Experimental Test	FE Model	$P_{Rk,ex}/P_{Rk,FE}$	Experimental Test	FE Model	$k_{sc,exp}/k_{sc,FE}$	Experimental Test	FE Model	$\delta_{u,exp/}\delta_{u,FE}$
	$P_{Rk,exp}$	$P_{Rk,FE}$		$k_{sc,exp}$	$k_{sc,FE}$		$\delta_{u,exp}$	$\delta_{u,FE}$	
LNSC-Test_1	89.2	89.4	1.00	70.1	82.6	0.85	8.5	8.5	1.00
LNSC-Test_2	139.8	139.6	1.00	70.6	86.3	0.82	14.3	14.3	1.00
LNSC-Test_3	162.7	158.4	1.03	82.1	112.1	0.73	16.2	14.6	1.11
LNSC-Test_4	165.5	170.6	0.97	112.1	107.6	1.04	14.9	15.1	0.99

The FE model was also able to predict the actual failure modes of the push-out test specimens. FEA and experimental deformed shapes of bolt connectors are compared in Figure 3.36. The FE model was capable to predict the gradual yielding of the bolts as well as the formation of two short length regions of high plasticity, due to combined shear, bending and axial internal stresses. Apart from bolt deflection, extensive concrete crushing was observed in front of the conical nut and the bolt shank at both experimental and numerical results, as shown in Figure 3.37.

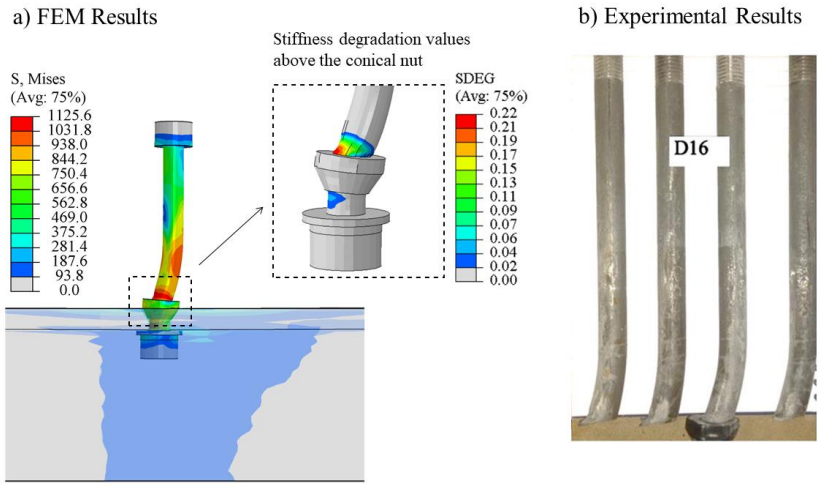

Figure 3.36: Deflected shapes of the bolt connectors in LNSC push-out test 12.

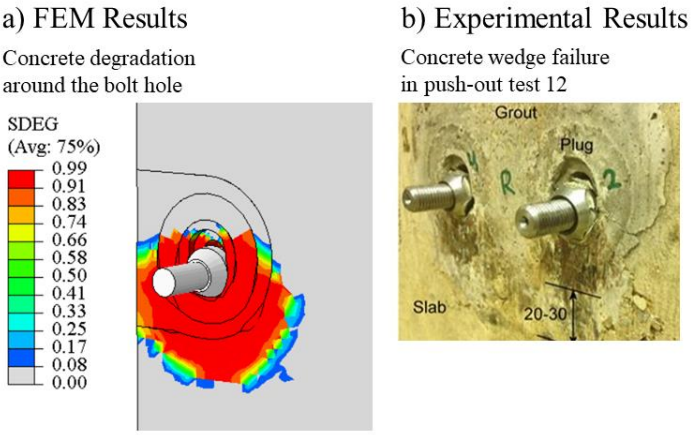

Figure 3.37: Concrete wedge failure in LNSC push-out tests (experimental and FEA).

3.9 Parametric study

The effects of variations in bolt diameter, bolt pretension force, bolt tensile strength, plugs compressive strength and height to diameter ratio of bolt connectors on the shear resistance, slip capacity and stiffness of the LNSC are evaluated by carrying out an extensive parametric study. The details of the push-out specimens used for the parametric study are summarised in Table 3.4.

Table 3.4: Details of the push-out specimens for the parametric study.

Parameter	Specimen	Bolt diameter (mm)	Bolt pretension force (kN)	Plugs compressive strength (MPa)	Bolts height to diameter ratio (-)	Bolts tensile strength (MPa)
Bolt diameter	LNSC-D1	**12**	25	90	9	950
	LNSC-D2	**14**	25	90	9	950
	LNSC-D3	**16**	25	90	9	950
	LNSC-D4	**20**	25	90	9	950
	LNSC-D5	**22**	25	90	9	950
Bolt pretension force	LNSC-B1	16	**25**	90	9	950
	LNSC-B2	16	**40**	90	9	950
	LNSC-B3	16	**60**	90	9	950
	LNSC-B4	16	**80**	90	9	950
	LNSC-P1	16	25	**50**	9	950

Plugs compressive strength	LNSC-P2	16	25	**70**	9	950
	LNSC-P3	16	25	**90**	9	950
Bolts height to diameter ratio	LNSC-HD1	16	25	90	**6.75**	950
	LNSC-HD2	16	25	90	**7.25**	950
	LNSC-HD3	16	25	90	**8**	950
	LNSC-HD4	16	25	90	**9**	950
Bolts tensile strength	LNSC-SB1	16	25	90	9	**800**
	LNSC-SB2	16	25	90	9	**865**
	LNSC-SB3	16	25	90	9	**950**
	LNSC-SB4	16	25	90	9	**1115**

3.9.1 Effect of bolt diameter

Previous experimental studies conducted by Suwaed et al. [31] have shown that the diameter of the bolts is among the most influential parameters on the structural behaviour of the LNSC. Suwaed et al. [31] conducted push-out tests on LNSC specimens using M12, M14 and M16 bolts and it was concluded that an increase in the bolt diameter led to an increase in the shear capacity of the specimens. The behaviour of the specimens was also numerically verified, and the numerical results showed that an increase in bolt diameter from 12mm to 16mm, almost doubled both the shear resistance and slip capacity of the LNSC specimens.

To expand the experimental databank, LNSC push-out specimens with M20 and M22 bolts were also numerically tested as part of the parametric study. The FE models were built using the same boundary conditions, loading, and analysis procedures used in verified LNSC-Test_12 FE model. Similarly, the material properties of LNSC components and the mesh sizes used in the FE analysis of the parametric models remain unchanged. The geometry of the various parts of the LNSC was defined according to Cl. 3.1. However, the dimensions of the central hole of the plugs were increased to enable them to accommodate the M20 and M22 bolts. More specifically, Figure 3.38 shows that the diameter of the hole was increased from 26mm to 30mm, to accommodate an M20 bolt with 10mm clearance and an M22 bolt with 8mm clearance.

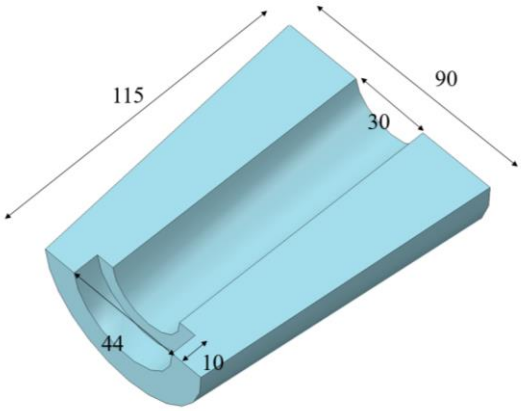

Figure 3.38: Dimensions of precast concrete plugs for M20 and M22 bolts.

The load-slip behaviour of the parametric specimens is shown in Figure 3.39 that shows that the bolt diameter clearly affects the behaviour of the LNSC. Table 3.5 compares the shear resistance, stiffness and slip capacity of the parametric LNSC specimens. The FE results revealed that the shear resistance and stiffness of the specimens were considerably increased by increasing the diameter of the bolt connectors. More specifically, up to approximately 2.5 times increased shear resistance was observed for specimens equipped with M22 bolts compared to the specimens with M12 bolts. The specimens with M12 bolts were classified as ductile connectors according to EC4 even though they showed limited slip capacity. M14 and M16 bolts offered the higher slip capacity to the specimens (up to 14.9 mm). A further increase in the bolt diameter caused a significant decrease in the slip capacity of the specimens. The decreased slip capacity is attributed to the fact that the predominant failure mode of LNSC specimens with M20 and M22 bolts was altered from shear failure of the bolts to concrete failure of the slabs.

Table 3.5: Effect of bolt diameter on the characteristic shear resistance, stiffness and slip capacity of the LNSC.

Specimen	Bolt Diameter	Shear Resistance	Shear Resistance ratio	Stiffness	Stiffness ratio	Slip capacity	Slip capacity ratio
	(mm)	(kN)	$P_{rk,Di}/P_{rk,D1}$	(kN/mm)	$k_{sc,Di}/k_{sc,D1}$	(mm)	$\delta_{u,Di}/\delta_{u,D1}$
LNSC-D1	12	105.7	-	83.0	-	8.2	-
LNSC-D2	14	146.0	1.38	101.3	1.22	14.3	1.74
LNSC-D3	16	187.9	1.78	116.1	1.40	14.9	1.82
LNSC-D4	20	241.4	2.28	141.5	1.70	11.9	1.45
LNSC-D5	22	254.7	2.41	181.5	2.19	7.1	0.87

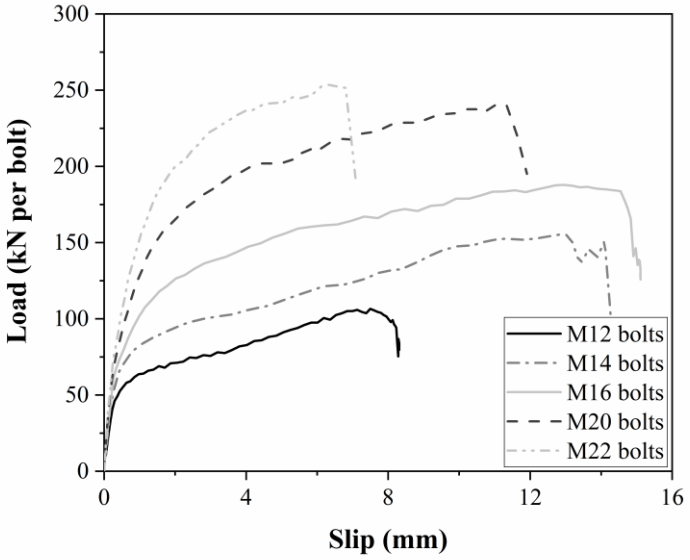

Figure 3.39: Effect of bolt diameter on the load-slip response of the LNSC connector.

The failure modes of the LNSC specimens using bolts with various diameters are compared in Figure 3.40 to Figure 3.42. Two failure modes were observed in the FE analysis: bolt deflection due to combined shear, axial and bending stresses and concrete crushing at the steel beam – plugs interface. The predominant failure mode of the LNSC specimens with M12, M14 and M16 bolts was the failure of the bolts. The deflection angle varied from 8.8° to 12°. The grout in front of the conical nut start to degrade from the first increments of the analysis, allowing the bolts to fully bear against the precast concrete plugs. As the loading was increasing, extensive crushing of the precast plug and slab was observed, in a limited area below the conical nut.

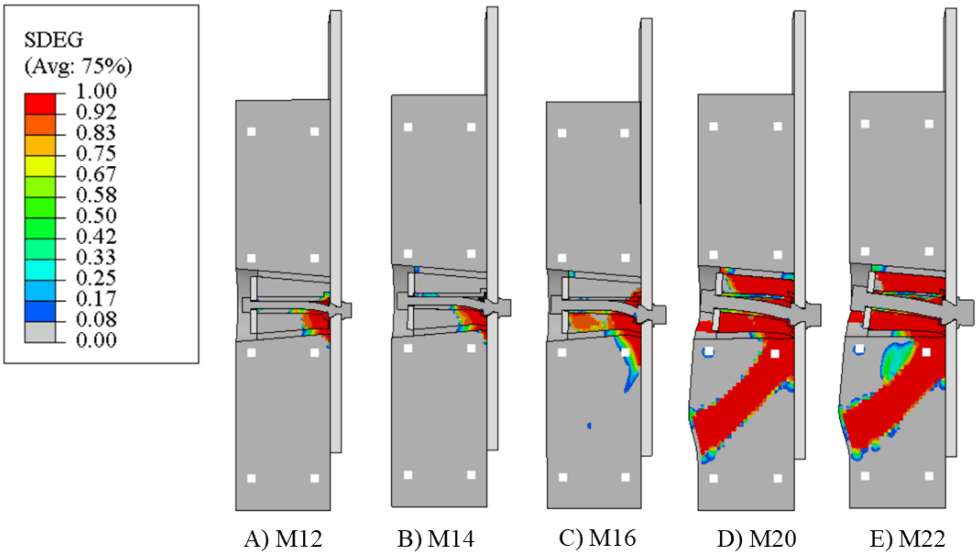

Figure 3.40: Concrete damage of the LNSC specimens with various bolt diameters.

On the contrary, the predominant failure mode of the LNSC specimens with M20 and M22 bolts was concrete failure. The precast concrete plugs were severely damaged due to bearing of the bolts. As a result, the specimens failed due to the extensive crushing and cracking of the precast concrete slabs. The slip capacity of the specimens was significantly reduced, since the failure mode of the specimens was altered from shear failure of bolts to concrete failure of the slabs.

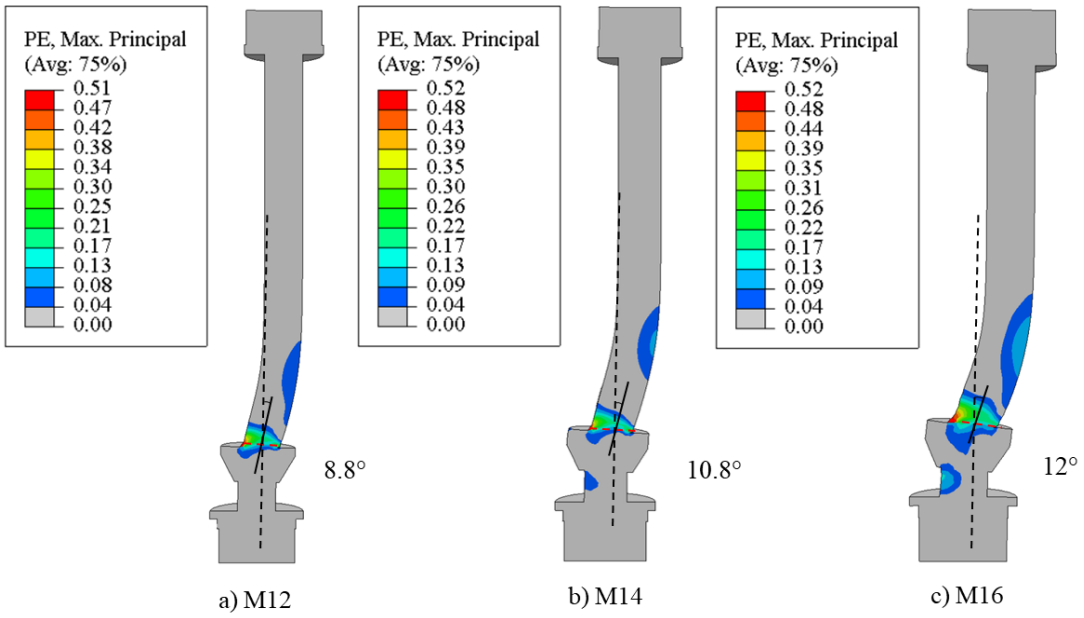

Figure 3.41: Deflected shapes of M12, M14 and M16 bolt connectors.

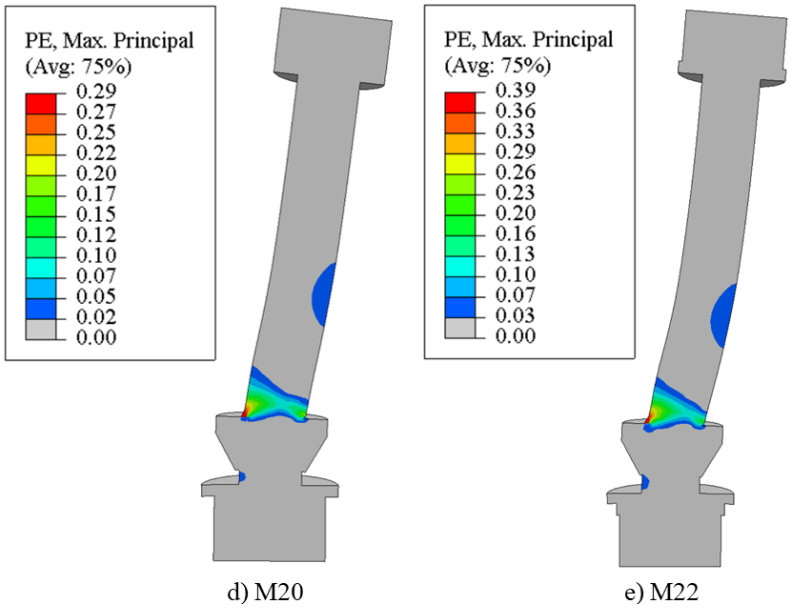

Figure 3.42: Deflected shapes of M20 and M22 bolt connectors.

3.9.2 Effect of bolt pretension force

The tightening of the upper hexagonal nut allows the distribution of the load to the connector components through the bolt and the nuts. This paragraph studies the effect of bolt pretension force on the load-slip behaviour and the capacity of the LNSC. The bolt pretension force between the conical nut and the upper hexagonal nut varied from 25 kN to 80 kN.

The pre-tensioning of the bolts was simulated using an in-built ABAQUS function named “Bolt load”, available in ABAQUS Standard. Subsequently, the predefined temperature field option available in ABAQUS Explicit was used to create the same effect by thermal contraction of the bolt. The smooth amplitude option was used to express the field variable as function of time. The required temperature value was calibrated to ensure a good agreement between the applied and the actual stresses on the bolts.

A “path” was created along the bolt shank to plot the axial stresses developed in the bolt connectors. The distribution of axial stresses along the shank of the bolts using the implicit and the explicit solver is shown in Figure 3.43 to Figure 3.46. A relatively good agreement between the two methods can be observed.

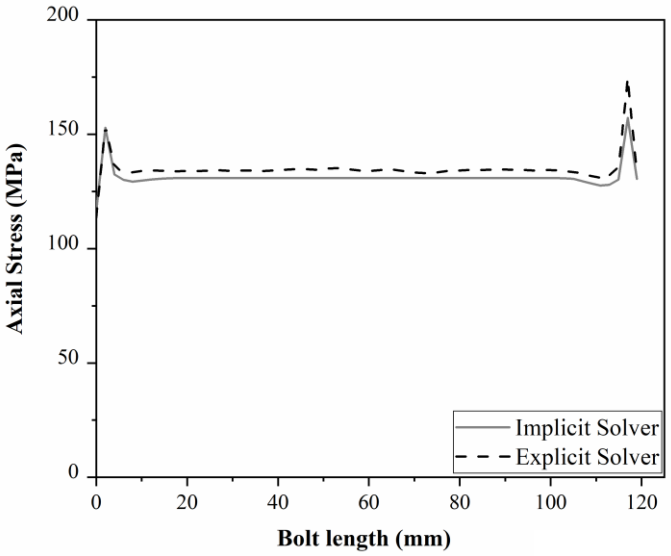

Figure 3.43: Distribution of axial stresses through the bolt length for 25kN bolt preload using ABAQUS/Implicit and ABAQUS/Explicit.

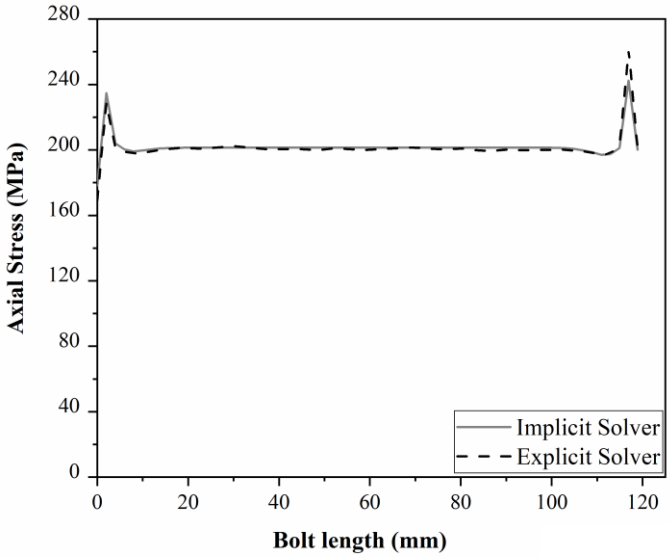

Figure 3.44: Distribution of axial stresses through the bolt length for 40kN bolt preload using ABAQUS/Implicit and ABAQUS/Explicit.

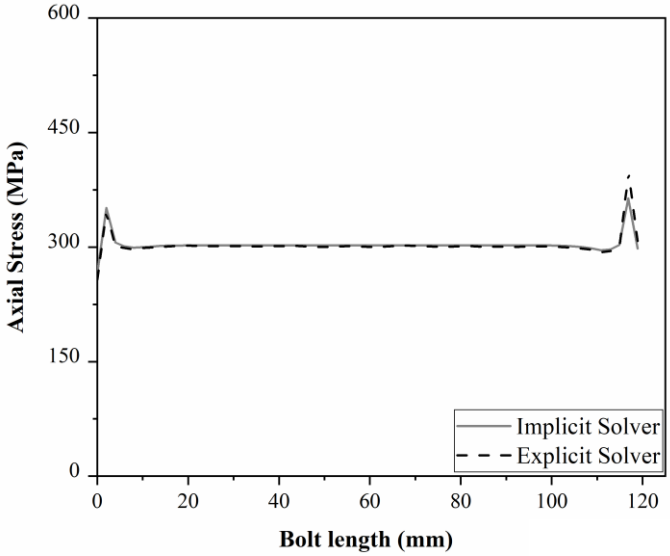

Figure 3.45: Distribution of axial stresses through the bolt length for 60kN bolt preload using ABAQUS/Implicit and ABAQUS/Explicit.

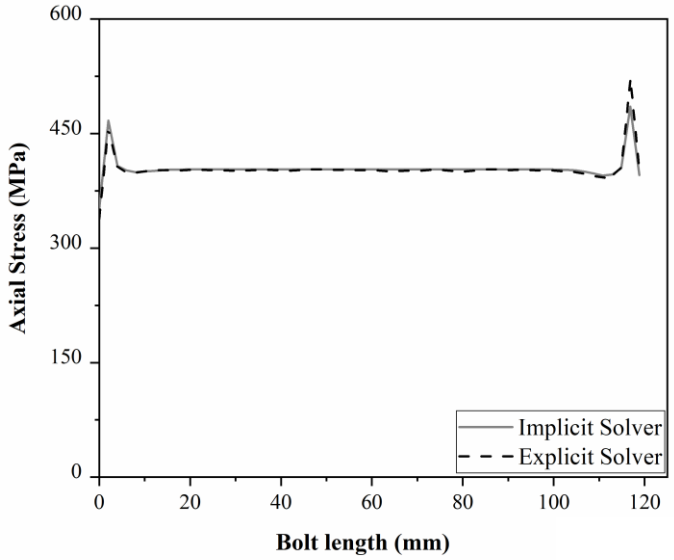

Figure 3.46: Distribution of axial stresses through the bolt length for 80kN bolt preload using ABAQUS/Implicit and ABAQUS/Explicit.

An additional method to ensure that the bolts were preloaded to the required bolt pretension force, was to compare it with the internal load of the bolts at the end of the first step of the analysis. As shown in Figure 3.47, there is a good agreement between the required bolt load and actual internal load of the bolts for all the parametric specimens.

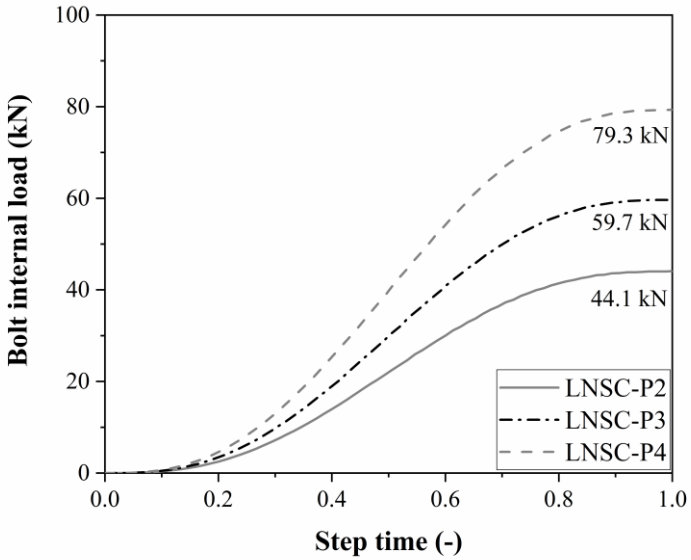

Figure 3.47: Bolt internal load at the first step of the FE analysis.

The results of the parametric study showing the effect of bolt pretension between the conical nut and the upper hexagonal nut on the load-slip behaviour of the LNSC specimens are illustrated in Figure

3.48. The parametric results showed that the bolt pretension force did not have any substantial effect on the shear resistance and slip capacity of the specimens.

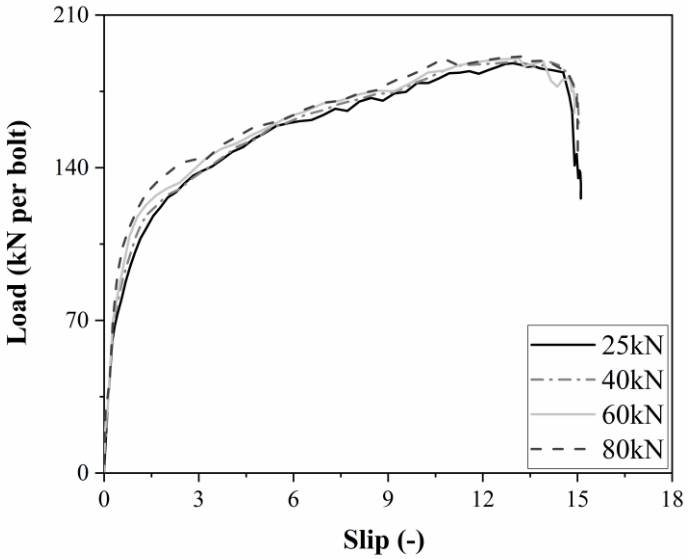

Figure 3.48: Effect of bolt diameter on the load-slip response of the LNSC connector.

The failure modes were similar to those observed in the reference specimens. Two failure modes where: deflection of bolt connectors and extensive crushing of concrete plugs and slab. The deflected shapes of high-strength bolts due to combined shear, bending and axial stresses are shown in Figure 3.49. A region of high plastic strains was formed above the conical nut that indicates the location of the failure. Concrete degradation is shown in Figure 3.50. Extensive grout crushing was observed in front of the conical nut and bolt shank. Plugs and slabs were also severely damaged mainly in front of the conical nut.

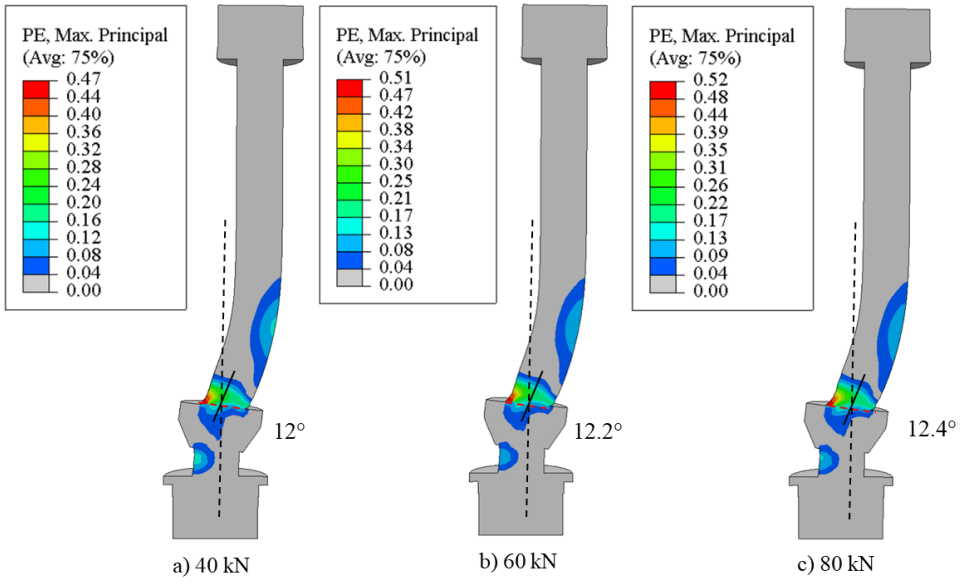

Figure 3.49: Deflected shapes of the bolt connectors with various bolt loads.

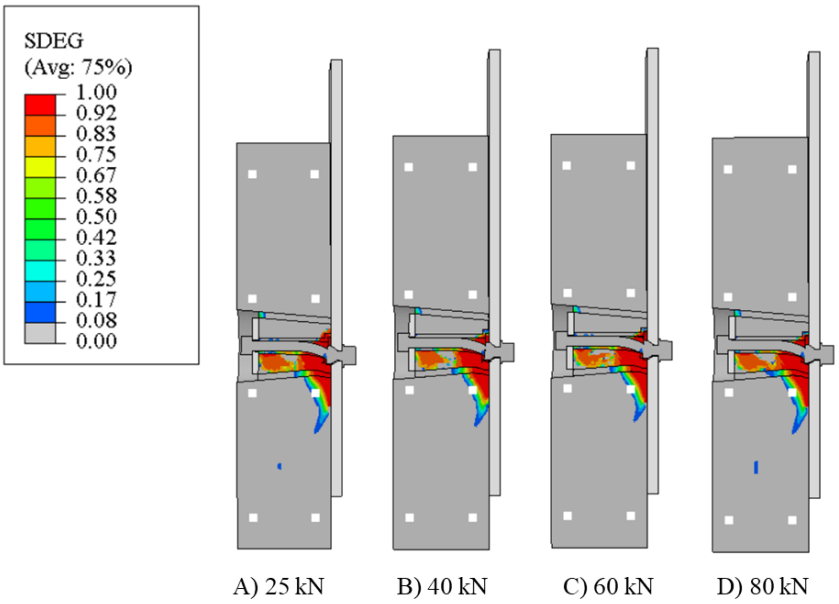

Figure 3.50: Concrete damage of the LNSC specimens with various bolt loads.

3.9.3 Effect of plugs compressive strength

A parametric study to study the effect of the compressive strength of precast concrete plugs on the shear behavior of the LNSC is presented in this paragraph. The compressive strength of the precast concrete plugs used in the parametric analysis varied from 50 MPa to 90 MPa, while the material properties of all the other components of the LNSC remained the same as in LNSC-Test 12. The material properties of the plugs are listed in Table 3.6. The characteristic cylinder compressive strength, the elastic modulus and the tensile strength of the plugs were defined according to BS EN 1992-1-1 [41], while the strain at the peak stress was calculated using Eq. (3.22).

Table 3.6: Material properties of the precast concrete plugs used in the LNSC parametric analysis.

Concrete type	Concrete class $f_{ck}/ f_{ck,cube}$	Characteristic cylinder compressive strength f_{ck}	Elastic modulus E_{cm}	Strain at peak stress ε_c'	Tensile strength f_{ctm}
	(-)	(MPa)	(MPa)	(-)	(MPa)
C50	C50/60	50	37278	0.00204	4.07
C70	C70/85	70	40743	0.00218	4.6
C90	C90/105	90	43631	0.00232	5.0

The compressive stress-strain behavior of the plugs was defined using the model proposed by Hsu and Hsu [45], which is clearly described in Eq. (3.20). The compressive behavior of plugs with various compressive strengths is illustrated in Figure 3.51, where the yield strength of the plugs is given as a function of inelastic strain. Extensive crushing was observed in the area in front of the conical nut in both experimental and numerical results. Therefore, the stress-strain curves were

extended beyond the nominal ultimate strain (εc_{u1}) to avoid an unreal overestimation of concrete crushing strength. The curves were extended up to an inelastic strain of 0.01, which was considered large enough so as not to be achieved in the FE analysis.

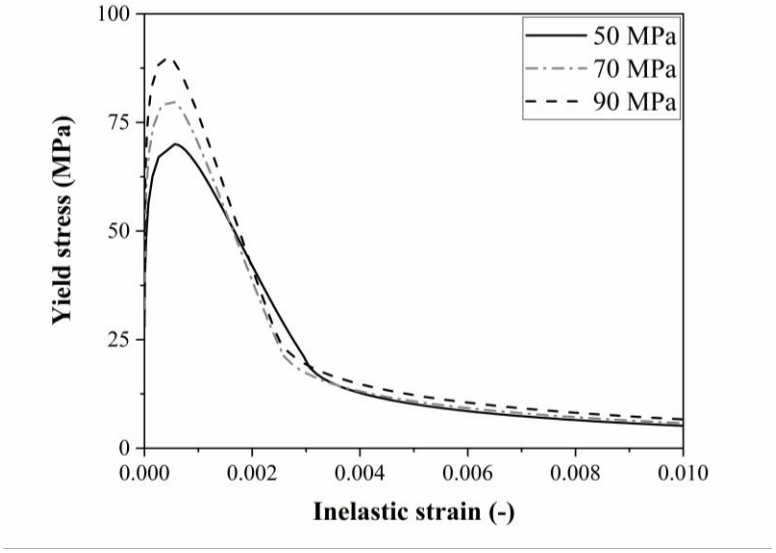

Figure 3.51: Precast concrete plugs compressive stress-strain behaviour.

The initial tensile behaviour of the concrete plugs was assumed to be linear up to its ultimate tensile strength. After this point, Hillerborg's [49] fracture energy approach, was adopted for the analysis to minimize the mesh sensitivity of the results. The concrete damage plasticity (CPD) model was used to simulate the complex behaviour of the precast concrete plugs. The damage parameters and the scalar damage variables were defined according to Cl. 3.7. The compressive damage behaviour of the plugs is shown in Figure 3.52.

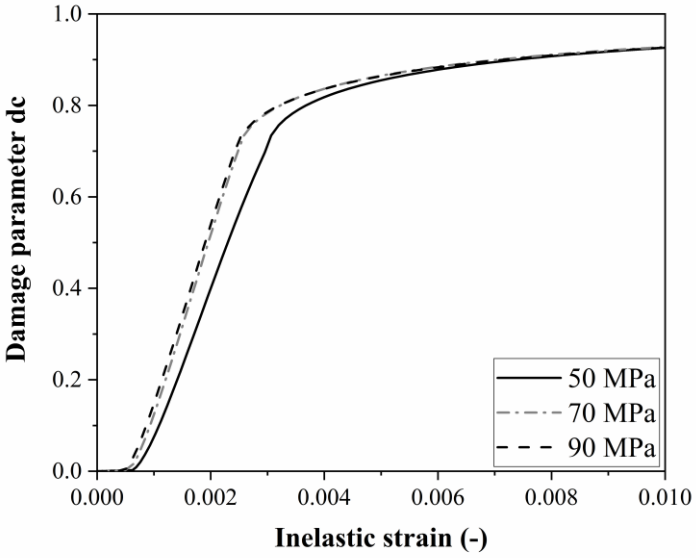

Figure 3.52: Precast concrete plug compression damage.

The load-slip behaviour of the LNSC using precast concrete plugs with different compressive strengths is presented in Figure 3.60. The results of the parametric study are summarized in Table 3.7, where the effect of the plugs compressive strength on the shear resistance, stiffness and slip capacity of the specimens is evaluated. It was concluded that the increase of the plug compressive strength had a minor influence on the shear resistance, stiffness and slip capacity of the LNSC specimens.

Table 3.7: Effect of plugs compressive strength on the characteristic shear resistance, stiffness and slip capacity of the LNSC.

Specimen	Plugs compressive strength	Shear Resistance	Shear Resistance ratio	Stiffness	Stiffness ratio	Slip capacity	Slip capacity ratio
	(mm)	(kN)	$P_{rk,Pi}/P_{rk,P1}$	(kN/mm)	$k_{sc,Pi}/k_{sc,P1}$	(mm)	$\delta_{u,Pi}/\delta_{u,P1}$
LNSC-P1	50	177.1	-	108.0	-	14.6	-
LNSC-P2	70	180.0	1.02	112.5	1.04	14.7	1.00
LNSC-P3	90	187.9	1.05	116.1	1.07	14.9	1.02

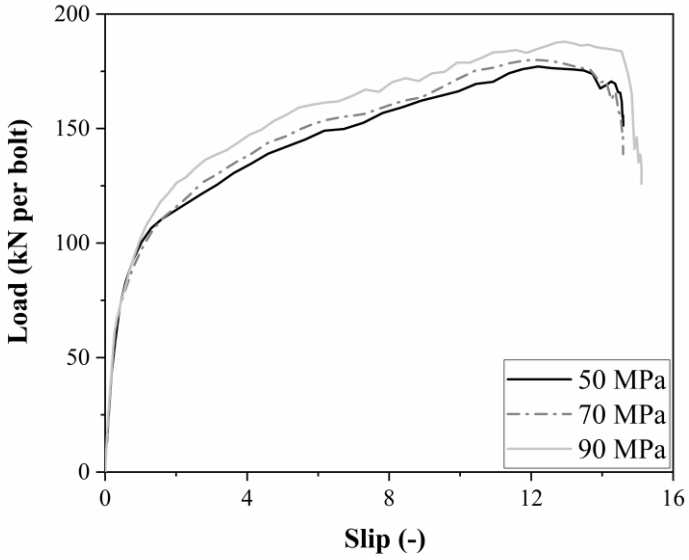

Figure 3.53: Effect of plugs compressive strength on the load-slip response of the LNSC.

The failure modes of the parametric LNSC specimens are illustrated in Figure 3.54 and Figure 3.55. The high-strength bolts deflected with an angle that varied from 12° to 12.8° due to combined axial, shear and bending stresses. A region of high plastic strains was formed above the conical nut which shows that the predominant failure mode of the LNSC push-out specimens was the shear failure of the bolts. Extensive concrete crushing was also observed in the LNSC specimens in the area above the conical nut.

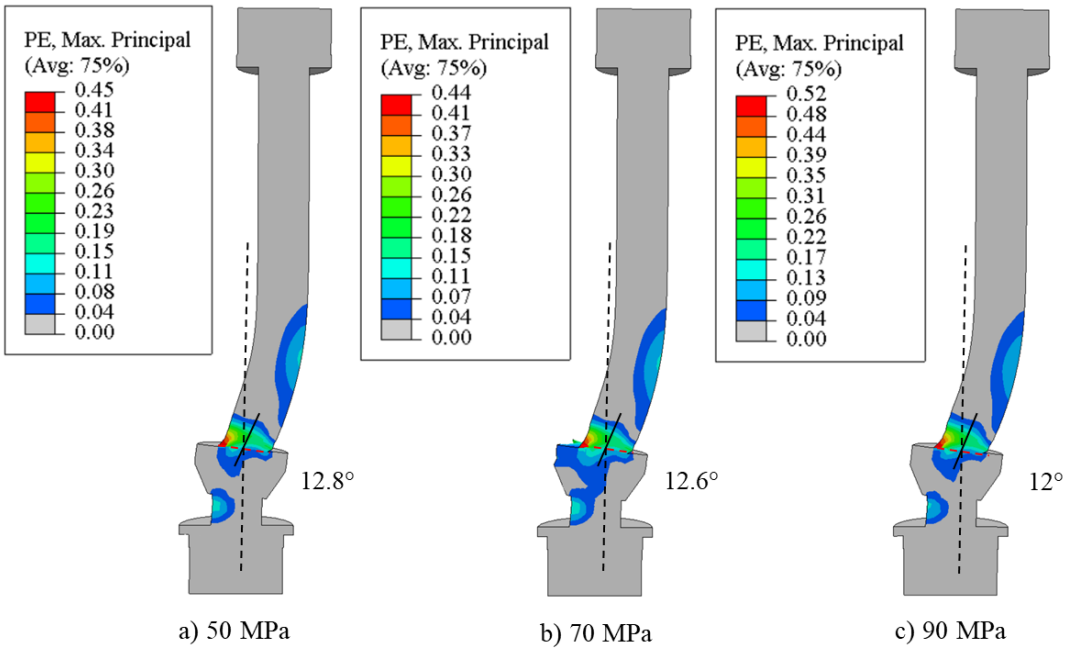

Figure 3.54: Deflected shapes of the bolt connectors with various bolt loads.

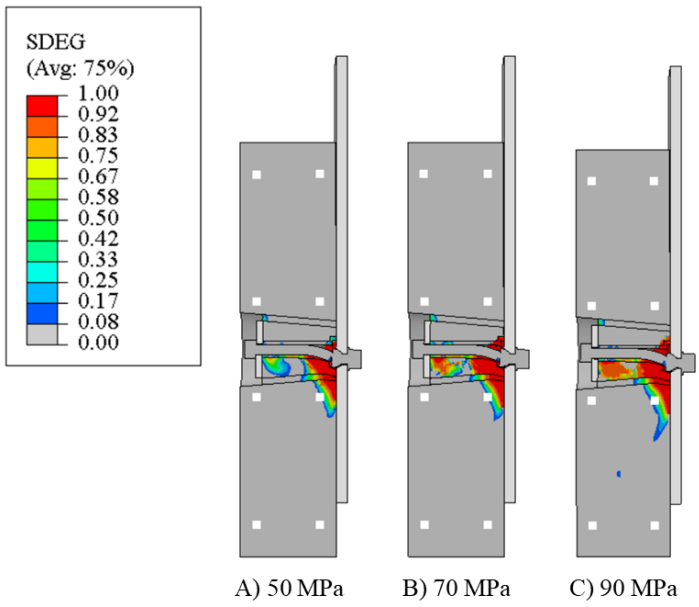

Figure 3.55: Concrete damage of the LNSC specimens with various bolt loads.

3.9.4 Effect of bolts height to diameter ratio

This paragraph presents a parametric study to evaluate the bolt connectors' height to diameter ratio on the shear behaviour of the LNSC. For the analysis, the bolt diameter remained constant, while the height of the bolts varied from 108mm to 144mm. All the other parameters of the FE models, such as the material properties of the various LNSC components, the boundary conditions and the mesh sizes remained the same as in LNSC-Test 12.

The load-slip behaviour of the LNSC, using bolts with various height to diameter ratios, is illustrated in Figure 3.56. The tested connectors are also compared in Table 3.8 in terms of shear resistance, stiffness and slip capacity. The results showed that bolts with higher height to diameter ratios can offer up to 8% higher shear resistance, but they don't have any substantial effect on the slip capacity of the specimens. Finally, a significant increase of the LNSC stiffness was observed, when bolts with increased height to diameter ratios were used in the analysis.

Table 3.8: Effect of bolt connectors' height on the characteristic shear resistance, stiffness and slip capacity of the LNSC.

Specimen	h/d ratio	Shear Resistance	Shear Resistance ratio	Stiffness	Stiffness ratio	Slip capacity	Slip capacity ratio
	(-)	(kN)	$P_{rk,HDi}/P_{rk,HD1}$	(kN/mm)	$k_{sc,HDi}/k_{sc,HD1}$	(mm)	$\delta_{u,HDi}/\delta_{u,HD1}$
LNSC-HD1	6.75	173.4	-	94.3	-	14.7	-
LNSC-HD2	7.25	178.2	1.03	100.1	1.06	14.8	1.01
LNSC-HD3	8	183.4	1.06	105.5	1.12	14.8	1.01
LNSC-HD4	9.	187.9	1.08	116.1	1.23	14.8	1.01

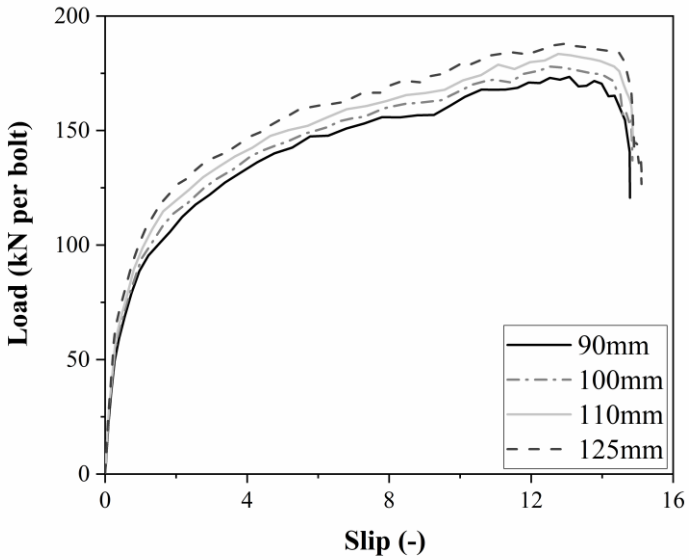

Figure 3.56: Effect of bolt connectors' height on the load-slip response of the LNSC.

Deformed shapes and concrete damage plots for different bolted shear connector's height are shown in Figure 3.57 and Figure 3.58, respectively. The failure of the parametric LNSC specimens was governed by the failure of the bolts due to axial, shear and bending stresses. The deflection angle of the bolts varied from 9.4° for height to diameter ratio equal to 6.75 to 12° for height to diameter ratio equal to 9. Extensive concrete crushing was observed in the area in front of the conical nut and the bolt shank. It was observed that for specimens with low height to diameter ratio bolts, the concrete plugs were more severely damaged.

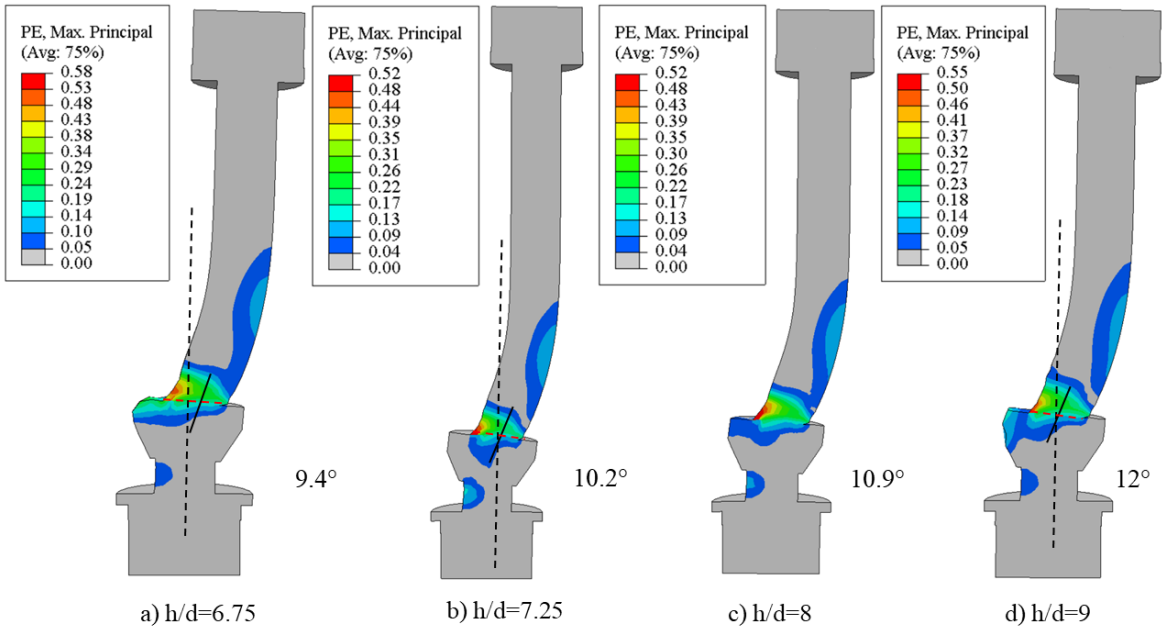

Figure 3.57: Deflected shapes of the bolt connectors with various bolt loads.

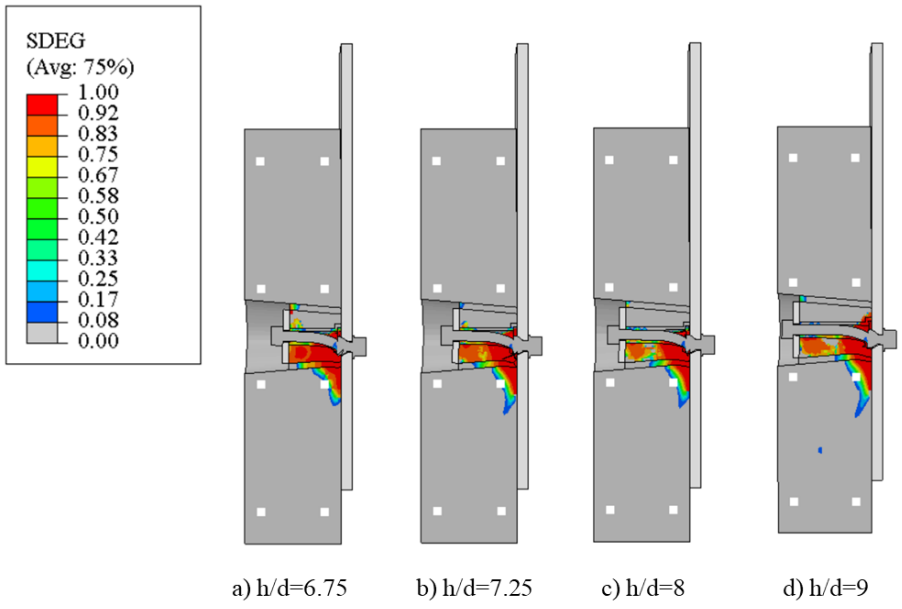

Figure 3.58: Concrete damage of the LNSC specimens with various bolt loads.

3.9.5 Effect of bolt tensile strength

A parametric study was conducted to assess the effect of bolts tensile strength on the shear behaviour of the LNSC. The bolts tensile strength varied from 800 MPa to 1115 MPa, while the material properties of all the other components of the connector remained unchanged. M16 bolts were used in this parametric analysis, since they offer high shear resistance and slip capacity.

The stress-strain behaviour of M16 high-strength steel bolts used in the parametric study was defined by using the stress-strain relationship presented in Eq (3.31) to Eq (3.35). The relationship is a

modification of the model proposed by Mander et al. [52], in order to include the post-peak behaviour of high-strength bolts.

$$f(\varepsilon) = \begin{cases} E\varepsilon, & for\ \varepsilon_y \le \varepsilon < \varepsilon_{sh} \\ E_1 \times (\varepsilon - \varepsilon_y) + f_y, & for\ \varepsilon_y \le \varepsilon < \varepsilon_{sh} \\ f_u - (f_u - f_y) \times \left(\dfrac{\varepsilon_u - \varepsilon}{\varepsilon_u - \varepsilon_{sh}}\right)^{p_1}, & for\ \varepsilon_{sh} \le \varepsilon < \varepsilon_u \\ k - \left[f_f - (f_f - f_u) \times \left(\dfrac{\varepsilon_f - \varepsilon}{\varepsilon_f - \varepsilon_u}\right)^{p_2}\right], & for\ \varepsilon_u \le \varepsilon < \varepsilon_f \end{cases} \quad (3.31)$$

Where,

$$\varepsilon_{sh} = 0.018 * (f_y/f_u) \quad (3.32)$$

$$k = 2 \times \left[\frac{f_f - f_u}{(\varepsilon_f - \varepsilon_u)} \times (\varepsilon - \varepsilon_u) + f_u\right] \quad (3.33)$$

$$p_1 = 2 * E_1 \times \frac{\varepsilon_u - \varepsilon_{sh}}{f_u - f_y} \ \ \& \ \ p_2 = 2 * E_2 \times \frac{\varepsilon_f - \varepsilon_u}{f_f - f_u} \quad (3.34)$$

$$E_1 = \frac{f_u - f_y}{1.1 \times (\varepsilon_u - \varepsilon_{sh})} \ \ \& \ \ E_2 = \frac{f_f - f_u}{1.1 \times (\varepsilon_f - \varepsilon_u)} \quad (3.35)$$

The accuracy of the model was verified by comparing the predicted stress-strain response of the bolts with experimental data presented by Suwaed at al. [42] and Pavlovic et al. [24]. Figure 3.59 shows that a relatively good agreement between the predicted and the experimental [31] stress-stain behaviour of bolts with tensile strength equal to 950 MPa was achieved. The tensile test data presented by Suwaed et al. [42], Pavlovic et al. [24] and Panga et al. [53] were used to construct the stress-strain relationship for M16 bolts with tensile strength equal to 800MPa, 865MPa and 1114MPa. The tensile data are summarized in Table 3.9, while the stress-strain curves for bolts with various tensile strengths are presented in Figure 3.60.

Table 3.9: Tensile test data used to develop the proposed stress-strain relationship for M16 high-strength bolts.

Specimen	Elastic modulus E (GPa)	Yield strength fy (MPa)	Ultimate strength fu (MPa)	Strain at ultimate strength ε_u	Strain at fracture ε_f
LNSC-SB1	210	599	800	0.08938	0.1879
LNSC-SB2	211.7	668	865	0.08235	0.18028
LNSC-SB3	211.4	845	950	0.06788	0.15259
LNSC-SB4	214.5	1085	1114	0.04455	0.1472

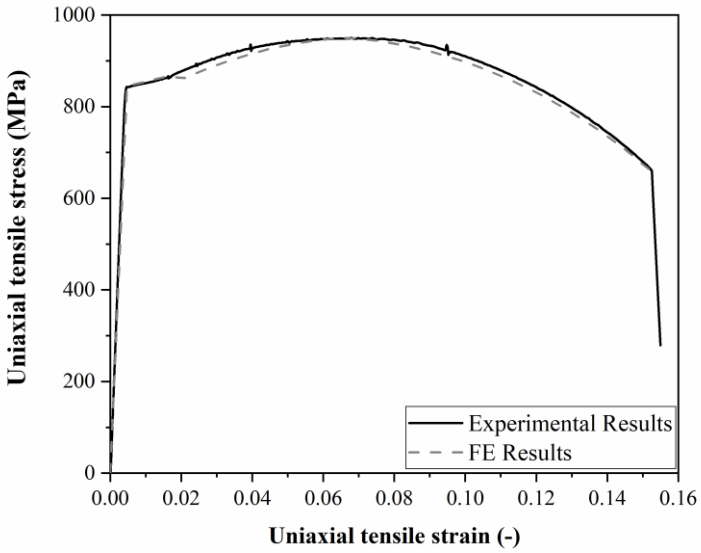

Figure 3.59: Numerical and experimental results [31] for high-strength bolts with 950MPa tensile strength.

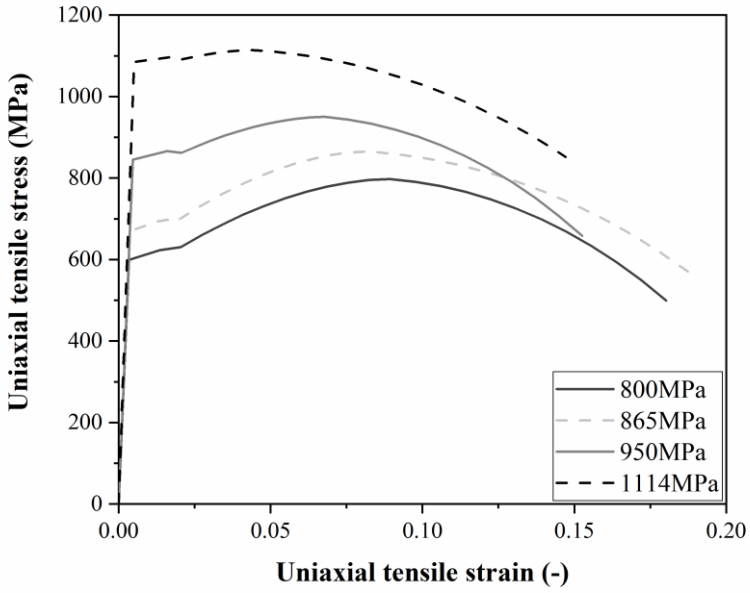

Figure 3.60: Stress-strain curves for M16 high-strength bolts.

Experimental results of the LNSC showed that the prenominal failure mode of the specimens was the failure of the bolts due to combined shear, axial and bending stresses. Therefore, damage material models were included in the analysis to capture the failure of the bolt connectors. To calibrate the ductile damage parameters for high-strength bolts, four tensile coupon tests were built in ABAQUS software, according to the procedure described in Cl. 3.7.1. The damage initiation and evolution parameters used in the FE analysis are summarized in Table 3.10.

Table 3.10: Damage initiation and evolution parameters.

High-strength bolts with 800MPa ultimate strength				
Damage initiation criterion			Damage evolution	
Fracture strain	Triaxiality	Strain rate	Damage variable	Displacement
0.23154	-0.33	0.001	0	0
0.14114	0	0.001	0.27	0.3162
0.08603	0.33	0.001	0.45	0.7227
0.05166	0.67	0.001	1	0.7528
0.03149	1	0.001		
0.01919	1.33	0.001		
0.01152	1.67	0.001		
0.00702	2	0.001		
High-strength bolts with 865MPa ultimate strength				
Damage initiation criterion			Damage evolution	
Fracture strain	Triaxiality	Strain rate	Damage variable	Displacement
0.21403	-0.33	0.001	0	0
0.13047	0	0.001	0.23	0.3154
0.07953	0.33	0.001	0.45	0.7609
0.04775	0.67	0.001	1	0.7985
0.02911	1	0.001		
0.01774	1.33	0.001		
0.01065	1.67	0.001		
0.00649	2	0.001		
High-strength bolts with 950MPa ultimate strength				
Damage initiation criterion			Damage evolution	
Fracture strain	Triaxiality	Strain rate	Damage variable	Displacement
0.19251	-0.33	0.001	0	0
0.11735	0	0.001	0.33	0.8125
0.07153	0.33	0.001	1	0.9411
0.04295	0.67	0.001		
0.02618	1	0.001		
0.01591	1.33	0.001		
0.00958	1.67	0.001		
0.00584	2	0.001		
High-strength bolts with 1114MPa ultimate strength				
Damage initiation criterion			Damage evolution	
Fracture strain	Triaxiality	Strain rate	Damage variable	Displacement
0.11788	-0.33	0.001	0	0
0.07186	0	0.001	0.1	0.2521
0.04380	0.33	0.001	0.3	0.6797
0.02630	0.67	0.001	1	0.5706
0.01603	1	0.001		
0.00977	1.33	0.001		
0.00586	1.67	0.001		
0.00357	2	0.001		

As shown in Figure 3.61 to Figure 3.64, the FE modes were capable to accurately predict the axial load-displacement behaviour of the tensile test specimens. The behaviour of the specimens was initially linear elastic, followed by plastic yielding with strain hardening until their ultimate strength. After this point a reduction in load-carrying capacity was observed and the strains were localized in a neck region as shown in Figure 3.65. Element deletion option was included in the analysis to remove from mesh the elements that have reached the maximum degradation specified ($D_{max} = 1$), that gradually led to the tensile fracture of the specimen.

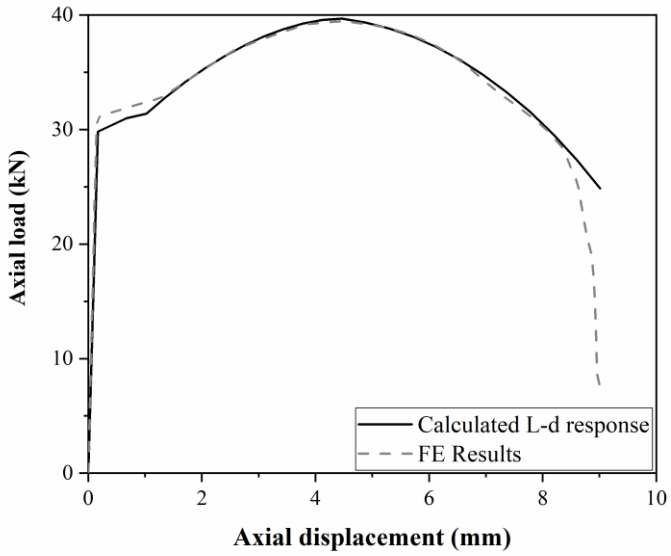

Figure 3.61: Experimental [31] and numerical axial load-displacement response of tensile coupon specimen SB-1.

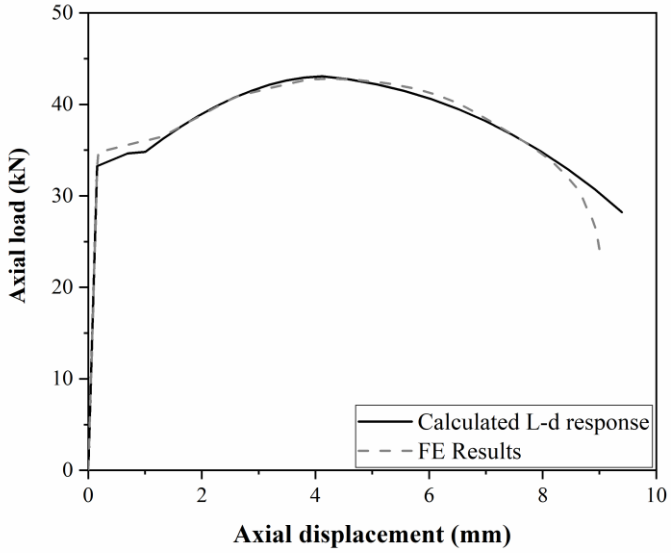

Figure 3.62: Experimental [31] and numerical axial load-displacement response of tensile coupon specimen SB-2.

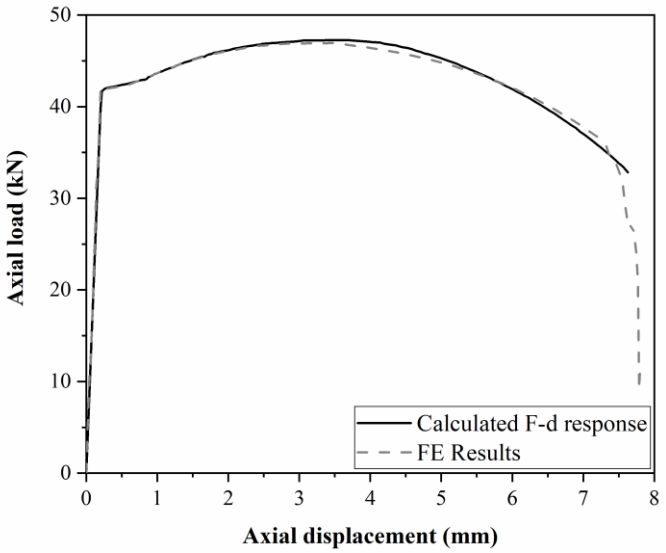

Figure 3.63: Experimental [31] and numerical axial load-displacement response of tensile coupon specimen SB-3.

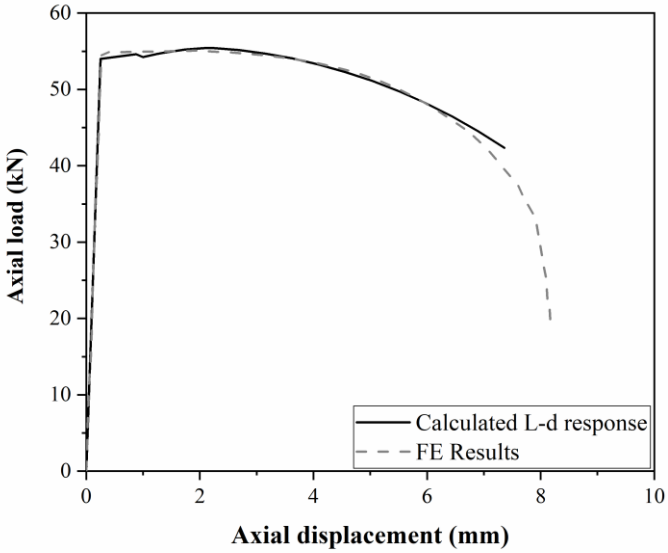

Figure 3.64: Experimental [31] and numerical axial load-displacement response of tensile coupon specimen SB-4.

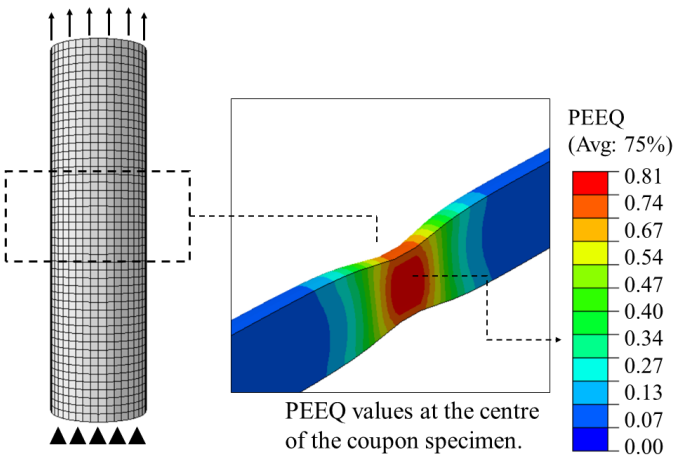

Figure 3.65: Localized strains and formation of a "necking" region at the centre of the coupon specimens.

After the calibration of the damage parameters, the parametric FE push-out tests specimens where built in ABAQUS software. The effect of the tensile strength of the bolt connectors on the load-slip behaviour of the LNSC is illustrated in Figure 3.66, while the shear resistance and slip capacity of the specimens are compared in Table 3.11. The results of the parametric analysis showed that a variation in the tensile strength of the bolts highly affects the overall stress-strain behaviour of the LNSC. A direct correlation between the shear resistance of the LNSC specimens and the tensile strength of bolt connectors can be observed. For example, an increase in bolt's tensile strength from 800MPa to 1115MPa, caused a 26% increase of the shear resistance of the specimen. Similarly, both the slip capacity and the stiffness of the specimens were increased by using bolts with high tensile strength.

Table 3.11: Effect of the yield strength of the bolt connectors on the characteristic shear resistance, stiffness and slip capacity of the LNSC.

Specimen	Bolts tensile strength	Shear Resistance	Shear Resistance ratio	Stiffness	Stiffness ratio	Slip capacity	Slip capacity ratio
	(MPa)	(kN)	$P_{rk,Di}/P_{rk,D1}$	(kN/mm)	$k_{sc,Di}/k_{sc,D1}$	(mm)	$\delta_{u,Di}/\delta_{u,D1}$
LNSC-T1	800	149.6	-	103.9	-	12.3	-
LNSC-T2	865	158.6	1.06	107.5	1.03	14.1	1.15
LNSC-T3	950	168.1	1.13	116.1	1.12	14.9	1.21
LNSC-T4	1115	188.6	1.26	120.4	1.16	15.7	1.28

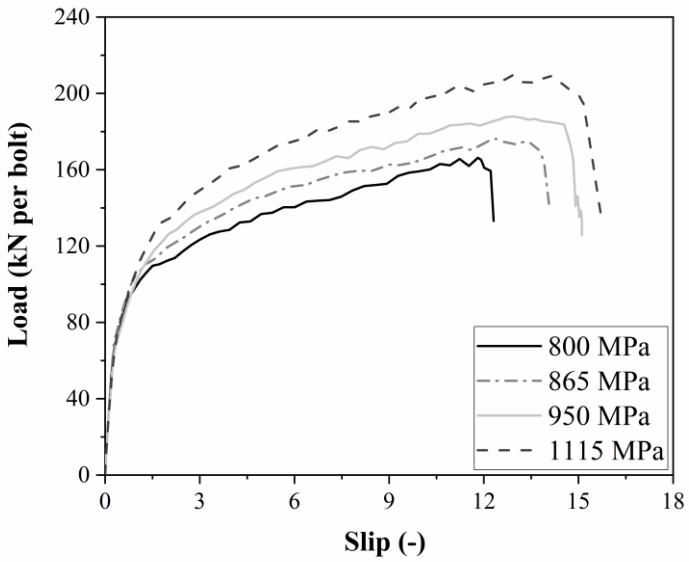

Figure 3.66: Effect of tensile strength of bolts on the load-slip response of the LNSC connector.

Extensive concrete crushing was observed in front of the conical nut and bolt shank in all parametric specimens, as shown in Figure 3.67. As expected, the grout inside the central holes of the precast plugs was completely damaged at the first increments of the FE analysis, allowing the bolts to deflect and bear against the plugs. The deflected shapes of the bolts are shown in Figure 3.68. The deflection angle of the bolts varied from 8.6° for bolts with tensile strength of 800 MPa to 12.9° for bolts with tensile strength of 1115 MPa.

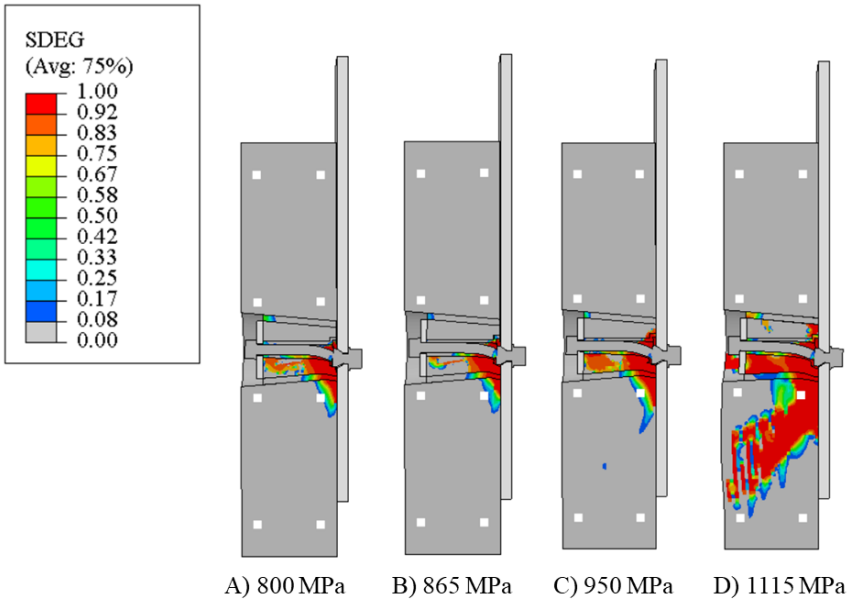

Figure 3.67: Concrete damage of the LNSC specimens with various bolt loads.

Plugs were considerably damaged, mainly in front of the conical nut. The degradation of the precast concrete slabs was limited to a small area in front of conical nut, when bolts with tensile strength up

to 950 MPa were used in the analysis. However, extensive crushing and cracking of the precast concrete slabs was observed when bolts with 1115 MPa tensile strength were used. It was concluded that the predominant failure mode of specimens LNSC-SB1, LNSC-SB2 and LNSC-SB3 was the failure of the bolt connectors due to combined shear, axial and bending stresses. On the contrary, the failure mode of specimen LNSC-B4 was the concrete failure of precast plugs and slabs.

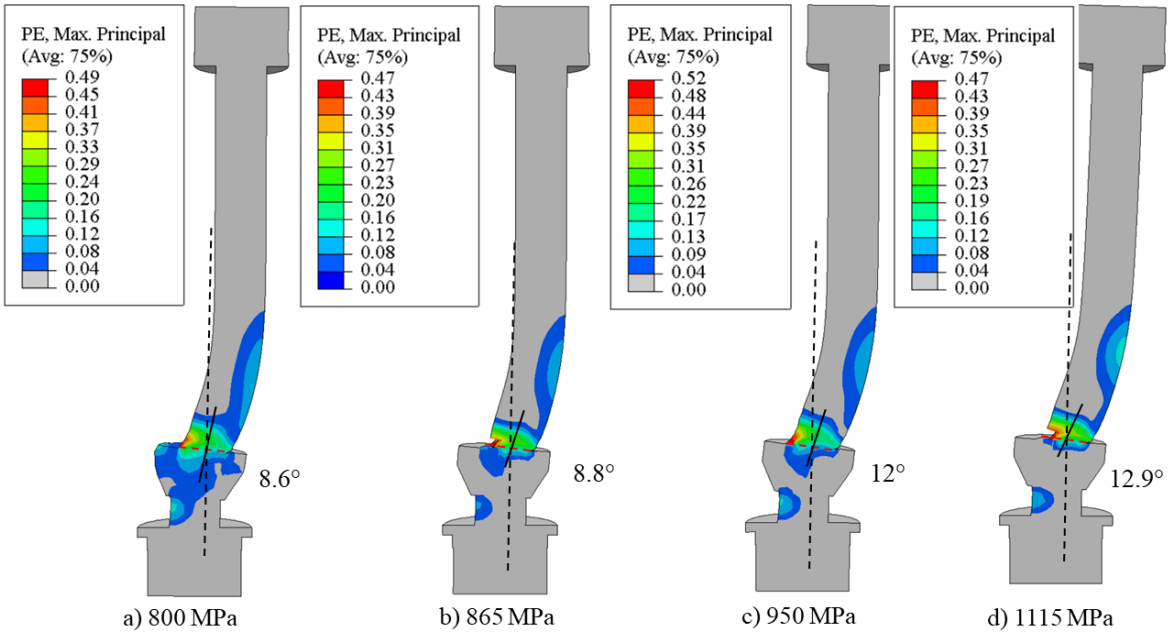

Figure 3.68: Deflected shapes of the bolt connectors with various bolt tensile strengths.

3.10 Comparison with the welded studs

A shear resistance comparison between the LNSC connectors and welded headed studs is presented in this paragraph. The height of the upper conical nut above the top surface of the beam flange was chosen to resemble the collar of welded headed studs. The compressive cube strength of slabs was considered equal to 42 MPa in all specimens. The design shear resistance of welded headed studs that fail by shearing of the bolts was calculated based on the recommendations of Eurocode 4 [6] using Eq.(3.36).

$$P_{Rd} = 0.8 f_u \left(\frac{\pi d^2}{4} \right) \tag{3.36}$$

Where f_{ck} is the characteristic cylinder compressive strength of concrete, f_{cm} is the mean concrete cylinder strength which equals to $f_{ck} + 8$ (MPa), and E_{cm} is the secant elastic modulus of concrete which equals to $22000(f_{cm}/10)^{0.3}$. d stands for the shank diameter of the shear connector and f_u is the tensile strength of bolts.

The results are compared in Table 3.12, where it can be observed that the shear resistance of the LNSC is significantly higher than that of the corresponding welded studs. The high shear capacity of the LNSC is mainly attributed to the structural details of the LNSC that promote failure in the shank of the bolts. It should be mentioned that even though welded studs with tensile strength higher than 800MPa were used for the calculations, welded studs with tensile strength higher than 500MPa are not recommended by Eurocode 4 [6], due to difficulties of welding steel structural components with high amounts of carbon and manganese. According to Ellobody et al. [54], high amounts of carbon and manganese, which are necessary to achieve high strength steel, make the steel harder and consequently more difficult to weld [31]. On the contrary, in the LNSC connector, high strength bolts that provide high shear resistance on the connection, can be used.

Table 3.12: Shear resistance of the LNSC resulted from the FE analysis and the corresponding welded studs using EC4 recommendations.

Specimen	Bolts tensile strength [f_u]	Diameter of bolt connectors [d]	Shear resistance	
			LNSC [FE analysis]	Welded studs [EC4 equations]
	(MPa)	(kN)	(kN)	(kN/mm)
LNSC-D1	950	12	89.6	40.7
LNSC-D2	950	14	139.8	55.4
LNSC-D3	950	16	168.1	72.3
LNSC-B1	800	16	143.6	72.3
LNSC-B2	865	16	155.1	72.3
LNSC-B3	950	16	168.1	72.3
LNSC-B4	1115	16	181.2	72.3
LNSC-P1	950	16	159.4	72.3
LNSC-P2	950	16	162.0	72.3
LNSC-P3	950	16	169.1	72.3
LNSC-HD1	950	16	156.1	72.3
LNSC-HD2	950	16	160.4	72.3
LNSC-HD3	950	16	165.1	72.3
LNSC-HD4	950	16	169.1	72.3
LNSC-SB1	950	16	149.6	72.3
LNSC-SB2	950	16	158.6	72.3
LNSC-SB3	950	16	169.1	72.3
LNSC-SB4	950	16	186.6	72.3

3.11 Design recommendations

The parametric study presented in Clause 3 showed that the tensile strength and the diameter of the bolts highly affect the resistance of the LNSCs. To further study these two parameters, 12 additional parametric tests were conducted, and the results are presented together with the results of the initial parametric study in Table 3.13. Based on these results, simple design rules to calculate the resistance of the LNSCs are proposed.

Table 3.13: Effect of bolts diameter and tensile strength on the ultimate resistance of the LNSCs.

Specimen	F_{ult} [kN]	Failure [kN]
M12_T800	87.9	Bolt
M12_T865	95.9	Bolt
M12_T950	105.7	Bolt
M12_T1115	123.6	Bolt
M14_T800	128.8	Bolt
M14_T865	136.3	Bolt
M14_T950	146.0	Bolt
M14_T1115	161.7	Bolt
M16_T800	166.3	Bolt
M16_T865	176.2	Bolt
M16_T950	187.9	Bolt
M16_T1115	209.5	Bolt
M20_T800	222.0	Concrete
M20_T865	231.6	Concrete
M20_T950	241.4	Concrete
M20_T1115	245.2	Concrete
M22_T800	243.9	Concrete
M22_T865	251.9	Concrete
M22_T950	254.7	Concrete
M22_T1115	260.9	Concrete

The initial non-slip behaviour of the LNSCs is attributed to the friction between the steel-concrete plug interfaces. Both bolt pretension force (T) and friction coefficient at the steel-concrete interface (μ) influence the slip resistance of the connector, which can be calculated using Eq. (3.37). The pretension of the bolts was assumed to be 25kN, according to the experimental work on LNSCs presented by Suwaed and Karavasilis [31]. The coefficient of friction was considered to be equal to 0.5, which is in line with the recommendations of BS 5400-5 [55] for steel-concrete interfaces.

$$F_R = \mu \cdot T \tag{3.37}$$

For the specimens that failed due bolt fracture, the resistance of the LNSCs obtained from both experimental and numerical analysis was found to be much higher than the pure shear resistance of the bolts, which according to BS EN 1993-1-8 [56] can be calculated using Eq. (3.38). The increase of the load-bearing capacity of the bolts is attributed to the friction at the steel-concrete plug interface and the inclination of the deflected shape of the bolts.

$$F_s = \alpha_v \cdot f_{ub} \cdot A_s \tag{3.38}$$

After slip initiation, the bolts gradually elongate in tension. The tensile force F_t can be analysed in two components, one vertical to the steel flange $F_{t,V}$ that increases the tensile force in the bolts and thus increases the clamping action and one horizontal $F_{t,H}$ that coincide with the direction of F_s and therefore increases the bolt resistance to vertical shear. Taking all the above into consideration, the resistance of the LNSC is using Eq. (3.39).

$$F_{R,s} = F_s + \mu\, F_{t,V} + F_{t,H} = 0.6 f_{ub} A_s + F_t\, [\mu \cos(\beta) + \sin(\beta)] \tag{3.39}$$

The values of angle β and the tensile force F_t are shown in Table 3.14. The angle β was obtained at the last increment of the analysis prior to specimen failure. The tensile force of the bolts F_t was calculated based on the total force due to contact pressure and frictional stress at the upper hexagonal nut – washer cell interaction. As shown in Table 3.14, the tensile force F_t was on average equal to $0.54 f_{ub} A_s$, while $\mu \cos(\beta) + \sin(\beta)]$ was on average equal to 0.67. Therefore, Eq. (3.40) can be simply expressed as:

$$F_{R,s} = 0.96 f_{ub} A_s \tag{3.40}$$

Table 3.14. Obtained values of the tensile force Ft angle β .

Specimen	F_t	$F_t/(f_{ub}A_s)$	Angle β	μcos(β) + sin(β)
	[kN]	-	[Degrees]	-
M12_T800	49.4	0.54	8.2	0.64
M12_T865	55.9	0.57	8.6	0.64
M12_T950	61.8	0.57	8.8	0.65
M12_T1115	74.4	0.58	9.6	0.66
M14_T800	66.1	0.53	9.6	0.66
M14_T865	71.9	0.53	9.9	0.66
M14_T950	77.1	0.52	10.8	0.68
M14_T1115	94.5	0.54	11.9	0.70
M16_T800	79.9	0.49	11.3	0.69
M16_T865	83.9	0.47	11.6	0.69
M16_T950	110.7	0.57	12.0	0.70
M16_T1115	125.5	0.55	12.5	0.70

The accuracy of Eq. (3.40) was verified by comparing the predicted ultimate resistance of the LNSCs with the results of the parametric study. As shown in Table 3.15, the proposed equation was able to predict the resistance of the LNSCs with less than 10% difference.

Table 3.15. Comparison between the predicted shear resistance of LNSCs using Eq. (3.40) and the results of the parametric study using the proposed FE model.

Specimen	$F_{ult,FE}$	$F_{R,s}$	$F_{ult,FE} / F_{R,s}$
	[kN]	[kN]	[-]
M12_T800	87.9	86.8	0.99
M12_T865	95.9	93.9	0.98
M12_T950	105.7	103.1	0.98
M12_T1115	123.6	121.0	0.98
M14_T800	128.8	118.2	0.92
M14_T865	136.3	127.8	0.94
M14_T950	146.0	140.3	0.96
M14_T1115	161.7	164.7	1.02
M16_T800	166.3	154.3	0.93
M16_T865	176.2	166.9	0.95
M16_T950	187.9	183.3	0.98
M16_T1115	209.5	215.1	1.03

Eq. (3.42) proposed by Eurocode 4 [6] was used to predict the resistance of the specimens where concrete failure occurred. In this equation, E_{cm} is the elastic modulus of concrete calculated

according to BS EN 1992-1-1, Table 3.1, and f_{ck} is the characteristic cylinder compressive strength of concrete. The compressive strength of the plugs is these specimens was equal to 78 MPa. As shown in Table 3.16, Eq. (3.42) was able to predict the resistance of the specimens with a maximum difference of 14%.

$$F_{R,c} = 0.29d^2\sqrt{f_{ck}E_{cm}} \quad (351)$$

Table 3.16. Comparison between the predicted ultimate resistance of LNSCs using Eq. (3.41) and the results of the parametric study using the proposed FE model.

Specimen	F_{FE}	$F_{R,c}$	$F_{ult,FE} / F_{R,c}$
	[kN]	[kN]	[-]
M20_T800	222.0	209.8	0.95
M20_T865	231.6	209.8	0.91
M20_T950	241.4	209.8	0.87
M20_T1115	245.2	209.8	0.86
M22_T800	243.9	253.9	1.04
M22_T865	251.9	253.9	1.01
M22_T950	254.7	253.9	1.00
M22_T1115	260.9	253.9	0.97

3.12 Conclusions

Three - dimensional FE models were developed to study the behaviour of LNSCs in push-out tests. Abaqus/ Explicit was employed for the analysis to deal with complex contact interactions and highly non-linear materials. Progressive damage models were used for both concrete and steel components of the connector. Double vertical symmetry was used for computational efficiency. Ductile damage models were used for high-strength bolts, since plasticity models were unable to capture the material degradation of the bolts. Supplementary models were built to simulate the tensile behaviour of high-strength bolts. Concrete damage plasticity was used for grout, precast concrete slab and precast concrete plugs to capture the concrete's brittle behaviour. Numerical models were verified against experimental results published in literature [42]. The FE results showed good agreement with experimental results and therefore they were used to conduct a parametric study to further analyse the failure modes and the behaviour of LNSCs in steel-concrete composite beams.

The effect of various parameters on the shear behaviour and capacity of LNSCs in steel-concrete composite structures was presented in this chapter. The effects of variations in the compressive strength of plugs, the diameter and tensile strength of bolt connectors, the bolt height and pretension force on the shear resistance, stiffness and the slip capacity of the connection were presented in this parametric study. The following conclusions have been drawn:

- A variation in bolt preloading showed to have limited influence of the behaviour of the LNSC shear connectors. The shear resistance was increased by less than 2% by increasing the bolt preload force, while the slip capacity of the specimens remained the same.

- Shear connectors with large diameter bolts achieved higher shear resistance compared to connectors with relatively small diameter. However, the slip capacity of these connectors was noticeably decreased since the predominant mode of failure was shifted from shear failure of bolts to concrete due to the extensive damage of the precast concrete plugs.
- The bolt pretension force did not have any substantial effect on the load-slip behaviour of the LNSC.
- The plugs compressive strength had a minor influence on the behaviour of the LNSC. More specifically, the shear resistance was increased by 6%, the stiffness by 7% and the slip capacity by 2% by increasing the concrete strength from 50 MPa to 70 MPa.
- Increasing the height to diameter ratio of the bolt connectors minimized the damage of the concrete in front of the conical nut and the bolt shank. However, the results showed that the shear resistance was not considerably affected by the height of the connector (up to 8% increase was observed). On the contrary, a significant increase of the stiffness of the specimens was observed when bolts with increased height to diameter ratio were used.
- The tensile strength of the bolts connectors highly affects the shear resistance, the stiffness and the slip capacity of the specimens. It was concluded that bolts with high tensile strength offer better load-slip characteristics to the connection.

A comparison between LNSCs and welded studs was also presented in this chapter. Shear resistance of LNSC connectors was considerably higher than that of welded studs, due to the structural details of the LNSC connector. Therefore, it was concluded that Eurocode 4 [6] recommendations to calculate the shear resistance of welded studs cannot be applied for LNSC connectors. Therefore, an equation was proposed to calculate the shear resistance of the LNSC. The accuracy of the equation was verified by using data from the parametric study.

Chapter 4 Finite element modelling of the friction-based shear connectors in push-out tests and parametric study

4.1 Introduction

The chapter presents a finite element (FE) analysis conducted as part of this research program to analyse the behaviour of friction-based shear connectors (FBSCs) in steel-concrete composite structures. The FE models were developed using the commercial software ABAQUS. The geometry, the boundary conditions, the load application, the analysis method and the mesh used for the modelling are clearly described. The FE models were validated by comparing the FE results with the experimental results available in the literature [32]. The connectors were evaluated based on the shear resistance, the stiffness and the slip capacity that they can offer to the steel-concrete composite connection. A discussion regarding the failure modes of the specimens observed during the FE analysis is also included in this chapter.

Subsequently, a parametric study is presented, that evaluates the effect of various parameters on the shear behaviour of FBSCs. The parameters studied include the compressive strength of precast concrete plugs, the diameter, the pretension force and tensile strength of bolt connectors, as well as the bolt height to diameter ratio. The shear resistance, the stiffness and the slip capacity of the specimens are compared, and their failure modes are discussed. Design rules, regarding the shear resistance of FBSCs, are also presented based on Eurocodes recommendations.

4.2 Summary of the literature push-out tests

Details of the geometry of the push out specimens are shown in Figure 4.1. The FBSC consists of a pair of high-strength steel bolts (e.g. Grade 8.8 or higher) with standard diameter (e.g. M16). The bolts are positioned through the chamfered countersunk seat holes of the upper flange of the beam with the aid of retaining washers designed as per BS EN 3386 [57]. The washers are used to hold the bolts in position prior to grout casting, insertion of the concrete plugs and installation of the upper nuts. The radial gaps of these washers ensure the penetration of grout into the chamfered countersunk seat holes and into the clearance gaps between the bolts and their holes in the steel beam. As a result, a complete linkage between the bolts and the steel beam is formed that prevent the sudden slippage observed in previous demountable shear connectors when the friction resistance at steel-concrete interface is overcome.

The chamfered countersunk of the steel beams is similar to those existed in the LNSC specimens, with geometry that follows an angle of 60°. All the other bolting assembly components are the same as those used in the LNSC specimens. The dimensions of the slab pockets remained unchanged. The plugs are also practically the same as in LNSC, but without the enlargement in the lower part of the central hole that was previously created to accommodate the conical nut of the LNSC. The typical geometry of the plug is shown in Figure 4.1.

Both lower and upper nuts are tightened with a proof load of 75-100% to provide a robust locking configuration that prevents slip under service loading by creating friction resistance between the lower surface of the concrete plug and the upper surface of the flange of the steel beam.

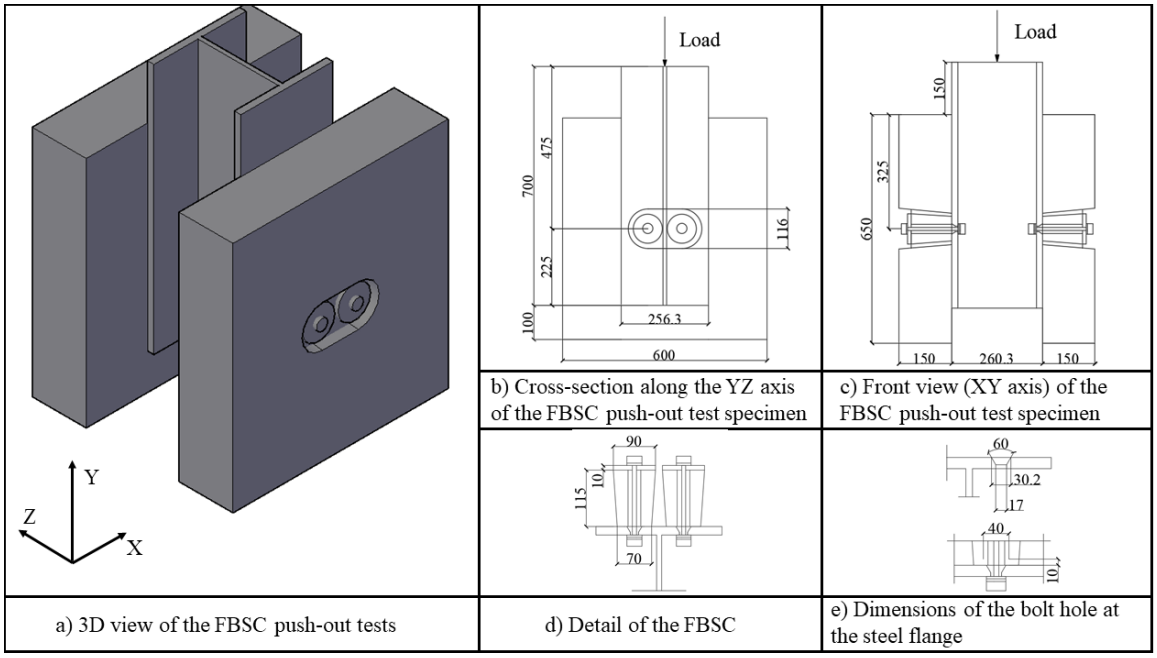

Figure 4.1: Details of the push-out specimens with FBSC connectors.

The specifications of the FE models are given in Table 4.1. The FBSC Test 1 corresponds to the experimental test 6, the FBSC Test 2 corresponds to the experimental test 8 and the FBSC Test 3 corresponds to the experimental test 10 conducted by Suwaed and Karavasilis [32]. The table presents the bolt diameter, the bolts' pretension force as well as the compressive and tensile strength of the grout and precast concrete materials used in each specimen.

Table 4.1: Specifications of the FBSC push-out tests.

Test Number	Bolt Diameter	Bolt preload*	Slab		Plugs		Grout
			Compressive strength	Tensile strength	Compressive strength	Tensile strength	Compressive strength
	(mm)	(kN)	(MPa)	(MPa)	(MPa)	(MPa)	(MPa)
FBSC-Test 1	16	63	50	4.0	90	4.8	41
FBSC-Test 2	12	47-56	40	3.7	80	4.3	51
FBSC-Test 3	14	55	40	3.7	85	4.7	40

*Washer load cell actual readings.

4.3 Geometry and mesh

The geometry of the FE models is shown in Figure 4.2. The models consist of all the connection components used in the push-out tests to accurately predict the behaviour of the FBSC: steel beam, precast concrete plugs and slabs, high-strength bolts, plate washers, grout and steel reinforcement. One quarter of the push-out test arrangement was modelled using double vertical symmetry condition. High-strength bolts, hexagonal nuts and washers were modelled as one part, while the grout inside the bolt hole was modelled as two different parts (shown in Figure 4.3) to avoid convergence difficulties due to complicated contact interactions. The retaining washers were not included in the model since they are used only for construction purposes. The reinforcement details are shown in Figure 4.4.

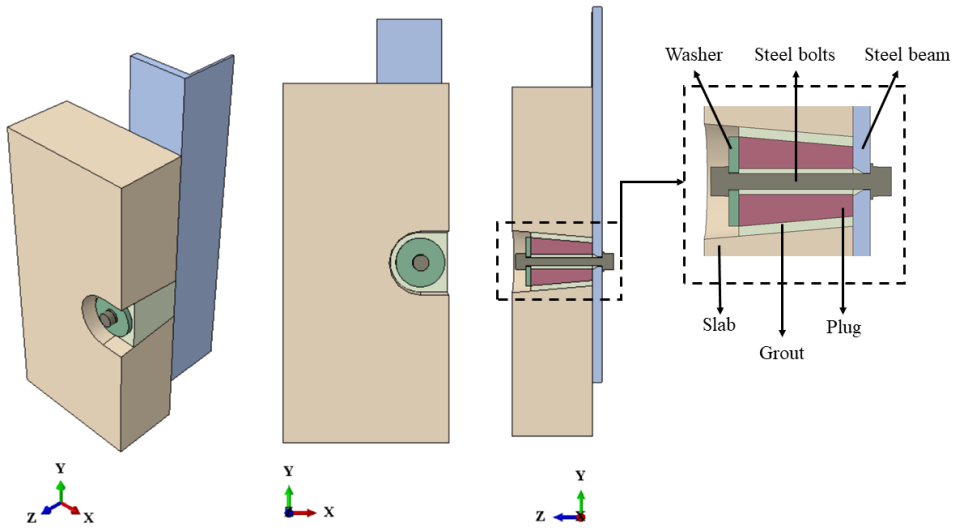

Figure 4.2. Geometry of the FBSC FE model.

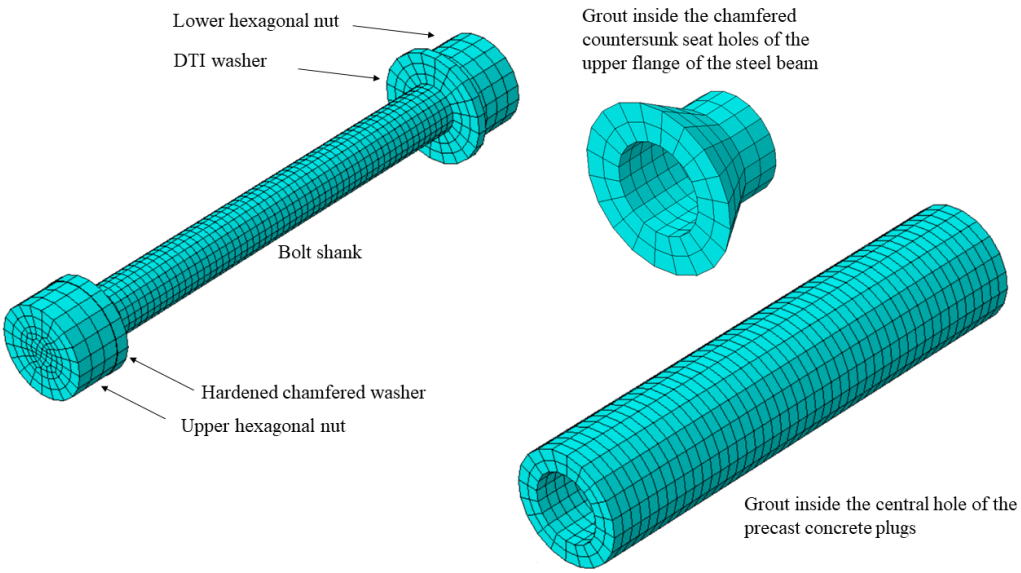

Figure 4.3. FE modelling of the bolts and grout inside the bolt holes.

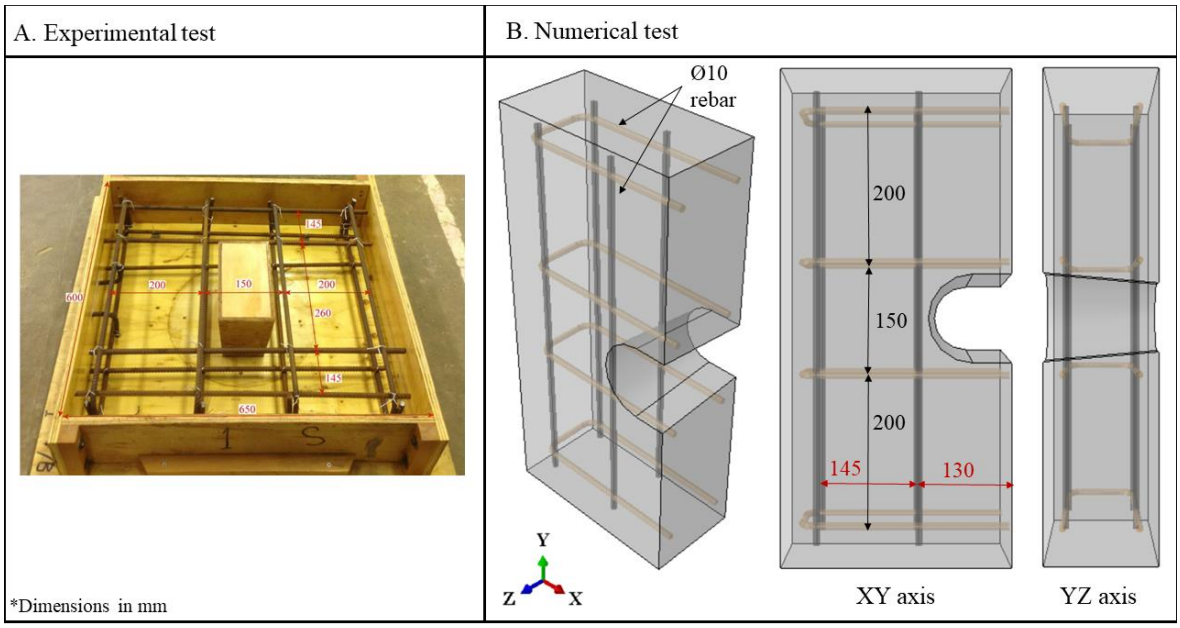

Figure 4.4: Reinforcement details of the FBSC push-out specimens.

The precast concrete parts of the FBSC, the grout, the steel beam and the high-strength bolts were modelled using three-dimensional eight node linear hexahedral solid elements with reduced integration and hourglass control (C3D8R). Elements with reduced integration were adopted as they could reduce the computational time and improve the convergence rate. The reinforcing bars were modelled with two node linear three-dimensional truss elements (T3D2). To reduce the computational time, a coarse mesh was adopted for the overall push-out specimen, with a fine mesh being used for the region around the shear connector to improve the accuracy of the model. The mesh of the different components of the FBSC are shown in Figure 4.5.

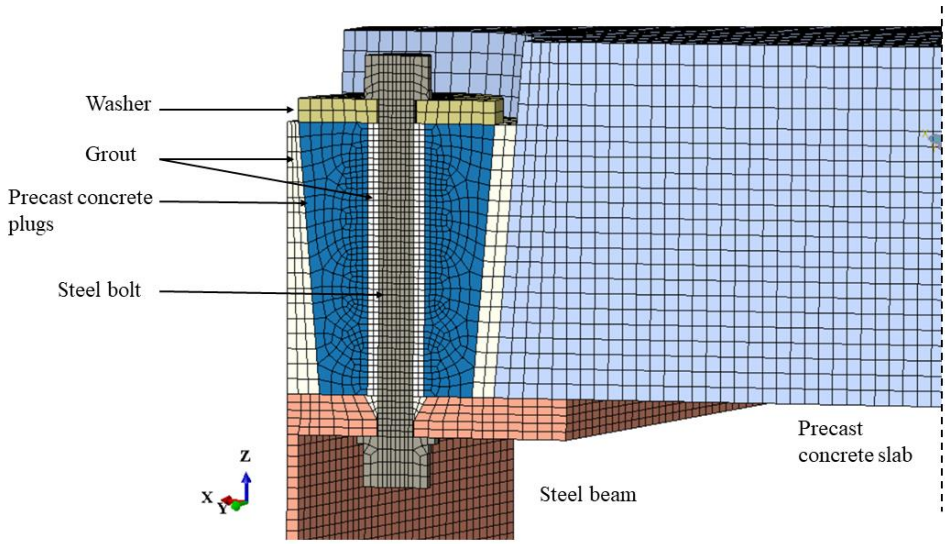

Figure 4.5: Mesh size of the FBSC models.

The mesh size of the various components of the FBSC were defined according to the mesh sensitivity analysis presented in Cl. 3.3. The mesh sizes adopted summarized in Table 3.2**Error! Reference source not found.**. The mesh of each part was not uniform to allow the smooth load transfer at contact interactions. Therefore, the mesh size of each element is given in terms of minimum and maximum element size.

4.4 Interactions and boundary conditions

The interactions between the various components of the FBSC were modelled using appropriate interaction and constraint conditions available in ABAQUS software. The surface-to-surface contact interaction was applied at all the interfaces in the model, by using the 'Hard' and 'Penalty' options to describe the normal and tangential behaviour between the contact surfaces respectively.

Based on the experimental study of Suwaed and Karavasilis [32] the friction coefficient at steel beam - concrete interface is 0.9, which is larger than the typical one for steel beam - concrete interfaces (i.e. 0.5-0.6). Therefore, it was concluded that other factors contribute to the shear resistance during phase one. Suwaed and Karavasilis estimated that these factors are the chemical bond (adhesion) between the grout and the steel flange and the interlocking between the grout and the steel flange due to roughness of the flange surface. However, as the applied load increases, the previously mentioned resistance due to interlocking and chemical bond is exceeded, resulting in decreasing stiffness.

In the FE analysis, a friction coefficient equal to 0.9 was used for steel beam - concrete interface up to the first slip (0.35mm for an M16 bolt) to take into account the chemical bond between the grout and the steel flange and the interlocking between the grout and the steel flange due to roughness of the flange surface. The friction coefficient was then gradually decreased to the typical value of 0.6 for the rest of the analysis.

A friction coefficient equal to 0.45 was used for the contact interaction between the steel bolt and grout, while the friction coefficient was taken as 0.25 for the contact interaction between the steel beam and high-strength bolts [38]. Finally, the embedded constraint option was applied to the reinforcement bars and concrete slab, in order to constrain the translational DOF of the nodes on the rebar elements to the interpolated values of the corresponding DOF of the concrete elements.

The boundary conditions used in the FE analysis are presented in Figure 4.6. For the quarter models, two planes of symmetry were taken into consideration – Surface 1 and Surface 2. Surface 1 was restrained from translating in the Z direction and rotating in the X and Y directions, while Surface 2 was restrained from translating in the X direction and rotating in the Y and Z directions. All nodes at the bottom end of the concrete slab (Surface 3) were restrained against all translational and rotational degrees of freedom.

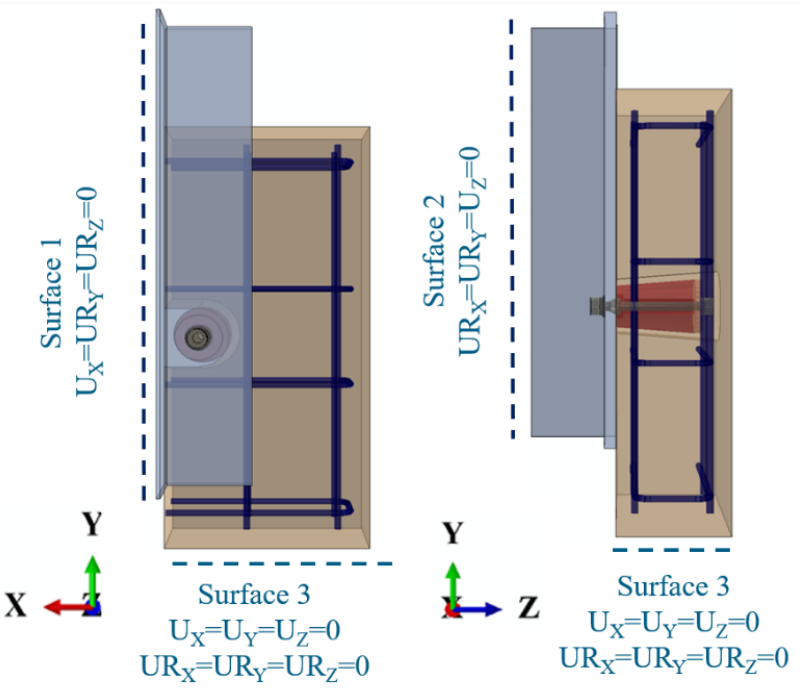

Figure 4.6. Boundary conditions.

4.5 Material Properties

The material models used to describe the material behaviour of the different components of the FBSC were the same as in LNSC and they are described in detail in Chapter 3. Concrete Damage Plasticity (CDP) model was employed to simulate the behaviour of the concrete components of the LNSC; precast concrete plugs, precast concrete slabs and grout. The compressive and tensile strengths of grout, precast concrete plugs and slabs used in the FE analysis are summarized in Table 4.1. The uniaxial stress-strain relationship proposed by Hsu & Hsu [45] was used to describe the compressive behaviour of concrete and grout components of the FBSC. The model is defined using Eq. (3.20) and the compressive stress-strain curves are illustrated in Figure 4.7.

The tensile behaviour of concrete was assumed linear until the tensile strength of concrete was reached. Beyond the failure stress, Hillerborg's [49] fracture energy approach was adopted in order to minimize the mesh sensitivity of the results. The tensile softening response of concrete was characterized by means of fracture energy. Eq. (3.31) was used to define the energy required to open a unit area of crack as a material parameter, G_f. Assuming the maximum coarse aggregate size equal to d_{max}=10mm, the required energy to open a unit area of crack is calculated in Table 4.2.

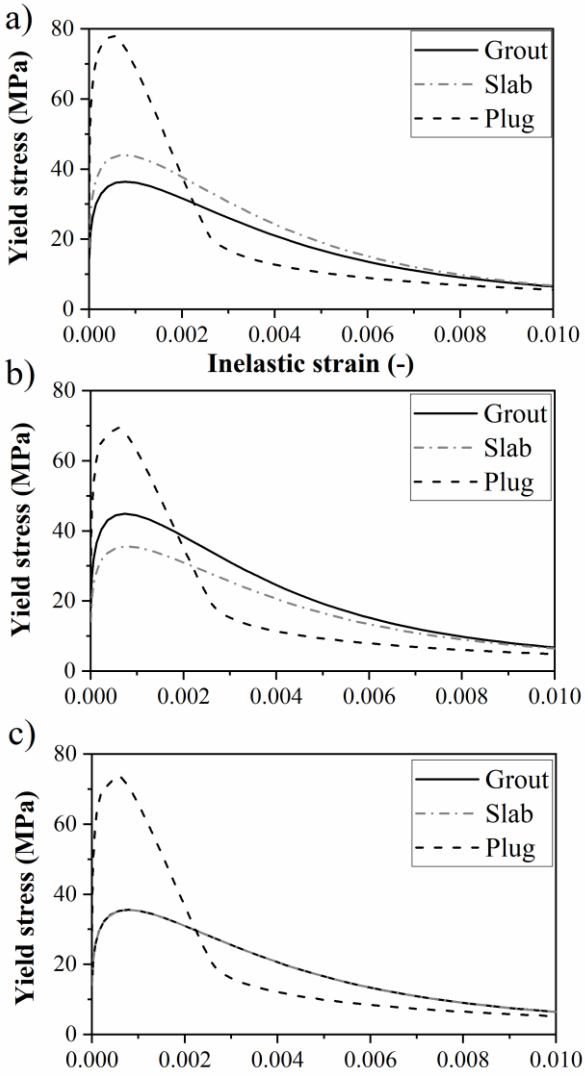

Figure 4.7: Compressive behaviour of grout and concrete parts of a) FBSC – Test 1 b) FBSC – Test 2 c) FBSC – Test 3.

Table 4.2: Tensile behaviour of precast concrete parts of the FBSC.

Test Number	Bolt Diameter	Slab		Plugs	
		Tensile strength	G_f	Tensile strength	G_f
	(mm)	(MPa)	(J/m^2)	(MPa)	(J/m^2)
6	16	4.0	67.8	4.8	77.0
8	12	3.7	64.2	4.3	71.3
10	14	3.7	64.2	4.7	75.9

To take into account the complex nature of passively confined concrete, key material parameters were defined. The ratio of the compressive strength under biaxial loading to uniaxial compressive strength (f_{b0}/f_c') was calculated using Eq. (3.29) that was proposed by Papanikolaou and Kappos. Dilation angle values were iteratively calibrated to match push-out tests results. A value of e = 0.1 was adopted for the flow potential eccentricity, according to ABAQUS user manual recommendations. The default value 1 was also adopted for the viscosity parameter. The ratio of the

second stress invariant on the tensile meridian to that on the compressive meridian (K_c) was defined using Eq. (3.30).

The degradation of the elastic stiffness on the strain softening branch of the compressive stress-strain curve is characterized by a scalar damage variable, d_c, which is defined in cl. 3.7.2. The degradation of the material is given as a function of the inelastic strain in Figure 4.8. It should be mentioned that the damage of precast concrete plugs is more rapid than the damage of grout and slabs. This is due to their high strength, since high strength concrete is far more brittle. On the contrary, grout and precast concrete slabs degrade in a similar manner since their strength is approximately the same (40-50 MPa).

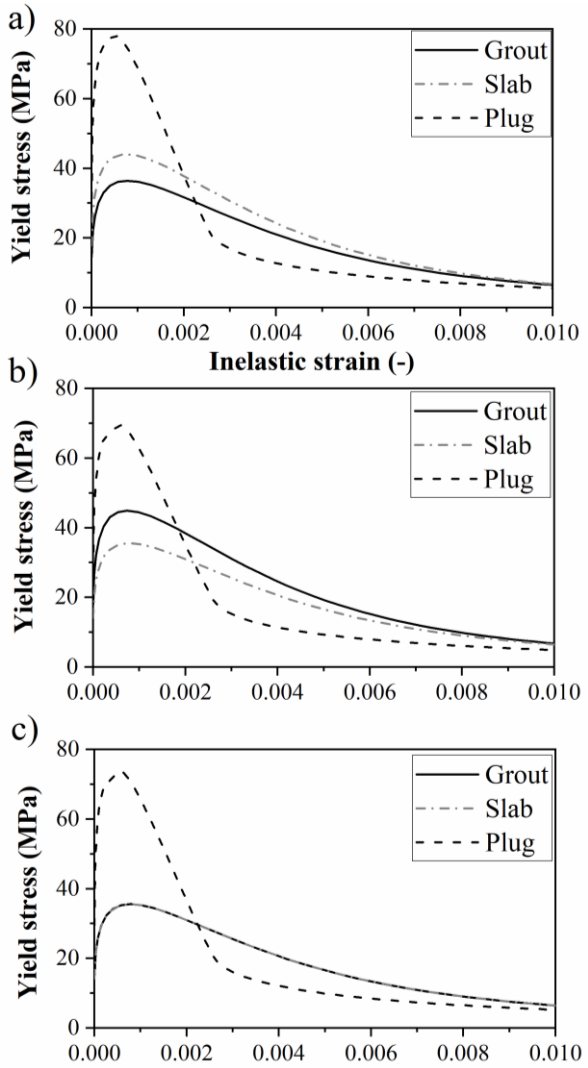

Figure 4.8: Compressive damage input data of grout and concrete materials for a) FBSC - Test 1 b) FBSC - Test 2 c) FBSC - Test 3.

The material properties of the steel components of the FBSC (i.e. steel beam, high-strength bolts and steel reinforcement) remained the same as in LNSC specimens and they are described in cl. 3.7.1. A bilinear plus nonlinear hardening model proposed by Yun et al. [40] was used to represent the

material stress-strain behaviour of the steel beam. A simpler elastic-perfectly plastic model, without strain hardening and yield strength equal to 500 MPa was employed in the analysis to model the behaviour of steel reinforcement. The material properties of high-strength bolts were defined using data obtained from standard tensile tests conducted by Suwaed et al. [32].

4.6 Analysis procedure

A quasi-static analysis was performed using the ABAQUS/Explicit solver to allow for the use of damage and failure models with element deletion in the models. The explicit dynamic analysis method is suitable for models with complex geometries and contact interactions, for which the implicit formulation usually encounters convergence issues. The mass of the model was increased artificially by using the mass scaling option with time increment of 0.00001 sec for computational efficiency. Both kinetic and internal energy were monitored throughout the analysis, to ensure that the quasi-static conditions are maintained; the kinetic energy was less than 5% of the internal energy.

The loading was defined in two steps, corresponding to the experimental testing. In the first step of the analysis, the pre-tensioning of the high-strength bolts was simulated by using the predefined temperature field option. The smooth amplitude option was used to express the field variable as function of time. The desired temperature value was calibrated to ensure a good agreement between the required bolt load and actual internal load the bolt. An example is shown in Figure 4.9, where the internal load of the bolt in Test 10 during the first step of the analysis is illustrated. Bolt internal load was calculated equal to 53.1 kN which is less than 4% difference than the required bolt load for Test 10, which according to Table 4.1 is equal to 55 kN.

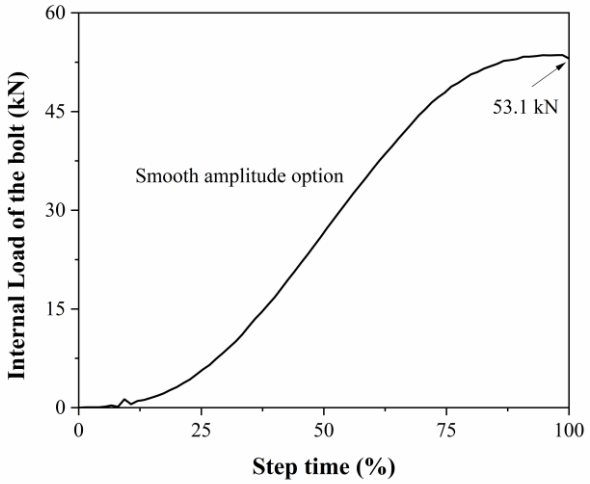

Figure 4.9: Bolt internal load during the first step of the Analysis – Test 10.

A prescribed push down displacement was applied on the upper edge of the beam flange, along the Y direction as shown in Figure 4.10, at the second step of the analysis.

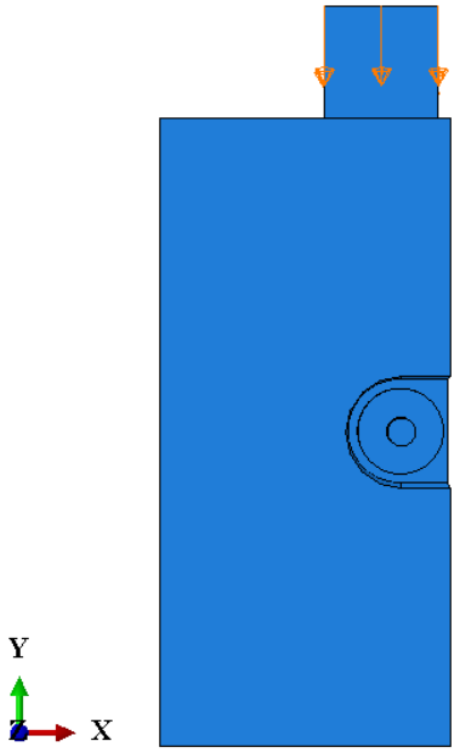

Figure 4.10: Load application at the second step of the FE analysis.

4.7 Validation of the numerical results

Load-slip response, deformation/damage patterns and failure modes of the specimens were predicted and verified against the experimental results [32]. The specifications of the push-out specimens used for the validation of the FE model are presented in Table 4.1. The load-slip response of the push-out specimens with FBSC are compared with the FE predictions in Figure 4.11 to Figure 4.13, where a relatively good agreement between the predicted and the experimental curves is observed.

The FE models could predict the load-slip response characteristics exhibited by the FBSCs with great accuracy. Initially, the shear load – slip behaviour of the specimens was linear up to about 25% of the ultimate shear resistance of the FBSCs. The applied forces were transmitted smoothly from the steel beam to the concrete slab through friction resistance at the interface. As the applied force increased, the friction resistance of the FBSC was overcome and the bolted connection started resisting the shear force through bearing. The response of the connectors became nonlinear with gradual yielding of the bolts and crushing of the grout in front of the bolt shank. As the shear load reached its maximum values, the bolts started to bear against the precast concrete plugs causing excessive damage.

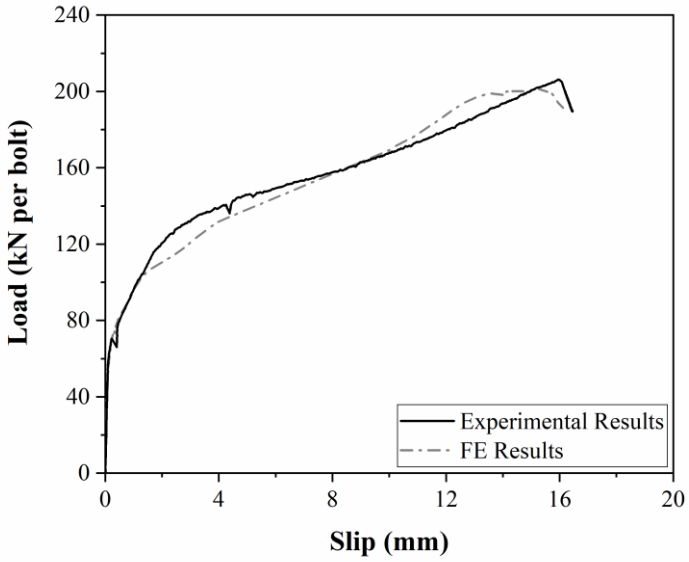

Figure 4.11: Experimental and numerical load – slip curve for FBSC Test 1.

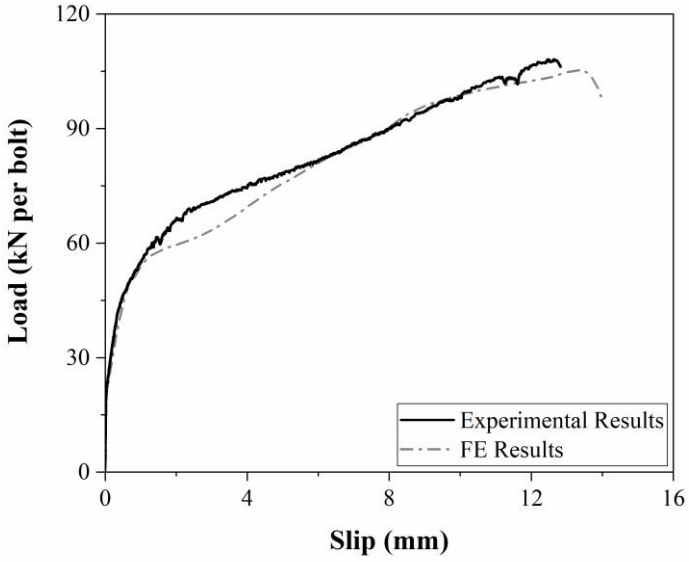

Figure 4.12: Experimental and numerical load – slip curve for FBSC Test 2.

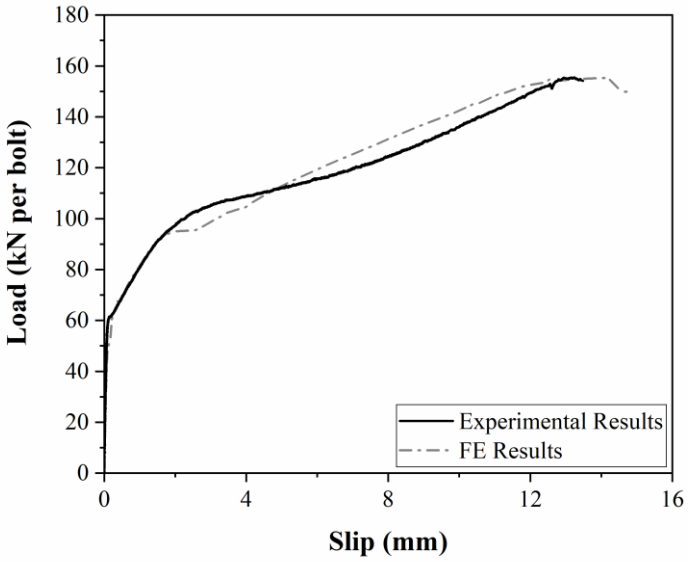

Figure 4.13: Experimental and numerical load – slip curves for FBSC Test 3.

The FE model was also validated against the experimental results [32] in terms of characteristic resistance, slip capacity and stiffness of the connection and the results are summarized in Table 4.3. According to BS EN 1994-1-1 [6], the characteristic resistance P_{Rk} of the specimens was measured as the minimum failure load (divided by the number of the connectors) reduced by 10%. It was concluded that the FE model was able to predict the characteristic shear resistance of the FBSC specimens with great accuracy; less than 3% difference between numerical and experimental results. The stiffness of the FBSC was defined following the recommendations of Annex A of BS EN 1994-1-1 [6] as 0.7PRk/s, where s is the slip at a load of $0.7P_{Rk}$. The characteristic slip capacity of the specimens was defined as the slip measured at the characteristic load level reduced by 10%.

Table 4.3: Comparison of the shear resistance, stiffness and slip capacity captured by the FE models with experimental data.

Test Number	Characteristic Resistance (kN)			Shear connection stiffness (kN/mm)			Characteristic slip capacity (mm)		
	Experimental Test $P_{Rk,exp}$	FE Model $P_{Rk,FE}$	$P_{Rk,ex}/P_{Rk,FE}$	Experimental Test $P_{Rk,exp}$	FE Model $P_{Rk,FE}$	$P_{Rk,ex}/P_{Rk,FE}$	Experimental Test $P_{Rk,exp}$	FE Model $P_{Rk,FE}$	$P_{Rk,ex}/P_{Rk,FE}$
FBSC-Test 1	185.6	181.5	1.02	103.1	100.8	1.02	16.5	16.1	1.02
FBSC-Test 2	97.3	94.8	1.03	77.3	69.3	1.11	12.8	14.0	0.91
FBSC-Test 3	139.9	139.8	1.00	90.4	91.3	0.99	13.5	14.8	0.91

FEA and experimental deformed shapes of bolt connectors are compared in Figure 4.14. It was concluded that the FE model was able to predict the actual failure modes of the push-out test specimens. The FE model was capable to predict the gradual yielding of the bolts as well as the

formation of two short length regions of high plasticity, due to combined shear, bending and axial internal stresses. Apart from bolt deflection, extensive concrete crushing was observed around the bolt shank at both experimental and numerical results, as shown Figure 4.15.

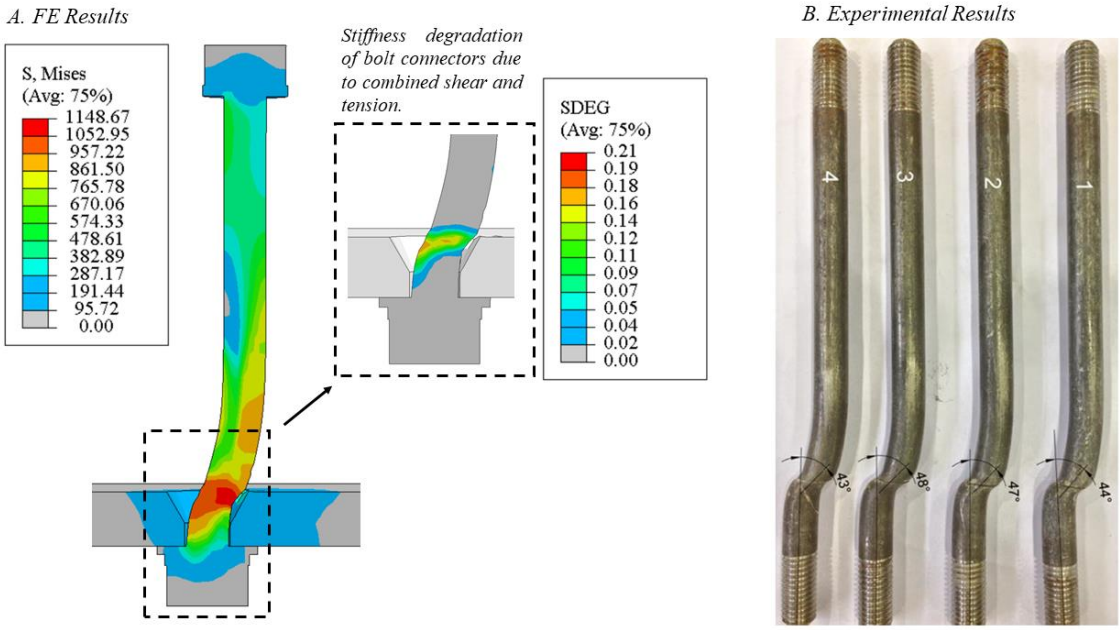

Figure 4.14: Deflected shapes of the bolts.

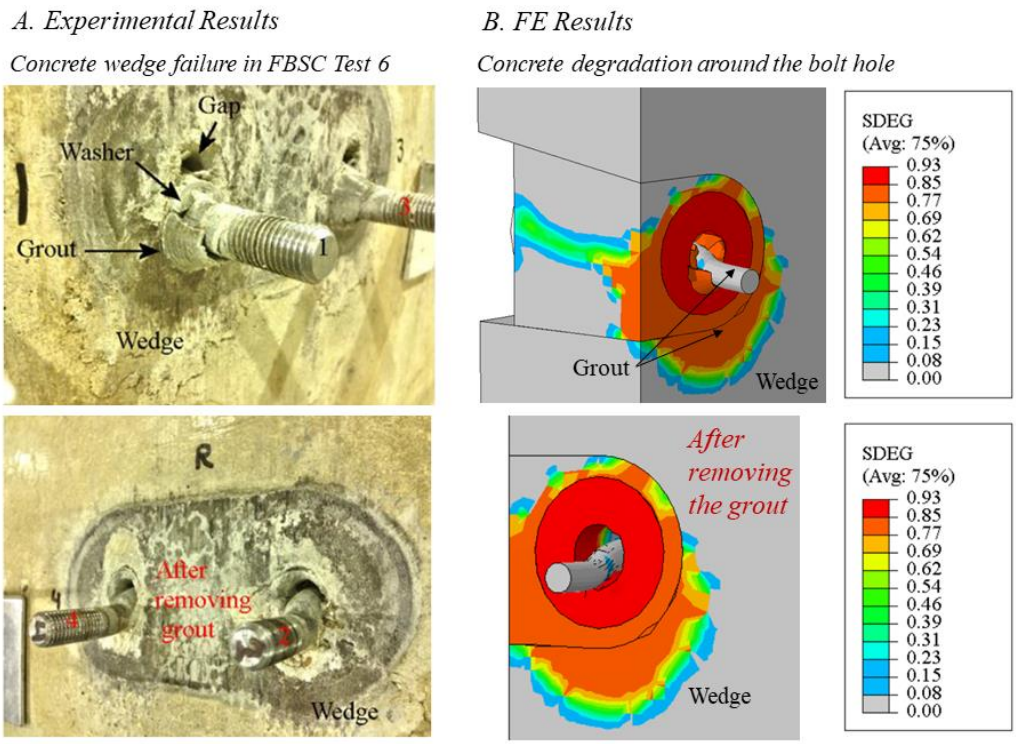

Figure 4.15: Concrete wedge failure.

4.8 Parametric study

An extensive parametric study was conducted to evaluate the parameters that significantly affect the behaviour of the FBSC, and the results are presented in this chapter. The effects of variations in bolt diameter, bolt preload, plugs compressive strength, bolt height to diameter ratio and bolt tensile strength on the shear resistance, slip capacity and stiffness of the FBSC are investigated. The load-slip response of the specimens and their failure modes are also discussed in this chapter. The parametric study is performed based on the verified FE models presented in this chapter. Boundary conditions, loading, analysis method and mesh sizes were defined according to the verified FE models. The details of the FBSC push-out specimens investigated in this parametric study are given in Table 4.4.

Table 4.4: Details of the FBSC push-out specimens for the parametric study.

Parameter	Specimen	Bolt diameter (mm)	Bolt preload/Proof load (-)	Plugs compressive strength (MPa)	Bolt height to diameter ratio (-)	Bolts tensile strength (MPa)
Bolt diameter	FBSC - D1	**12**	0.6	100	8.9	950
	FBSC - D2	**14**	0.6	100	8.9	950
	FBSC – D3	**16**	0.6	100	8.9	950
	FBSC – D4	**20**	0.6	100	8.9	950
	FBSC – D5	**22**	0.6	100	8.9	950
Bolt pretension force	FBSC –B1	16	**0.4**	100	8.9	950
	FBSC – B2	16	**0.5**	100	8.9	950
	FBSC – B3	16	**0.6**	100	8.9	950
	FBSC – B4	16	**0.7**	100	8.9	950
Plugs compressive strength	FBSC – P1	16	0.6	**50**	8.9	950
	FBSC – P2	16	0.6	**70**	8.9	950
	FBSC – P3	16	0.6	**90**	8.9	950
	FBSC – P4	16	0.6	**100**	8.9	950
Height of bolt connectors	FBSC – H1	16	0.6	100	**8.9**	950
	FBSC – H2	16	0.6	100	**7.3**	950
Bolts tensile strength	FBSC – T1	16	0.6	100	8.9	**800**
	FBSC – T2	16	0.6	100	8.9	**865**
	FBSC – T3	16	0.6	100	8.9	**950**
	FBSC – T4	16	0.6	100	8.9	**1115**

4.8.1 Effect of bolts diameter

A parametric study is presented in this paragraph to evaluate the effect of variations in bolt diameter on the shear resistance and ductility of FBSC. Suwaed and Karavasilis [32] experimentally tested FBSC push-out tests with M12, M14 and M16 bolts. The experimental results showed that the diameter of the bolts is among the most influential parameters on the structural behaviour of the FBSC. More specifically, an increase in the bolt diameter offered higher shear resistance, stiffness and slip capacity to the FBSC specimens. The behaviour of the tested specimens was also numerically investigated to study the behaviour of the FBSC using various diameter in more detail. To expand the experimental databank, FBSC specimens with M20 and M22 bolts were also included in the FE analysis and the load-slip curves obtained are shown in Figure 4.16.

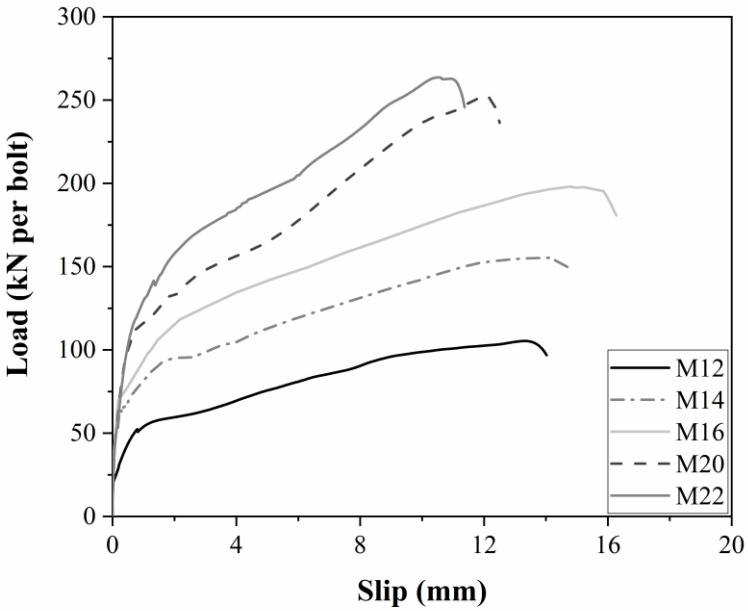

Figure 4.16: Effect of bolt diameter on the load-slip response of the FBSC connector.

The FBSC specimens are compared in Table 4.5 in terms of characteristic shear resistance, stiffness and slip capacity that they provide to the connection. The parametric results revealed that both shear resistance and stiffness of the FBSC specimens are considerably increased with increasing the bolt diameter. More specifically, up to approximately 2.5 times increased shear resistance and 80% increased stiffness was observed for specimens with 22mm diameter bolts compared to the specimens with 12mm diameter bolts. The slip capacity of the specimens was also affected. For specimens with less than 16mm bolt diameter, their slip capacity was increased when the bolt diameter was increased. For specimens with larger bolt diameter, a reduced slip capacity was observed.

Table 4.5. Effect of bolt diameter on shear resistance, stiffness and slip capacity of the FBSC.

Specimen	D	P_{ult}	Shear Resistance ratio	k_{sc}	Stiffness ratio	δ_{ult}	Slip capacity ratio
	(mm)	(kN)	$P_{ult,Pi}/P_{ult,P1}$	(kN/mm)	$k_{sc,Pi}/k_{sc,P1}$	(mm)	$\delta_{u,Pi}/\delta_{u,P1}$
FBSC – D1	12	108.1	-	69.3	-	13.4	-
FBSC – D2	14	155.4	1.44	91.3	1.32	14.2	1.06
FBSC – D3	16	201.7	1.87	100.8	1.45	14.8	1.10
FBSC – D4	20	252.2	2.33	105.1	1.52	12.0	0.90
FBSC – D5	22	262.6	2.43	123.2	1.78	10.5	0.78

The failure modes of the FBSC specimens are compared in Figure 4.17 and Figure 4.18. Two failure modes of the FBSC specimens were observed throughout the analysis: bolt deflection due to combined shear, bending and axial stresses and concrete crushing at the steel beam – plugs interface.

The parametric results showed that the predominant failure mode of the FBSC specimens with M12, M14 and M16 bolts was the shear failure of the bolts. The deflection angle of the bolts was calculated

at the last increment of the analysis and varied from 30° to 41°. The grout in front of the bolt connectors was completely destroyed form the first steps of the analysis allowing the bolts to bear against the precast concrete plugs. As the loading was increasing, extensive crushing of the plugs and the slab was observed in a limited area at the steel – concrete interface as shown in Figure 4.18.

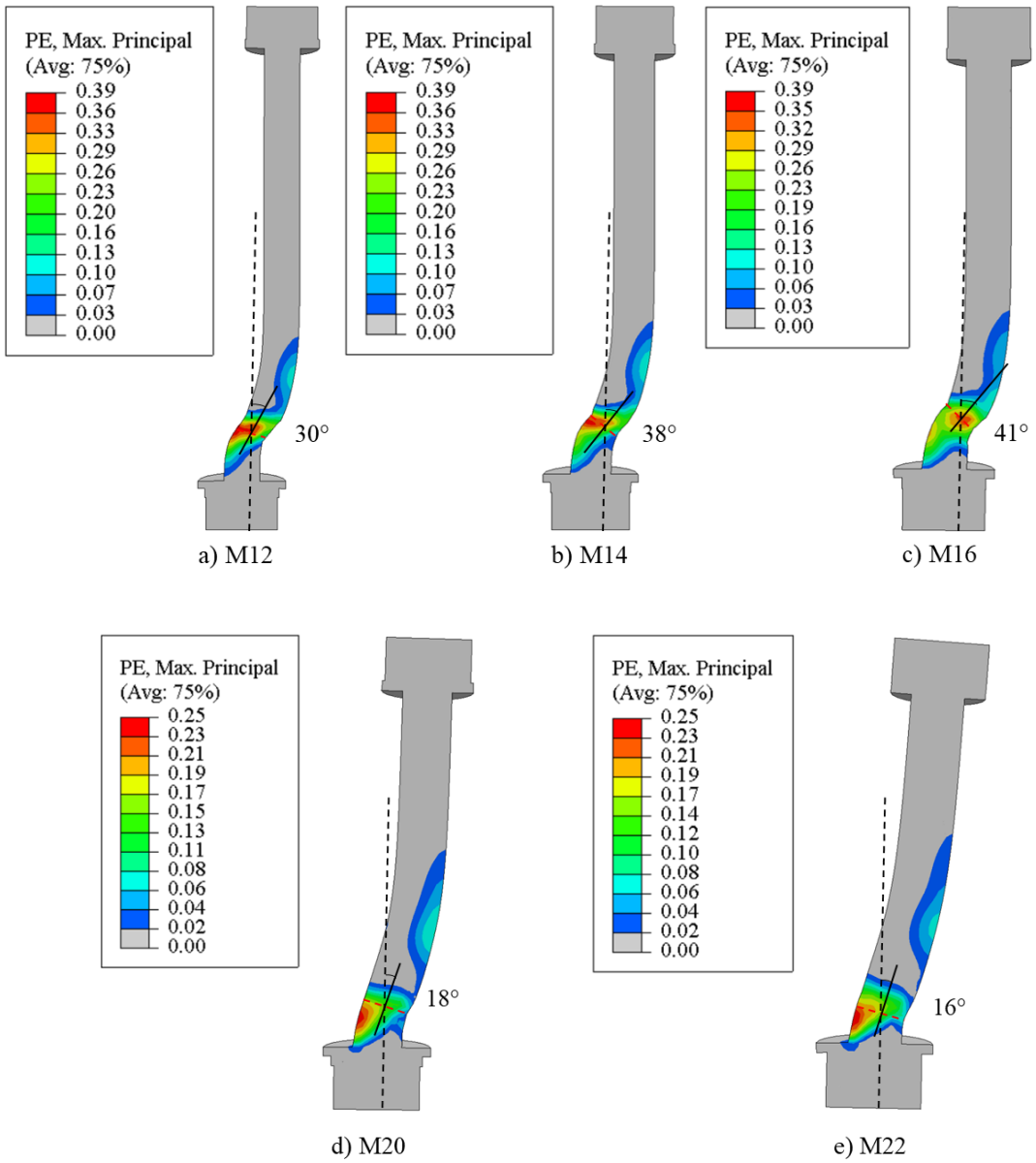

Figure 4.17: Deflected shapes of the bolt connectors with various diameter sizes.

On the contrary, the predominant failure mode of the FBSC specimens with M20 and M22 bolts was the failure of the precast concrete slab. Severe concrete crushing was observed in the area in front of the bolt shank. The precast concrete plugs were severe damaged due to the bearing of the bolts which considerably decreased their load-carrying capacity. The brittle failure of the plugs caused severe tensile cracking in the precast concrete slab resulted to the complete failure of the push-out specimen. A reduced slip capacity was observed in these specimens. In general, the high slip capacity offered by FBSCs is attributed to their capability to deflect and bear against the concrete plugs. As shown in Figure 4.18, the deflection angles of M20 and M22 bolts were less than 20°, which are significant smaller than the deflection angles of M12, M14 and M16 bolts. This is attributed to the fact that a premature concrete failure occurred that didn't allow the bolts to deflect and fail due to shear, bending and axial stress concentrations.

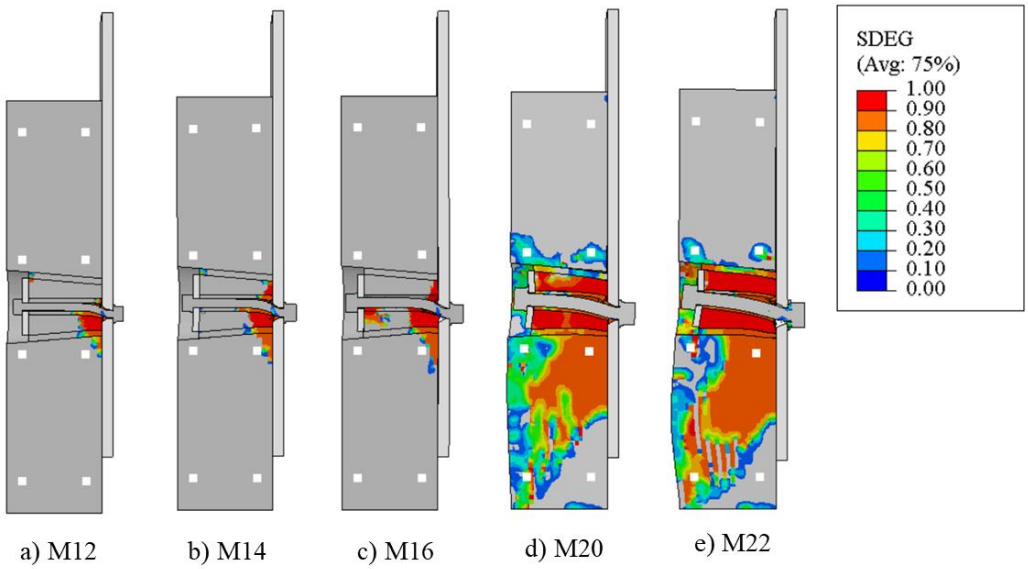

Figure 4.18: Concrete damage of the FBSC specimens with various bolt diameter sizes.

Figure 4.19 shows the degradation of the concrete parts of the FBSC – D4 specimen during the FE analysis. The first slip occurs when the friction at the plug – steel beam interface is overcome. After this point, the bolts start to gradually yield. At this stage, crushing of the grout in front of the bolt connectors is observed. As the load increases, the bolts start to bear against the precast concrete plugs which causes severe damage to them (Figure 4.19 (a)). As the concrete plugs in front of the bolt connectors lose their load transfer capacity, tensile cracks appeared at the longitudinal direction of the precast concrete slab (Figure 4.19 (b). At this point, a sudden drop at the load-slip curve of the FBSC is observed in Figure 4.16. The crushing of the slab continues until the FBSC specimen is completely destroyed (Figure 4.19 (c)).

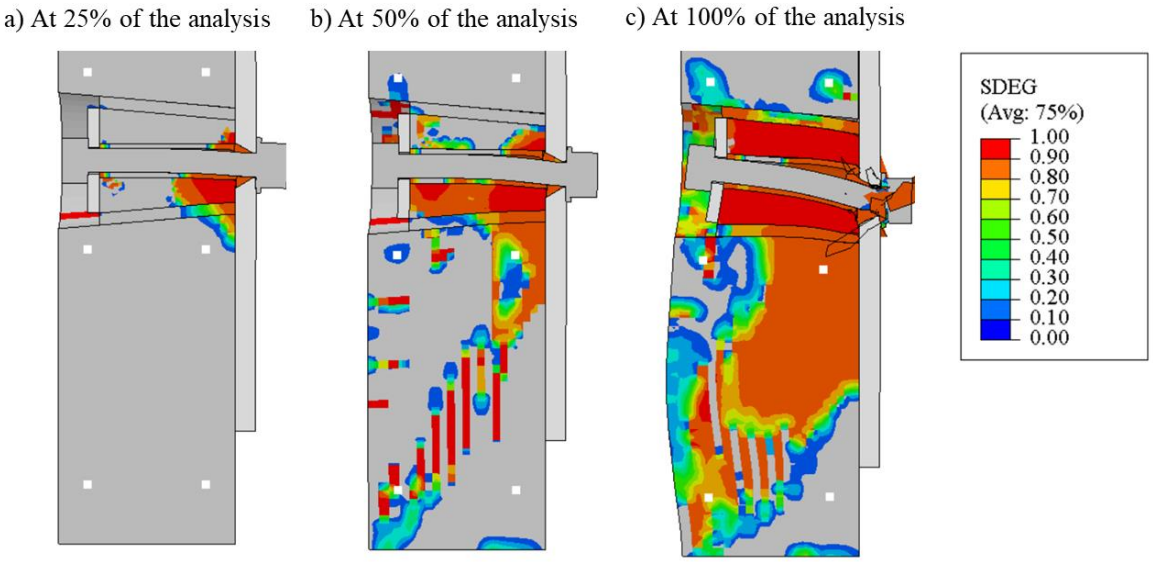

Figure 4.19: Concrete degradation of the FBSC - D4 specimen.

4.8.2 Effect of bolts tensile strength

This paragraph presents a parametric study that was conducted to assess the effect of bolts tensile strength on the shear behaviour of the FBSC. The bolts tensile strength varied from 800 MPa to 1115 MPa, while all the other parameters of the model, such as concrete strength, mesh sizes, load application and boundary conditions remained the same as in FBSC Test 6. Tensile test data [24, 32, 53] were used to establish the stress-strain relationship for M16 bolts presented in Eq. (3.31) to Eq. (3.35). Tensile coupon tests were built in ABAQUS and numerically tested to calibrate the damage parameters used in the material modelling of the bolts. The FE analysis and the results of the material modelling of the bolts are summarized in Cl. 3.9.5.

The load-slip curves of the examined specimens are illustrated in Figure 4.20. Table 4.6 compares the shear resistance, the stiffness and the slip capacity of the FBSC specimens using bolts with various tensile strengths. The bolt tensile resistance highly affects the characteristic shear resistance of the specimens, since 45% increase of shear resistance was observed when the tensile strength of bolts increased from 800 MPa to 1115 MPa. The stiffness of the specimens was also affected, with maximum stiffness decrease due to changing the bolts tensile strength was calculated around 9%. Finally, the results showed that the bolts tensile strength did not have any substantial effect on the slip capacity of the specimens.

Table 4.6. Effect of bolt tensile strength on shear resistance, stiffness and slip capacity of the FBSC.

Specimen	f_u	P_{ult}	Shear Resistance ratio	k_{sc}	Stiffness ratio	δ_{ult}	Slip capacity ratio
	(kN)	(kN)	$P_{ult,Pi}/P_{ult,P1}$	(kN/mm)	$k_{sc,Pi}/k_{sc,P1}$	(mm)	$\delta_{u,Pi}/\delta_{u,P1}$
FBSC – T1	800	146.1	-	91.4	-	16.1	-
FBSC – T2	865	171.9	1.18	95.5	1.04	16.2	1.01
FBSC – T3	950	201.7	1.38	100.8	1.10	16.1	1.00
FBSC – T4	1115	212.2	1.45	101.1	1.11	16.5	1.02

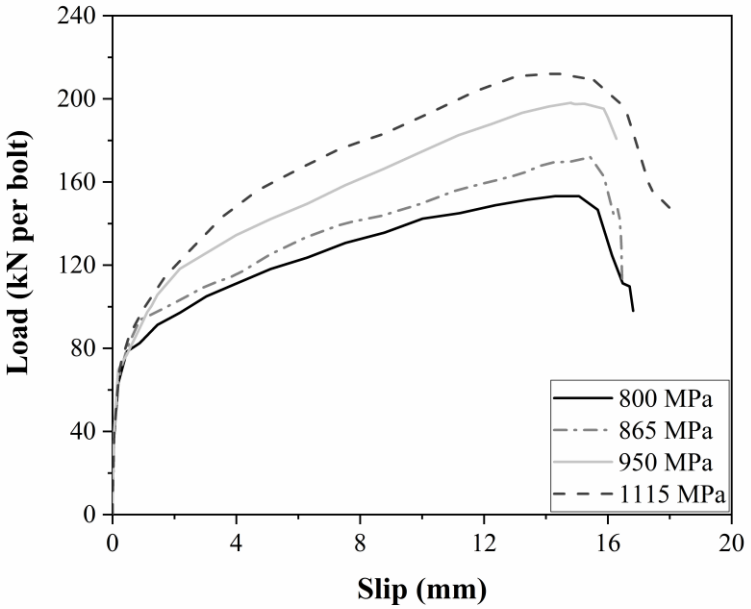

Figure 4.20: Effect of bolts tensile strength on the load-slip response of the FBSC.

The failure modes of the FBSC specimens were also monitored during the FE analysis and the results are presented in Figure 4.21 and Figure 4.22. Bolt deflection due to combined shear, bending and axial stresses was observed in all specimens with the deflection angle from 32° to 41°. Extensive concrete crushing was also observed in all FBSC specimens in front of the bolt connector at the steel – concrete interface, as well as in the plug underneath the upper hexagonal nut.

It was concluded that for shear connectors with high tensile strength (e.g. 1115 MPa), the shear resistance was dominated by the concrete crushing and splitting. On the other hand, for shear connectors with tensile strength equal to 950 MPa or less, the shear capacity was dominated by the bolt's strength and therefore the failure mode was the shear failure of the bolts at the steel beam – concrete plug interface.

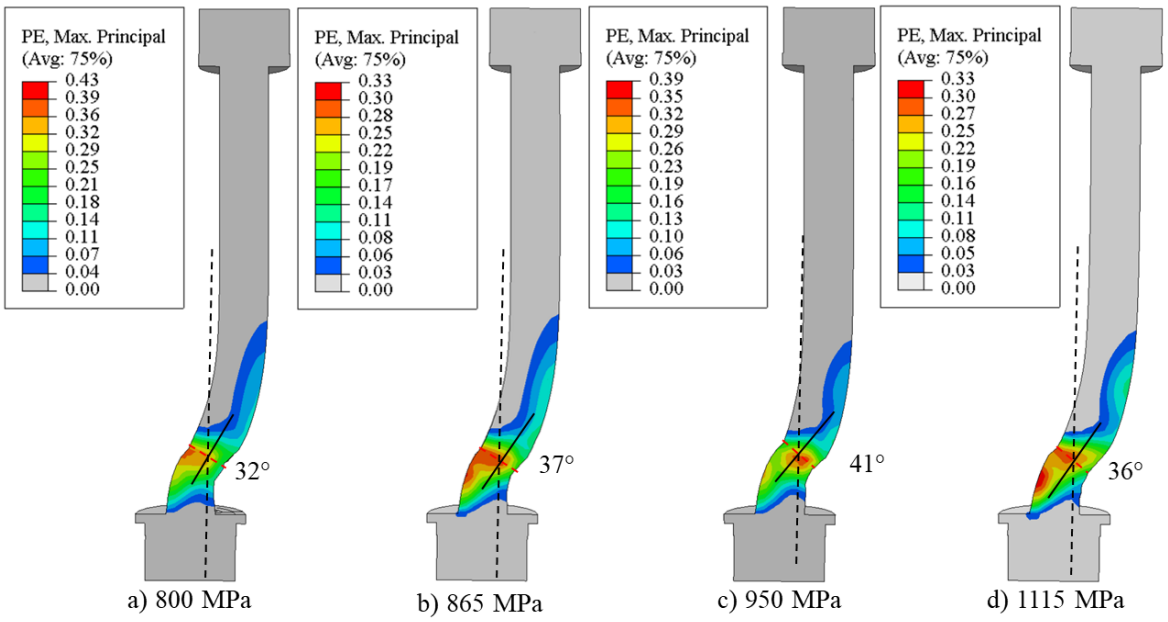

Figure 4.21: Deflection shapes of the bolt connectors with various diameter sizes.

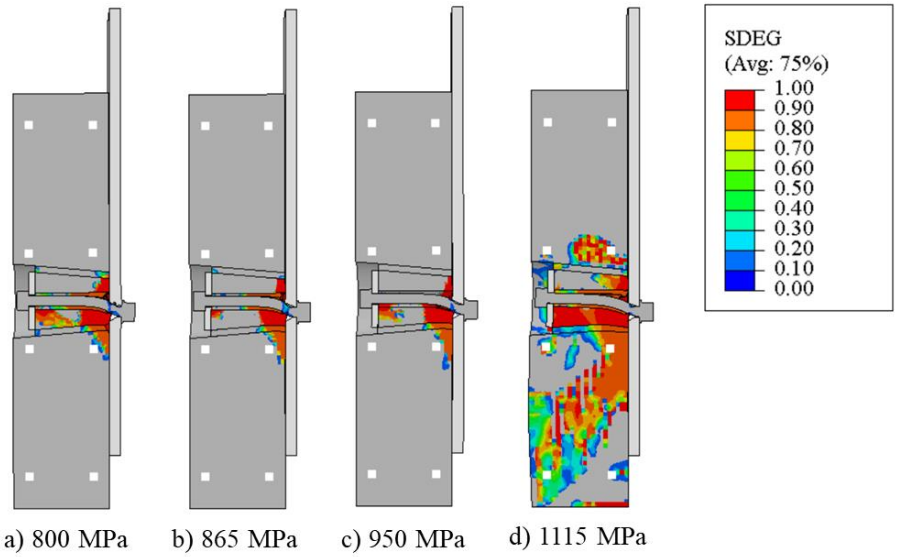

Figure 4.22: Concrete damage of the FBSC specimens with various bolt tensile strengths.

4.8.3 Effect of plugs compressive strength

The effect of the compressive strength of precast concrete plugs on the shear behaviour of the FBSC is analysed in this paragraph. The compressive strength of precast concrete plugs varied from 50 MPa to 90 MPa, while the material properties of all the other components remain the same as in Test 6. Analysis procedure, mesh sizes, boundary conditions and loading procedure were also remained unchanged. The material properties of the precast concrete plugs used in the parametric analysis are listed in Table 4.7. The characteristic cylinder compressive strength, the elastic modulus and the tensile strength of the FBSC specimens were defined according to BS EN 1992-1-1 [41]. The strain at the peak stress was calculated using Eq. (3.22) proposed by Hsu & Hsu [45].

Table 4.7. Material properties of precast concrete plugs used in the parametric analysis.

Concrete type	Concrete class $f_{ck}/ f_{ck,cube}$	Characteristic cylinder compressive strength f_{ck}	Elastic modulus E_{cm}	Strain at peak stress ε_c'	Tensile strength f_{ctm}
	(-)	(MPa)	(MPa)	(-)	(MPa)
C50	C50/60	50	37278	0.00204	4.07
C70	C70/85	70	40743	0.00218	4.6
C90	C90/105	90	43631	0.00232	5.0

The compressive behaviour of the plugs was defined using the model proposed by Hsu & Hsu [45], which can predict the stress-strain behaviour of high-strength concrete. The compressive behaviour of the plugs with various compressive strengths in illustrated in Figure 4.23 in terms of yield stress and inelastic strain. Extensive damage was observed in the area in front of bolt shank in both experimental [32] and FE verified specimens. Therefore, considering concrete compression behaviour only up to nominal ultimate strain (ε_{cu1}) as advised by BS EN 1992-1-1 [41] would lead to unreal overestimation of concrete crushing strength. As a result, the curves were extended beyond the nominal ultimate strain up to an inelastic strain of 0.01, which is large enough so as not to be achieved in the analyses. The tensile behaviour of concrete was assumed to be linear until its ultimate tensile strength. After this point, Hillerborg's fracture energy approach was adopted in order to minimize the mesh sensitivity of the results. The fracture energy required to open a unit crack area was specified using Eq. (3.31).

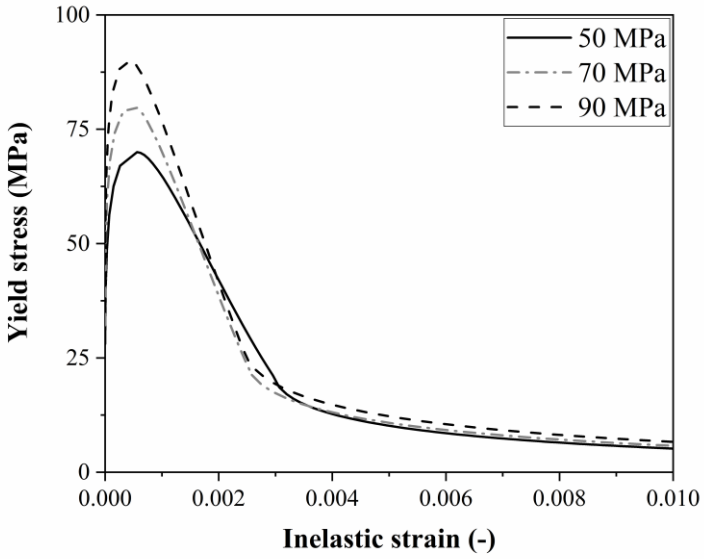

Figure 4.23: Precast concrete plugs compressive stress-strain behaviour.

The concrete damage plasticity (CDP) model was employed in the analysis to capture the complex behaviour of concrete. The concrete damage parameters were defined according to Cl.3.7.2. Scalar damage variables were included in the parametric FE models as shown in Figure 4.24 to account for compressive and tensile damage of the plugs, similar to verified FE models.

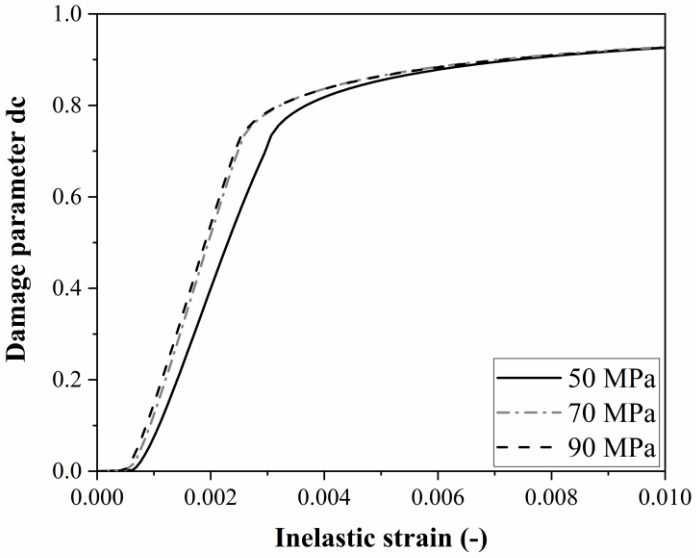

Figure 4.24: Precast concrete plug compression damage.

Figure 4.25 shows the effect of the plug's compressive strength on the load-slip behaviour of the FBSC specimens. Table 4.8 compares the characteristic shear resistance, stiffness and slip capacity of the FBSC specimens for different plug strengths. According to the analysis results, the compressive strength of the precast concrete plug does not have a significant effect on the load-slip behaviour of the FBSC. More specifically, the shear resistance of the FBSC increases slightly (around 5%) when the plug concrete strength increases from 50 MPa to 100 MPa. Similarly, the slip capacity of the specimens varies slightly from 15.8 to 16.2 mm.

Table 4.8. Effect of plugs compressive strength on the shear resistance, stiffness and slip capacity of the FBSC.

Specimen	Plugs compressive strength	P_{ult}	Shear Resistance ratio	k_{sc}	Stiffness ratio	δ_{ult}	Slip capacity ratio
	(mm)	(kN)	$P_{rk,Pi}/P_{rk,P1}$	(kN/mm)	$k_{sc,Pi}/k_{sc,P1}$	(mm)	$\delta_{u,Pi}/\delta_{u,P1}$
FBSC – P1	50	169.8	-	96.2	-	16.1	-
FBSC – P2	70	176.1	1.04	99.8	1.04	15.8	0.98
FBSC – P3	90	181.5	1.07	100.8	1.05	16.1	1.00
FBSC – P4	100	187.2	1.10	113.4	1.18	16.1	1.00

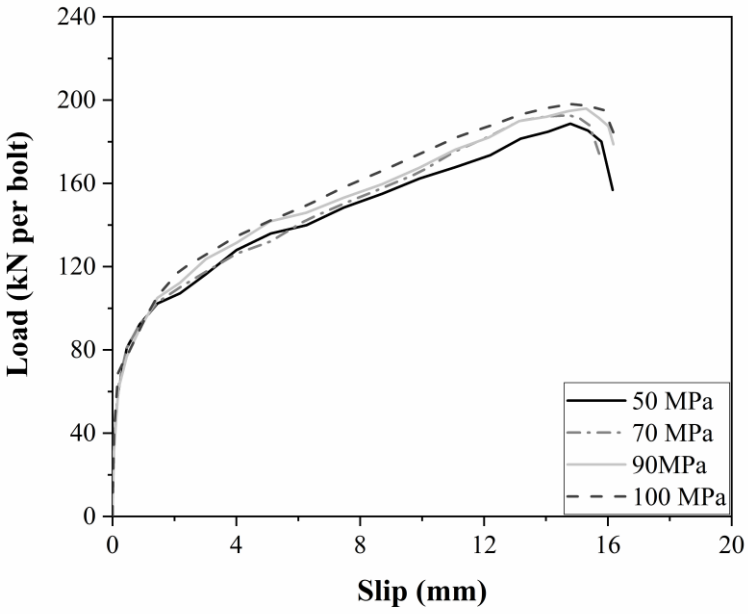

Figure 4.25: Effect of plugs compressive strength on the load-slip response of the FBSC.

Two failure modes were observed during the FE analysis. First, the bolt connectors deformed due to combined shear, bending and axial stresses. The deformed shapes of the bolted connectors at the last increment of the analysis are illustrated in Figure 4.26. The deflection angle of the bolts was calculated around 40° in all specimens, which shows that there is not clear dependency between the deflection angle of the bolts and the plugs compressive strength. A region of high plastic strains was formed above the steel beam – precast concrete plugs interface that indicates that the predominant failure mode of the FBSC push-out specimens was the shear failure of the bolts.

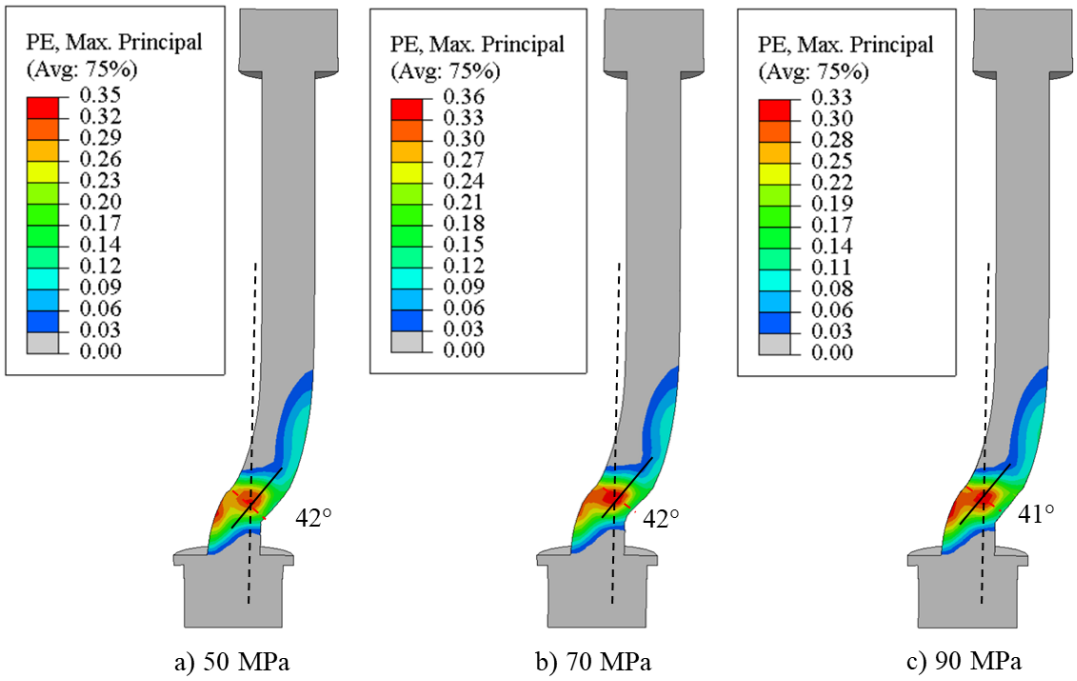

Figure 4.26: Deflection shapes of the bolt connectors with various diameter sizes.

Extensive concrete crushing was also observed in the parametric FBSC specimens. The concrete damage at ultimate loads for different plugs compressive strengths is illustrated in Figure 4.27. The results showed that severe concrete crushing is observed in front of the bolt connector regardless the plugs compressive strength.

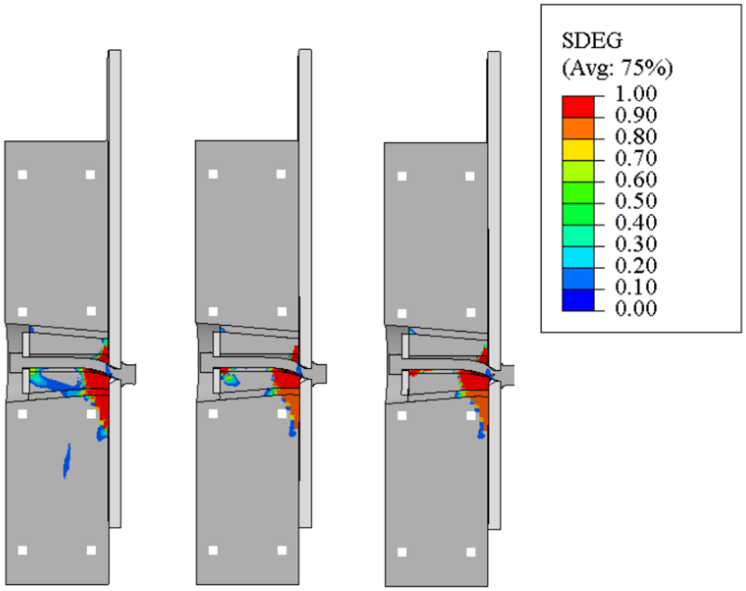

Figure 4.27: Concrete damage of the FBSC specimens with various plug compressive strengths.

4.8.4 Effect of bolts pretension force

FBSC exploits the friction resistance between the lower face of the precast concrete plug and the upper face of the top flange of the steel beam. Friction resistance is achieved with bolt axial pretension. Therefore, a parametric study was conducted to evaluate the effect of bolt pretension force to the shear behaviour of the FBSC. Suwaed and Karavasilis [32] proposed that the design of the FBSC should be done assuming 60% of proof load pretension, since 40% of proof load pretensions is expected to be lost during the first 24 hours after tightening. The loss of bolt pretension with time was observed due to creep, concrete shrinkage, and bolt steel relaxation. The proof load represented 70% of the ultimate capacity of the bolts.

A parametric study was conducted to assess the effect of bolt pretension force to the shear behaviour of the FBSC and the results are presented in this paragraph. The FBSC specimens were built using four different preloading forces varied between 50 kN and 80 kN. The results of the FE analysis are listed in Table 4.9, where the characteristic shear resistance, stiffness and slip capacity of the FBSC specimens are compared.

Figure **4.28** illustrates the effect of preload variations on the load – slip behaviour of the FBSC.

The results showed that when the bolt pretension force increased from 50 kN to 80 kN, the load at the first slip increased (i.e. the frictional resistance). affects the behaviour of the FBSC because it increases the friction at the steel-concrete interface. Therefore, it was assumed that an increase of 60% in preload results in an increase of frictional resistance by 17%. According to Table 4.9, the stiffness of the FBSC specimens increased up to 10% by increasing the bolts pretension force. However, the bolt preload did not have any substantial effect on the slip capacity of the FBSC specimens.

Table 4.9. Effect of bolt pretension force on the shear resistance, stiffness and slip capacity of the FBSC.

Specimen	Pretension force	P_{ult}	Shear Resistance ratio	k_{sc}	Stiffness ratio	δ_{ult}	Slip capacity ratio
	(kN)	(kN)	$P_{ult,Pi}/P_{ult,P1}$	(kN/mm)	$k_{sc,Pi}/k_{sc,P1}$	(mm)	$\delta_{u,Pi}/\delta_{u,P1}$
FBSC – B1	50	158.7	-	91.6	-	15.9	-
FBSC – B2	60	164.7	1.04	94.3	1.03	16.0	1.00
FBSC – B3	70	178.3	1.12	98.0	1.07	15.8	1.00
FBSC – B4	80	181.5	1.14	100.8	1.10	16.1	1.00

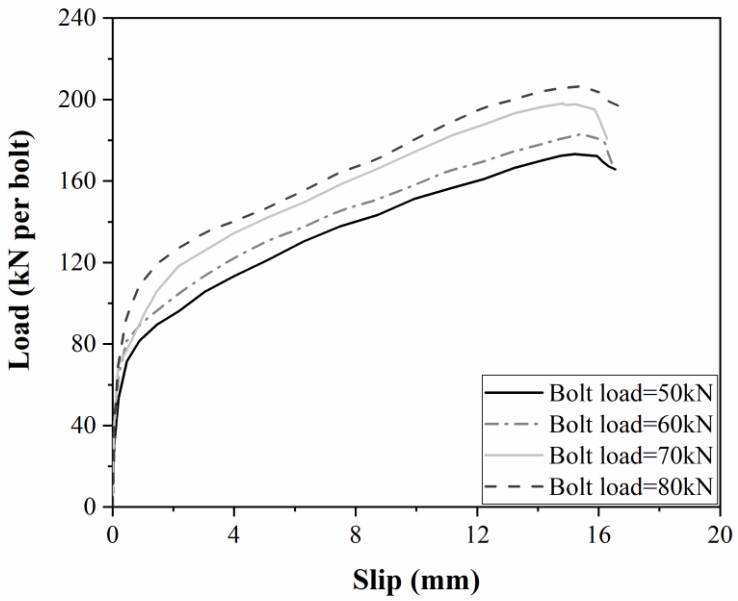

Figure 4.28: Effect of bolt pretension force on the load-slip response of the FBSC.

The failure modes of the FBSC specimens are presented in Figure 4.29 and Figure 4.30, which remained the same as those observed in FBSC-Test 1. The bolt connectors deflected and bear against the precast concrete plugs. The deflection angles of the bolts were calculated at the last increment of the analysis and they varied from 36° to 43° for bolt preload equal to 50 kN to 80 kN respectively. Concrete crushing in front of the bolt connectors was also reported throughout the FE analysis.

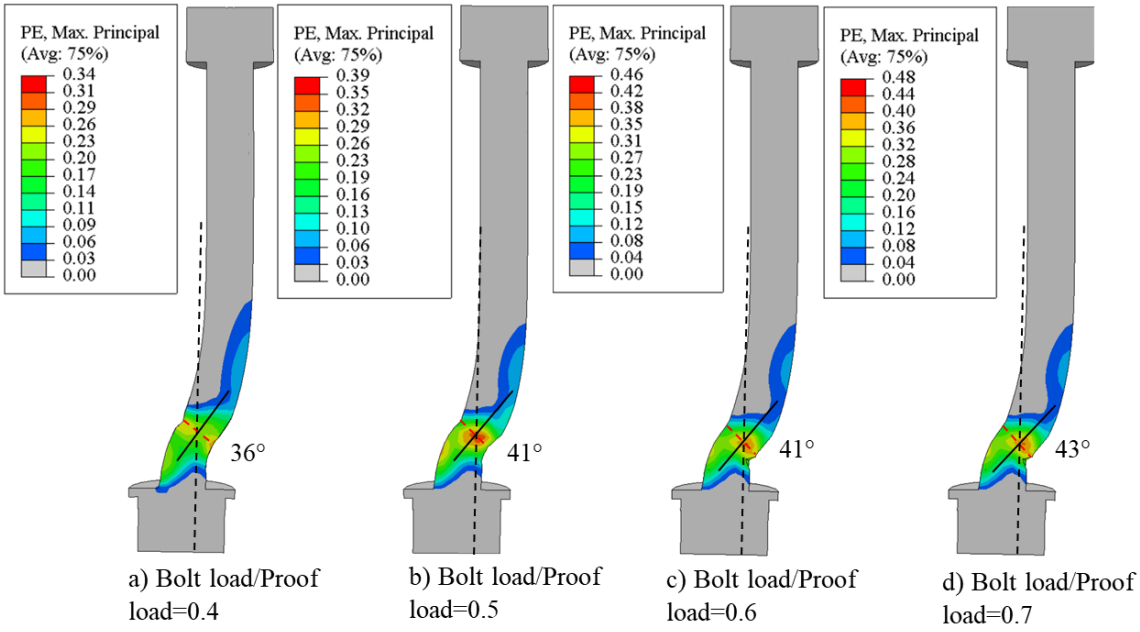

Figure 4.29: Deflection shapes of the bolt connectors with various bolt preloads.

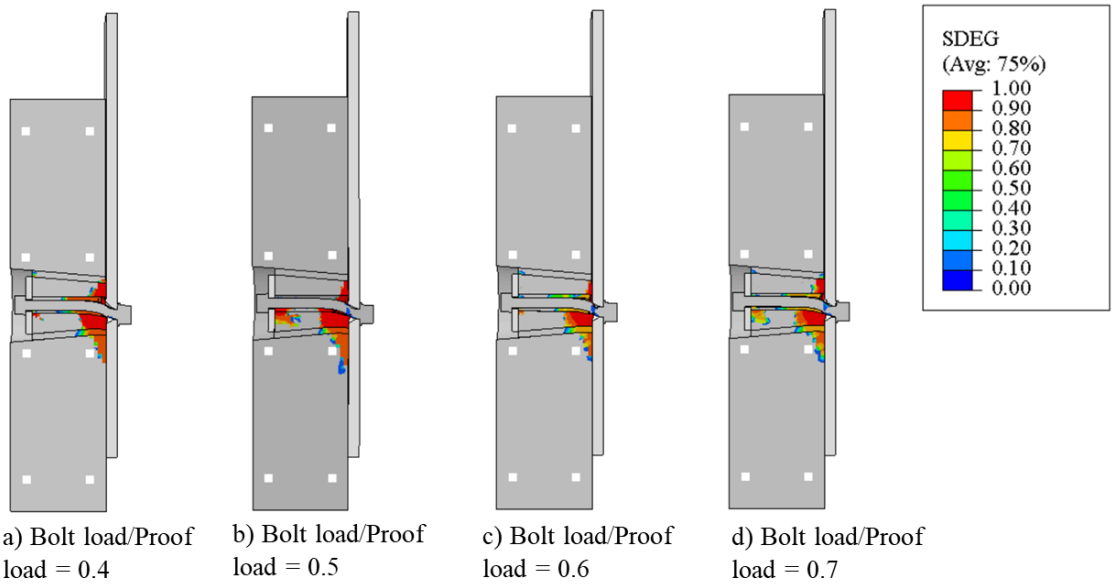

Figure 4.30: Concrete damage of the FBSC specimens with various bolt preloads.

4.8.5 Effect of bolt height to diameter ratio

Previous FE analysis by Pavlovic [24] have shown that the bolt height to diameter ratio of is among the most influential parameters on the structural behaviour and failure mode of bolted connectors. The parametric analysis presented in Chapter 3, also proved that the bolt height to diameter ratio of the connectors highly affected the behaviour of the LNSC specimens.

In this paragraph, a parametric study was conducted to demonstrate the potentially significant influence of the bolt height to diameter ratio on the behaviour of the FBSC specimens. All the other

parameters of the push-out tests, such as the material properties of the various FBSC components, the bolt diameter and bolt preload remained the same. The boundary conditions, load application, meshing and analysis procedure used for the FE modelling of the Test 6 were used for the parametric FE analysis. The load-slip behaviour of the FBSC specimens using bolt connectors with height to diameter ratio equal to 8.9 and 7.3 are compared in Figure 4.31. Table 4.10 presents the characteristic shear resistance, stiffness and slip capacity of the FBSC push-out specimens that were investigated in this parametric study.

It was concluded that decreasing the height to diameter ratio caused a 3% decrease on the shear resistance of the FBSC specimen. Similarly, the height to diameter ratio did not have any substantial effect on the stiffness and the slip capacity of the FBSC.

Table 4.10. Effect of bolt height to diameter ratio on the shear resistance, stiffness and slip capacity of the FBSC.

Specimen	Bolts height to diameter ratio	P_{Rk}	Shear Resistance ratio	k_{sc}	Stiffness ratio	δ_{ult}	Slip capacity ratio
	(-)	(kN)	$P_{rk,Hi}/P_{rk,H1}$	(kN/mm)	$k_{sc,Hi}/k_{sc,H1}$	(mm)	$\delta_{u,Hi}/\delta_{u,H1}$
FBSC – H1	8.9	201.7	-	100.8	-	16.1	-
FBSC – H2	7.3	195.7	0.97	101.8	1.01	15.3	0.95

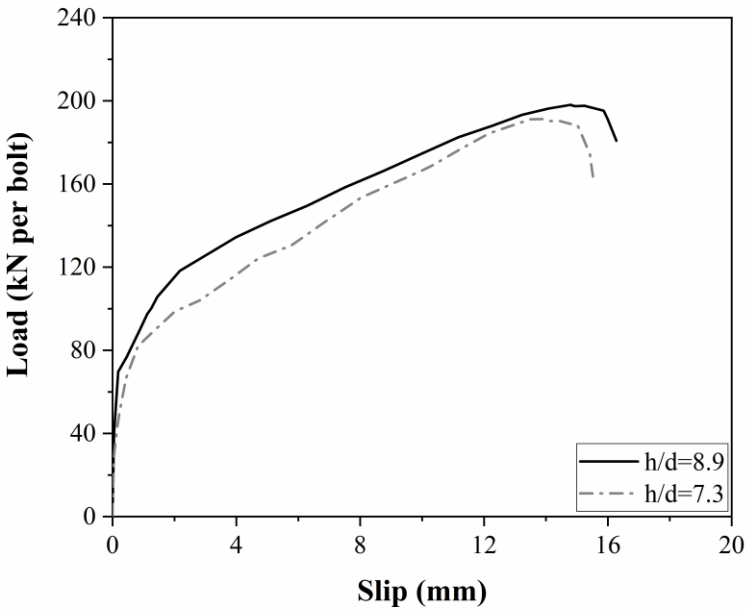

Figure 4.31: Effect of the bolt height to diameter ratio on the load-slip response of the FBSC.

Deformed shapes of the bolts and concrete damage plots for different bolted shear connector's height to diameter ratios are shown in Figure 4.32 and Figure 4.33 . It is obvious that the failure of the FBSC – H2 specimen, where shear connectors with bolt diameter to height ratio equal to 7.3 were used, is governed by the concrete pry-out and not by shearing of the bolts at the steel-concrete interface as in

FBSC – H1 specimen. This conclusion was extracted because the deflection angle of the bolt connectors was relatively smaller in FBSC - H2 (25°) compared to FBSC – H2 (41°). The precast concrete slab was also significantly damaged due to concrete crushing and cracking in FBSC – H2, while for FBSC – H2, the concrete crushing was limited to a small area in front of the bolt connector at the steel-concrete interface.

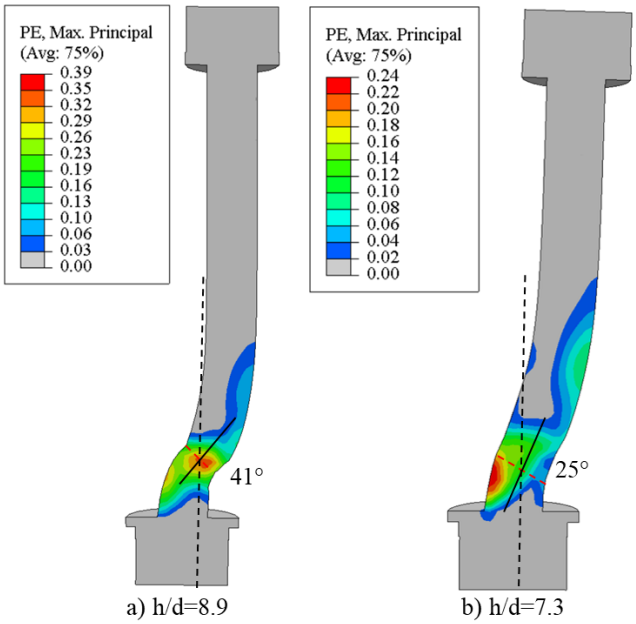

Figure 4.32: Deflection shapes of the bolt connectors with various bolt height to diameter ratio.

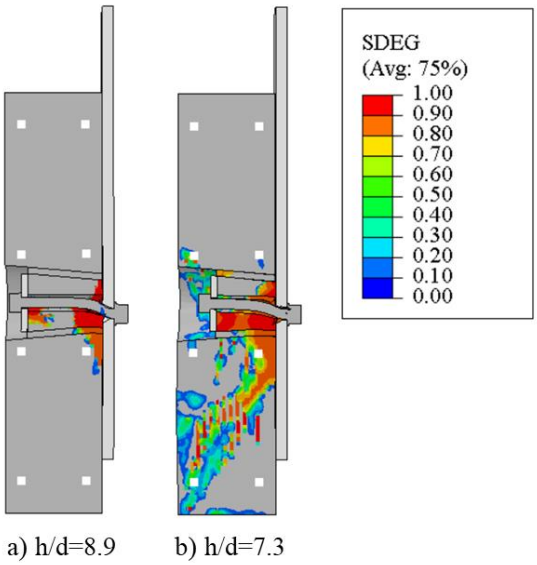

Figure 4.33: Concrete damage of the FBSC specimens with various bolt height to diameter ratio.

4.9 Design recommendations

EC4 [6] does not provide design recommendations for bolted shear connectors for steel-concrete composite bridges. In steel structures, the characteristic shear resistance of high-strength bolts in bolted connections is calculated according to BS EN 1993-1-8 using Eq. (4.1).

$$F_{V,Rd} = \frac{\alpha_V \, f_{ub} \, A}{\gamma_{M2}} \tag{4.1}$$

In FBSC, the shear plane passes through the un-threaded portion of the bolt and therefore A is the gross-section on the bolt and α_V is equal to 0.6.

The load resistance of the push-out tests using FBSC obtained through the experimental tests and the numerical analysis is 50-80% higher than the pure shear resistance of the bolts. The increase in the load-bearing capacity of the FBSC is attributed to the friction at steel beam – concrete plug interface as well as to the catenary effects in the bolt. These effects are illustrated in Figure 4.34, where the deformed geometry of the connector is shown at the ultimate load prior to failure.

The pure shear resistance of the bolts F_s is defined using Eq. (4.2), according to previously mentioned BS EN 1993-1-8.

$$F_S = \alpha_V \, f_{ub} \, A \tag{4.2}$$

The initial non-slip behaviour of the FBSC is due to the friction between the steel beam - concrete plug interface. Therefore, at this stage the slip resistance of the connector is given as a function of the bolt pretension force (T) and the friction coefficient at the steel-concrete interface (μ) and can be calculated using Eq. (4.3). The coefficient of friction was taken equal to 0.45 as recommended by BS 5400-5 [55] for steel-concrete interfaces, while the pretension of the bolts was assumed to be equal to 60% of the proof load. According to the experimental findings of Suwaed and Karavasilis [32], a large percent of loss in bolt pretension occurred during the first 24 hours after the tightening of the bolts. Therefore, it was recommended to design the FBSC for 60% of proof load pretension and tighten the bolts to 100% of proof load by assuming a 40% loss with time.

$$F_{friction} = \mu \cdot T \tag{4.3}$$

When the slip load of the connection is overcome by external loading, the bolts gradually elongate in tension. The tensile force F_t can be analysed in two components, one vertical to the steel flange $F_{t,V}$ that increases the tensile force in the bolts and thus increases the clamping action and one horizontal $F_{t,H}$ that coincide with the direction of F_s and therefore increases the bolt resistance to vertical shear. As a result, the resistance of the FBSC due to friction at this stage can be calculated using Eq. (4.4).

$$F_{friction} = \mu \cdot F_{t,\mathrm{v}} = \mu \cdot F_t \cdot \cos(\beta) \quad (4.4)$$

Taking all the above into consideration, the resistance of the LNSC is using Eq. (4.5).

$$F_{total} = F_{t,\mathrm{h}} + F_{friction} + F_s = 0.6 f_{ub} A_s + F_t [\mu \cos(\beta) + \sin(\beta)] \quad (4.5)$$

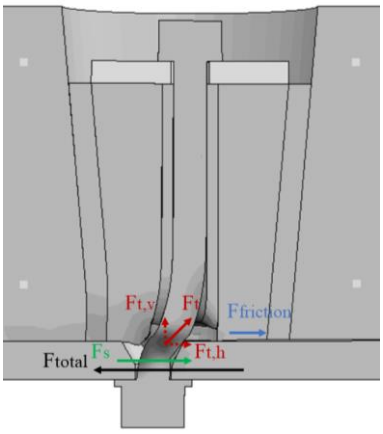

Figure 4.34: Load transfer mechanism for FBSC.

The angle β was obtained at the last increment of the analysis prior to specimen failure and it ranged from 30° to 42°. Therefore, $\mu \cos(\beta) + \sin(\beta)]$ ranged from 0.93 to 1.03. The average value was then 0.98 ≈ 1. The tensile force of the bolts F_t was calculated to be on average equal to 60% proof load. Therefore, Eq. (4.5) can be simply expressed as:

$$F_{total} = f_{ub} A_s \quad (4.6)$$

The accuracy of Eq. (4.6) was verified by comparing the predicted ultimate resistance of the FBSCs with the results of the parametric study. As shown in Table 4.11, the proposed equation was able to predict the resistance of the FBSCs with less than 10% difference.

Table 4.11. Comparison between the predicted shear resistance of FBSCs using Eq. (4.6) and the results of the parametric study using the proposed FE model.

Specimen	$F_{ult,FE}$ [kN]	F_{total} [kN]	$F_{ult,FE} / F_{total}$ [-]
FBSC-D1	108.1	107.4	0.99
FBSC-D2	155.4	146.2	0.94
FBSC-D3	201.7	190.9	0.95
FBSC-T1	146.1	160.8	1.10
FBSC-T2	171.9	173.8	1.01
FBSC-T3	201.7	190.9	0.95
FBSC-B1	176.3	190.9	1.08
FBSC-B2	183.0	190.9	1.04
FBSC-B3	198.1	190.9	0.96
FBSC-B4	201.7	190.9	0.95
FBSC-H1	201.7	190.9	0.95
FBSC-P1	188.7	190.9	1.01
FBSC-P2	195.7	190.9	0.98
FBSC-P3	201.7	190.9	0.95
FBSC-P4	208.0	190.9	0.92

4.10 Conclusions

Three-dimensional FE models were built and presented in this chapter using the commercial software ABAQUS to study the behaviour of a novel demountable friction-based shear connector (FBSC) for steel-concrete composite structures. A quasi-static FE analysis using dynamic explicit procedure was adopted for the analysis to deal with complex contact interactions and highly non-linear materials. The material degradation of the various components of the connector was monitored during the analysis by employing failure criteria and progressive damage models. The FE models were validated against experimental results available in the literature and it was concluded that they were capable to capture the fundamental behaviour of the shear connections. The shear resistance, stiffness and slip capacity of the shear connections were predicted with great accuracy and compared well with the experimental results available in literature.

A parametric study was conducted to investigate the effect of various parameters on the shear behaviour and capacity of the FBSC. The push-out test arrangement, the boundary conditions, the mesh sizes, the load application and the analysis procedure used for the parametric FE modes were defined according to the verified FE models presented in the same chapter. The parameters studied were the compressive strength of plugs, the diameter and tensile strength of bolt connectors, the bolt height to diameter ratio and bolt preload. The parameters were evaluated by comparing their effect on the shear resistance, stiffness and the slip capacity of the FBSC specimens. The following conclusions have been drawn:

- Push-out specimens with M12, M14 and M16 connectors failed by shear fracture of the bolts, while specimens with M20 and M22 bolts fail by tensile cracking of the precast concrete slab.
- Decreasing the height to diameter ratio from 8.9 to 7.3 caused severe concrete crushing in front of the bolt shank which result to the brittle failure of the plugs and the extensive tensile cracking of the precast concrete slabs.
- A variation in plugs compressive strength had limited influence of the shear resistance of the FBSC; less than 5% difference was observed between the specimens.
- Up to approximately 2.5 times increased shear resistance was observed for specimens with M22 bolts compared to the specimens with M12 diameter bolts. However, specimens with M20 and M22 bolts had limited capacity due to the shift of the predominant failure mode of the specimen from shear fracture of the bolts to tensile cracking of the slab.
- All FBSC specimens high slip capacity (> 6 mm) and therefore can be categorized as ductile shear connectors according to BS EN 1994-1-1 [6].
- A 45% increase in shear resistance of the specimens was achieved by increasing the bolt tensile strength from 800 MPa to 1115 MPa.

The results of the parametric study were compared to the design recommendations given by BS EN 1994-1-1 for welded headed studs. It was concluded that FBSCs can offer higher shear resistance than corresponding conventional headed studs due to the friction developed at the steel beam – plug interface, as well as the smart structural details of the connector, such as the high-strength of the bolts and the high-strength precast concrete plugs.

An equation was proposed at the end of this chapter to calculate the shear resistance of the FBSC. The accuracy of the equation was verified by using data from the parametric push-out tests. It was concluded that the proposed equation was able to predict the shear resistance of the FBSC with less than 10% difference.

Chapter 5 Finite element modelling of the friction-based shear connectors in beam specimens and parametric study

5.1 Introduction

A simply supported steel-concrete composite beam with friction-based shear connectors (FBSCs) is numerically tested in a four-point bending configuration as part of this research project. The FE models were validated against the experimental findings of Suwaed and Karavasilis [36]. The aim of this chapter is to assess the flexural behaviour of the composite beam and study its moment capacity. The beam model will then be used as a reference specimen to conduct a parametric study to evaluate the parameters that affect its behaviour.

5.2 Description of the experimental FBSC beam test

A simply supported steel-concrete composite beam with FBSCs was experimentally tested by Suwaed and Karavasilis [36]. Testing was conducted in a four-point bending configuration. The test set up is shown in Figure 5.1. The distance between the supports was 8.5 m. The steel beam had a UB 457×191×89 steel section and length equal to 9.173 m. The concrete slab had 9×1.25×0.15 m dimensions. The beam used a roller bearing support in one end (left side of beam) and a pinned bearing support in the other end (right side of beam). The test rig consisted of a steel frame with a 100t lifting hydraulic jack in the middle. The load was transferred through a ball joint to avoid any possible rotations due to eccentricity. The point load of the ball joint was converted to two-point loads (3 m apart) using a stiff spreader beam of UC 305×305×283 that was supported over the concrete slab through pinned and roller supports.

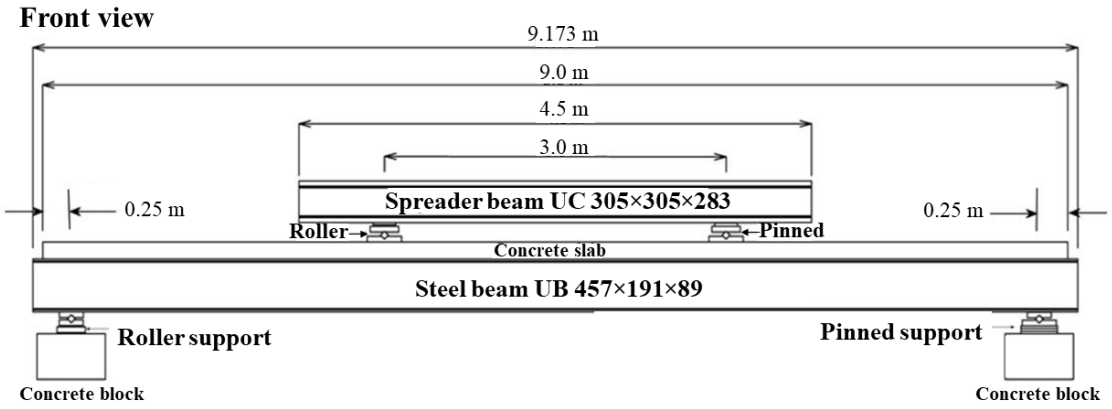

Figure 5.1: Overview of the four-point bending test of the steel-concrete composite beam.

The concrete slab consisted of two precast panels, each one had 4.05m length, leaving a 0.9m gap between them, where cast in-situ concrete was poured. The concrete used to fill the 0.9 m gap had similar strength with the concrete used in the panels. Fifteen pockets were spread along the centre of the slab to accommodate the shear connector, with a centre-to-centre spacing of 600 mm that leaves a length of 300 mm without pocket at each end of the slab as shown in Figure 5.2. The geometry of the pockets is shown in Figure 3.2.

Figure 5.2: Experimental testing of a steel-concrete composite beam with FBSC [36].

The concrete slab was properly positioned over the steel beam so that each row of holes in the upper flange of the steel beam aligns with a pocket in the slab. Thirty M16 grade 8.8 bolts as per BS EN 14399-3 [58] were positioned through the chamfered countersunk holes of the steel beam using retaining washers and M16 nuts. Rapid hardening grout, with compressive strength listed in Table 5.1, was poured inside the pockets and then precast concrete plugs with dimensions shown in Figure 3.2, were gradually inserted around the bolt connectors. Finally, the tightening of the upper nut was performed to finish the construction process.

Table 5.1: Concrete average properties of composite beam test.

Slab panels	
Mean cylinder compressive strength (N/mm^2), f_{cm}	56
Characteristic cylinder compressive strength (N/mm^2), f_{ck}	48
Tensile strength (N/mm^2)	4.5
Elastic Modulus (kN/mm^2)	31
Slab mid-span gap	
Mean cylinder compressive strength (N/mm^2), f_{cm}	51
Characteristic cylinder compressive strength (N/mm^2), f_{ck}	43
Tensile strength (N/mm^2)	3.7
Plug	
Compressive strength (N/mm^2)	89
Tensile strength (N/mm^2)	4.7
Elastic modulus (N/mm^2)	39
Grout	
Compressive strength (N/mm^2)	49

5.3 Design of the FBSC beam

A steel-concrete composite beam is designed by assuming that either the steel beam, concrete slab or shear connectors governs the design. Full composite connection is assumed when either the concrete slab or the steel beam yield and there are enough shear connectors to transfer the maximum longitudinal shear force from the steel to the concrete, so as the full plastic resistance moment of the composite section can be achieved. On the contrary, if fewer shear connectors are provided, then the longitudinal shear force transferred from the steel beam to the concrete slab is reduced and the shear connection is considered partial. Usually, the neutral axis of the composite section at the maximum bending is designed to be in the concrete slab, while the steel section is under tension. In this project, the composite beam is used to study the behaviour of the FBSC is assessed, and therefore the partial shear design connection was chosen.

5.3.1 Effective width

The effective width of the concrete flanges was determined in accordance with Cl. 5.4.1.2 of BS EN 1994-2 [7].

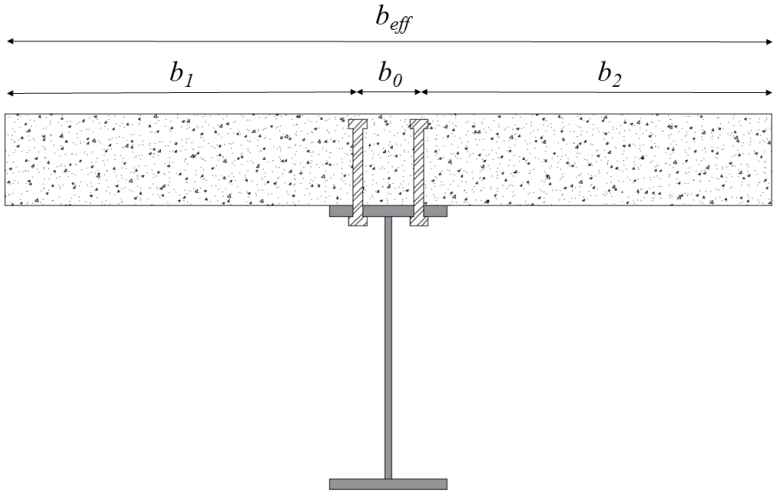

Figure 5.3: Effective width of the concrete flanges of the composite beam.

At mid-span, the total effective width b_{eff} may be determined as:

$$b_{eff} = b_0 + \sum b_{ei} \tag{5.1}$$

Where b_0 is the distance between the centres of the outstand shear connectors, b_{ei} is the value of the effective width of the concrete flange on each side of the web and taken as $L_e/8$ ($= 8500$ mm$/8 =$ 1062.5 mm)but not greater than the geometric width b_i. The value b_i should be taken as the distance from the outstand shear connector to a point mid-way between adjacent webs, measured at mid-depth of the concrete flange. Therefore, $b_1 = b_2 =$ (1250-100)/2=575mm.

$$b_{eff} = b_0 + b_1 + b_2 = 100 + 575 + 575 = 1250mm \quad (5.2)$$

5.3.2 Plastic resistance moment of the composite section

According to BS EN 1994-2, Cl. 6.2.1.2 [7], to calculate the plastic resistance moment of the composite section, the structural steel beam is assumed to be stressed in its yield strength, while the concrete slab resists a stress of $0.85f_{ck}$, constant over the whole depth between the plastic neutral axis and the most compressed fibre of the concrete.

Referring to Figure 5.4, the axial force of the concrete can be calculated as:

$$N_c = b_{eff} \times h_c \times 0.85f_{ck} = \frac{1250 \times 150 \times 0.85 \times 43}{1000} = 6853\ kN \quad (5.3)$$

The axial force of the steel beam can be calculated using Eq.(5.4):

$$N_s = f_y \times A_S = \frac{355 \times 11400}{1000} = 4047\ kN \quad (5.4)$$

where A_S is the nominal area of the steel section.

Because $N_s < N_c$, the neutral axis (N.A.) is located inside the concrete and the steel strength is governing the design; therefore $N_c = N_s$ = 4047 kN. The tensile force in the steel element acts at the mid-depth of the steel element. The compressive force in the concrete element, which in this case equals the tensile force of the steel, acts over an area of concrete of depth C, as shown in Figure 5.4. To sustain equilibrium, the whole steel element must yield in tension, the concrete above the N.A. must fully yield in compression and the concrete below the N.A. must be cracked under tensile stress. Therefore, the location of the N.A. of the cross-section can be calculated at a distance C from the top fibre of the concrete slab using Eq. (5.5):

$$b_{eff} \times C \times 0.85f_{ck} = f_y \times A_S \rightarrow 1250 \times C \times 0.85 \times 43 = 355 \times 11400 \rightarrow$$
$$\rightarrow C = 88.58mm \quad (5.5)$$

The plastic resistance moment of the composite section with full shear connection can be calculated using Eq.(5.6):

$$M_{pl} = f_y \times A_S \times \left(\frac{h_s}{2} + h_c - \frac{C}{2}\right) = \left[4047 \times 1000 \times \left(\frac{463.4}{2} + 150 - \frac{88.58}{2}\right)\right] /1000$$
$$\rightarrow M_{pl} = 1365\ kNm \quad (5.6)$$

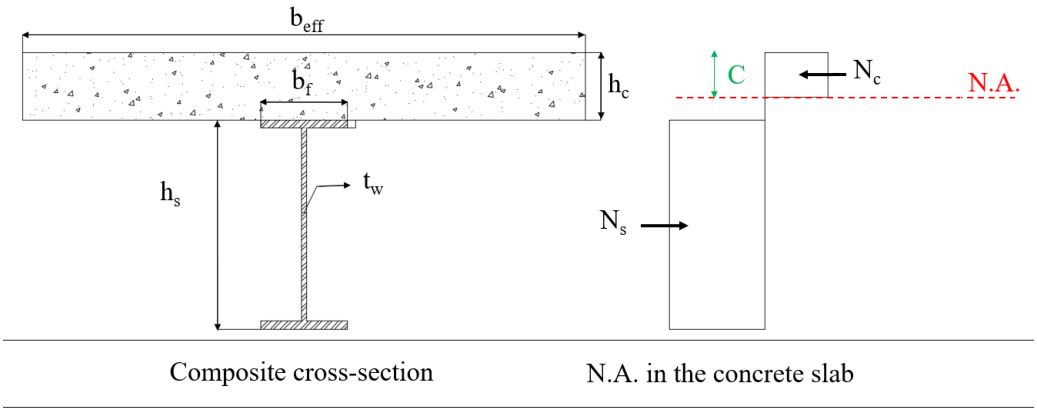

Figure 5.4: Full shear connection analysis.

In order to achieve this moment capacity, the strength of the FBSCs in each shear span of the beam (i.e. the distance between the end of the beam (point of zero moment) to the maximum bending moment) must be greater than or equal to the governing force in the composite section, which in this case is steel force (i.e. 4047 kN). The ultimate shear resistance of the FBSC was experimentally and numerically defined to be around 200 kN [32] for M16, Glade 8.8 bolts. Therefore, theoretically the total number of connectors required in each span to achieve the plastic resistance moment of the composite section is 4047/200 ≈ 20. The composite beam tested by Suwaed and Karavasilis [30] was equipped with 30 FBSCs through the whole length of the beam (15 pairs at 600 mm spacing), which means that it was designed with 50% less shear connectors that are required according to the design to achieve the plastic moment resistance.

5.4 Geometry and mesh

The FE model consisted of all connection components used in the beam test to accurately predict its flexural behaviour: steel beam, precast concrete plugs and slabs, high-strength bolts, plate washers, grout and steel reinforcement. Due to the symmetry of the beam specimen along its length, only half of the beam was modelled. The dimensions of the FE beam model were the same as the dimensions of the experimental beam specimen and they are clearly explained in paragraph 7.2. The geometry of the FE beam model is shown in Figure 5.5. High-strength bolts, hexagonal nuts and washers were modelled as one part, while grout was modelled as three different parts to avoid convergence difficulties due to complicated contact interactions. The retaining washers were not modelled since they are mainly used for construction purposes; hold the bolts into position during the fabrication of the specimens.

The reinforcement details of the concrete slab are shown in Figure 5.6. The bottom mesh consists of Ø12 longitudinal rebars at 250mm spacing, except from boundary bars where the spacing is reduced to 225mm. The transverse reinforcement consists of Ø10mm at 200mm spacing, except from

boundary bars where the spacing is reduced to 175mm. The upper mesh of reinforcement is the same as the bottom mesh, but it consists of Ø10mm instead of Ø12mm longitudinal bars.

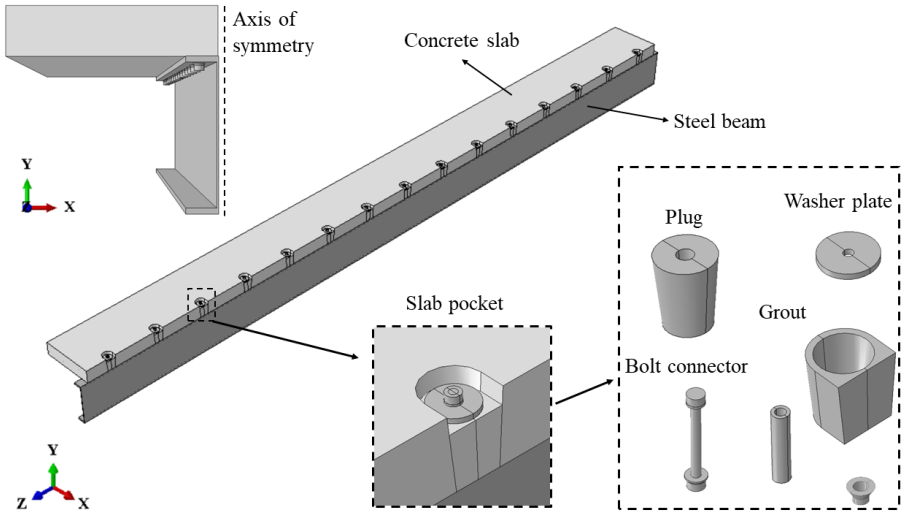

Figure 5.5: Geometry of the FBSC beam specimens.

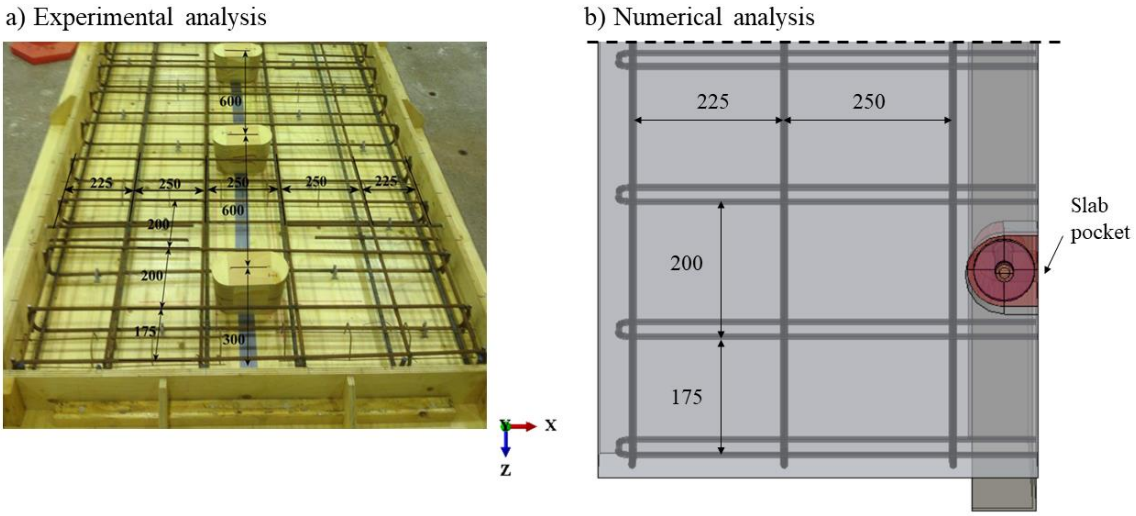

Figure 5.6: Reinforcement details of the FBSC beat tests.

Three-dimensional eight node linear hexahedral solid elements with reduced integration and hourglass control (C3D8R) were used to model the precast concrete parts of the FBSC, the grout, the steel beam and the high-strength bolts. According to ABAQUS manual, elements with reduced integration reduce the computational time and improve the convergence rate of the model. Two node linear three-dimensional truss elements (T3D2) were used to model the steel reinforcement. To reduce the computational time, a coarse mesh was adopted for the overall push-out specimen, with a fine mesh being used for the region around the shear connector to improve the accuracy of the model. The mesh sizes for each part of the steel-concrete composite beam is summarized in Table 3.2.

5.5 Interactions and boundary conditions

The interactions between the various components of the beam models were simulated using the surface-to-surface contact interaction. The normal and tangential behaviour between the contact surfaces was defined using the "Hard" and "Penalty" options respectively. The "Master" and "Slave" surfaces of these interactions were appropriately defined by taking the mesh density and the material strength of each component into consideration. A friction coefficient equal to 0.25 was used for the contact interaction between the steel beam and high-strength bolts. For steel-concrete interfaces, a friction coefficient equal to 0.45 was adopted. Finally, the embedded constraint option was applied to the reinforcement bars and concrete slab, in order to constrain the translational DOF of the nodes on the rebar elements to the interpolated values of the corresponding DOF of the concrete elements.

The degrees of freedom of the actual supports were taken into consideration in order to define the boundary conditions of the FE beam models. The boundary conditions adopted for the FE analysis are shown in Figure 5.7 and Figure 5.8. The beams are symmetric along their length and therefore "Sym_surface" was restrained from translating in the X direction and rotating in the Y and Z directions. For the hinged support, the corresponding nodes at the bottom of the beam were restrained from translating in the Y and Z directions, while the roller support was restrained from translating in the Y direction only. The load was applied on the model as an imposed displacement on the concrete slab selecting two 250mm wide loading strips across the width of the slab at a distance of 1500mm away from the centreline of the beam to match the experimental set-up. The 250mm wide loading strips are noted at Figure 5.8 as "Surface A" and "Surface B".

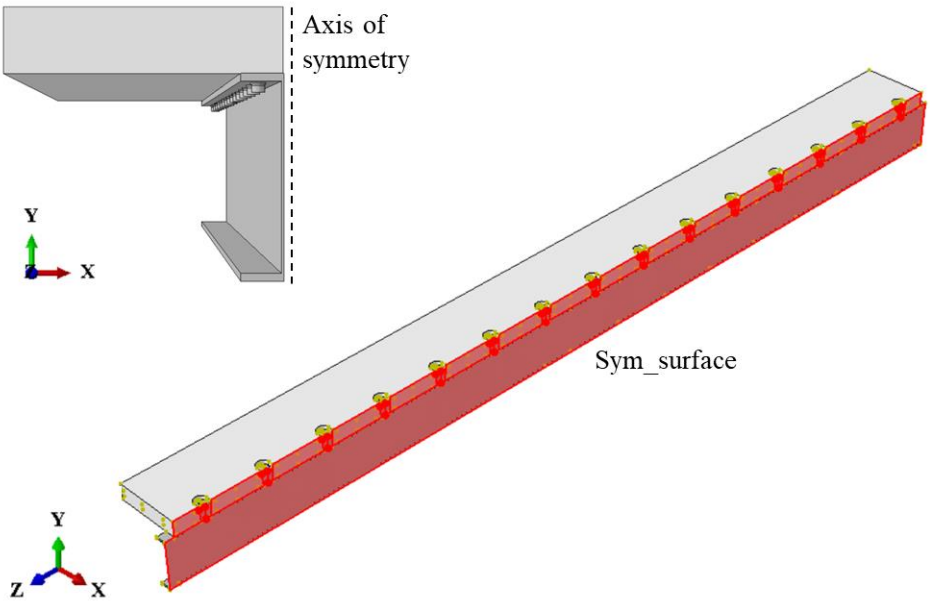

Figure 5.7: Boundary conditions and load application.

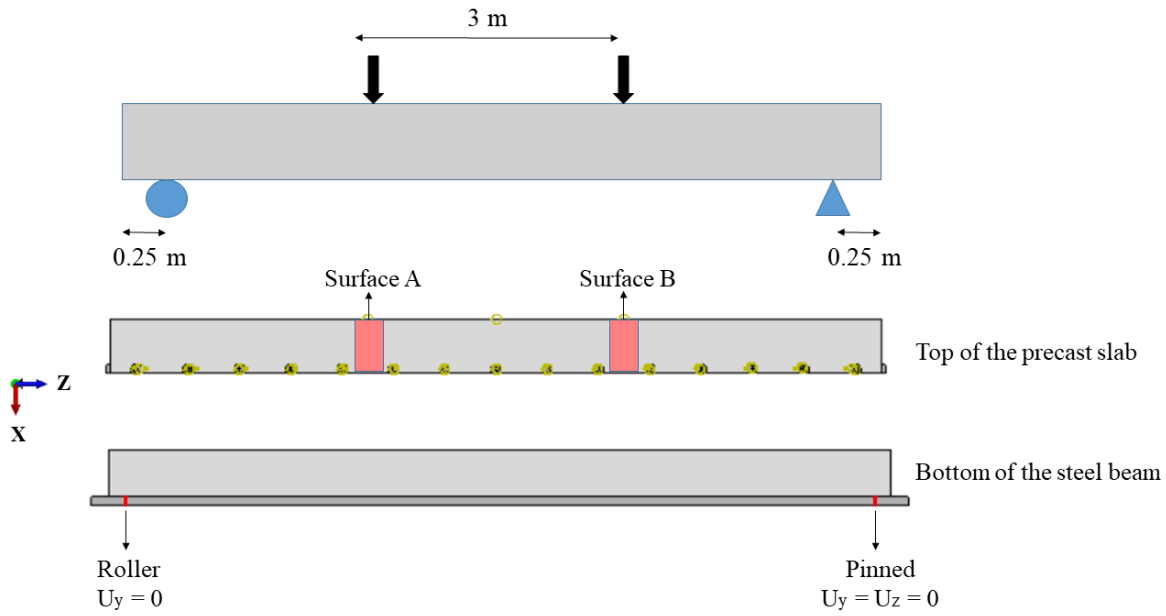

Figure 5.8: Boundary conditions and load application.

5.6 Material properties

5.6.1 Concrete

The material properties of the grout and concrete components of the beam tests are summarized in Table 5.1. The complex behaviour of grout and precast concrete components of the beam specimens was simulated using the Concrete Damage Plasticity (CDP) model. More details about the CDP model can be found in Cl. 3.7.2.

The compressive behaviour of grout and concrete components of the FBSC beam tests was described using the uniaxial stress-strain relationship proposed by Hsu & Hsu [45]. Eq. (3.20) is a modified form of the stress-strain equation proposed by Carreira and Chu [44]: parameter n is added to the original equation to accurately predict the compressive behaviour of high strength concrete. Parameter n is used to define the descending branch of the stress-strain curve and it varies according to the compressive strength of the concrete. The higher the compressive strength of the material, the higher the parameter n. For grout and slab with compressive strengths equal to 49 and 56 MPa respectively, parameter n is equal to 1. However, for precast concrete plugs, parameter n is equal to 3. The compressive behaviour of grout, slab and precast concrete plugs is illustrated in Figure 5.9. It is obvious that plugs are far more brittle than slab and grout due to their high compressive strength.

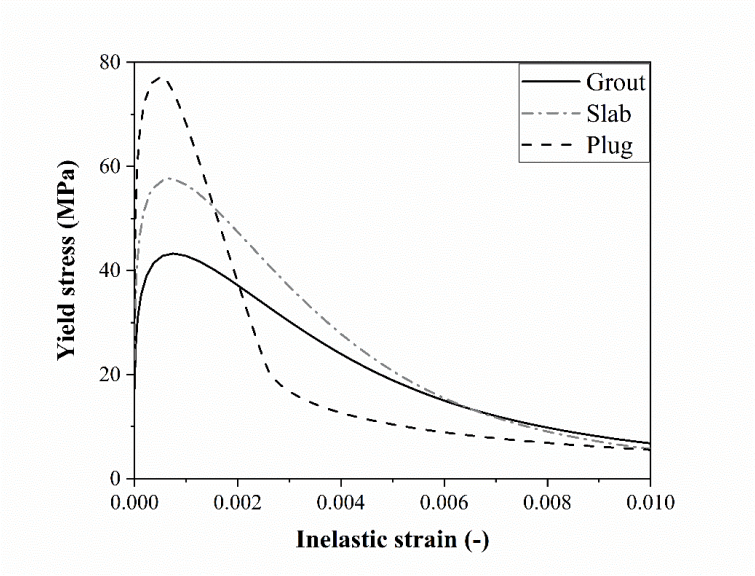

Figure 5.9: Compressive behaviour of grout and concrete components of the FBSC beam tests.

For concrete in tension, the tensile stress was assumed to increase linearly with respect to the strain until the concrete cracks (Figure 5.10). After the concrete cracks, Hillerborg's [49] fracture energy approach was used to minimize the mesh sensitivity of the results. Hillerborg defined the energy required to open a unit area of crack, G_f, as a material parameter, using fracture concepts. In the FBSC beam tests, the fracture energy, G_f, was specified as a material property in the model. More specifically, the post-failure stress was given as a tabular function of the cracking displacement which is defined in Eq. (3.31). The model assumes a linear loss of strength after cracking, as shown in Figure 5.10.

The CDP model considers two damage mechanisms for concrete: tensile cracking and compressive crushing. The degradation of the elastic stiffness is characterized by two damage parameters d_t and d_c, which are assumed to be functions of the inelastic strains. The damage variables can take values from zero, representing the undamaged material, to one, which represented total loss of strength. The uniaxial compression damage variable d_c, was defined as a tabular function of inelastic (crushing) strain as shown in Figure 5.10. The uniaxial tension damage variable d_t, was defined as a tabular function of cracking displacement as shown in Figure 5.11.

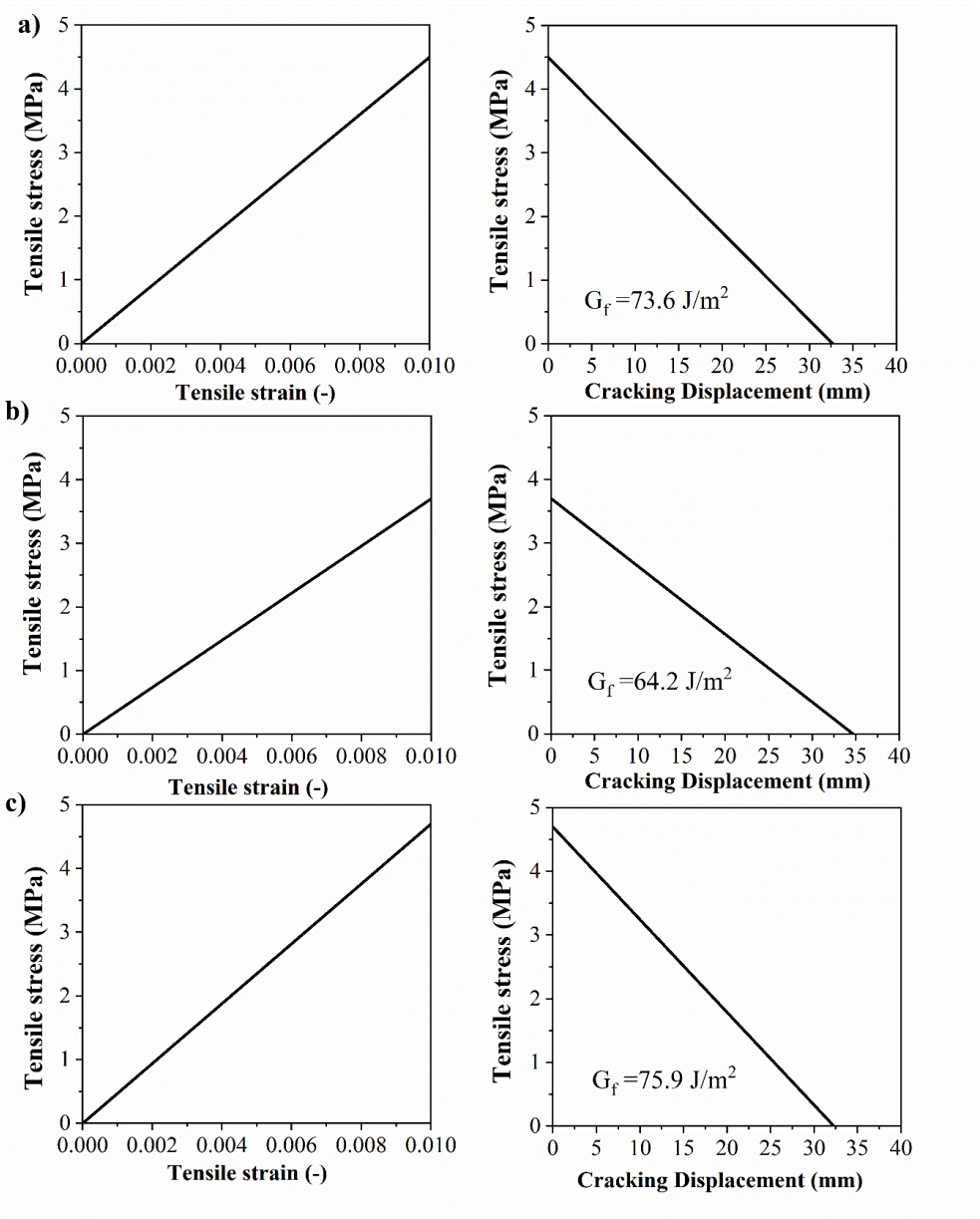

Figure 5.10: Tensile behaviour of grout and concrete parts of the FBSC beam tests for a) slab panels b) slab mid-span gap and c) plugs.

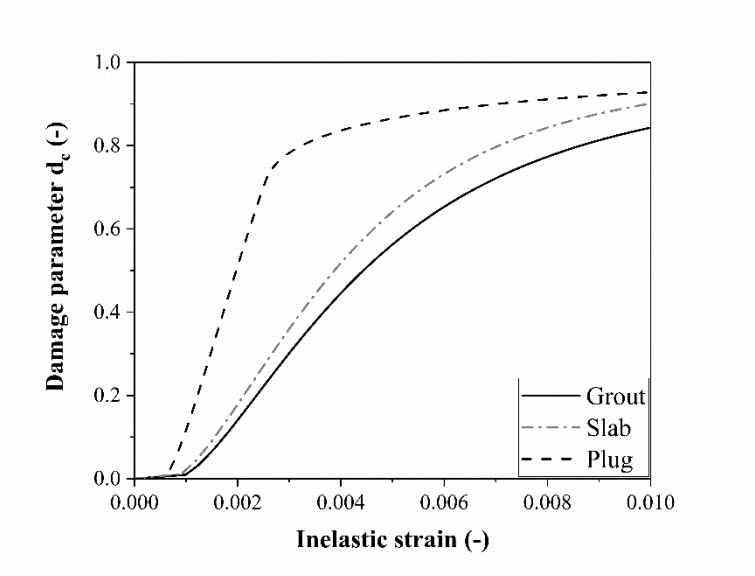

Figure 5.11: Grout and concrete materials degradation due to compression.

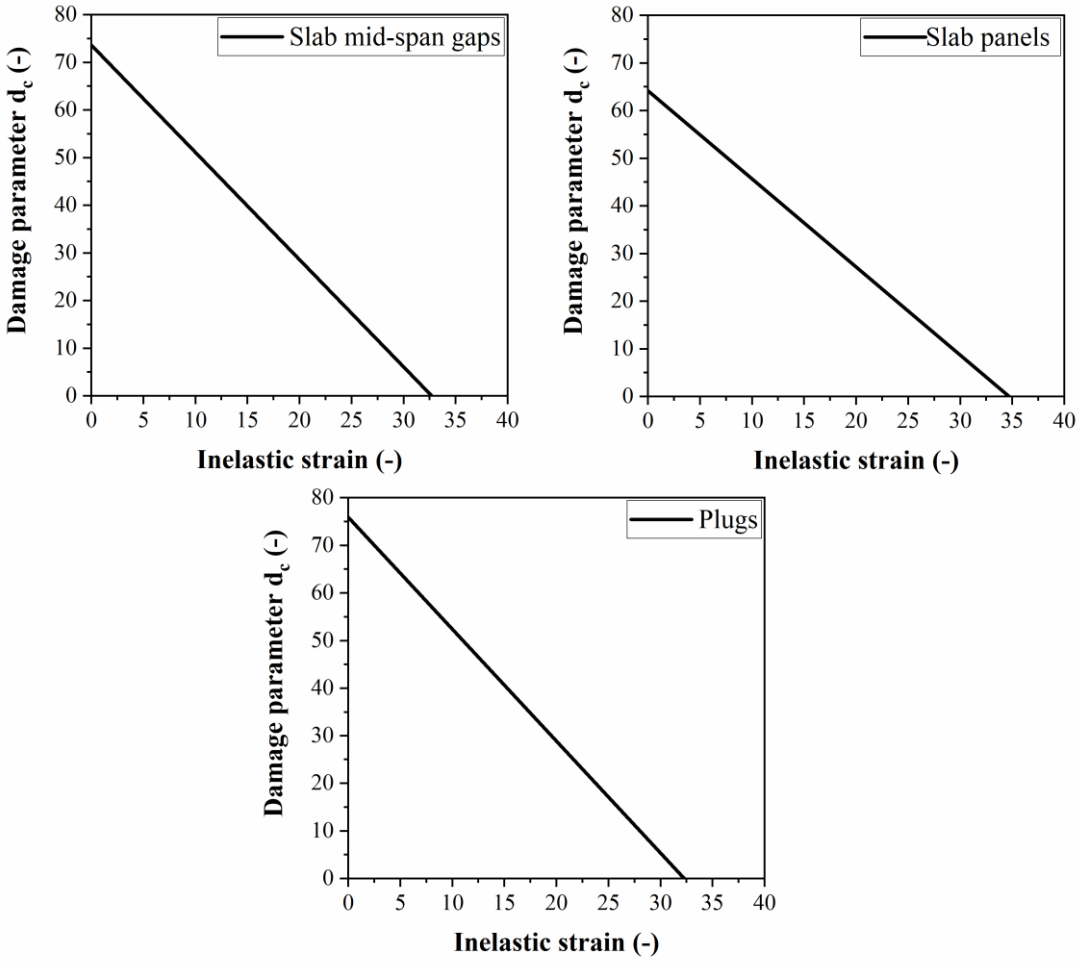

Figure 5.12: Grout and concrete materials degradation due to tension.

The concrete plasticity is described in CDP by the following key parameters:

- The ratio of the compressive strength under biaxial loading to uniaxial compressive strength (f_{b0}/f_c').
- Dilation angle.
- Flow potential eccentricity.
- Viscosity parameter.
- The ratio of the second stress invariant on the tensile meridian to that on the compressive meridian (K_c).

Eq. (3.29), proposed by Papanikolaou and Kappos, was used to define the ratio of the compressive strength under biaxial loading to uniaxial compressive strength (f_{b0}/f_c'). Dilation angle values were iteratively calibrated to match push-out tests results. The default value of e = 0.1 was adopted for the flow potential eccentricity, according to ABAQUS user manual recommendations. The default value was also adopted for the viscosity parameter, which was considered to be equal to 1. The ratio of the second stress invariant on the tensile meridian to that on the compressive meridian (K_c) was defined using Eq. (3.30).

5.6.2 Steel

The material properties of the steel beam were defined using the experimental data obtain by Suwaed and Karavasilis [36]. Three steel coupons were taken from the beam flange where severe yielding is expected to take place and tested according to BS EN ISO 6892-1 [59]. A typical stress-strain relationship from one coupon test is shown in Figure 5.13. The average values of the material properties of the steel beam are summarized in Table 5.2.

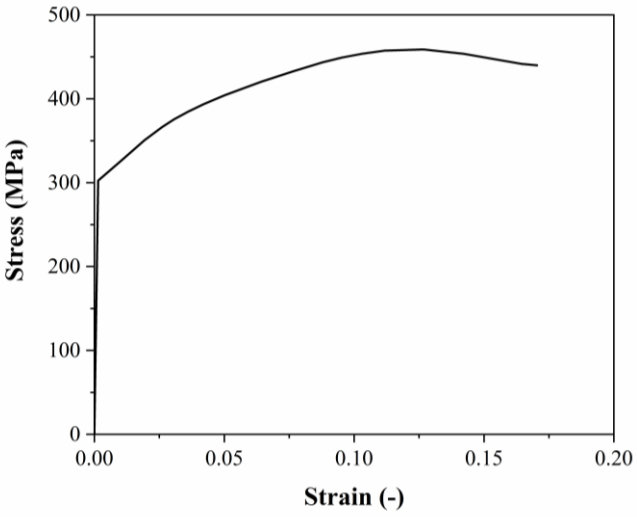

Figure 5.13: Coupon tensile tests of the steel beam [36].

Table 5.2: Average values of the material properties of the steel beam.

Tensile strength (MPa), f_u	457
Yield strength (MPa), f_y	355
Modulus of elasticity, E_s	210.1
Yield strain, ε_y	0.001625
Strain at maximum stress, ε_u	0.12
Strain at fracture, ε_f	0.17

A simpler elastic-perfectly plastic model, without strain hardening and yield strength equal to 500 MPa was employed in the analysis to model the behaviour of steel reinforcement.

The material properties of high-strength bolts are the same as in LNSC and FBSC push-out tests and they are clearly described in Cl.3.7.1. The plastic behaviour of the bolts was described using a true stress – true strain relationship as shown in Figure 3.15. Progressive damage models were included in the analysis to predict a possible ductile fracture of the bolts due to nucleation, growth and coalescence of voids. A damage initiation criterion was established to predict the onset of damage which assumes that the equivalent plastic strain at the onset of damage is a function of stress triaxiality. Subsequently, a damage evolution law was established to describe the rate of degradation of the material stiffness once the corresponding initiation criterion has been reached. Both damage initiation criterion and damage evolution law adopted in the analysis are illustrated in Figure 3.19 and Figure 3.20 respectively.

5.7 Analysis procedure

The dynamic explicit analysis method available in ABAQUS software was employed for the analysis. The dynamic explicit analysis method can be applied for quasi-static analysis and is exceptionally efficient for solving discontinuous and contact problems, for which implicit formulation might encounter convergence issues. To reduce the computational processing time and effort, the mass of the model was artificially increased. This was achieved by using the mass scaling option, which requires the specification of a minimum stable time increment to be used in the analysis. The appropriate minimum time increment was determined to be 10^{-6}s. To ensure that the quasi-static conditions are maintained, both kinetic and internal energy were monitored throughout the analysis; the kinetic energy was less than 5% of the internal energy.

The analysis progress was divided into two steps. For the first step, the post-tensioning forces were applied to the bolts by using the predefined temperature field option. The desired temperature value was calibrated to ensure a good agreement between the required bolt load, which according to Suwaed and Karavasilis [36] was 88-106 kN.

5.8 Validation of the FE model

The load versus mid-span deflection behaviour of the beam model is illustrated in Figure 5.14. The figure shows that the FE model was capable to predict the behaviour of the beam accurately. In addition, the FE analysis allowed the prediction of the ultimate moment and deflection of the specimen since the FE beam specimen was loaded until fracture. On the contrary, the experimental specimen was loaded up to a vertical deflection of 275 mm due to experimental limitations. Therefore, the ultimate moment and deflection of the beam specimen were unknown.

According to Dallam and Harpster [15], a common technical problem in full-scale beam tests with large spans (e.g. 8.5 m) is that due to large vertical displacement (e.g. > 200 mm), the hydraulic jack is run out of stroke during the test. The same situation was described by Suwaed and Karavasilis [36]. during the experimental testing of the FBSC beam test. More specifically, the capacity of the 100t hydraulic jack is 175 mm. Therefore, the load was applied in six cycles as shown in Figure 5.14. The test was stopped after cycle 6 without a collapse failure, due to technical safety cautions. Therefore, the maximum load recorded was 939 kN associated with a mid-span deflection of 263 mm. It was stated that even though the load was stopped at a deflection of 263 mm, the beam continued to deflect until 275 mm due to creep. On the other hand, the FE model was able to predict the ultimate load, which was 961 kN, while the maximum deflection at the end of the test was 416 mm. The maximum load caused a maximum moment at the mid-span equal to 1321 kNm. The maximum moment was therefore only 3% less than the plastic resistance moment of the composite section, even though 50% less shear connectors than those needed to achieve composite connection according to Eurocode 4 where provided. This is mainly attributed to the high slip capacity that FBSCs can offer.

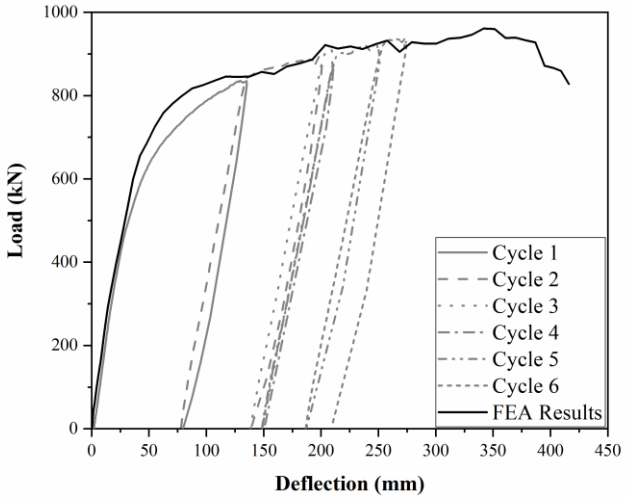

Figure 5.14: Load - deflection curve for FE model and experiment.

The transverse force and moment diagrams for the FBSC beam are shown in Figure 5.15. The maximum bending moment 1321 kNm is constant along the middle part between the two-point loads. The maximum shear force was calculated equal to 961/2=480.5 kN and is located for the aforementioned two-point loads to the ends of the composite beam, while the shear force at the middle part between the two-point loads is assumed to be zero.

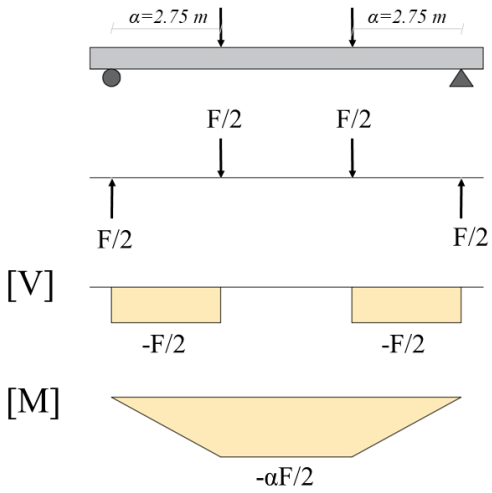

Figure 5.15: Transverse force and bending moment diagrams for beams under four-point bending test.

As shown in Figure 5.15, the maximum shear force and the maximum moment coexist at the same point of the span (i.e. under the point loads). According to Cl. 6.2.8 of BS EN 1993-1-1 [60], when shear force is present, allowance should be made for its effect on the moment resistance. However, where the shear force is less than half the plastic shear resistance, its effect on the moment resistance may be neglected. The shear resistance of the steel beam was calculated according to Cl. 6.2.6 of BS EN 1993-1-1 [60] using Eq. (5.14), where A_v is the shear area. After substitution into Eq. (5.14), the shear resistance was calculated equal to 997 KN, which is larger than Vmax. Therefore, the influence of the applied shear when combining with bending moment was ignored.

$$V_{pl,Rd} = A_v \frac{f_y}{\sqrt{3}} \tag{5.7}$$

Figure 5.16 shows the distribution of slips along the length of the composite beams at different levels of applied load. The x axis represents the distance from the mid-span, while the y-axis represents the corresponding slip measured at the steel-concrete interface. The results are compared with those presented by Suwaed et al [36]. It can be concluded that both experimental and numerical results follow the same pattern, with the numerical results to show higher slip values. This is attributed to the fact the ultimate moment obtained during the experimental and numerical results is different. Therefore, a direct comparison is not possible.

The results showed that up to 50% of maximum load, the slip at steel-concrete interface is relatively low; up to 1 mm. Even when the load has reached the 75% of its ultimate value, the slip is up to 3 mm. The maximum slip recorded at 100% of ultimate load was 15.4 mm at right edge of the beam.

In addition, almost constant maximum slip can be seen at the shear spans in all load levels, which sharply decreases to zero at mid-span. Indeed, the bolts connectors in the shear spans were severely deflected or even failed. This means that the contribution of the shear connectors in the areas of no shear and constant moment is limited.

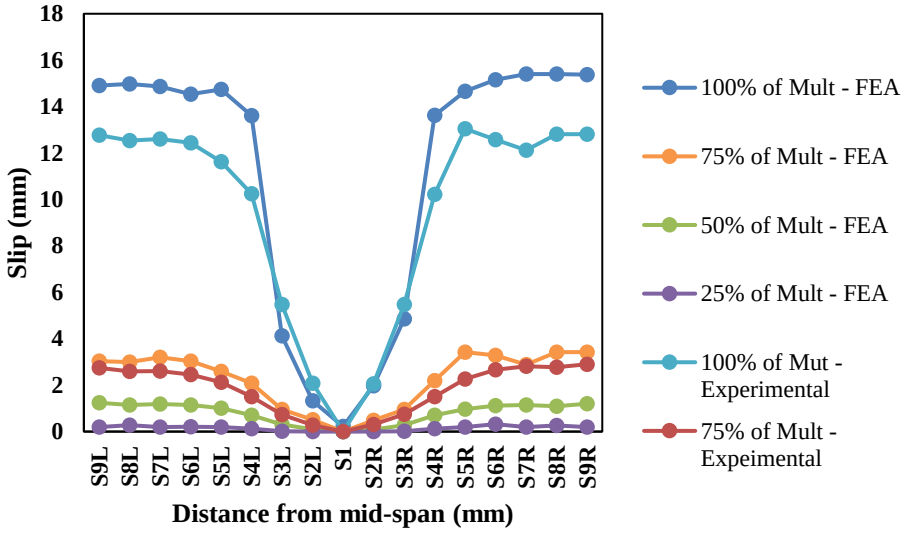

Figure 5.16: Distribution of slips along composite beam length.

Figure 5.17 Figure 5.18 and Figure 5.19 show the effect of slip on the beam deflection. The slip readings were taken from the left half of the composite beam as specified in Figure 5.17 and compared with the experimental data given by Suwaed et al [36]. The deflection was measured at the mid-span. The FE model was capable to predict the relationship between the deflection and slip that was recorded in the experiment, which consists of an initial frictional resistance followed by a linear response in all locations except S3, where a nonlinear behaviour is observed after 100mm.

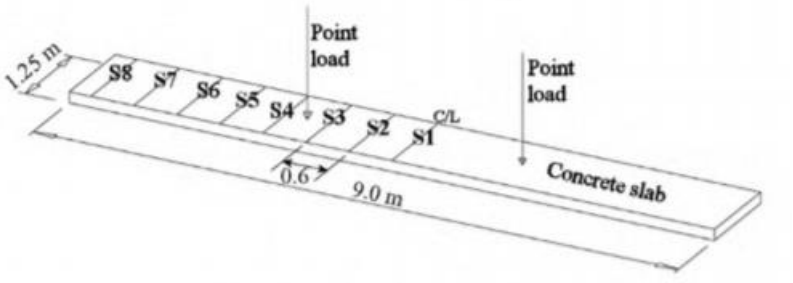

Figure 5.17: Location of load cells (Suwaed at al.) [36].

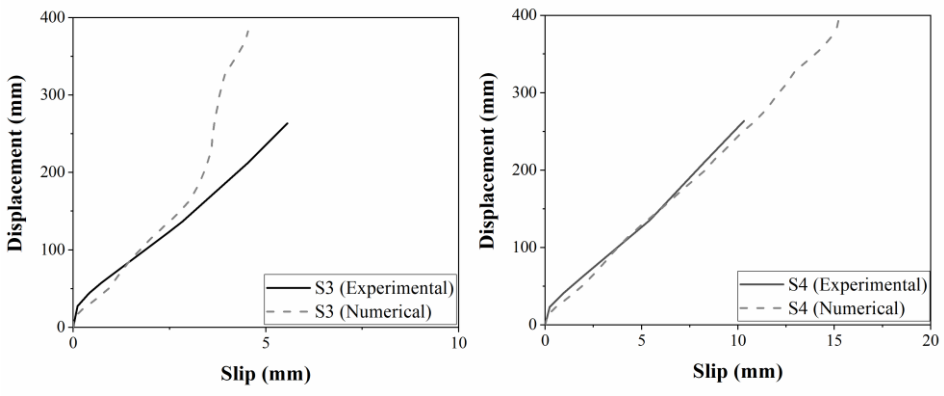

Figure 5.18: The effect of slip on deflection (S3-S4).

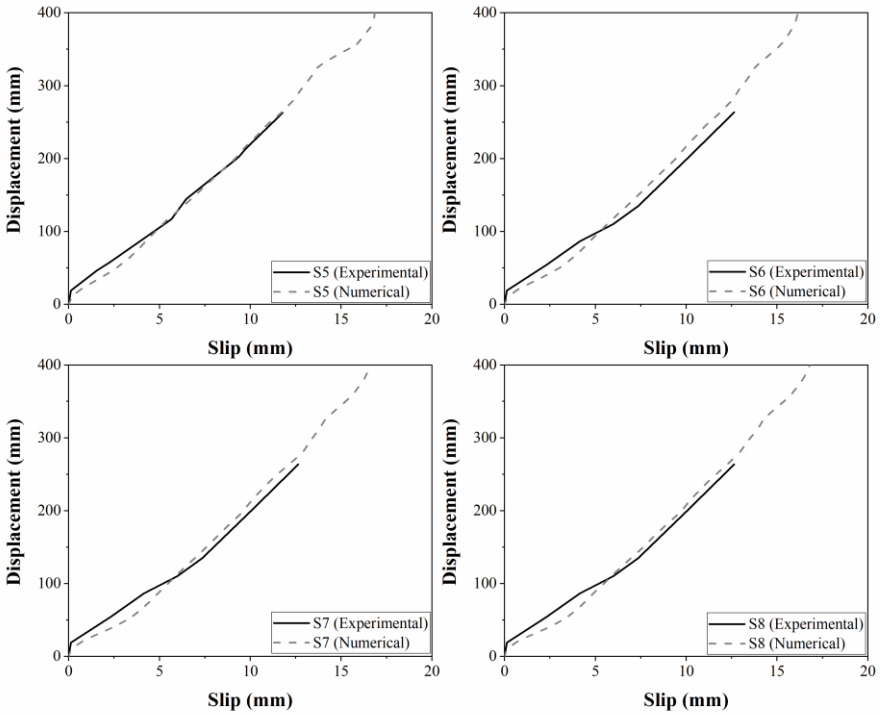

Figure 5.19: The effect of slip on deflection (S5-S8).

The deflected shape of the steel-concrete composite beam equipped with FBSCs is shown in Figure 5.20. The maximum deflection recorded was 416 mm.

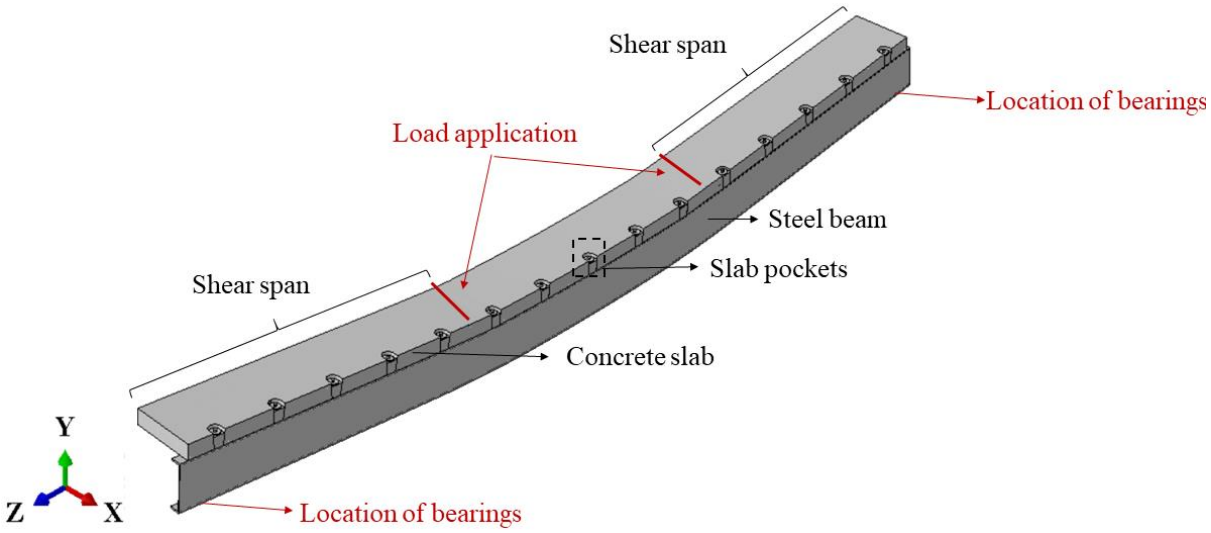

Figure 5.20: Deflection shape of the steel-concrete composite beam.

The failure modes of the specimens are discussed below. As described by Suwaed et al. [36], as the bottom face of the concrete slab is subjected to tensile strains, hairline cracks spread upwards. Figure 5.21 shows the hairline cracks observed at the end of the test. The cracks were evenly spaced and hardly extended further than the mid-thickness of the slab. Similarly, in the FE analysis, concrete degradation due to tensile strains was observed on the side of the beam, started from the bottom, and going upwards. The material degradation was mainly observed in the midspan.

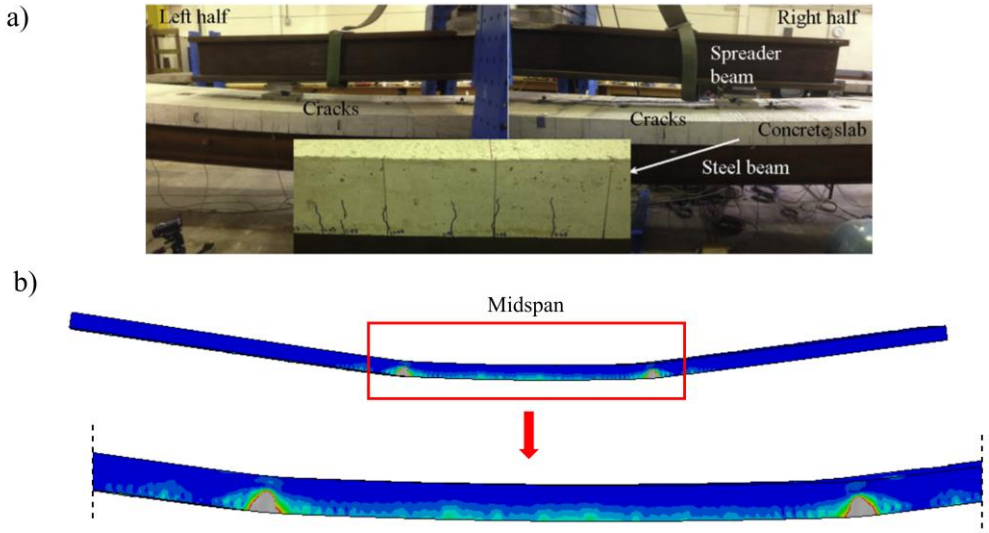

Figure 5.21: Side view of concrete slab cracks a) at the end of the experimental test - Suwaed et al. b) at the end of the FE analysis.

As shown in Figure 5.22, hairline cracks were also observed at the bottom of the slab, during the experimental test of the composite beam. The cracks were concentrated near FBSCs. A similar pattern was observed in the FE analysis of the beam, where concrete degradation was observed at the bottom of the slab, near the FBSCs.

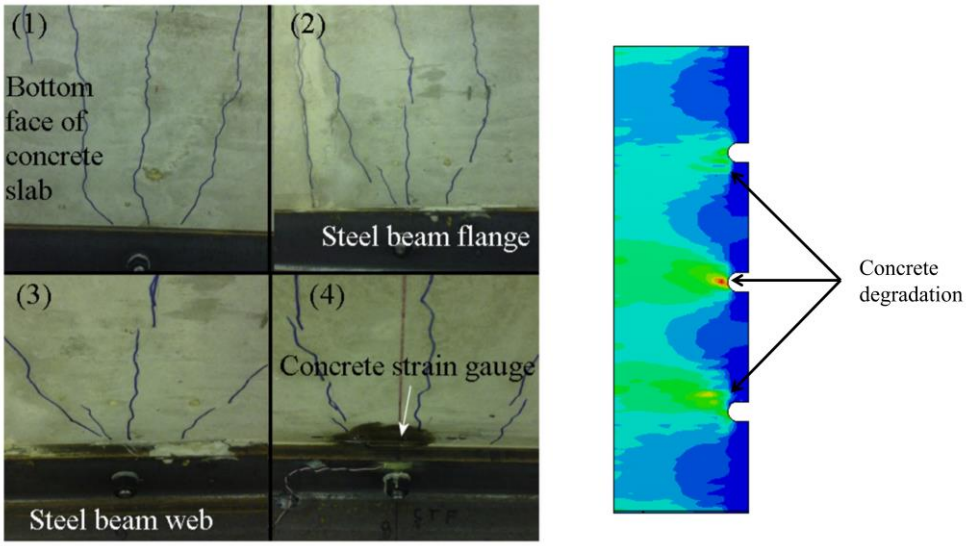

Figure 5.22: Concrete cracks at the bottom of the slab.

Other failure modes observed during the analysis were the yielding of the steel beam, concrete crushing of the precast concrete slab and the failure of bolt connectors due to combined tensile and shear stresses. In Figure 5.23, the stress (principal stresses in the Z direction) contours at failure of the composite beam are plotted. A concentration of tensile stresses is observed at the mid-span of the beam. The average stress in this area is around 427 MPa, which means that the yield strength of the steel beam (355 MPa) has been reached and exceeded. In the same figure, the compressive failure of the steel beam around the bolt holes is also plotted. The average compressive stress is approximately 504 MPa which means that the tensile strength of the steel beam (490 MPa) has been exceeded and the steel beam is completely degraded and cannot resist any loads in this area.

As shown in Figure 5.24, extensive concrete crushing was observed at the bottom of the precast concrete slab, in the area around the slab pockets. Figure 5.25 shows the concrete crushing observed at the top of the concrete slab in the area where the loads were applied. Material degradation due to concentration of tensile stresses was also observed at the bottom of the slab as shown in Figure 5.26 at the location of the loads.

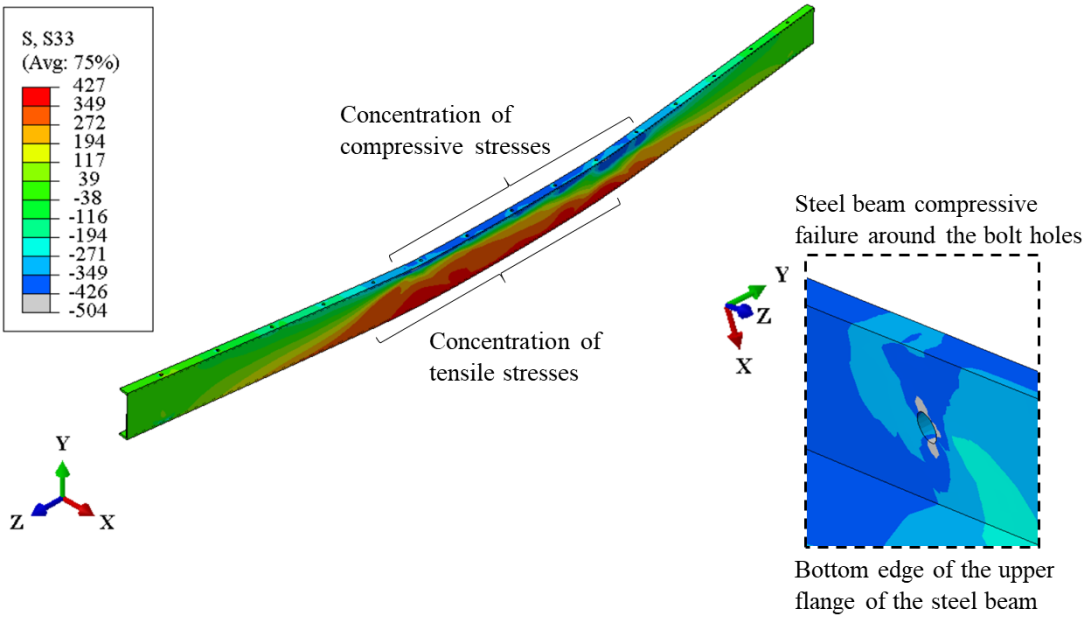

Figure 5.23: Yield of the steel beam.

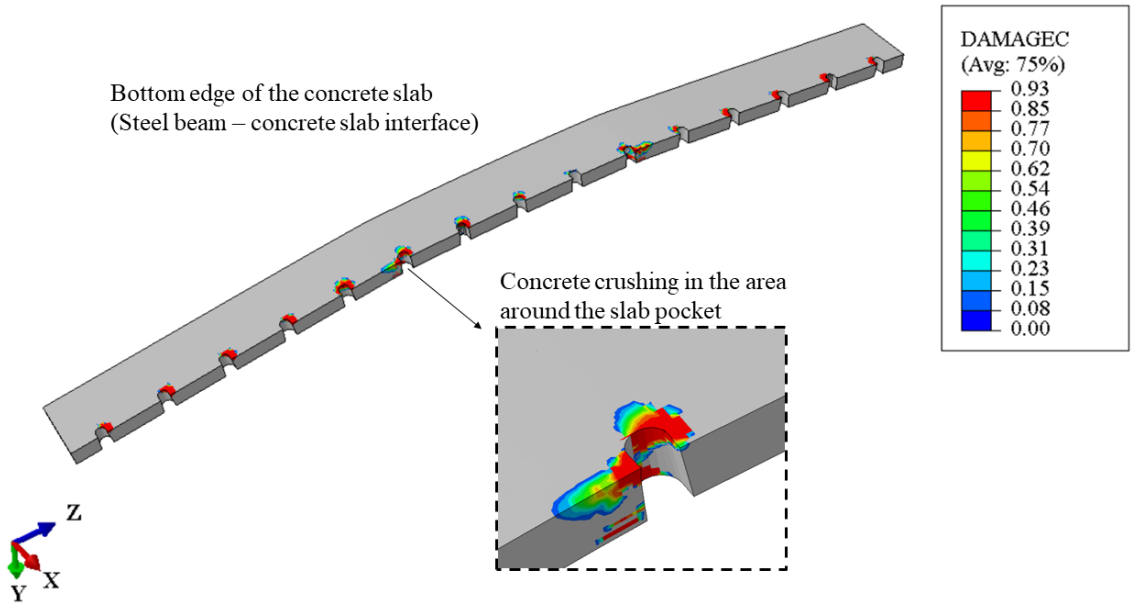

Figure 5.24: Concrete crushing at the bottom of the precast slab.

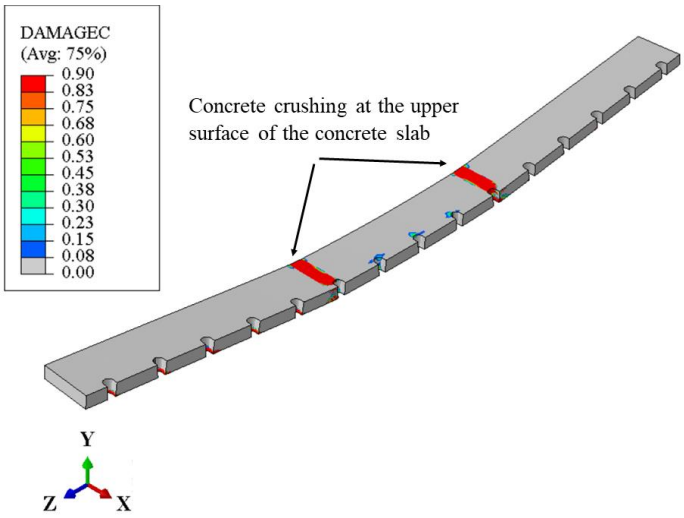

Figure 5.25: Concrete crushing at the top of the precast slab.

Several bolts failed during the numerical analysis. In general, this is a desirable failure mode, since the beam was design with partial shear connection to test the capacity of the connectors. In practice, the replacement of the bolt connectors is a procedure that does not require expensive equipment and special-trained labour. In addition, their replacement can be done relatively quick, which means that there is not a major disruption in transport networks. As shown in Figure 5.27, the deflection of the bolts at the mid-span of the beam was relatively small. On the contrary, the bolts at the shear spans were severely degraded or even fractured due to combined shear, tensile and bending stresses. Therefore, it can be concluded that the shear connectors can be used only in the shear span. However, for safety reasons, it is recommended to distribute the shear connectors along the whole length of the beam, even if the connectors at the mid-span don't contribute to the capacity of the beam.

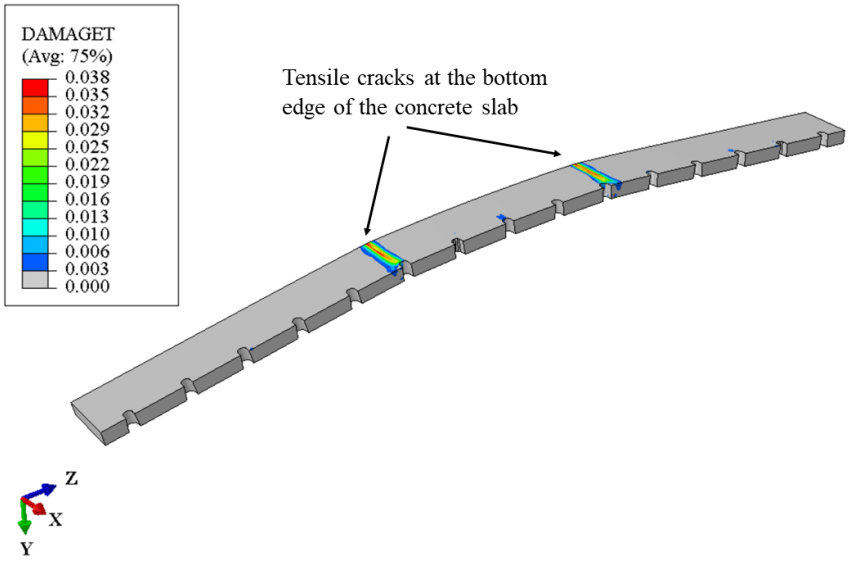

Figure 5.26: Tensile damage of the concrete slab.

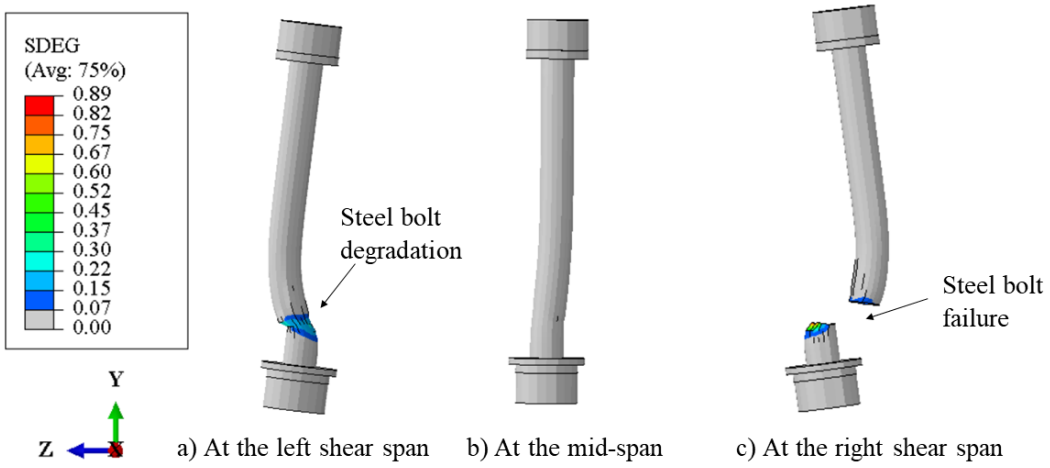

Figure 5.27: Bolt deflected shapes.

5.9 Parametric study

The chapter presents the effect of several parameters on the structural behaviour of a full-scale 9 m long steel-concrete composite beam with FBSCs. The compressive strength of the precast concrete slab, the tensile strength of bolt connectors and the yield strength of the steel beam are the key parameters that are considered in this study. The details of the tested beam specimens are given in Table 5.3.

Table 5.3: Details of the beam specimens for the parametric study.

Parameter	Specimen	Bolt tensile strength [MPa]	Beams tensile strength [MPa]	Compressive strength of slabs [MPa]	Shear connection ratio [-]
Bolt tensile strength	BT_T1	**800**	355	50	0.36
	BT_T2	**865**	355	50	0.36
	BT_T3	**950**	355	50	0.36
Yield strength of steel beams	BT_SB1	950	**235**	50	0.36
	BT_SB2	950	**275**	50	0.36
	BT_SB3	950	**355**	50	0.36
	BT_SB4	950	**450**	50	0.36
Compressive strength of slabs	BT_S1	950	355	**50**	0.36
	BT_S2	950	355	**60**	0.36
	BT_S3	950	355	**70**	0.36

5.9.1 Effect of bolts tensile strength

Previous numerical analyses on FBSC push out tests presented in Chapter 4 showed that the tensile strength of bolts is among the most significant parameters that affect the shear resistance of the connection. Therefore, in this paragraph, the effect of the tensile strength of bolt connectors on the structural behaviour of FBSC composite beams is discussed. The bolts tensile strength varies from 800 MPa to 950 MPa. Bolts with higher tensile strength were not considered in this parametric study,

since the numerical results presented in Clause 6.3 showed that the push-out specimens with high strength bolts with tensile strength higher than 950 MPa, failed by tensile cracking of the concrete slab instead of shear failure of the bolts. Tensile cracking of concrete slab prior to shear failure of the bolt connectors is an undesirable behaviour, due to its brittle nature.

Figure 5.28 shows the moment-deflection behaviour of steel-concrete composite beams specimens using bolts with different tensile strengths. It can be concluded that the tensile strength of bolt connectors does not have a significant influence of the moment capacity of the beams. The moment capacity achieved using bolts with 950 MPa (i.e. 1321 kNm) was only 2% and 5% higher than using bolts with 865 MPa (i.e. 1289 kNm) or 800 MPa (i.e. 1260 kNm) tensile strength respectively.

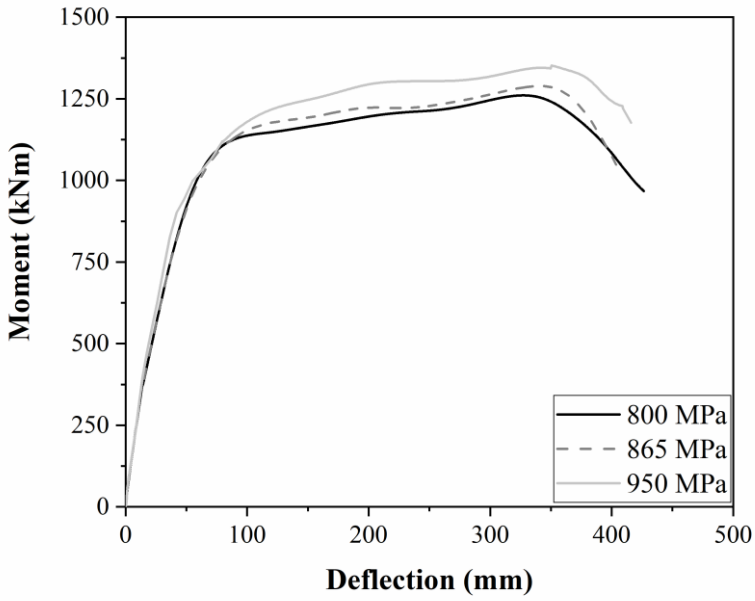

Figure 5.28: Moment-deflection behaviour of steel-concrete composite beams with FBSCs, using bolts with various tensile strengths.

The predicted moment capacities of the beam specimens are compared with the plastic resistance moment of the composite section in Table 5.4. It was concluded that the predicted moment capacities were less than 10% lower than the plastic resistance moment of the composite section with partial shear connection, even though less shear connectors than those required from Eurocode 4 were used.

Table 5.4. Effect of bolts tensile strength on the moment capacity of the FBSC beams.

Specimen	Bolts tensile strength	$M_{u,FE,i}$	$M_{pl,i}$	$M_{u,FE,i}/M_{pl,i}$
	(MPa)	(kN)	(kN)	(-)
BT_T1	800	1260	1365	0.93
BT_T2	865	1289	1365	0.95
BT_T3	950	1321	1365	0.97

5.9.2 Effect of beams yield strength

Steel beams with various steel grades were used in this parametric study to evaluate the effect of their yield strength on the structural behaviour of steel-concrete composite beams with FBSC. The yield strength of the steel beams varied from 235 N/mm^2 to 450 N/mm^2, since according to BS EN 1994-2, Cl. 3.3(2) [7], steel beams with nominal yield higher than 460 N/mm^2 cannot be used in composite bridges.

The yield strength f_y and the ultimate strength f_u of the steel beams were defined according to BS EN 1993-1-1, Table 3.1 [60] for structural elements with nominal thickness less than 40 mm and the obtained values are summarized in Table 5.5. The modulus of elasticity of the steel beams was considered equal to 210 GPa and Poisson's ratio was taken equal to 0.3, according to BS EN 1993-1-1, Cl. 3.2.6 [60]. A bilinear plus non-linear hardening model proposed by Yun et al. [40], described in clause 3.7.1, was used to describe the tensile stress-strain behaviour of the steel beams.

Table 5.5. Nominal values of yield strength f_y and ultimate tensile strength f_u for the steel beams in N/mm^2.

Description	Symbol	S235	S275	S355	S450
Yield strength	f_y	235	275	355	450
Tensile strength	f_u	360	430	490	550

As shown in Table 5.6, the yield strength of the steel beams has a very significant effect on the ultimate load carrying capacity of steel-concrete composite beams with FBSCs. More specifically, the ultimate load carrying capacity of the composite beams was increased by almost 43%, when the yield strength of the steel beam was increased from 235 N/mm^2 to 450 N/mm^2.

Table 5.6. Ultimate load carrying capacity of steel-concrete composite beams with FBSCs, using steel beams with various yield strengths.

Specimen	Steel grade	$F_{u,FE,i}$	$F_{u,FE,i}$/ $F_{u,FE,1}$
	(-)	(kN)	(%)
BT_SB1	S235	729	-
BT_SB2	S275	817	1.12
BT_SB3	S355	983	1.35
BT_SB4	S450	1049	1.44

Figure 5.29 shows the behaviour of the steel-concrete composite beams equipped with FBSCs is initially linear, followed by a non-linear response with severe stiffness reduction. In general, the specimens with high-strength steel beams offered higher load-carrying capacity. The maximum deflection of the specimens recorded at the end of the analysis was on average 360 mm (i.e. L/25). However, specimen BT_SB4, where S450 steel beam was used, showed very limited deflection capacity. The steel beam started to yield at 182.3 mm mid-span deflection (i.e. L/50). After this point, the load-carrying capacity of the composite beam started to drop, and concrete crushing occurred at the mid-point of the concrete slab. This behaviour can be explained by the fact that the ultimate tensile strain of S450 steel is relatively small (i.e. 12‰). The failure modes of the parametric

specimens were similar to those observed in the validation model and they are described in detail in clause 8.2.2 of this thesis. Failure of the bolt connectors occurred first, followed by yielding of the steel beam and concrete crushing and cracking of the concrete slab.

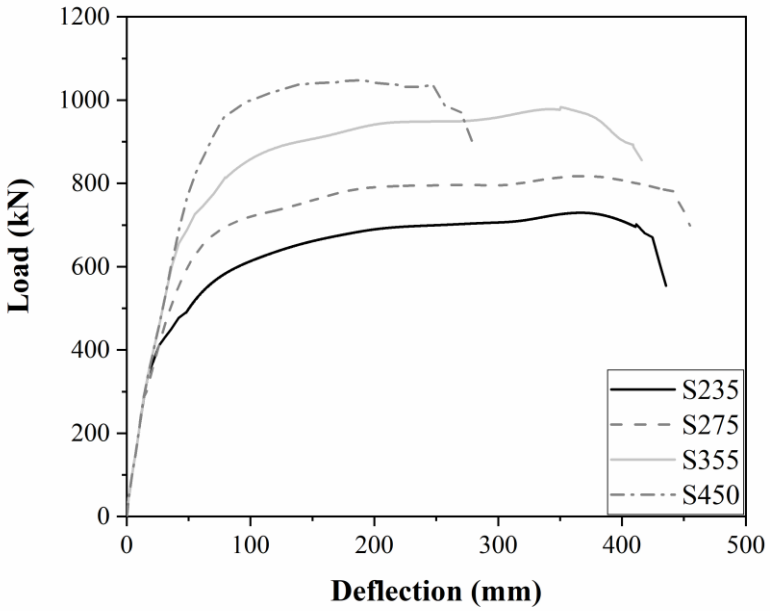

Figure 5.29: Load-deflection curves for various yield strengths of steel beams.

The moment-deflection behaviour of the beam specimens is shown in **Error! Reference source not found.**. The results from the FE analysis were compared with the plastic resistance moment of the composite section, calculated based on the recommendations of BS EN 1994-2. It was revealed that the steel-concrete composite beams with S235 and S275 steel beams were able to achieve the plastic resistance moment and even to exceed it. On the contrary, for specimens S355 and S450 more shear connectors are needed to achieve moment capacity equal to the plastic resistance moment of the composite section.

Table 5.7. Effct of steel beams yield strength on the moment capacity of the FBSC beams.

Specimen	Steel grade	$M_{u,FE,i}$	$M_{pl,,i}$	$M_{u,FE,i}/M_{pl,,i}$
	(-)	(kN)	(kN)	(%)
BT_SB1	S235	1003	944	1.07
BT_SB2	S275	1124	1089	1.04
BT_SB3	S355	1321	1365	0.97
BT_SB4	S450	1442	1670	0.88

5.9.3 Effect of slab compressive strength

The standard concrete strength values considered in this analysis are listed in Table 5.8. The compressive strength of slabs varies from 50 MPa to 70 MPa to comply with the European standards (Eurocodes) for bridges. According to NA to BS EN 1992-2 [61], the concrete classes that can be used in bridge construction range from C25/30 to C70/85. The characteristic cylinder compressive

strength, the elastic modulus, the compressive strain at the peak stress and the mean tensile strength of concrete were defined according to BS EN 1992-1-1 [6] and summarized in Table 5.8.

Table 5.8. Material properties of precast concrete slabs used in the parametric analysis.

Specimen	Concrete class	f_{ck}	E_{cm}	ε_{c1}	f_{ctm}
	(-)	(MPa)	(GPa)	(‰)	(MPa)
C50	C50/60	50	37.3	2.5	4.1
C60	C60/75	60	39.1	2.6	4.4
C70	C70/85	70	40.7	2.7	4.6

The compressive behaviour of the precast concrete slabs was effectively modelled using the model proposed by Hsu & Hsu [45]. The compressive stress-strain curves for slabs with different compressive strengths are illustrated in Figure 5.30.

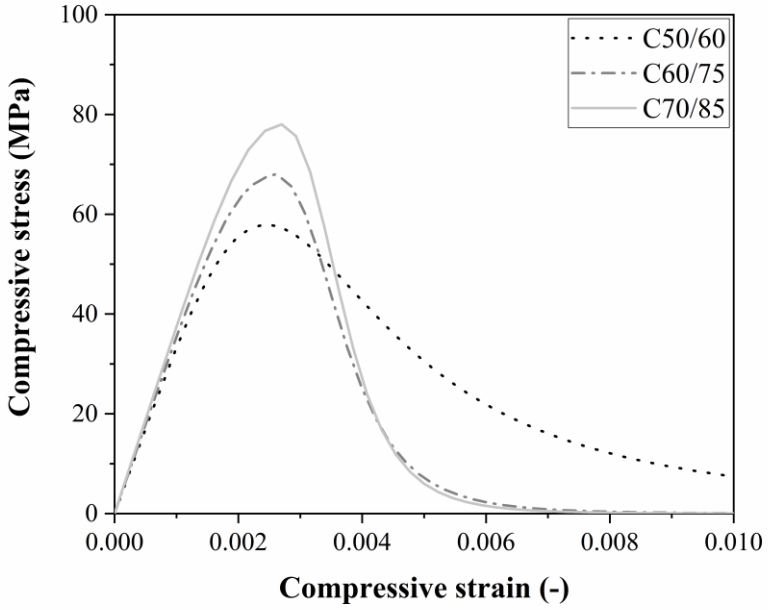

Figure 5.30: Compressive stress-strain curves for precast concrete slabs.

The numerical results of LNSC and FBSC push-out tests presented in previous chapter showed that extensive damage was observed in the area around the connectors. Therefore, the definition of the compressive stress-strain behaviour of slabs up to the nominal ultimate strain (ε_{cu}) according to BS EN 1992-1-1 [41], would overestimate the concrete crushing strength. More specifically, the nominal ultimate strain (ε_{cu}), according to BS EN 1992-1-1 [41], is 3.5‰ for concrete classes up to C50/60, 2.8‰ for concrete class C60/75 and 2.8‰ for concrete class C70/85. To consider the extensive crushing of concrete around the bolts, the curves were extended above these values up to an inelastic strain of 0.01, which was considered large enough so as not to be achieved in the numerical analysis. The tensile behaviour of concrete was assumed to be linear until the ultimate tensile strength of concrete was reached. After this point, Hillerborg's [49] fracture energy approach was adopted to minimize the mesh sensitivity of the results.

The concrete damage plasticity (CDP) model, which is a plasticity-based, damage model for concrete was employed to model the main two failure mechanisms of concrete; tensile cracking and compressive crushing. . The model uses scalar damage variables to account for progressive damage of concrete slabs due to compressive and tensile loads. Concrete in confinement condition is also depended on plasticity parameters that were also defined in the CDP model. Flow potential eccentricity was set equal to 1, as recommended by Abaqus manual. The dilation angle was defined equal to 36°. The ratio of the compressive strength under biaxial loading to uniaxial compressive strength (f_{b0}/f_c') was defined according to Eq. (3.29), while the ratio of the second stress invariant on the tensile meridian to that on the compressive meridian (K_c) was defined according to Eq. (3.30).

The effect of slab compressive strength on the moment capacity of the beam specimens is shown in Table 5.9. A very small increase in the moment capacity of the beams with higher concrete strengths is observed; the maximum strength increase was approximately 3%. It was concluded that the specimens were able to achieve a moment capacity less than 1% lower than the plastic moment resistance of the specimens, even thought they were designed with 50% less shear connectors than those required according to BS EN 1994-2.

Table 5.9. Effect of slab compressive strength on the moment capacity of the FBSC beams.

Specimen	Concrete class	$M_{u,FE,i}$	$M_{pl,f}$	$M_{u,FE,i}/M_{pl,f}$
	(-)	(kN)	(kN)	(%)
BT_S1	C50	1368	1391	0.99
BT_S2	C60	1387	1416	0.99
BT_S3	C70	1412	1435	0.99

In terms of failure modes, bolt failure due to combined shear and tensile stresses occurred in all specimens, followed by yielding of the steel beams and concrete crushing and cracking. However. As shown in Figure 5.31, the specimen BT_S3, the slab was extremely damaged; severe concrete crushing was observed around the slab pockets, as well as in the area where the loads were applied. In addition, severe tensile cracking was observed at the bottom of the slab.

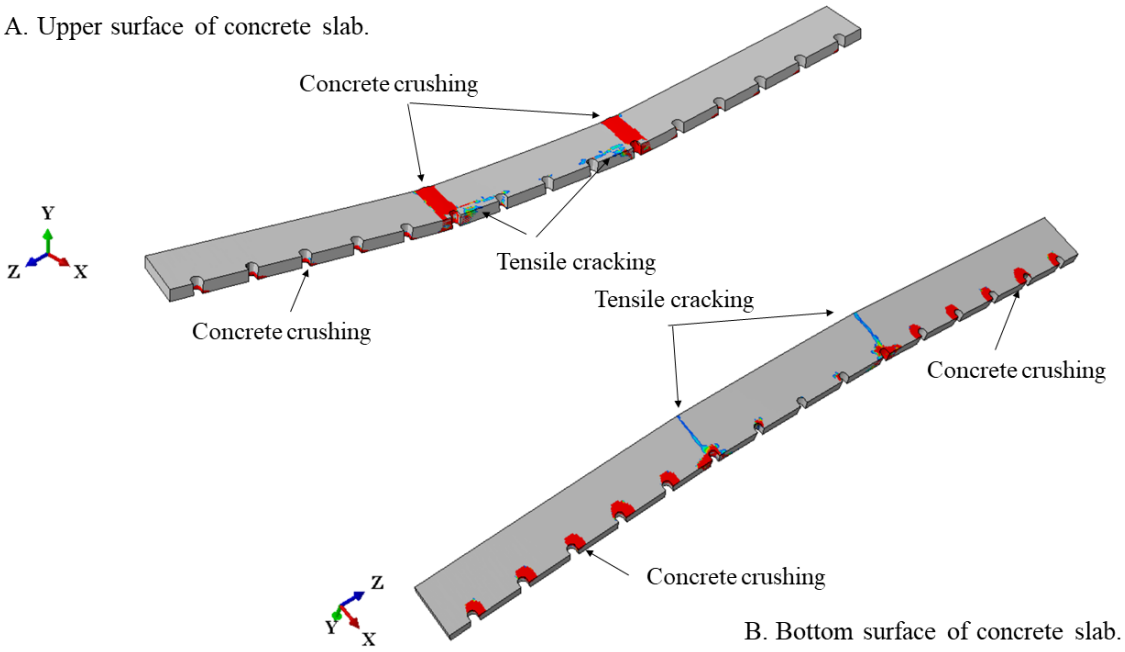

Figure 5.31: Concrete slab failure in specimen BT_S3.

5.10 Conclusions

A three-dimensional FE model was developed to investigate the behaviour of steel-concrete composite beams using FBSCs. The beam was designed with 50% less shear connectors than those required according to the design to achieve plastic moment resistance M_{pl} of the composite section. A total of 30 M16, Grade 8.8 bolt connectors were distributed in pairs of 0.6 m along the length of the beam. The FE model was validated using experimental results available in the literature [36] and it was concluded that it was able to predict the load-deflection response of the beam specimens with high accuracy.

The chapter also presents the results of a parametric study that was conducted to evaluate the effect of several parameters on the behaviour of steel-concrete composite beams equipped with FBSCs. The compressive strength of the precast concrete slab, the tensile strength of bolt connectors and the yield strength of the steel beam are the key parameters that were considered in this study. It was concluded that the tensile strength of bolt connectors did not have a significant influence of the moment capacity of the beams. More specifically, up to 5% increased moment capacity was recorded by increasing the tensile strength of the bolts from 800 MPa to 950 MPa. Similarly, increasing the compressive strength of the slabs from C50 to C70, increased the moment capacity of the composite beams only by 3%. On the contrary, the yield strength of the steel beam highly affected the moment capacity of the composite beams. Up to 44% increased moment capacity was observed when S450 instead of S235 steel beams were used.

Chapter 6 Summary and Conclusions

6.1 Summary

The structural behaviour of two novel demountable shear connectors, namely locking-nut shear connector (LNSC) and friction-based shear connector (FBSC) were investigated in this research project. The investigated shear connectors allow full disassembly of steel composite structures and therefore facilitate installing and dismantling of composite structures. The LNSC uses a conical nut that resembles in geometry the collar of welded headed studs and prevents local failure within the threaded part of the bolts to achieve higher shear resistance and ductility, while FBSC uses the friction resistance at steel beam – concrete interface to achieve higher shear resistance at serviceability limit state (SLS). Both connectors use high-strength bolts which are fastened to the top flange of the steel beam using either a locking nut (LNSC) or grouted countersunk hole configurations (FBSC) that prevent slip of bolts inside their holes. The bolts are surrounded by conical precast plugs with high compressive strength and dimensions that allow them to fit within the precast slab pockets. Rapid hardening grout is used to fill the gaps between the bolts, the precast concrete plugs and the precast slab pockets, while the tightening of the nut at the top of the connectors secures the plugs in place before the hardening of the grout.

The behaviour of the connectors was analysed by developing three-dimensional finite element (FE) models in ABAQUS software. The FE models were validated by using experimental results available in the literature review [31, 32, 36]. An extensive parametric analysis was conducted to expand the experimental data bank; 20 parametric models were built to identify the significant parameters that may affect the behaviour of LNSC, and 19 parametric models were built for the FBSC. The effect of various parameters, such as the bolt diameter and tensile strength, on the load-slip behaviour of the connectors has been discussed. Other parameters considered in the analysis were the bolts pretension, bolts height to diameter ratio and the compressive strength of the precast concrete plugs.

A change in the diameter or the tensile strength of the bolt connectors had a significant impact on the shear resistance of both LNSC and FBSC. More specifically, up to 2.5 times higher resistance was achieved when M22 bolts were used instead of M12 in both connectors. Similarly, the increase of the tensile strength of the bolts from 800MPa to 1115MPa increased the shear resistance of LNSC by almost 25%, while the shear resistance of LNSC by 45%. Specimens with high tensile strength or high diameter (M22/M20) failed by concrete failure in both FBSC and LNSC specimens. The plugs' compressive strength had a limited impact on the shear resistance of the specimens. Increasing the plugs' compressive stress from 50MPa to 90MPa caused a 5% increase in the shear resistance of the LNSC, while increasing the plugs' compressive stress from 50MPa to 100MPa caused a 10% increase in the shear resistance of the FBSC. The bolt pretension had a negligible effect on the shear resistance of LNSC. On the contrary, increasing the bolt pretension in FBSC specimens from 50kN

to 80kN led to a 14% increase in their shear resistance. Finally, the bolt diameter to height ratio seem to affect the concrete degradation in front of the connectors in both LNSC and FBSC. In the FBSC, decreasing the connector height to diameter ratio, the damage of the concrete in front of the connector was so extensive, that caused the plug to fail, and subsequently the slab to crack.

To have a better understanding of the structural behaviour of the demountable connectors, full-scale beam specimens were built and tested using FE analysis. The steel concrete composite beams used FBSC to achieve composite action between the steel beam and the concrete slab. FBSC was chosen instead of LNSC due to the availability of experimental results in literature that allowed the validation of the FE models. The behaviour of the composite beams was analysed using various shear connection ratios.

6.2 Conclusions

Based on the verification FE analysis and FEA parametric results of the LNSC, the following main conclusion can be drawn:

- The LNSC has high shear resistance and therefore less shear connectors may be required to achieve composite action in steel-concrete composite beams in comparison with welded studs or previously proposed bolted shear connectors.
- The LNSC has large slip capacity (up to 14.9 mm for M16 bolts). However, the slip capacity of M20 or M22 is limited, due to the failure of the precast plug and slab.
- Two failure modes of the push-out test specimens were observed during the FE analysis: deflection of the bolts due to combined shear, bending and axial internal stresses and extensive concrete crushing in front of the conical nut and the bolt shank. The predominant failure mode of most of the specimens was the fracture of the high-strength bolts. However, the mode of failure was shifted from shear failure of the bolts to tensile cracking of the precast slab in the specimens where either large diameter bolts (M20 or M22) or bolts with high tensile strength (1115 MPa) were used.
- Increasing the diameter of the bolts was found to considerably increase the shear resistance of the specimens. More specifically, up to 2.5 times increased shear resistance was observed for specimens with M22 bolts compared to the specimens with M12 bolts. Slip capacity and stiffness of the specimens were also affected by changing the bolt diameter.
- Increasing the bolt pretension between the conical nut and the upper hexagonal nut from 25 kN to 80 kN, was found to have negligible effect on the shear resistance and slip capacity of the LNSC.
- An increase of the plug compressive strength from C50 to C90 had a minor influence on the shear resistance (5% increase), stiffness (7% increase) and slip capacity (2% increase) of the LNSC specimens.

- Increasing the bolts height to diameter ratio from 6.75 to 9 had a minor influence on the shear resistance (8% increase) and the slip capacity (less than 1% increase) of the specimens. However, the height to diameter ratio has a significant impact on the stiffness of the specimens (up to 23% increase).
- The tensile strength of the bolts was found to be a significant parameter that highly affects the shear behaviour of the LNSC. It was concluded that both the shear resistance and the slip capacity of the LNSC push-out specimens increased by 25%, when the tensile strength of the bolts was increased from 800 MPa to 1115 MPa. Similarly, the stiffness of the specimens was increased by almost 15%.
- The equation proposed by the Cl. 6.6.3.1. of BS EN 1994-1-1 [6] to define the design shear resistance of headed studs cannot be used to predict the shear resistance of the LNSC. This is because the load-bearing capacity of the LNSC is not only attributed to the pure shear resistance of the bolts, but also to the friction at steel beam – concrete plug interface and to the ability of the bolts to deflect.
- The proposed design equation for the LNSC was evaluated against parametric results from specimens with various bolt diameters, plug concrete strength, bolt heights, bolt preloads and bolt tensile strengths. It was concluded that the design equation was able to predict the shear resistance of the LNSC with maximum absolute deviation less than 10%.

Based on the verification FE analysis and FEA parametric results of the FBSC, the following main conclusion can be drawn:

- FBSCs have large slip capacity with up to 16 mm for M16 bolts. The slip capacity of M20 and M22 bolts was relatively low due to the extensive tensile cracking of the slab prior to the bolt failure but higher than the 6 mm required according to the BS EN 1994-1-1 [6] for a ductile connector.
- The predominant failure mode of the most FBSC specimens was the fracture of the bolt connectors due to combined shear, bending and axial internal stresses. Extensive concrete crushing was also observed in all specimens in a limited area in front of the conical nut and the bolt shank. However, in specimens where bolts with large diameter (M20 or M22) or high tensile strength were used (1115 MPa), extensive tensile cracking was observed before the shear fracture of the bolt connectors.
- Specimens with M22 bolts showed higher shear resistance (up to 2.5 times higher) compare to the specimens with M12 bolts.
- The tensile strength of the bolts was found to highly affect the shear resistance of the specimens. Increasing the bolt tensile strength from 800 MPa to 1115 MPa, increased the shear resistance of the specimens up to 45%.

- Increasing the bolt pretension of the bolts, caused up to 14% increase on the shear resistance and up to 10% increase on the stiffness of the specimens. This is because the friction at steel beam – concrete plugs interface was increased as well.
- An increase in the plug's compressive strength from C50 to C100 had a limited influence on both shear resistance of the specimens; max increase was 10%.
- Decreasing the bolts height to diameter ratio from 8.9 to 7.3 had a severe impact on the behaviour of the FBSC. Extensive concrete compression was observed in the area in front of the bolt shank, which resulted to the tensile cracking of the precast concrete slab. However, the slip capacity, the shear resistance and the stiffness of the specimens were not severely affected.
- The proposed design equation that predicts the shear resistance of the FBSC was evaluated against parametric results from specimens with various bolt diameters, plug concrete strength, bolt heights, bolt preloads and bolt tensile strengths. It was concluded that the design equation was able to predict the shear resistance of the FBSC with maximum absolute deviation less than 10%.

Based on the verification FE analysis and FEA parametric results of the steel-concrete composite beams equipped with FBSCs, the following main conclusion can be drawn:

- The FE model was able to capture the load-deflection behaviour of the composite beam up to failure, which is a significant task, since the failure of the specimen was not captured by the experimental investigation.
- The moment capacity of the steel-concrete composite beams was around 1320 kNm, which is only 3% less than the plastic moment resistance of the composite section (i.e. 1365 kNm) calculated according to BS EN 1994-2.
- The slip distribution along the length of the beam showed that the maximum slip at 50% of the ultimate applied load was less than 1 mm. This indicated that full composite action can be achieved for moment up to 660 kNm.
- The slip along the shear spans of the composite beam was almost constant, while a sharp decrease was observed at the mid-span. This verifies the assumption that shear connectors are not required in the areas where there is no shear and the moment is constant.
- Severe deflection of the bolt connectors at the shear spans of the beam and failure due to combined axial, shear and bending stresses was observed during the analysis. The shear connectors in the area of constant moment were not deflected.
- Concentration of tensile stresses was observed at the mid-span of the steel beam which exceeded the yield strength of the beams. In addition, compressive stresses that exceed the tensile strength of the beam were observed in the area around the bolts holes. This indicates that the steel beam has yielded in the mid-span, while small cracks were formed around the bolts connectors.

- Extensive concrete crushing was observed at the bottom of the precast concrete slab, in the area around the slab pockets as well as at the top of the concrete slab, in the area where the loads were applied. Material degradation due to concentration of tensile stresses was also observed at the bottom of the slab at the location of the loads.
- The results of the parametric study showed that the tensile strength of bolt connectors did not have a significant influence of the moment capacity of the beams. More specifically, up to 5% increased moment capacity was recorded by increasing the tensile strength of the bolts from 800 MPa to 950 MPa.
- Increasing the compressive strength of the slabs from C50 to C70 did not have any substantial effect on the moment capacity of the beams; the moment capacity of the composite beams was increased by 3%.
- The yield strength of the steel beam highly affects the moment capacity of the composite beams. Up to 44% increased moment capacity was observed when S450 instead of S235 steel beams were used.

Based on the analysis approach that was adopted for the FE analysis, the following conclusions can be drawn:

- The FE models developed in this research thesis were capable to capture the fundamental behaviour of the shear connectors investigated. The shear resistance, stiffness and slip capacity of the connectors were predicted accurately and compared well with the experimental results available in literature.
- The ductile progressive damage models used to simulate the behaviour of high-strength bolts were capable to capture the material degradation due to void nucleation, growth and coalescence of voids. The models were calibrated using standard tensile test results available in the literature and subsequently, they were used in the FE analysis of the push-out and beam tests.
- Concrete damage plasticity (CPD) was successfully used to capture the extensive concrete crushing in front of the shear connectors in the FE analysis of the push-out tests, as well as the tensile cracking of the precast concrete slabs in specimens where bolts with large diameter or high tensile strength were used.
- The Explicit solver was successfully employed for the analysis of the push-out tests. The kinetic energy was maintaining under 5% of the corresponding internal energy throughout the analysis to ensure that the quasi-static conditions are met.
- The mass scaling option offered by ABAQUS/Explicit was successfully used for computational efficiency without compromising the accuracy of the results.

6.3 Recommendations for further research

Based on the conclusions drawn in this chapter, the following recommendations can be suggested for further research:

- Fatigue is often a major problem limiting the load-carrying capacity of steel-concrete composite beams. Therefore, it is crucial to evaluate fatigue shear resistance of the FBSC and LNSC with experimental and numerical tests.
- Precast composite beams using LNSC should be conducted to have a better overview of its capabilities.
- The design of long beams with partial shear connection using LNSC and FBSC should be tested to expand their use.
- Geopolymer concrete instead of Portland can be used for precast slabs to reduce the carbon emissions to the environment.
- A life cycle cost assessment can be conducted to estimate the cost reductions when LNSCs and FBSCs are used instead of welded studs.

List of References

[1] Gkoumas, K., Marques Dos Santos, F.L., van Balen, M., Tsakilidis, A., Ortega Hortelano, A., Grosso, M., Haq, G., Pekar, F., Research and Innovation in bridge maintenance, inspection and monitoring, Joint Research Centre (JRC), Luxembrourg: Publications Office of the European Union, 2019.

[2] ASCE, Infrastructure Report Card, www.infrastructurereportcard.org/cat-item/bridges, 2017.

[3] Tadros, M.K., Baishya, M.C., Rapid replacement of bridge deck, NCHRP Rep. 407, Transportation Research Board, Washington, DC, 1998.

[4] Ritchie, H., Roser, M., CO2 and greenhouse gas emissions, Retrieved from http://ourworldindata.org/co2-and-other-greenhouse-gas-emissions, Published online at OurWorldInData.org, 2019.

[5] White Paper on Transport. Directorate-General for Mobility and Transport. Commision, E. Luxembourg; 2011.

[6] Eurocode 4: Design of composite steel and concrete structures. Part 1-1: General rules and rules for buildings. BS EN 1994-1-1. BSI (British Standards Institution). London; 2004.

[7] Eurocode 4: Design of composite steel and concrete structures. Part-2: General rules and rules for bridges. BS EN 1994-2. BSI (British Standards Institution). London; 2004.

[8] Viest, M.I. Investigation of Stud Shear Connectors for Composite Concrete and Steel T-Beams. ACI Journal. 1956; 52: (4): 875-892.

[9] Oehlers, D.J., Bradford, M.A., Elementary behavior of composite steel & concrete structural members, Butterworth-Heinemann, Oxford, 1999.

[10] Ollgaard, J.G., Slutter, R.G., Fisher, J.W. Shear strength of stud connectors in lightweight and normal-weight concrete. Engineering Journal, American Institute of Steel Construction. 1971; 8: 55-64.

[11] Oehlers, D.J., Coughlan, C.G. The shear stiffness of stud shear connections in composite beams. Journal of Constructional Steel Research. 1986; 6: (4): 273–284.

[12] Johnson, R.P., Composite Structures of Steel and Concrete: Volume 1: Beams, Slabs,

Columns, and Frames for Buildings. 3rd edition

Blackwell scientific publications, Oxford, UK, .

[13] BS EN ISO 14555:2017. Welding. Arc stud welding of metallic materials. (BSI), B.S.I. UK; 2017.

[14] Dallam, L. High strength bolt shear connectors - Pushout tests. ACI Journal. 1968; 65: 767-769.

[15] Dallam, L., Harpster, J., Composite beam tests with high strength bolt shear connectors, Dept. of Civil Engineering, Univ. of Missouri, Columbia, MO, 1968.

[16] Marshall, W.T., Nelson, H.M., Banerjee, H.K. An experimental study of the use of high-streength friction-grip bolts as shear connectors in composite beams. The structural engineer: journal of the Institution of Structural Engineers. 1971; 49: (4): 171-178.

[17] Dedic, D.J., Klaiber, F.W. High Strength Bolts as Shear Connectors in Rehabilitation Work. Concrete International, Americal Concrete Institute (ACI). 1984; 6: (7): 41- 46.

[18] Kwon, G., Engelhardt, M.D., Klingner, R.E. Behavior of post-installed shear connectors under static and fatigue loading. Journal of Constructional Steel Research. 2010; 66: (4): 532-541.

[19] Kwon, G., Engelhardt Michael, D., Klingner Richard, E. Experimental Behavior of Bridge Beams Retrofitted with Postinstalled Shear Connectors. Journal of Bridge Engineering. 2011; 16: (4): 536-545.

[20] Lam, D., Saveri, E., Shear Capacity of Demountable Shear Connectors, Proceedings of the 10th International Conference on Advances in Steel Concrete Composite and Hybrid Structures, vol 2012, Singapore, 2012.

[21] Lam, D., Dai, X.H., Saveri, E. Behaviour of demountable shear connectors in steel-concrete composite beams. Composite construction in steel and concrete. 2013; 7: 618-631.

[22] Lee, M.S.S., Bradford, M.A., Sustainable composite beams with deconstructable bolted shear connectors, Taylor & Francis Group, London, 2013.

[23] Moynihan, M.C., Allwood, J.M. Viability and performance of demountable composite connectors. Journal of Constructional Steel Research. 2014; 99: 47-56.

[24] Pavlović, M., Marković, Z., Veljković, M., Buđevac, D. Bolted shear connectors vs. headed studs behaviour in push-out tests. Journal of Constructional Steel Research. 2013; 88: 134-149.

[25] Spremić, M., Marković, Z., Veljković, M., Budjevac, D. Push–out experiments of headed shear studs in group arrangements. Advanced Steel Construction 2013; 9: (2): 170-191.

[26] Chen, Y.T., Zhao, Y., West, J.S., Walbridge, S. Behaviour of steel–precast composite girders with through-bolt shear connectors under static loading. Journal of Constructional Steel Research. 2014; 103: 168-178.

[27] Ataei, A., Bradford, M.A., Liu, X. Experimental study of composite beams having a precast geopolymer concrete slab and deconstructable bolted shear connectors. Engineering Structures. 2016; 114: 1-13.

[28] Pathirana, S.W., Uy, B., Mirza, O., Zhu, X. Bolted and welded connectors for the rehabilitation of composite beams. Journal of Constructional Steel Research. 2016; 125: 61-73.

[29] Pathirana, S.W., Uy, B., Mirza, O., Zhu, X. Flexural behaviour of composite steel-concrete beams utilising blind bolt shear connectors. Engineering Structures. 2016; 114: 181-194.

[30] Rehman, N., Lam, D., Dai, X., Ashour, A. Experimental study on demountable shear connectors in composite slabs

with profiled decking. Journal of Constructional Steel Research. 2016; 122: 178-189.

[31] Suwaed, A.S., Karavasilis, T.L. Novel demountable shear connector for accelerated disassembly, repair, or replacement of precast steel-concrete composite bridges. Journal of Bridge Engineering. 2017; 22: 04017052.

[32] Suwaed, A.S.H., Karavasilis, T.L. Removable shear connector for steel-concrete composite bridges. Steel and Composite structures. 2018; 29: (1): 107-123.

[33] Feidaki, E., Vasdravellis, J., He, J., Wang, S. Steel-yielding demountable shear connector for composite floors with precast hollow-core slab units. Journal of Structural Engineering. 2019; 145: (8).

[34] Yang, F., Liu, Y., Jiang, Z., Xin, H. Shear performance of a novel demountable steel-concrete bolted connector under static push-out tests. Engineering Structures. 2018; 160.

[35] Kozma, A., Odenbreit, C., Braun, M.V., Veljkovic, M., Nijgh, M.P. Push-out tests on demountable shear connectors of steel-concrete composite structures. Structures. 2019; 21: (45-54).

[36] Suwaed Ahmed, S.H., Karavasilis, T.L. Demountable steel-concrete composite beam with full-interaction and low degree of shear connection. Journal of Constructional Steel Research. 2020; 171: 106152.

[37] Liu, X., Bradford Mark, A., Lee Michael, S.S. Behavior of High-Strength Friction-Grip Bolted Shear Connectors in Sustainable Composite Beams. Journal of Structural Engineering. 2015; 141: (6): 04014149.

[38] Liu, X., Bradford, M.A., Chen, Q.-J., Ban, H. Finite element modelling of steel–concrete composite beams with high-strength friction-grip bolt shear connectors. Finite Elements in Analysis and Design. 2016; 108: 54-65.

[39] Dai, X.H., Lam, D., Saveri, E. Effect of Concrete Strength and Stud Collar Size to Shear Capacity of Demountable Shear Connectors. Journal of Structural Engineering. 2015; 141: (11): 04015025.

[40] Yun, X., Gardner, L. Stress-strain curves for hot-rolled steels. Journal of Constructional Steel Research. 2017; 133: 36-46.

[41] Eurocode 2: Design of concrete structures - Part 1-1 : General rules and rules for buildings BS EN 1992-1-1. BSI (British Standards Institution). London; 2004.

[42] Suwaed, A.S.H., Karavasilis, T.L. Novel Demountable Shear Connector for Accelerated Disassembly, Repair, or Replacement of Precast Steel-Concrete Composite Bridges. Journal of Bridge Engineering. 2017; 22: (9): 04017052.

[43] Fisher, J., Ramseier, P., Beedle, L. Strength of A440 steel joints connected with A325 bolts. Publication IABSE. 1963; 23: (Reprint 245).

[44] Carreira, D., Chu, K. Stress–strain relationship for plain concrete in compression. ACI Journal. 1985; 82: (797-804).

[45] Hsu, L., Hsu, C. Complete stress - strain behaviour of high-strength concrete under compression. Magazine of Concrete Research. 1994; 169: (301-312).

[46] Papanikolaou, V., Kappos, A. Confinement-sensitive plasticity constitutive model for concrete in triaxial compression. International Journal of Solids and Structures. 2007; 44: 7021–7048.

[47] Yu, T., Teng, J.G., Wong, Y.L., Dong, S.L. Finite element modeling of confined concrete-I: Drucker–Prager type plasticity model. Engineering Structures. 2010; 32: (3): 665-679.

[48] ABAQUS. ABAQUS/CAE User's Manual. Hibbitt, Karlsson & Sorensen, Inc. 2010.

[49] Hillerborg, A., Modéer, M., Petersson, P.E. Analysis of crack formation and crack growth in concrete by means of fracture mechanics and finite elements. Cement and Concrete Research. 1976; 6: (6): 773-781.

[50] Bažant, Z.P., Becq-Giraudon, E. Statistical prediction of fracture parameters of concrete and implications for choice of testing standard. Cement and Concrete Research. 2002; 32: (4): 529-556.

[51] CEB-FIP Model Code 1990. FIP. London; 1993.

[52] Mander, J., Seismic design of bridge piers., Department of Civil Engineering, vol PhD, University of Canterbury,, Christchurch, New Zealand, 1983.

[53] Panga, X., Hua, Y., Tanga, S., Xianga, Z., Wud, G., Xue, T., Wang, X. Physical properties of high-strength bolt materials at elevated temperatures. Results in Physics. 2019; 102156.

[54] Ellobody, E., Finite Element Analysis and Design of Steel and Steel-Concrete Composite Bridges, Butterworth-Heinemann, Oxford, 2014, p. 47-111.

[55] Steel, concrete and composite bridges. Part 5: Code of practice for design of composite bridges. BS 5400-5. BSI (British Standards Institution). London; 1979.

[56] UK National Annex to Eurocode 3: Design of steel streuctures, Part 1-8: Design of Joints. NA to EN 1993-1-8. BSI (British Standars Institute). London; 2005.

[57] Aerospace series - Rings retaining, radial mounting, steel, phosphated. BS EN 3386. BSI (British Standards Institution). London; 2012.

[58] High-strength structural bolting assemblies for preloading, Part 9: System HR or HV – Direct tension indicators for bolt and nut assemblies. BS EN 14399-9. BSI (British Standards Institution). London, UK; 2009.

[59] "Metallic materials — Tensile testing, Part 1: Method of test at ambient temperature. BS EN ISO 6892-1. BSI (British Standards Institution). London, UK; 2009.

[60] Eurocode 3: Design of steel structures - Part 1-1: General rules and rules for bridges. BS EN 1993-1-1: 2005+A1: 2014. BSI (British Standards Institution). London; 2005.

[61] UK National Annex to Eurocode 2: Design of concrete structures. Concrete bridges. Design and detailing rules. NA to EN 1992-2: 2005. BSI (British Standars Institute). London; 2005.